

---

Electronic Thesis and Dissertation Repository

---

11-27-2012 12:00 AM

## Strategies for visco-acoustic waveform inversion in the Laplace-Fourier domain, with application to the Nankai subduction zone

Rie Kamei  
*The University of Western Ontario*

Supervisor  
R. Gerhard Pratt  
*The University of Western Ontario*

Graduate Program in Geophysics  
A thesis submitted in partial fulfillment of the requirements for the degree in Doctor of  
Philosophy  
© Rie Kamei 2012

Follow this and additional works at: <https://ir.lib.uwo.ca/etd>



Part of the [Geophysics and Seismology Commons](#)

---

### Recommended Citation

Kamei, Rie, "Strategies for visco-acoustic waveform inversion in the Laplace-Fourier domain, with application to the Nankai subduction zone" (2012). *Electronic Thesis and Dissertation Repository*. 1061. <https://ir.lib.uwo.ca/etd/1061>

This Dissertation/Thesis is brought to you for free and open access by Scholarship@Western. It has been accepted for inclusion in Electronic Thesis and Dissertation Repository by an authorized administrator of Scholarship@Western. For more information, please contact [wlsadmin@uwo.ca](mailto:wlsadmin@uwo.ca).

STRATEGIES FOR VISCO-ACOUSTIC WAVEFORM INVERSION IN  
THE LAPLACE-FOURIER DOMAIN, WITH APPLICATION TO  
THE NANKAI SUBDUCTION ZONE

(Spine title: Strategies for visco-acoustic waveform inversion)

(Thesis format: Integrated Article)

by

Rie Miyoshi (Kamei)

Graduate Program in Geophysics

A thesis submitted in partial fulfillment  
of the requirements for the degree of  
Doctor of Philosophy

The School of Graduate and Postdoctoral Studies  
The University of Western Ontario  
London, Ontario, Canada

© Rie Miyoshi (Kamei) 2012

THE UNIVERSITY OF WESTERN ONTARIO  
School of Graduate and Postdoctoral Studies

**CERTIFICATE OF EXAMINATION**

Examiners:

.....  
Dr. Kristy Tiampo

Supervisor:

.....  
Dr. R. Gerhard Pratt

.....  
Dr. Robert Shcherbakov

.....  
Dr. Blaine Chronik

.....  
Dr. Andrew J. Calvert

The thesis by

**Rie Miyoshi (Kamei)**

entitled:

**Strategies for visco-acoustic waveform inversion in the Laplace-Fourier domain, with application to the Nankai subduction zone**

is accepted in partial fulfillment of the  
requirements for the degree of  
Doctor of Philosophy

.....  
Date

.....  
Chair of the Thesis Examination Board

## Co-Authorship Statement

Versions of Chapter 2, 3, 4, and 5 of this thesis have either been previously published in a journal or have been submitted to a journal.

The co-authors of Chapter 2, 3 and 4 are Dr. R. Gerhard Pratt, and Dr. Takeshi Tsuji from Kyushu University. Dr. Pratt provided mentorship, instructions, and manuscript editing. Dr. Pratt also provided the base program code for the applications of the Laplace-Fourier domain waveform modelling and inversion; significant modifications to this base code are my own responsibility. Dr. Tsuji provided instructions for geological interpretation, and background information of the Nankai subduction zone.

The co-author of Chapter 5 is Dr. R. Gerhard Pratt, who provided a mentorship, and guidance in theoretical understanding of visco-acoustic waveform inversion and regularization, as well as manuscript editing.

In all Chapters, data processing, and synthetic model building was conducted entirely by myself, with suggestions and advice from my co-authors. Inversion strategies developed in Chapter 2, 3, and 4 were adopted and implemented by myself.

## Acknowledgement

First and foremost, I would like to express my sincere gratitude to my supervisor, R. Gerhard Pratt for his great insights into waveform inversion, for extensive manuscript editing, for his dedicated mentorship and support, for his patience and generosity throughout the course of my PhD work both at Queen's University and Western University.

The administrative staffs at Western and Queen's Universities were greatly appreciated for their prompt and continuous assistance, especially Marie Schell, Kevin Jordan and Diane Hyde. I also received a fair amount of technical support at Western from Bernie Dunn, John Brunet, and Barry Price.

I spent a fruitful internship at TOTAL. The mentorship provided by Paul Williamson, and Fuchun Gao was greatly appreciated and broadened my scientific perspectives.

I had great and helpful conversations with my fellow geophysicists; Andrew Benders, Michael Afanasiev, Brendan Smithyman, Eric Takam Takougang, Florian Bleibinhaus, Marco Paschke and Nori Nakata. Visits to GFZ Potsdam, LMU, University of Wisconsin, Madison stimulated my scientific interests, thanks to Klaus Bauer, Karin Sigloch and Harold Tobin. My mentors, colleagues and friends who specialize in geology boosted my geological understanding; especially Takeshi Tsuji, Ayumu Miyakawa, Joanne Tudge, and Yasuhiro Yamada. I also thank Takeshi Tsuji for introducing me to the data set from the Nankai subduction zone, which changed the course of PhD project, and my academic life. I also thank Matsuoka Toshifumi for introducing me to wave propagation in random heterogeneous media during my Masters program in Kyoto University. The programming code written during the period was used for Chapter 5.

I cannot express enough my gratitude to my friends at Western, Soushyant Kiarasi, Hadi Ghofrani Attieh Eshaghi, Samira Alipour, Linada Kachi, Zhongying Mi, and Laura Sanchez, for the joy, difficulties, and laughs we shared. I also thank Alan Baird from Queen's University for being a wonderful friend who helped me adjust to a new life. Also I thank deeply my wonderful personal friends, Bernadette Pratt and Martine Bresson, who always expressed love, and sincere support throughout this long journey. I thank my parents and parents-in-law for continuous financial support and understanding during the last 6 years.

Finally of course, I thank my husband Takayuki Miyoshi and my children from the bottom of the heart for enduring days and years of difficult time, late nights, long absences, and most of all for their love.

# Abstract

Waveform inversion is a non-linear and ill-posed inverse problem, with the objective of utilizing the full information content of recorded seismic waveforms. A Laplace-Fourier domain implementation allows a natural ‘multiscale’ approach that mitigates the non-linearity and ill-posedness by inverting low-frequency, early arrival data in the initial stages of inversion. High-frequency components and late arrivals are incorporated at a later stage. This allows the development of robust inversion strategies capable of handling large wide-angle crustal surveys, leading to reliable, high-resolution velocity and attenuation models of crustal structures.

I apply waveform inversion to extract a P-wave velocity model of the active mega-splay fault system in the seismogenic Nankai subduction zone offshore Japan, using controlled-source Ocean Bottom Seismograph data. The resulting velocity model includes detailed thrust structures and low velocity zones not previously identified. The connection of large low-velocity zones in the inner and outer wedge suggests a significant distribution of over-pressured regions in the vicinity of the mega-splay fault, with the potential to strongly influence coseismic rupture propagation.

I identify six-fold key strategies for successful waveform inversion; i) the availability of low-frequency and long offset data, ii) a highly accurate starting model, iii) a hierarchical approach in which phase spectra are inverted first and amplitude information is only incorporated in the final stages, iv) a Laplace-Fourier domain approach, v) careful preconditioning of the gradient, vi) strategies for source estimation. Chequerboard tests and point-scatter tests demonstrate the resolution and the limitations of the acoustic implementation. I also compare four misfit functionals for optimization, and demonstrate that velocity information may be reliably extracted from phase alone, and that amplitude information is secondary in updating the velocity model.

Finally I develop inversion strategies for retrieving both velocity and attenuation models. Cross-talk between these two classes of parameter estimates arises from the lack of parameter scaling in the gradient of the objective function, and primarily affects the attenuation model. I show that the cross-talk can be suppressed by the combination of an appropriate attenuation damping parameter, and by the use of smoothing constraints. Initial velocity-only inversions also help in reducing the effects of cross-talk in subsequent velocity-attenuation inversion.

**Keywords:** non-linear inverse problem, seismic waveform, waveform inversion, velocity, attenuation

# Contents

Certificate of Examination	ii
Co-Authorship Statement	iii
Acknowledgement	iv
Abstract	v
List of Figures	xi
List of Tables	xxii
<b>1 Introduction</b>	<b>1</b>
1.1 Tomography . . . . .	3
1.2 Waveform inversion . . . . .	6
1.2.1 Application of waveform inversion in the controlled source seismology	7
1.2.2 Non-linearity and non-uniqueness of waveform inversion . . . . .	9
1.3 Objectives of thesis . . . . .	10
1.4 Thesis outline . . . . .	11
References . . . . .	12
<b>2 Waveform tomography imaging of a mega-splay fault system in the seismogenic Nankai subduction zone</b>	<b>21</b>
2.1 Introduction . . . . .	21
2.2 Geological background . . . . .	23
2.3 Long offset OBS data . . . . .	27
2.4 Frequency-domain acoustic waveform tomography . . . . .	27
2.5 Results . . . . .	30
2.5.1 Interpretation . . . . .	34
2.5.1.1 Mega-splay fault and velocity discontinuities . . . . .	34
2.5.1.2 Low velocity zones . . . . .	35

2.5.1.3	Structures underneath the outer ridge . . . . .	35
2.5.2	Verification . . . . .	36
2.5.3	Comparison with the pre-stack migration section . . . . .	36
2.6	Discussions . . . . .	37
2.7	Conclusions . . . . .	39
	References . . . . .	40
<b>3</b>	<b>On acoustic waveform tomography of wide-angle OBS data — Strategies for preconditioning and inversion</b>	<b>47</b>
3.1	Introduction . . . . .	47
3.1.1	Outline of the chapter . . . . .	52
3.2	Geological background, survey description, and travelttime tomography result	53
3.2.1	Geological background . . . . .	53
3.2.2	Survey description . . . . .	55
3.2.3	Travelttime tomography result . . . . .	55
3.3	Theory . . . . .	56
3.3.1	The Laplace-Fourier domain . . . . .	56
3.3.2	Forward modelling . . . . .	57
3.3.3	Optimization . . . . .	58
3.3.4	Source estimation . . . . .	61
3.4	Data and Preprocessing . . . . .	62
3.4.1	Data description . . . . .	62
3.4.2	Preprocessing . . . . .	64
3.5	Inversion Strategies . . . . .	67
3.5.1	Waveform inversion parameter choices . . . . .	69
3.5.2	Starting model . . . . .	70
3.5.3	Scheduling of Laplace-Fourier domain parameters . . . . .	71
3.5.3.1	Frequency sampling . . . . .	71
3.5.3.2	Decay constant sampling . . . . .	73
3.5.4	Gradient preconditioning . . . . .	73
3.6	Results and validation . . . . .	76
3.6.1	Waveform tomography results . . . . .	76
3.6.2	Evaluation and verification of waveform tomography results . . . . .	83
3.6.2.1	Comparison with a Pre-stack migration image . . . . .	83
3.6.2.2	Time-domain waveforms . . . . .	85
3.6.2.3	Improvement in source estimation coherency . . . . .	88



3.6.3	Resolution tests . . . . .	88
3.6.3.1	Chequerboard testing . . . . .	89
3.6.3.2	Point-scatter testing . . . . .	93
3.7	Discussion and conclusions . . . . .	94
3.7.1	Data acquisition . . . . .	94
3.7.2	Starting model and geological complexity . . . . .	96
3.7.3	Hierarchical inversion strategies to mitigate non-linearity . . . . .	96
3.7.4	Acoustic waveform inversion of elastic field data . . . . .	97
3.7.5	Appraisal of results . . . . .	98
3.7.6	Conclusions . . . . .	99
	References . . . . .	100
<b>4</b>	<b>On misfit functionals in waveform inversion, with application to wide-angle OBS data</b>	<b>108</b>
4.1	Introduction . . . . .	108
4.1.1	Outline of the chapter . . . . .	112
4.2	Theory . . . . .	112
4.2.1	The Laplace-Fourier domain . . . . .	112
4.2.2	Forward modelling . . . . .	113
4.2.3	Optimization . . . . .	114
4.2.3.1	Misfit functionals - four alternative definitions . . . . .	114
4.2.3.2	Optimization algorithms . . . . .	116
4.3	Waveform inversion of OBS data from the Nankai subduction zone . . . . .	118
4.3.1	Data acquisition and preprocessing . . . . .	118
4.3.2	Inversion settings . . . . .	119
4.4	Results . . . . .	123
4.4.1	Gradient images . . . . .	123
4.4.2	Comparison of velocity images . . . . .	125
4.4.2.1	Velocity images . . . . .	125
4.4.2.2	Synthetic waveforms . . . . .	130
4.4.2.3	Reduction of misfits during the inversion . . . . .	130
4.4.3	Amplitude information . . . . .	134
4.4.3.1	Synthetic waveforms . . . . .	135
4.4.3.2	Misfit functionals . . . . .	140
4.5	Discussion and conclusions . . . . .	142
4.5.1	Dynamic range of data . . . . .	143

4.5.2	Kinematic and dynamic components of wavefields . . . . .	143
References	. . . . .	144
<b>5</b>	<b>Inversion strategies for visco-acoustic waveform inversion</b>	<b>149</b>
5.1	Introduction . . . . .	149
5.1.1	Outline of the chapter . . . . .	153
5.2	Theory . . . . .	153
5.2.1	Laplace-Fourier domain . . . . .	153
5.2.2	Forward modelling . . . . .	154
5.2.3	Optimization . . . . .	155
5.2.3.1	Computation of the gradient $\nabla_{\mathbf{m}}E$ . . . . .	158
5.2.3.2	Numerical implementation . . . . .	159
5.2.3.3	Coordinate change to reference frequency . . . . .	162
5.3	Synthetic tests . . . . .	163
5.3.1	Model description and waveforms . . . . .	163
5.3.2	Inversion settings . . . . .	167
5.3.3	Effects of cross-talk . . . . .	170
5.3.4	Simultaneous inversion . . . . .	176
5.3.5	Sequential inversion . . . . .	177
5.3.5.1	Stage 1: Velocity inversion . . . . .	177
5.3.5.2	Stage 2: Velocity and attenuation inversion . . . . .	182
5.3.6	Smoothing of the model gradient . . . . .	183
5.3.7	Effects of time-damping . . . . .	185
5.3.8	Sensitivity to noise . . . . .	189
5.4	Discussion and conclusions . . . . .	192
Appendix 5A	Relationships between preconditioning matrix and model covariance . . . . .	194
Appendix 5B	Alternative expression for gradient and anti-causal propagation . . . . .	196
Appendix 5C	Choice of $\xi$ based on trade-off curves . . . . .	197
References	. . . . .	198
<b>6</b>	<b>General Conclusions and Discussions</b>	<b>204</b>
6.1	Conclusions . . . . .	204
6.2	Future study . . . . .	206
6.2.1	Perspective on the Nankai subduction data . . . . .	206
6.2.2	Perspective on waveform inversion . . . . .	207
6.2.2.1	Visco-acoustic waveform inversion . . . . .	207
6.2.2.2	Laplace-domain waveform inversion . . . . .	208

6.2.2.3	Optimization methods . . . . .	209
6.2.2.4	Towards 3D full elastic waveform inversion . . . . .	210
	References . . . . .	211
	<b>Curriculum Vitae</b>	<b>214</b>

# List of Figures

1.1	Schematic diagram of marine reflection- and refraction-survey examples. Seismic energy is excited by an air gun for both surveys. In the reflection survey, reflected waves (yellow) are recorded at hydrophones on a streamer cable. In the refraction survey, refracted waves (white) are recorded at Ocean Bottom Seismographs (either or both of geophones and hydrophones). Note that other acquisition settings are possible for both surveys. . . . .	2
2.1	Maps of southwest Japan and the Nankai Trough. An ocean bottom seismograph (OBS) survey was conducted in 2004 (solid black line). Circles indicate OBS positions; red circles indicate OBS positions used for waveform tomography in this chapter. The 3D reflection survey area used by Moore et al. (2009) is shown as a grey-shaded area. Dark blue contours show the coseismic slip distribution of the 1944 Tonankai earthquake (Kikuchi et al., 2003). The subduction direction of the Philippine Sea Plate is based on the MORVEL vector of DeMets et al. (2010). . . . .	24
2.2	Interpreted pre-stack migration section (after Figure F6B in Moore et al., 2009). Two low velocity zones identified by previous researchers are outlined in magenta and identified as LVZ <sub>1</sub> (Bangs et al., 2009) and LVZ <sub>2</sub> (Park et al., 2010). PTZ stands for protothrust zone, BSR for bottom simulating reflector, DF for deformation front, and VE for vertical exaggeration. DS represents the décollement stepdown interpreted in Park et al. (2002a). Large black arrow indicates subduction direction of the Philippine Sea Plate. . . . .	25

2.3 (a) P-wave velocity model obtained by travelttime tomography (Nakanishi et al., 2008), and used as a starting model for waveform tomography in this chapter. Areas with poor wavepath coverage are shaded. The horizontal axis is the landward distance from the deformation front (see Fig. 2.2). Yellow circles show the location of the OBS used for analysis in this study. (b) Velocity structure after waveform tomography. (c) Vertical profiles of the velocity structures at the distances of 25, 35, 45, and 55 km from the deformation front (red triangles in (a) and (b)). Grey lines in (c) represent the velocities in the starting model in (a), the black lines correspond to the waveform tomography results in (b), and the dashed lines correspond to the background model as the 3rd order polynomial  $V_o(x, z) = a(z - z_0(x))^3 + b(z - z_0(x))^2 + c(z - z_0(x)) + d$ , best fitting the travelttime tomography result (Fig. 2.5a). . . . . 28

2.4 Background velocity model defined by  $V_o(x, z) = a(z - z_0(x))^3 + b(z - z_0(x))^2 + c(z - z_0(x)) + d$ , where  $z_0$  is the depth of the seafloor. Red triangles indicate the locations of the vertical profiles shown in Figs 2.3c and 2.5c. . . . . 29

2.5 De-trended  $\Delta V(x, z)$  velocity structures obtained by removing the best-fit  $V_o(x, z)$  background velocity of the analyzed area displayed in Fig. 2.4. (a) The de-trended waveform tomography result shown in colour. The horizontal axis represents the landward distance from the deformation front (see Fig. 2.2). Yellow circles show the location of the OBSs. (b) The same model as (a), depicted in grey scale. (c) Vertical profiles of the de-trended velocity structures at distances of 25, 35, 45, and 55km from the deformation front, (red triangles in (a) and (b)). Grey lines in (c) represent de-trended velocities from the starting model in Fig. 2.3a, and the black lines represent de-trended velocities from the waveform tomography results in Fig. 2.3b. . . . . 31

2.6 (a) The de-trended waveform tomography result with an overlay taken from the nearest 2D slice of the 3D migration volume (Moore et al., 2009). (b) The de-trended waveform tomography result with a geological interpretation. The strong velocity discontinuity appearing along the mega-splay fault between 20-60 km distance was divided into lines A, B and C. Lines B' and B'' represents the most seaward branching of the mega-splay fault. The low velocity zones are labelled LVZ<sub>1</sub> (landward), LVZ<sub>2</sub> (seaward), and LVZ<sub>3</sub> (under the outer ridge). Dashed line represents lithology boundaries unclear in waveform tomography, and interpreted in conjunction with the reflectors evident on the migration image in (a). Area D indicates the accretionary prisms which exhibit higher velocity values with respect to the  $V_o(x, z)$  background model. Area E shows a fourth low velocity layer within the older accretionary prisms in the inner wedge. . . . . 32

2.7 (a) Representative vertical component seismic waveforms recorded at the OBS located 65 km landward of the deformation front (Fig. 2.2). The red line indicates the picked first arrivals, and the yellow overlay indicates the interpreted wide angle reflection from the mega-splay fault. (b) Synthetic waveforms predicted in the starting velocity model (Fig. 2.3a) at the same OBS location, computed with a visco-acoustic finite difference method. Early arrival times in (b) correspond well with the observed data in (a), but the gather lacks the wide-angle reflections from the mega-splay fault. (c) Synthetic waveforms computed in the final waveform tomography result (Fig. 2.3b); these successfully reproduce the wide-angle reflections in the observed data in (a). . . . . 33

3.1 (a) Traveltime tomography result of Nakanishi et al. (2008), also used as a starting model for our waveform inversion, (b) de-trended model of (a) in colour, and (c) same as (b) in grey scale. The horizontal axis is the distance from the deformation front (see Fig. 2.2). Yellow circles show the location of the 16 bit OBS instruments, and red circles show the location of the 24 bit OBS instruments used in this study. . . . . 54

3.2	(a) Representative vertical component seismic waveforms recorded at OBS 47, located 65 km landward of the deformation front. The yellow line indicates the picked first arrivals. (b) RMS amplitude spectra from OBS 47. Amplitudes are normalized to the value at 5 Hz. The black line shows the amplitude spectrum of (a), the grey line after deconvolution (Fig. 3.4b), the dashed blue line shows the spectrum after bandpass filter (Fig. 3.4c), and the red line shows the spectrum after all preprocessing (Fig. 3.4d). . . . .	63
3.3	The preprocessing flow used to bring time-domain data through to Laplace-Fourier domain waveform inversion . . . . .	65
3.4	Processing of vertical component seismic waveforms from OBS 47. The yellow line indicates the picked first arrivals. (a) Raw data (b) Deconvolved wavefield (c) After band pass filter (2.5-8.0 Hz) (d) After Time-windowing and amplitude correction . . . . .	66
3.5	(a) Flowchart outlining waveform inversion. (b) Details of update step used in both stages in (a), corresponding to grey shaded boxes in (a) . . .	68
3.6	Synthetic OBS gather from the starting model (Fig. 3.1) at OBS 47, computed using a visco-acoustic forward modelling code. Picked first arrivals from the comparable real data are shown in yellow. . . . .	70
3.7	Observed wavefield with $\tau =$ (a) 0.167, (b) 0.333, and (c) 0.5 sec. The damped wavefields are displayed with the application of $\exp(t_0/\tau)$ to compensate for the amplitude loss, where $t_0$ is the picked arrival times. . . .	72
3.8	Effects of gradient filtering. (a) Raw P-wave gradient for the starting model, obtained with $f = 2.25, 2.50, 2.75, 3.00$ Hz, and $\tau = 2.0$ sec, and (b) the same gradient after the application of wavenumber filtering, and gradient masking. The logarithmic phase-only objective function (Eq.(3.13)) was used. Yellow circles show the location of the 16 bit OBS instruments, and red circles show the location of the 24 bit OBS instruments used in this study. . . . .	74
3.9	P-wave velocity structure after Stage 1 of waveform inversion. (a) $V_p$ model, (b) de-trended model of (a) in colour, and (c) same as (b) but shown in greyscale. . . . .	77
3.10	P-wave velocity structure after Stage 2 of waveform inversion. (a) $V_p$ model, (b) de-trended model of (a) in colour, and (c) same as (b) but shown in greyscale. . . . .	78

3.11	(a) Vertical velocity profiles and (b) de-trended velocity profiles at distances 55, 45, 35, 25 km (from left to right). Dashed grey lines show the velocity trend before removal $V_o(z)$ (only present in (a)), grey lines the starting model, dashed black lines the intermediate velocity models after Stage 1, black lines the final velocity, and grey dotted lines the velocities from the MVA of Park et al. (2010). . . . .	79
3.12	De-trended final waveform tomography result with interpretation. The strong velocity discontinuity appearing at depths of 5 - 11 km between distances between 20 km and 60 km is identified as lines A, B and C. Lines B' and B'' represent the seaward branching of the mega splay fault. The low velocity zones are labelled LVZ <sub>1</sub> (landward), LVZ <sub>2</sub> (seaward), and LVZ <sub>3</sub> (under the outer ridge). Dashed lines represent lithological boundaries as interpreted in conjunction with the reflectors evident on the migration image in Fig. 3.13. Area D indicates the seaward accretionary prism, exhibiting higher velocity values with respect to the $V_o(x, z)$ trend. Area E shows a fourth low velocity layer within the older accretionary prisms in the inner wedge. . . . .	80
3.13	De-trended final waveform tomography velocity model overlaid by the nearest 2D slice of 3D PSDM results in Moore et al. (2009), (a) in colour and (b) in grey scale . . . . .	81
3.14	(a) The nearest 2D slice of the 3D migration velocity model presented in Park et al. (2010), (b) de-trended velocity model of (a) in colour and (c) the de-trended velocity model in grey-scale. . . . .	82
3.15	(a) Representative vertical component seismic waveforms recorded at OBS 47. Data preprocessing was applied although bottom muting is omitted here so that later waveforms may be compared. (b) Predicted pressure wavefield at OBS 47 computed from the intermediate velocity model after Stage 1, and (c) from the final velocity model. The yellow lines indicate the picked first arrivals. . . . .	86
3.16	Source waveforms estimated individually at each OBSs for (a) the starting model, and (b) the final velocity models. Source estimates from the OBSs with a 24bit A/D converter are shown in yellow. There is an evident improvement in the coherence of the source wavelets estimated in the final model. . . . .	87



3.17	Acoustic chequerboard test results. Acoustic waveform inversion results of acoustic wavefields are shown for (a) 1.0 km × 0.5 km and (b) 0.7 km × 0.35 km chequerboard patterns. . . . .	89
3.18	Elastic chequerboard test results. Acoustic waveform inversion results of elastic wavefields are shown for (a) 1.0 km × 0.5 km and (b) 0.7 km × 0.35 km chequerboard patterns. . . . .	90
3.19	Point scatter test results. Acoustic waveform inversion of (a) acoustic wavefields, and (b) elastic wavefields. . . . .	92
4.1	(a) Traveltime tomography result of Nakanishi et al. (2008), also used as a starting model for our waveform inversion, (b) de-trended model of (a) in colour, and (c) de-trended model of (a) in grey scale. The horizontal axis is the distance from the deformation front. Yellow circles show the location of the OBS instruments. . . . .	120
4.2	(a) Synthetic OBS gather of OBS 47 at distance 65 km, computed from the starting model by a visco-acoustic forward modelling code. (b) Overlay of (a) in grey on the observed OBS gather in black. Picked first arrivals from the comparable real data are shown (a) in yellow, and (b) in red. . . . .	121
4.3	Representative vertical component seismic waveforms recorded at the OBS 47 located 65 km landward of the deformation front (Nakanishi et al., 2002). All data preprocessing was applied except for bottom muting. The yellow line indicates the picked first arrivals. . . . .	122
4.4	Gradient images at a frequency set of 2.25, 2.50, 2.75 and 3.0 Hz, and $\tau = 0.333$ sec obtained using as the objective function, (a) the conventional phase-amplitude misfit functional $E^1$ , (b) the logarithmic phase-amplitude misfit functional $E^3$ , (c) the conventional phase-only misfit functional $E^2$ , and (d) the logarithmic phase-only misfit functional $E^4$ . . . . .	124
4.5	De-trended velocity models in colour obtained by (a) the conventional phase-amplitude inversion $E^1$ ( $\tau \geq 0.333$ sec), (b) the logarithmic phase-amplitude inversion $E^3$ ( $\tau \geq 0.333$ sec), (c) the conventional phase-only inversion $E^2$ ( $\tau \geq 0.167$ sec), and (d) the logarithmic phase-only inversion $E^4$ ( $\tau \geq 0.167$ sec). . . . .	126

4.6	De-trended velocity models of Fig. 4.5 in grey-scale obtained by (a) the conventional phase-amplitude inversion $E^1$ ( $\tau \geq 0.333$ sec), (b) the logarithmic phase-amplitude inversion $E^3$ ( $\tau \geq 0.333$ sec), (c) the conventional phase-only inversion $E^2$ ( $\tau \geq 0.167$ sec), and (d) the logarithmic phase-only inversion $E^4$ ( $\tau \geq 0.167$ sec). . . . .	127
4.7	Geological interpretation overlaying the de-trended velocity model in Fig. 4.5c. The mega-splay fault and its branches are shown with thick black lines. The low velocity zones are labelled LVZ <sub>1</sub> (landward), and LVZ <sub>2</sub> (seaward). Area D indicates a seaward accretionary prism, exhibiting higher velocity values with respect to the $V_o(z)$ trend. . . . .	128
4.8	Vertical de-trended velocity profiles of Fig. 4.5 at distances 44, 38, 34, 28 km (from left to right). (a) The dashed black lines indicate the inversion results obtained by $E^1$ , and the solid black lines by $E^2$ , (b) the dashed black lines by $E^3$ , and the solid black lines by $E^4$ . In both (a) and (b), and solid grey lines the starting model. . . . .	129
4.9	Predicted pressure wavefields at the OBS 47, computed from the velocity models shown in Fig. 4.5 retrieved by (a) $E^1$ , (b) $E^3$ , (c) $E^2$ , and (d) $E^4$ . The yellow curves indicate the picked first arrivals. . . . .	131
4.10	Predicted pressure wavefields overlaid by the observed wavefields at the OBS 47 computed from the velocity models shown in Fig. 4.5 retrieved by (a) $E^1$ , (b) $E^3$ , (c) $E^2$ , and (d) $E^4$ . Red lines indicate the picked first arrivals. . . . .	132
4.11	History of the misfit functionals through (a) the conventional phase-amplitude inversion b the logarithmic phase-amplitude inversion, (c) the conventional phase-only inversion, and (d) the logarithmic phase-only inversion. The conventional phase-amplitude misfit is shown as a grey solid line, the conventional phase-only misfit as a grey dashed line, the logarithmic phase-amplitude misfit is shown as a solid black line, the logarithmic phase-only misfit is as a dashed black line. The Y-axis indicates the $\tau$ values employed during the velocity inversion. The misfit functionals show local increases each time $\tau$ value in the inversion is changed. . . . .	133
4.12	De-trended velocity models in colour (a) after Stage 2 of the two-stage conventional inversion (minimizing $E^1$ ) and (b) after Stage 2 of the two-stage logarithmic inversion (minimizing $E^4$ ). (c,d) are the same figures as in (a,b) but in grey scales. . . . .	136

4.13	Velocity update from Stage 1 following Stage 2 of (a) the two-stage conventional waveform inversion, and of (b) the two-stage logarithmic waveform inversion. . . . .	137
4.14	Vertical profiles of de-trended velocity model at $X = 44, 38, 34, 28$ km (from left to right) after (a) the two-stage conventional waveform inversion, and (b) the two-stage logarithmic waveform inversions. Grey solid lines indicate the starting model, black dashed lines the de-trended velocity model after Stage 1, and black solid lines the de-trended velocity after Stage 2. . . . .	138
4.15	Predicted pressure wavefield at the OBS 47 generated from Fig. 4.12 after two-stage inversions using (a) the conventional misfit functionals, and (b) the logarithmic misfit functionals. (c,d) the same synthetic wavefields in grey as (a,b) overlaying the observed wavefields in black. Picked first arrivals from the comparable real data are shown (a) in yellow, and (b) in red. . . . .	139
4.16	History of the cumulative misfit functionals through (a) the two-stage conventional inversion, and (b) the two-stage logarithmic inversion. Stage 1 results are the same as in Fig. 4.11c and d. The conventional phase-amplitude misfit is shown as a grey solid line, the conventional phase-only misfit as a grey dashed line, the logarithmic phase-amplitude misfit is shown as a solid black line, the logarithmic phase-only misfit is as a dashed black line. The y-axis indicates the $\tau$ values employed during the velocity inversion. The misfit functionals show local increases each time $\tau$ value in the inversion is changed. . . . .	141
5.1	Schematic model of a synthetic cross-well survey test after Kamei & Pratt (2008). Source and receiver wells are located 150 m apart, and indicated by two vertical solid lines . . . . .	164
5.2	(a) True velocity model, (b) true attenuation model, (c) synthesized common-level gather. Yellow curve indicates the first arrivals. . . . .	164
5.3	(a) Initial velocity model, (b) initial attenuation model, and (c) synthesized common level gather. . . . .	167
5.4	(Left) Phase residuals and (right) logarithmic amplitude residuals of the starting model at 500 Hz and $\tau = 0.051$ sec. . . . .	168

5.5	Impact of cross-talk on attenuation imaging: Simultaneous inversion results of Data-V. (Top) Velocity models and (bottom) the attenuation models obtained by simultaneous inversion with $\xi = 1.0$ . (b) Vertical profiles of at $X = 50$ m. Black lines indicate the inversion results, thick solid grey line the starting models, and grey dashed line the true models. . . . .	170
5.6	Impact of cross-talk on velocity imaging: Simultaneous inversion results of Data-Q. (Top) Errors in the inverted velocity model, and (bottom) the attenuation model obtained by simultaneous inversion with $\xi = 1.0$ . (b) Vertical profiles of (a) at $X = 50$ m. Black lines indicate the inversion results, thick solid grey line the starting models, and grey dashed line the true models. . . . .	171
5.7	Simultaneous inversion results of noise-free data at $\tau = 0.051$ sec generated from the model in Fig. 5.2: (Top) velocity models, and (bottom) $Q^{-1}$ models obtained using (a) $\xi = 1.0$ (b) 0.1, (c) 0.01. . . . .	173
5.8	Vertical profiles of simultaneous inversion results shown in Fig. 5.7 at $X = 50$ m: (Top) velocity models, and (bottom) attenuation models obtained using (a) $\xi = 1.0$ , (b) 0.1, and (c) 0.01. Thick grey solid lines indicate the starting model, grey dashed lines the true model, black solid lines the inversion results. . . . .	174
5.9	Synthetic common level gathers from the simultaneous waveform inversion results (Fig. 5.7) obtained using (a) $\xi = 1.0$ , (b) 0.1, and (c) 0.01. These may be compared with the original data in Fig. 5.2c. . . . .	175
5.10	(Top) Phase residual ( $\delta\mathbf{d}^p$ ) and (bottom) logarithmic amplitude residual ( $\delta\mathbf{d}^a$ ) at 500 Hz and $\tau = 0.051$ sec, computed from figures 5.7a-c. These may be compared with the residuals from the starting model in Fig. 5.4 (Note the range of colour bars differ from this figure). . . . .	175
5.11	Stage 1 of sequential inversion tests of noise-free data at $\tau = 0.051$ sec generated from Fig. 5.2: (a) Velocity model obtained by velocity inversion using the logarithmic phase-only objective function. (b) Vertical profile of (a) at $X = 50$ m. Thick grey lines indicate the starting model, grey dashed lines the true model, black solid lines the inversion result. (c) Predicted common-level gather after velocity inversion. . . . .	177
5.12	(Left) Phase residual ( $\delta\mathbf{d}^p$ ) and (right) logarithmic amplitude error ( $\delta\mathbf{d}^a$ ) after velocity inversion at 500 Hz and $\tau = 0.051$ sec. . . . .	178
5.13	Sequential inversion results: (Top) velocity and (bottom) attenuation models obtained by using (a) $\xi = 1.0$ , (b) 0.1, and (c) 0.01. . . . .	179

5.14	Vertical profiles of sequential inversion (top) velocity models and (bottom) attenuation models at $X = 50$ m obtained by (a) $\xi = 1.0$ , (b) 0.1, and (c) 0.01. Thick grey solid lines indicate the starting model, grey dashed lines the true model, black solid lines the inversion results. . . . .	180
5.15	Synthetic common level gathers from the sequential inversion results shown in Fig. 5.13. The velocity and attenuation models were obtained with (a) $\xi = 1.0$ , (b) 0.1, and (c) 0.01. . . . .	181
5.16	(Top) Phase error ( $\delta\mathbf{d}^P$ ) and (bottom) logarithmic amplitude error ( $\delta\mathbf{d}^a$ ) after sequential inversion at 500 Hz and $\tau = 0.051$ sec, computed from 5.7a-c. . . . .	181
5.17	Impact of strong wavenumber filtering: (Top) Velocity and (bottom) attenuation models obtained by (a) simultaneous inversion and (b) sequential inversion. $\xi = 0.1$ . The attenuation component of model gradient was filtered by Filter 2. (c) Vertical profiles at $X = 50$ m of the models shown in (a), and (d) vertical profiles of (b). Thick grey solid lines indicate the starting model, grey dashed lines the true model, black solid lines the inversion results. . . . .	184
5.18	Effects of time-damping on waveforms at $\tau = 0.0015$ sec after muting before the first arrival picks indicated by a yellow line. . . . .	185
5.19	Impact of time damping: (Top) Velocity and (Bottom) attenuation models obtained by (a) simultaneous inversion with $\xi = 0.01$ , and (b) sequential inversion with $\xi = 0.1$ . (c) Vertical profiles at $X = 50$ m of (a), and (d) vertical profiles of (b). Thick grey lines indicate the starting model, grey dashed lines the true model, black solid lines the models in (b), and the black dash lines the models in (c) . . . . .	186
5.20	(Top) Phase residual ( $\delta\mathbf{d}^P$ ) and (bottom) logarithmic amplitude error ( $\delta\mathbf{d}^a$ ) at 500 Hz computed from the velocity models in Fig. 5.7. (a) Simultaneous inversion, and (b) sequential inversion. . . . .	187
5.21	The common-level gather of the synthetic “observed” waveforms with Gaussian noise (S/N=5) at (a) $\tau = 0.051$ sec (b) 0.0015 sec. . . . .	189
5.22	Impact of noise: (Top) Velocity and (Bottom) attenuation models obtained by (a) simultaneous inversion and (b) sequential inversion. (c) Vertical profiles of (b). Thick grey solid lines indicate the starting model, grey dashed lines the true model, black solid lines the inversion results. . . . .	190
5.23	(Top) Phase error and (bottom) logarithmic amplitude error at 500 Hz and $\tau = 0.051$ sec, computed from Fig. 5.22. . . . .	191

5.24 Trade-off curves between the total-conventional misfit  $E_{total}$  and the roughness of (a)  $\mathbf{s}_o^{(r)}$  and (b)  $\mathbf{s}_o^{(i)}$  for simultaneous (solid) and sequential inversion (dashed) at  $\tau = 0.051$ . Both velocity and attenuation components of the model gradient were weakly smoothed by Filter 1 with a suite of inversion results by varying  $\xi$ .  $E_{total}$  was plotted relative to the value from the starting models. . . . . 197

# List of Tables

3.1	List of mathematical symbols used in this chapter . . . . .	48
3.2	Damping factors, $\tau$ , the equivalent Laplace constants employed for phase-only and phase-amplitude inversions respectively. . . . .	71
4.1	List of mathematical symbols used in this chapter . . . . .	109
5.1	List of mathematical symbols used in this chapter. The superscript $(j=1)$ indicates the velocity class, and $(j=2)$ the attenuation class of the inversion parameter. . . . .	150
5.2	Correlation lengths used to generate the model: $a_x$ and $a_z$ are the correlation lengths for x- and z-directions, $a_x/\lambda_{800}$ and $a_z/\lambda_{800}$ indicate the size of the heterogeneities relative to $\lambda_{800}$ , where $\lambda_{800}$ is the mean wavelength of each layer at 800 Hz, the highest frequency used for the inversion. . .	163
5.3	Probability distribution used to generate the model: $r_{v_1}$ and $r_{Q_1^{-1}}$ are the ratio of sandstone, $\mu_{v_1}$ and $\sigma_{v_1}$ are the mean and standard deviation of velocity distribution for sandstone, and $\mu_{v_2}$ and $\sigma_{v_2}$ are for shale. $\mu_{Q_1^{-1}}$ and $\sigma_{Q_1^{-1}}$ are the mean and standard deviation of $Q^{-1}$ distribution for sandstone, $\mu_{Q_1^{-1}}$ and $\sigma_{Q_1^{-1}}$ for shale. . . . .	165

# Chapter 1

## Introduction

For many years, controlled source seismic imaging has been an essential method in retrieving spatial distributions of subsurface elastic parameters and lithological boundaries, and has contributed to understanding crustal and uppermost mantle structures in both academic and industrial applications (Levander et al., 2007). In controlled source seismic experiments, elastic energy is excited by an array of sources: seismic waves propagate through the subsurface, and are recorded at an array of seismographs (receivers) as a pressure field or a particle velocity field. The penetration depths and spatial resolution of the seismic methods are much greater than those of other active source geophysical imaging methods, and thus seismic imaging is a primary tool in deriving our structural understanding of the lithosphere. The resulting seismic images can be utilized to derive additional rock and geomechanical properties of the earth by combining with other geophysical measurements, or by employing empirical or analytical relationships (e.g. Mavko et al. 1998 and Saffer & Tobin 2011).

Controlled source seismic imaging is conventionally divided into reflection methods and refraction methods, each of which employ a distinct experimental design (Fig. 1.1). Reflection imaging usually aims to delineate subsurface interfaces at wavelength scales, i.e. the high-wavenumber components of the earth (Yilmaz, 2001). The reflection survey deploys fairly dense arrays of sources and receivers, while the source-receiver distances (offset) can be relatively short. The reflection method is extensively employed in the oil and gas industries to locate hydrocarbon reservoirs (Etgen et al., 2009), and has also been adopted in academic investigations of the lithosphere (Levander et al., 2007). One of the most common methods intended in reflection data processing is seismic migration, which ‘migrates’ diffracted and reflected seismic events in the data space to original scattering points in the model space: migration potentially retrieves impedance contrasts at wavelength scales (Yilmaz, 2001). Background velocity models are required for the map-



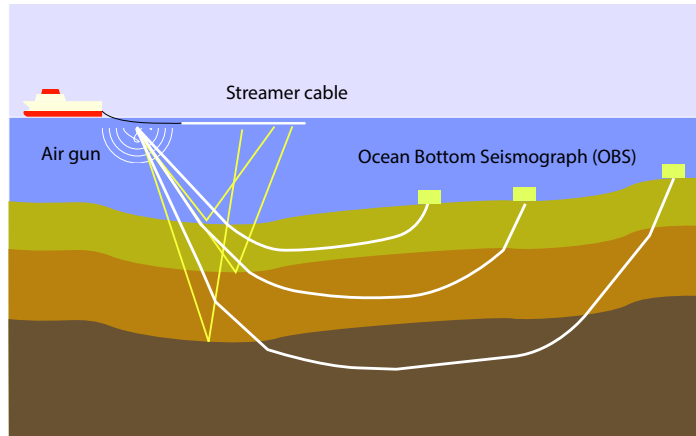


Figure 1.1: Schematic diagram of marine reflection- and refraction-survey examples. Seismic energy is excited by an air gun for both surveys. In the reflection survey, reflected waves (yellow) are recorded at hydrophones on a streamer cable. In the refraction survey, refracted waves (white) are recorded at Ocean Bottom Seismographs (either or both of geophones and hydrophones). Note that other acquisition settings are possible for both surveys.

ping, and are obtained supplementally through stacking velocity analysis, and through migration velocity analysis (Woodward et al., 2008).

In contrast, refraction imaging techniques are specifically intended to retrieve long-wavelength components of subsurface elastic parameters (typically velocities) primarily through tomographic methods (Levander et al., 2007). A popular refraction imaging method is travelttime tomography, capable of estimating a smooth subsurface structure from arrival information of distinct arrivals (Zelt & Smith, 1992; Zelt & Barton, 1998; Zhang & Toksoz, 1998). Source-receiver pairs need to extend to at large offsets to record post-critical arrivals, but the source and receiver distributions can be much sparser than in the reflection experiments. This latter property allows the refraction methods to economically retrieve large-scale structures, and thus the method is more often employed in academic deep crustal investigations than in the oil and gas industry.

Waveform inversion is an alternative imaging method, which ambitiously aims to retrieve a wide range of the wavenumber spectrum of the subsurface model by using an entire seismic record including both refractions and reflections (Tarantola, 1984; Lailly, 1983; Pratt et al., 1996; Virieux & Operto, 2009). Waveform inversion techniques require more densely sampled data than travelttime tomography and wider aperture data than

conventional reflection processing. The method once appeared elusive due to the unconventional acquisition requirements, and also due to its massive computational costs. However with advancements in computational architecture, with the increasing employment of dense source-receiver arrays in academic refraction surveys, and with the development of wide-angle and wide-azimuth reflection surveys in the oil and gas industry, this approach has emerged as an increasingly important subsurface imaging tool (Levander et al., 2007; Virieux & Operto, 2009). In the following sections, I review the development of waveform inversion as a tomographic method for refraction imaging. Sirgue (2003) provides an excellent review in the context of reflection imaging.

## 1.1 Tomography

The tomographic imaging technique was introduced to seismology by earthquake seismologists in late 1970s to form regional and global velocity models from the traveltimes of recorded earthquakes (e.g. Aki et al., 1977 and Dziewonski et al., 1977). Traveltime tomography then became one of the most commonly used tools for crustal controlled seismic imaging to develop two-dimensional (2D) and three-dimensional (3D) subsurface models of P-wave velocity (Zelt & Smith, 1992; Zelt & Barton, 1998; Zhang & Toksoz, 1998; Hole, 1992), S-wave velocity (Gohl & Pedersen, 1995; Bauer et al., 2003; Hyvönen et al., 2007), attenuation (Zelt & Ellis, 1990; White & Clowes, 1994; Quan & Harris, 1997; Li et al., 2006), and anisotropy (Caress et al., 1992; Chapman & Pratt, 1992; Środa, 2006). The tomographic method generally uses asymptotic ray theory, and seeks to infer the subsurface structure from the arrival information of distinct arrivals by numerical optimization methods. The method is robust and computationally affordable. However the information from traveltime tomography is limited to that observed along ray-paths, and the spatial resolution of traveltime tomography is limited to the Fresnel zone due to the method’s high-frequency approximation and inability to account for finite-frequency effects in wave propagation (Woodward, 1992; Williamson & Worthington, 1993; Chen & Schuster, 1999).

Seismic data recorded at seismographs are richer in subsurface information when the full waveform rather than the arrival time is considered. Diffraction tomography (Devaney, 1984; Wu & Toksoz, 1987) was one of the first wave-based methods that attempted to overcome the limitations of traveltime tomography, and is based on the generalized projection theorem. Instead of employing a full wave equation, the method linearizes the acoustic wave equation by the Born or Rytov approximation, and a plane wave decomposition is used to compute Green’s functions in a homogeneous model. In

practice this limited the application of diffraction tomography. However, the theory formed the basis for the subsequent development of ray+Born inversion (Jin et al., 1991; Lambare et al., 1992), waveform inversion (Pratt & Worthington, 1990; Sirgue & Pratt, 2004), and the illumination analysis used for these imaging techniques (Sirgue & Pratt, 2004; Xie et al., 2006).

By using the Born approximation, Wu & Toksoz (1987) derived a basic equation for diffraction tomography relating the mono-frequency seismic wavefield to the mono-wavenumber component of velocity perturbations,

$$\delta u(\hat{i}, \hat{\mathbf{r}}, \omega) = -k^2 \tilde{O} [k(\hat{\mathbf{r}} - \hat{i})], \quad (1.1)$$

where  $\delta u$  is the frequency-domain scattered wavefield,  $\hat{i}$  is the unit vector for the incident plane-wave direction,  $\hat{\mathbf{r}}$  is that for the scattering direction,  $\omega$  is the angular frequency, and  $k$  is the wavenumber of the background model.  $\tilde{O}$  is the 3D Fourier transform of the perturbation,  $O(\mathbf{r}) = 1 - c_o^2/c^2(\mathbf{r})$ , where  $c(\mathbf{r})$  is the velocity at the location  $\mathbf{r}$ , and  $c_o$  is the velocity of the background model. From this equation, it is possible to show the largest wavenumber that influences the scattered wavefield is  $2\omega/c_o$ ; i.e. the size of the smallest recoverable anomaly is a half wavelength. This resolution is substantially higher than the resolution of travelttime tomography, which is of order  $\sqrt{L\lambda}$ , where  $L$  is the propagation length (Williamson & Worthington, 1993). From Eq.(1.1), an important observation is further derived for the illumination analysis of any wave-based imaging method: A mono-frequency component from a single source-receiver pair can be associated with a single wavenumber component of the model (Sirgue, 2003). By recording at an array of receivers, a single source excitation illuminates an Ewald semi-circle of model wavenumbers (Ewald, 1921); the coverage of the semi-circle depends on receiver apertures. Thus the wavenumbers attainable from the mono-frequency components of many source-receiver pairs ranges from zero to  $2\omega/c_o$ , and thus multi-frequency components potentially lead to redundant wavenumber coverage depending on survey geometries (Wu & Toksoz, 1987; Devaney, 1984). However the coverage never is never complete due to practical acquisition restrictions; e.g. in surface reflection and refraction surveys, the sources and receivers can be only located on the surface, i.e. on one side of the imaging target.

From Eq.(1.1), Wu & Toksoz (1987) derived a generalized projection theorem for the 2D point-source by using a plane-wave decomposition

$$4\gamma_g\gamma_s\tilde{U}(k_r, k_s) \exp[-i(\gamma_r d_r + \gamma_s d_s)] = -k^2 \tilde{O} [k(\hat{\mathbf{r}} - \hat{i})], \quad (1.2)$$

where  $\tilde{U}(k_r, k_s)$  denotes the double Fourier transform of scattered wavefields along source and receiver lines,  $d_r$  and  $d_s$  are the distances of source-receiver line from the origin,  $k_r$  and  $k_s$  are the wavenumbers along source and receiver lines, and  $\gamma_s$  and  $\gamma_r$  are the wavenumbers perpendicular to source and receiver lines, and satisfy  $k^2 = k_s^2 + \gamma_s^2 = k_r^2 + \gamma_r^2$ . The equation recasts the imaging process of diffraction tomography as the operation of the inverse generalized projection slice theorem, and the 2D velocity perturbation can be obtained by the surface acquisition geometry as

$$O(x, z) = \frac{1}{\pi} \Re \left[ \int_{-k}^k dk_s \exp(ik_s x - i\gamma_s z) \int_{-k}^k dk_r \frac{|k_s \gamma_r + k_g \gamma_s|}{k^2} \exp(ik_r x - i\gamma_r z) \tilde{U}(k_r, k_s) \right], \quad (1.3)$$

where  $\Re[\cdot]$  indicates the real part of  $\cdot$ . By recognizing that  $\exp[i(k_r x - \gamma_r z)]$  is the back-propagation from the receiver to the scattering point, and  $\exp[i(k_s x - \gamma_s z)]$  represents the backpropagation from the scattering point to the source (i.e. that conjugate of incident wavefield), Eq.(1.3) suggests that the subsurface model can be retrieved by the weighted zero-lag correlation of the incident wavefield and the backpropagated scattered wavefields. The weighting term  $\frac{|k_s \gamma_r + k_g \gamma_s|}{k^2}$  corrects for the irregular angular coverage in the seismic experiments. The numerical integration of Eq.(1.3) requires a continuous distribution of sources and receivers along source and receiver arrays (Jin et al., 1991).

In order to use an inhomogeneous background model, the plane-wave decomposition method above must be replaced by numerical methods, but the integral equation can still be maintained to map between wavefields and model parameters in a similar form to that of Eq.(1.2). The numerical computation of the background Green's function can be attained by using the Wentzel-Kramers-Brillouin-Jeffreys (WKBJ) method (Aki & Richards, 1980) for a vertically varying background model (Wu et al., 1994), or by asymptotic ray theory for a smoothly varying background model (Beylkin, 1984; Beylkin & Burridge, 1990; Miller et al., 1987). In the second approach, the scattered wavefields are linearly related to the model perturbation by the 'Generalized Radon Transform' (GRT) (Beylkin, 1984; Beylkin & Burridge, 1990; Miller et al., 1987). However these methods still map the wavefields to the model by the numerical integration, and are restricted to acquisition geometries that allow effective integration.

Instead of analytically inverting the GRT, a linear optimization method can be used to estimate the subsurface model which satisfies the GRT, so that data from arbitrary acquisition geometries can be used for the imaging (Beydoun & Mendes, 1990; Jin et al., 1991; Lambare et al., 1992; Thierry et al., 1999; Lambaré et al., 2003). The linearized inversion method searches for the optimal model perturbation from the background model (model space) by fitting the perturbed wavefields (data space), and is often referred to

as “ray+Born inversion” (Thierry et al., 1999; Lambaré et al., 2003), or as “asymptotic diffraction tomography” (Ribodetti et al., 2004). The combination of ray theory and the Born approximation allows ray+Born inversion to retrieve structures at a half-wavelength scale. The sensitivity kernels for ray+Born inversion are broader than a ray-path, equivalent to the finite-frequency sensitivity kernel (Dahlen et al., 2000), and closely related to the ‘wavepath’ defined by Woodward (1992). However the approximations employed raise concerns over the applicability of the ray+Born method to complex structures: Both asymptotic and Born approximation force the background model to be smooth. The model perturbation needs be small in terms of both size and magnitude to satisfy the Born approximation. Furthermore the forward modelling method only account for first-order scattering effects, and neglects multipath propagation effects.

## 1.2 Waveform inversion

Waveform inversion is a non-linear inversion approach which fully utilizes an accurate and complete numerical solution of the wave equation (Tarantola, 1988; Pratt et al., 1998). The inversion seeks an optimum spatially varying model  $m(\mathbf{r})$  (model space) by iteratively minimizing waveform misfits (in data space), and forms the gradient of the objective function by utilizing the Born approximation in a manner similar to ray+Born inversion (Lailly, 1983; Tarantola, 1984; Pratt, 1990; Pratt & Worthington, 1990). (The ray+Born inversion was originally developed as a computationally affordable compromise for waveform inversion.) However, full waveform modeling allows the inversion to accurately account for complicated wave propagation even in a highly heterogeneous subsurface model. Furthermore, while each iteration is conducted within the Born approximation, iterative updating of the background model can potentially estimate a total perturbation in the model larger than is possible with the Born approximation allows, because higher-order scattering is fit once the first-order scattered fields are well reproduced (Pratt et al., 1998). Thus the waveform inversion method is potentially able to retrieve substantially detailed subsurface models (albeit at the expense of a significant increase in the computational cost when compared to the methods based on asymptotic approximations).

To reduce the computational cost, the expensive Fréchet derivatives are usually not calculated in waveform inversion, and the model gradient is instead formed by the adjoint method originally developed by Lailly (1983) and Tarantola (1984) in the time-space domain, and later by Pratt & Worthington (1990) and Pratt (1990) in the frequency-space domain. With the adjoint method, the gradient is constructed from the correlation

between the forward wavefields and the backpropagated residuals (as is the case in diffraction tomography). Following Pratt et al. (1998), the gradient of the objective function  $E$  with respect to a model parameter  $m(\mathbf{r})$  is described in the frequency-domain in matrix form as

$$\nabla_{m(\mathbf{r})}E = - \sum_{\omega} \mathbf{u}^T(\omega) \left[ \frac{\partial \mathbf{S}}{\partial m(\mathbf{r})} \right]^T [\mathbf{S}^{-1}]^* \delta \mathbf{d}, \quad (1.4)$$

where  $\mathbf{u}$  is the frequency-domain forward propagated wavefield,  $\mathbf{S}$  is the discretized impedance matrix,  $\delta \mathbf{d}$  is the data residuals,  $^T$  is the Hermite conjugate, and  $^*$  is the complex conjugate without a matrix transpose. The equation shows that the gradient is indeed a weighted correlation of the forward wavefield  $\mathbf{u}$  and the backpropagated field  $[\mathbf{S}^{-1}(\mathbf{m})]^* \delta \mathbf{d}$ . Note that the weighting term for the correlation  $\frac{\partial \mathbf{S}}{\partial m(\mathbf{r})}$  is independent of the source-receiver geometry, in contrast to the case of diffraction tomography; thus the irregularity of source-receiver geometry needs to be corrected by the Hessian matrix (Pratt & Worthington, 1990) or by iteration. Motivated by the close relationships between diffraction tomography and waveform inversion, Pratt & Worthington (1990) and Sirgue & Pratt (2004) adopted an illumination analysis based on Eq.(1.1), and illustrated that the redundant wavenumber coverage between frequencies allows frequency-domain waveform inversion to use imaging frequencies on much coarser intervals than the value required by the temporal sampling theorem: this property contributes to further reducing the computational costs of waveform inversion.

### 1.2.1 Application of waveform inversion in the controlled source seismology

Early applications of waveform inversion aimed to develop velocity structures from (mostly synthetic) reflection seismic data (Gauthier et al., 1986; Mora, 1987, 1988, 1989). Early researchers pointed out that waveform inversion is highly non-linear and non-unique (e.g. Gauthier et al. 1986), and also discovered that it is extremely difficult to recover a low-ballwavenumber velocity model from reflection data alone while high-wavenumber interfaces (reflectors) are retrievable (Mora, 1988, 1989). This is because short offset reflection data only illuminates the high-wavenumber components of the earth, as was illustrated by Sirgue & Pratt (2003) based on Eq.(1.1), and as also was discussed at length by Mora (1988) and Jannane et al. (1989), and also because there is a fundamental trade-off between the depths of a reflector and the velocity model (Mora, 1989; Hicks & Pratt, 2001). The highly non-linear nature of waveform inversion has also prompted the application of global optimization theories, but the computational costs of such schemes have

prevented the extraction of anything other than 1D structures (Sen & Stoffa, 1991, 1992; Singh & Minshull, 1994).

Cross-well seismic surveying is a technique used to acquire a wide-angle data set between two parallel bore-holes. In such surveys, the recorded waveforms consist dominantly of transmitted waveforms, which are understood to be more linear with respect to velocity fields, and also more sensitive to low-wavenumber components (Pratt & Worthington, 1990). In an early example, Song et al. (1995) successfully extracted a detailed P-wave velocity model from a real cross-well data set, and the resulting velocity image was of much higher resolution than the travelttime tomography image. The subsequent waveform inversions of cross-well data sets further proved the applicability of the approach to various targets including conventional hydrocarbon surveys (Pratt, 1999; Pratt & Shipp, 1999; Pratt et al., 2008), mineral deposits (Xu & Greenhalgh, 2010), and monitoring of gas-hydrate production (Pratt et al., 2004).

Motivated by the work of Song et al. (1995), Pratt et al. (1996) proposed to exploit the refraction (transmitted) components of synthetic wide-angle crustal-survey data, and illustrated the significant potential of acoustic waveform inversion of wide-angle reflection data in retrieving the subsurface velocity model. Brittan et al. (1997) applied their technique to a real crustal-scale data set, and successfully imaged the velocity structure at the edge of the Chicxulub impact structure. Further real data applications have proven the potential for estimating complex velocity structures using both marine and land surface seismic experiments; for the crustal exploration (Shipp & Singh, 2002; Dessa & Pascal, 2003; Ravaut et al., 2004; Operto et al., 2006; Bleibinhaus et al., 2007; Malinowski et al., 2011; Takam Takougang & Calvert, 2011; Arnulf et al., 2012), for near-surface engineering applications (Smithyman et al., 2009; Gao et al., 2005, 2006), and for hydrocarbon exploration (Brenders, 2011; Sears et al., 2010; Plessix & Cao, 2011; Sirgue et al., 2010; Vigh & Starr, 2008). While 2D acoustic waveform inversion is the most commonly used technique, 3D implementations are now being developed following the renewal of interest in the oil and gas industry where the 3D wide-azimuth surveys are extensively employed (Vigh & Starr, 2008; Sirgue et al., 2008; Ben-Hadj-Ali et al., 2008). 3D implementation is computationally expensive, and various techniques have been proposed to improve the computational efficiency (e.g. Krebs et al., 2009; Sirgue et al., 2008).

Waveform inversion of other elastic parameters beyond the P-wave velocity has been explored for P-wave attenuation (e.g. Tarantola, 1988; Song et al., 1995; Malinowski et al., 2011), for density (Choi et al., 2008; Jeong et al., 2012), for S-wave velocities (e.g. Mora, 1987; Crase et al., 1990; Tarantola, 1988; Shipp & Singh, 2002; Brossier et al., 2009a), and for anisotropic parameters (e.g. Barnes et al., 2008; Gholami et al., 2011a,b).

Successful field-data applications are relatively rare due to severe non-uniqueness, acquisition settings, and computational cost. Sometimes the inversion of these parameters is abandoned, and instead the parameters are incorporated into the forward model, in order to manage the effects on data of these parameters (Pratt et al., 2008; Prieux et al., 2011; Plessix & Cao, 2011). Intrinsic P-wave velocity attenuation is most often inverted via a visco-acoustic implementation, as the additional computational cost to acoustic inversion is negligible (Song et al., 1995; Liao & McMechan, 1996; Pratt et al., 2004; Smithyman et al., 2009; Malinowski et al., 2011; Hak & Mulder, 2011). S-wave imaging requires expensive full elastic forward modeling, and multi-component recording is critical to extract S-wave components (Shipp & Singh, 2002; Sears et al., 2010). Approximate anisotropic parameters can be incorporated into acoustic forward modeling at relatively low additional computational costs (Pratt, 1999; Operto et al., 2007), but the inversion for these parameters has been conducted exclusively with synthetic data sets due to the strong coupling between anisotropic parameters and low sensitivities (Gholami et al., 2011a,b).

### 1.2.2 Non-linearity and non-uniqueness of waveform inversion

Waveform inversion is a strongly non-linear and very ill-posed inverse problem (Mora, 1989; Plessix, 2006; Pratt, 2008). The solution is highly sensitive to the choice of a starting model, and considerable attention needs be paid to the construction of this starting model (Gauthier et al., 1986; Brenders & Pratt, 2007b). A first arrival tomography method or a reflection tomography approach have typically been employed to generate starting models for waveform inversion (Brenders & Pratt, 2007a; Brenders et al., 2010; Operto et al., 2006; Ravaut et al., 2004). Brenders & Pratt (2007a) and Pratt (2008) have referred to this hierarchical sequence of traveltime tomography followed by waveform inversion as “Waveform Tomography”, since the whole inversion process aims to extend the use of first arrival tomography to obtain high resolution subsurface models that fit the refracted (i.e. transmitted) parts of the seismic records.

Further mitigation of the non-linear and ill-posed nature of waveform inversion has been investigated by exploring an optimal objective function (Crase et al., 1990; Shin & Ha, 2008; Symes, 2008; Brossier et al., 2009b; Leeuwen & Mulder, 2010), by careful data preconditioning (Williamson & Pratt, 1995; Sirgue & Pratt, 2004; Brenders & Pratt, 2007b; Sears et al., 2010), by well-designed model preconditioning (Shin et al., 2002; Ravaut et al., 2004; Guitton & Díaz, 2011), and by the application of appropriate regularization methods (Abubakar et al., 2009). A multiscale approach (Bunks et al.,



1995) is recognized as one of the most effective inversion strategies for mitigating such effects by initially inverting large-scale features, and sequentially refining the spatial scale. The multiscale method is implemented by starting inversions at low temporal frequencies and sequentially fitting higher frequency components. and also by first restricting waveform inversion to early arrivals, and sequentially incorporating later arrivals (Sirgue & Pratt, 2004; Brenders & Pratt, 2007a). In time-domain waveform inversion, these may be implemented by the combination of convolutional bandpass filters and time-windowing functions (Sears et al., 2010). In the frequency domain, while the hierarchical usage of frequency windows is trivial, simple time windowing approaches require a convolutional operator over many frequencies. However, an exponential time-damping function may be introduced to rigorously extract early arrivals without a convolution operator (Sirgue & Pratt, 2004; Brenders & Pratt, 2007a). This approach was reformulated by Shin & Cha (2009) as “Laplace-Fourier domain” waveform inversion in which the Laplace constant is the inverse of the characteristic time of the exponential time-damping function.

### 1.3 Objectives of thesis

In this thesis, I explore effective inversion strategies to mitigate the ill-posed nature of waveform inversion. I employ two-dimensional visco-acoustic Laplace-Fourier waveform inversion, and apply it to two data configurations; one is the wide-angle surface survey, and the other is the cross-well survey geometry.

A densely-sampled wide-angle Ocean Bottom Seismograph (OBS) data set from the Nankai subduction zone (Nakanishi et al., 2008) is inverted for a P-wave velocity model in order to delineate an active mega-splay fault system. The Nankai subduction zone is one of the most extensively studied subduction zones worldwide, and the analyzed area is closely related to coseismic rupture propagation and tsunami generation (Tobin & Kinoshita, 2006). Previous 2D and 3D reflection surveys delineated the detailed fault structures, but there remain ambiguities which limit the complete illustration of the megasplay fault system (Moore et al., 2007; Nakanishi et al., 2002). I aim to supplement the structural information by applying waveform inversion to the OBS data set. During the course of the velocity imaging, I explore the inversion process, and generate strategies to mitigate non-uniqueness in waveform inversion, and to overcome the challenges specific to crustal imaging.

I also explore robust and computationally affordable inversion strategies to retrieve velocity and attenuation parameters using synthetic cross-well data. This two-parameter inversion is known to be much more ill-posed than the velocity inversion, and requires

additional considerations to stabilize the inversion process (Hak & Mulder, 2010; Malinowski et al., 2011). I demonstrate that the difficulties arise from the cross-talk between two parameter classes, and illustrate their effects on velocity and attenuation parameter classes. I propose regularization and inversion strategies to suppress the artifacts arising from the cross-talk, and retrieve reliable velocity and attenuation models. The insights into the two-parameter problem will contribute to more general classes of multiparameter waveform inversion.

## 1.4 Thesis outline

In Chapter 2, I apply acoustic Laplace-Fourier domain waveform inversion to the Ocean Bottom Seismograph (OBS) data set from the Nankai subduction zone. This chapter is a part of a paper published in *Earth and Planetary Science Letters* in 2012 as “Waveform Tomography Imaging of a Megasplay Fault System in the Seismogenic Nankai Subduction Zone” by Kamei, R., Pratt, R. G., and Tsuji, T. This chapter has an emphasis on the geological implication of the waveform inversion results, and the improvements from previous seismic images obtained by both travelttime tomography and migration. I briefly describe the data preprocessing, inversion procedures, and quality control of the inversion results.

In Chapter 3, I provide a detailed description of acoustic Laplace-Fourier waveform inversion of the OBS data set from the Nankai subduction zone. This chapter is a part of a manuscript submitted to *Geophysical Journal International* as “On Acoustic Waveform Tomography of wide-angle OBS data — Strategies for preconditioning and inversion” by Kamei, R., Pratt, R. G., and Tsuji, T. The chapter has a focus on providing detailed waveform inversion procedure starting from data preparation, through inversion strategies, to extensive quality controls tools, and also seeks to identify the key elements for successful crustal imaging with waveform inversion.

In Chapter 4, I explore four types of misfit functionals for Laplace-Fourier waveform inversion of surface seismic data sets; i) the conventional phase-amplitude misfits, ii) the conventional phase-only misfits, iii) the logarithmic phase-amplitude misfits, and iv) the logarithmic phase-only misfit functionals. This chapter is a part of a manuscript submitted to *Geophysical Prospecting* as “On misfit function for Laplace-Fourier waveform inversion, with applications to wide-angle OBS data” by Kamei, R., Pratt, R. G., and Tsuji, T. I employ the OBS data set from the Nankai subduction zone for these inversion experiments. I describe the discrepancies in the subsurface illumination and in the stability of waveform inversion. I then discuss how each misfit functional contributes

to improvements in the ill-posed nature of waveform inversion, and how a hierarchical inversion approach can be designed.

In Chapter 5, I expand Laplace-Fourier waveform inversion to incorporate attenuation imaging in addition to velocity imaging. The chapter is a part of a manuscript submitted to *Geophysical Journal International* as “Inversion strategies for visco-acoustic waveform inversion” by Kamei, R. and Pratt, R. G. I use a synthetic velocity and attenuation model, and adopt a cross-well survey. I discuss inherent and persistent cross-talk between parameter classes, and the resulting ill-posed nature of visco-acoustic waveform inversion. I propose computationally efficient and simple inversion strategies for visco-acoustic waveform inversion.

In Chapter 6, I summarize the results presented in Chapter 2-6, and discuss proposals for future study.

## References

- Abubakar, A., Hu, W., Habashy, T. M., & van den Berg, P. M., 2009. Application of the finite-difference contrast-source inversion algorithm to seismic full-waveform data, *Geophysics*, **74**(6), WCC47–WCC58.
- Aki, K. & Richards, P. C., 1980. *Quantitative seismology*, W. H. Freeman & Co.
- Aki, K., Christoffersson, A., & Husebye, E. S., 1977. Determination of the three-dimensional seismic structure of the lithosphere, *Journal of Geophysical Research*, **82**, 277–296.
- Arnulf, A. F., Harding, A. J., Singh, S. C., Kent, G. M., & Crawford, W., 2012. Fine-scale velocity structure of upper oceanic crust from full waveform inversion of downward continued seismic reflection data at the Lucky Strike Volcano, Mid-Atlantic Ridge, *Geophysical Research Letters*, **39**(8), 2–7.
- Barnes, C., Charara, M., & Tsuchiya, T., 2008. Feasibility study for an anisotropic full waveform inversion of cross-well seismic data, *Geophysical Prospecting*, **56**(6), 897–906.
- Bauer, K., Schulze, A., Ryberg, T., Sobolev, S. V., & Weber, M. H., 2003. Classification of lithology from seismic tomography: A case study from the Messum igneous complex, Namibia, *Journal of Geophysical Research*, **108**(B3), 1–15.
- Ben-Hadj-Ali, H., Operto, S., & Virieux, J., 2008. Velocity model building by 3D frequency-domain, full-waveform inversion of wide-aperture seismic data, *Geophysics*, **73**(5), VE101–VE117.
- Beydoun, W. & Mendes, M., 1990. North Sea reservoir description; benefits of an elas-

- tic migration/inversion applied to multicomponent vertical seismic profile data, *Geophysics*, **55**(2), 209–217.
- Beylkin, G., 1984. The inversion problem and applications of the generalized Radon transform, *Communications on pure and applied mathematics*, **37**, 579–599.
- Beylkin, G. & Burridge, R., 1990. Linearized inverse scattering in acoustics and elasticity, *Wave motion*, **12**, 15–52.
- Bleibinhaus, F., Hole, J. A., Ryberg, T., & Fuis, G. S., 2007. Structure of the California Coast Ranges and San Andreas Fault at SAFOD from seismic waveform inversion and reflection imaging, *Journal of Geophysical Research*, **112**, B0631.
- Brenders, A. J., 2011. *Strategies For Waveform Tomography of Long-offset, 2-D Exploration Seismic Data*, Ph.D. thesis, University of Western Ontario.
- Brenders, A. J. & Pratt, R. G., 2007a. Full waveform tomography for lithospheric imaging: results from a blind test in a realistic crustal model, *Geophysical Journal International*, **168**(1), 133–151.
- Brenders, A. J. & Pratt, R. G., 2007b. Efficient waveform tomography for lithospheric imaging: implications for realistic, two-dimensional acquisition geometries and low-frequency data, *Geophysical Journal International*, **168**(1), 152–170.
- Brenders, A. J., Pratt, R. G., & Charles, S., 2010. Evaluation of preconditioning strategies on waveform tomography of field data: Success with long offset seismic data in a thrust-fold belt, *SEG Technical Program Expanded Abstracts*, **29**(1), 4348–4353.
- Brittan, J., Forgues, E., Pratt, R., & Morgan, J., 1997. Wavefield inversion across the edge of the Chicxulub impact structure, *J. Conference Proceedings*, **1**(1), 65.
- Brossier, R., Operto, S., & Virieux, J., 2009a. Seismic imaging of complex onshore structures by 2D elastic frequency-domain full-waveform inversion, *Geophysics*, **74**(6), WCC105–WCC118.
- Brossier, R., Operto, S., & Virieux, J., 2009b. Robust elastic frequency-domain full-waveform inversion using the L1 norm, *Geophysical Research Letters*, **36**(20), L20310.
- Bunks, C., Saleck, F. M., Zaleski, S., & Chavent, G., 1995. Multiscale seismic waveform inversion, *Geophysics*, **60**(5), 1457–1473.
- Caress, D. W., Burnett, M. S., & Orcutt, J. A., 1992. Tomographic Image of the Axial Low-Velocity Zone at 1250’N on the East Pacific Rise, *Journal of Geophysical Research*, **97**(B6), 9243–9263.
- Chapman, C. H. & Pratt, R. G., 1992. Traveltime tomography in anisotropic media-I. Theory, *Geophysical Journal International*, **109**(1), 1–19.
- Chen, J. & Schuster, G. T., 1999. Resolution limits of migrated images, *Geophysics*, **64**(4), 1046–1053.

- Choi, Y., Min, D.-J., & Shin, C., 2008. Two-dimensional waveform inversion of multi-component data in acoustic-elastic coupled media, *Geophysical Prospecting*, **56**(6), 863–881.
- Cruse, E., Pica, A., Noble, M., McDonald, J., & Tarantola, A., 1990. Robust elastic nonlinear waveform inversion: Application to real data, *Geophysics*, **55**(5), 527–538.
- Dahlen, F. A., Hung, S.-H., & Nolet, G., 2000. Fréchet kernels for finite-frequency traveltimes-I. Theory, *Geophysical Journal International*, **141**(1), 157–174.
- Dessa, J.-X. & Pascal, G., 2003. Combined traveltime and frequency-domain seismic waveform inversion: a case study on multi-offset ultrasonic data, *Geophysical Journal International*, **154**(1), 117–133.
- Devaney, A. J., 1984. Geophysical Diffraction Tomography, *Geoscience and Remote Sensing, IEEE Transactions on*, **GE-22**(1), 3–13.
- Dziewonski, A., Hager, B., & O’Connell, R., 1977. Large-scale heterogeneities in the lower mantle, *Journal of Geophysical Research*, **82**(2), 239–255.
- Etgen, J., Gray, S., & Zhang, Y., 2009. An overview of depth imaging in exploration geophysics, *Geophysics*, **74**(6), WCA5–WCA17.
- Ewald, P. P., 1921. Das "reziproke gitter" in der struktur theorie, *Zeit. f. Kris.*, **56**, 129–156.
- Gao, F., Levander, A., Pratt, G., & Zelt, C., 2005. Seismic velocity, Q, geological structure and lithology estimation at a ground water contamination site, *SEG Technical Program Expanded Abstracts*, **24**(1), 1561–1564.
- Gao, F., Levander, A., & Zelt, C., 2006. An iterative approach for geophysical diffraction tomography: Implication for true amplitude migration, *SEG Technical Program Expanded Abstracts*, **25**(1), 3325–3329.
- Gauthier, O., Virieux, J., & Tarantola, A., 1986. Two-dimensional nonlinear inversion of seismic waveforms: Numerical results, *Geophysics*, **51**(7), 1387–1403.
- Gholami, Y., Brossier, R., Operto, S., Prioux, V., Ribodetti, A., Virieux, J., & Fourier, J., 2011a. Two-dimensional acoustic anisotropic ( VTI ) full waveform inversion : the Vallhall case study Annual Meeting, *SEG Technical Program Expanded Abstracts*, pp. 2543–2548.
- Gholami, Y., Brossier, R., Ribodetti, A., Virieux, J., & Fourier, J., 2011b. Acoustic VTI full waveform inversion : sensitivity analysis and realistic synthetic examples, *SEG Technical Program Expanded Abstracts*, pp. 2465–2470.
- Gohl, K. & Pedersen, L., 1995. Collisional tectonics of the Baltic Shield in the northern Gulf of Bothnia from seismic data of the BABEL project, *Geophysical Journal International*, **120**, 209–226.

- Guittou, A. & Díaz, E., 2011. Attenuating crosstalk noise with simultaneous source full waveform inversion, *Geophysical Prospecting*, **60**(4), 759–768.
- Hak, B. & Mulder, W. A., 2010. Migration for velocity and attenuation perturbations, *Geophysical Prospecting*, **58**(6), 939–951.
- Hak, B. & Mulder, W. A., 2011. Seismic attenuation imaging with causality, *Geophysical Journal International*, **184**(1), 439–451.
- Hicks, G. J. & Pratt, R. G., 2001. Reflection waveform inversion using local descent methods: Estimating attenuation and velocity over a gas-sand deposit, *Geophysics*, **66**(2), 598–612.
- Hole, J., 1992. Nonlinear high-resolution three-dimensional seismic travel time tomography, *Journal of Geophysical Research*, **97**(B5), 6553–6562.
- Hyvönen, T., Tiira, T., Korja, A., Heikkinen, P., & Rautioaho, E., 2007. A tomographic crustal velocity model of the central Fennoscandian Shield, *Geophysical Journal International*, **168**(3), 1210–1226.
- Jannane, M., Beydoun, W., Crase, E., Cao, D., Koren, Z., Landa, E., Mendes, M., Pica, A., Noble, M., Roeth, G., Singh, S., Snieder, R., Tarantola, A., Trezeguet, D., & Xie, M., 1989. Wavelengths of earth structures that can be resolved from seismic reflection data, *Geophysics*, **54**(7), 906–910.
- Jeong, W., Lee, H.-Y., & Min, D.-J., 2012. Full waveform inversion strategy for density in the frequency domain, *Geophysical Journal International*, pp. no–no.
- Jin, S., Madariaga, R., Virieux, J., & Lambare, G., 1991. Two-dimensional asymptotic iterative elastic inversion, *Geophysical Journal International*, **108**, 575–588.
- Krebs, J. R., Anderson, J. E., Hinkley, D., Neelamani, R., Lee, S., Baumstein, A., & Lacasse, M.-D., 2009. Fast full-wavefield seismic inversion using encoded sources, *Geophysics*, **74**(6), WCC177–WCC188.
- Lailly, P., 1983. The seismic inverse problem as a sequence of before stack migrations, in *Conference on inverse scattering: theory and application*, pp. 206–220, SIAM, Soc. Industr. appl. Math., Philadelphia, PA.
- Lambaré, G., Operto, S., Podvin, P., & Thierry, P., 2003. 3D ray + Born migration/inversion - Part 1 : Theory, *Geophysics*, **68**(4), 1348–1356.
- Lambare, G., Virieux, J., Madariaga, R., & Jin, S., 1992. Iterative asymptotic inversion in the acoustic approximation, *Geophysics*, **57**(9), 1138–1154.
- Leeuwen, T. V. & Mulder, W. A., 2010. Waveform Tomography by Correlation Optimisation, *EAGE extended abstract*, pp. 14 – 17.
- Levander, A., Zelt, C. A., & Symes, W. W., 2007. 1.08 - Crust and Lithospheric Structure - Active Source Studies of Crust and Lithospheric Structure, in *Treatise on Geophysics*,

- pp. 247–288, ed. Schubert, G., Elsevier, Amsterdam.
- Li, Q., Wilcock, W. S. D., Pratt, T. L., Snelson, C. M., & Brocher, T. M., 2006. Seismic Attenuation Structure of the Seattle Basin, Washington State, from Explosive-Source Refraction Data, *Bulletin of the Seismological Society of America*, **96**(2), 553–571.
- Liao, Q. & McMechan, G. A., 1996. Multifrequency viscoacoustic modeling and inversion, *Geophysics*, **61**(5), 1371–1378.
- Malinowski, M., Operto, S., & Ribodetti, A., 2011. High-resolution seismic attenuation imaging from wide-aperture onshore data by visco-acoustic frequency-domain full-waveform inversion, *Geophysical Journal International*, **186**(3), 1179–1204.
- Mavko, G., Mukerji, T., & Dvorkin, J., 1998. *The rock physics handbook: Tools for seismic analysis of porous media*, Cambridge University Press.
- Miller, D., Oristaglio, M., & Beylkin, G., 1987. A new slant on seismic imaging: Migration and integral geometry, *Geophysics*, **52**(7), 943.
- Moore, G. F., Bangs, N. L., Taira, A., Kuramoto, S., Pangborn, E., & Tobin, H. J., 2007. Three-Dimensional Splay Fault Geometry and Implications for Tsunami Generation, *Science*, **318**(5853), 1128–1131.
- Mora, P., 1987. Nonlinear two-dimensional elastic inversion of multioffset seismic data, *Geophysics*, **52**(9), 1211–1228.
- Mora, P., 1988. Elastic wave-field inversion of reflection and transmission data, *Geophysics*, **53**(6), 750–759.
- Mora, P., 1989. Inversion = migration + tomography, *Geophysics*, **54**(12), 1575–1586.
- Nakanishi, A., Takahashi, N., Park, J.-O., Miura, S., Kodaira, S., Kaneda, Y., Hirata, N., Iwasaki, T., & Nakamura, M., 2002. Crustal structure across the coseismic rupture zone of the 1944 Tonankai earthquake, the central Nankai Trough seismogenic zone, *Journal of Geophysical Research*, **107**(B1), 2326.
- Nakanishi, A., Kodaira, S., Miura, S., Ito, A., Sato, T., Park, J.-O., Kido, Y., & Kaneda, Y., 2008. Detailed structural image around splay-fault branching in the Nankai subduction seismogenic zone: Results from a high-density ocean bottom seismic survey, *Journal of Geophysical Research*, **113**, B03105.
- Operto, S., Virieux, J., Dessa, J.-X., & Pascal, G., 2006. Crustal seismic imaging from multifold ocean bottom seismometer data by frequency domain full waveform tomography: Application to the eastern Nankai trough, *Journal of Geophysical Research*, **111**, B09306.
- Operto, S., Ribodetti, A., Grini, M., & Virieux, J., 2007. Mixed-grid finite-difference frequency-domain viscoacoustic modeling in 2D TTI anisotropic media, *SEG Technical Program Expanded Abstracts*, **26**(1), 2099–2103.

- Plessix, R.-E., 2006. A review of the adjoint-state method for computing the gradient of a functional with geophysical applications, *Geophysical Journal International*, **167**(2), 495–503.
- Plessix, R.-E. & Cao, Q., 2011. A parametrization study for surface seismic full waveform inversion in an acoustic vertical transversely isotropic medium, *Geophysical Journal International*, **185**(1), 539–556.
- Pratt, R. G., 1990. Inverse theory applied to multi-source cross-hole tomography. Part 2: Elastic wave-equation method, *Geophysical Prospecting*, **38**(3), 311–329.
- Pratt, R. G., 1999. Seismic waveform inversion in the frequency domain, Part 1: Theory and verification in a physical scale models, *Geophysics*, **64**(3), 888–901.
- Pratt, R. G., 2008. Waveform Tomography - Successes, cautionary tales, and future directions, *the 69th Conference and Exhibition of the EAGE, Rome, Italy (Workshop 11, "Full Waveform Inversion - Current Status and Perspectives"*.
- Pratt, R. G. & Shipp, R. M., 1999. Seismic waveform inversion in the frequency domain, Part 2: Fault delineation in sediments using crosshole data, *Geophysics*, **64**(3), 902–914.
- Pratt, R. G. & Worthington, M. H., 1990. Inverse theory applied to multi-source cross-hole tomography. Part 1: Acoustic wave-equation method, *Geophysical Prospecting*, **38**(3), 287–310.
- Pratt, R. G., Song, Z.-M., Williamson, P., & Warner, M., 1996. Two-dimensional velocity models from wide-angle seismic data by wavefield inversion, *Geophysical Journal International*, **124**(2), 323–340.
- Pratt, R. G., Shin, C., & Hicks, G., 1998. Gauss-Newton and full Newton methods in frequency-space seismic waveform inversions, *Geophysical Journal International*, **133**(2), 341–362.
- Pratt, R. G., Hou, F., Bauer, K., & Weber, M. H., 2004. Waveform tomography images of velocity and inelastic attenuation from the Mallik 2002 Crosshole Seismic Surveys, in *Scientific results from the Mallik 2002 Gas Hydrate Production Research Well Program, Mackenzie Delta, North Territories, Canada*, vol. 585 of **Bulletin**, pp. 1–14, eds Dallimore, S. R. & Collet, T. S., Geological Survey of Canada.
- Pratt, R. G., Sirgue, L., Hornby, B., & Wolfe, J., 2008. Crosswell Waveform Tomography in fine-layered sediments: Meeting the challenges of anisotropy, *the 69th Conference and Exhibition of the EAGE, Rome, Italy*.
- Prieux, V., Brossier, R., Gholami, Y., Operto, S., Virieux, J., Barkved, O. I., & Kommedal, J. H., 2011. On the footprint of anisotropy on isotropic full waveform inversion: the Valhall case study, *Geophysical Journal International*, **187**(3), 1495–



1515.

- Quan, Y. & Harris, J. M., 1997. Seismic attenuation tomography using the frequency shift method, *Geophysics*, **62**(3), 895–905.
- Ravaut, C., Operto, S., Improta, L., Virieux, J., Herrero, A., & Dell’Aversana, P., 2004. Multiscale imaging of complex structures from multifold wide-aperture seismic data by frequency-domain full-waveform tomography: application to a thrust belt, *Geophysical Journal International*, **159**(3), 1032–1056.
- Ribodetti, A., Gaffet, S., Operto, S., Virieux, J., & Saracco, G., 2004. Asymptotic waveform inversion for unbiased velocity and attenuation measurements: numerical tests and application for Vesuvius lava sample analysis, *Geophysical Journal International*, **158**(1), 353–371.
- Saffer, D. M. & Tobin, H. J., 2011. Hydrogeology and Mechanics of Subduction Zone Forearcs: Fluid Flow and Pore Pressure, *Annual Review of Earth and Planetary Sciences*, **39**(1), 157–186.
- Sears, T. J., Barton, P. J., & Singh, S. C., 2010. Elastic full waveform inversion of multicomponent ocean-bottom cable seismic data: Application to Alba Field, U. K. North Sea, *Geophysics*, **75**(6), R109–R119.
- Sen, M. K. & Stoffa, P. L., 1991. Nonlinear one-dimensional seismic waveform inversion using simulated annealing, *Geophysics*, **56**(10), 1624–1638.
- Sen, M. K. & Stoffa, P. L., 1992. Rapid sampling of model space using genetic algorithms: examples from seismic waveform inversion, *Geophysical Journal International*, **108**(1), 281–292.
- Shin, C. & Cha, Y. H., 2009. Waveform inversion in the Laplace-Fourier domains, *Geophysical Journal International*, **177**(3), 1067–1079.
- Shin, C. & Ha, W., 2008. A comparison between the behavior of objective functions for waveform inversion in the frequency and Laplace domains, *Geophysics*, **73**(5), VE119–VE133.
- Shin, C., Marfurt, K. J., Park, K. G., Min, D.-J., Yoon, K., Yang, D., Ha, T., Ko, S., Kim, W., & Hong, S., 2002. Traveltime and amplitude calculation using a perturbation approach, *Geophysics*, **67**(5), 1648–1655.
- Shipp, R. M. & Singh, S. C., 2002. Two-dimensional full wavefield inversion of wide-aperture marine seismic streamer data, *Geophysical Journal International*, **151**(2), 325–344.
- Singh, S. C. & Minshull, T. a., 1994. Velocity structure of a gas hydrate reflector at Ocean Drilling Program site 889 from a global seismic waveform inversion, *Journal of Geophysical Research*, **99**(B12), 24221–24233.

- Sirgue, L., 2003. *Inversion de la forme d'onde dans le domaine frequential de donnees sismiques grands offsets.*, Ph.D. thesis, l'Ecole Normale Superieure de Paris.
- Sirgue, L. & Pratt, R. G., 2003. Waveform inversion under realistic conditions: Mitigation of non-linearity, *SEG Technical Program Expanded Abstracts*, **22**(1), 694–697.
- Sirgue, L. & Pratt, R. G., 2004. Efficient waveform inversion and imaging: A strategy for selecting temporal frequencies, *Geophysics*, **69**(1), 231–248.
- Sirgue, L., Etgen, J. T., & Albertin, U., 2008. 3D Frequency domain waveform inversion using time domain finite difference methods, in *Proceedings of the 70th European Association of Geoscientists and Engineers, Conference and Exhibition, Roma, Italy*, p. F, vol. 22.
- Sirgue, L., Barkved, O. I., Dellinger, J., Etgen, J., Albertin, U., & Kommedal, J. H., 2010. Full waveform inversion : the next leap forward in imaging at Valhall, *First Break*, **28**, 65–70.
- Smithyman, B., Pratt, R. G., Hayles, J., & Wittebolle, R., 2009. Detecting near-surface objects with seismic waveform tomography, *Geophysics*, **74**(6), WCC119–WCC127.
- Song, Z.-M., Williamson, P. R., & Pratt, R. G., 1995. Frequency-domain acoustic-wave modeling and inversion of crosshole data: Part II—Inversion method, synthetic experiments and real-data results, *Geophysics*, **60**(3), 796–809.
- Środa, P., 2006. Seismic anisotropy of the upper crust in southeastern Poland -effect of the compressional deformation at the EEC margin: Results of CELEBRATION 2000 seismic data inversion, *Geophysical Research Letters*, **33**(22), 1–6.
- Symes, W. W., 2008. Migration velocity analysis and waveform inversion, *Geophysical Prospecting*, **56**(6), 765–790.
- Takam Takougang, E. M. & Calvert, A. J., 2011. Application of waveform tomography to marine seismic reflection data from the Queen Charlotte Basin of western Canada, *Geophysics*, **76**(2), B55–B70.
- Tarantola, A., 1984. Inversion of seismic reflection data in the acoustic approximation, *Geophysics*, **49**(8), 1259–1266.
- Tarantola, A., 1988. Theoretical background for the inversion of seismic waveforms including elasticity and attenuation, *Pure and Applied Geophysics*, **128**(1-2), 365–399.
- Thierry, P., Operto, S., & Lambaré, G., 1999. Fast 2-D ray+ Born migration/inversion in complex media, *Geophysics*, **64**(1), 162–181.
- Tobin, H. J. & Kinoshita, M., 2006. NanTroSEIZE: the IODP Nankai Trough seismogenic zone experiment, *Scientific Drilling*, **2**(2), 23–27.
- Vigh, D. & Starr, E. W., 2008. 3D prestack plane-wave, full-waveform inversion, *Geophysics*, **73**(5), VE135–VE144.

- Virieux, J. & Operto, S., 2009. An overview of full-waveform inversion in exploration geophysics, *Geophysics*, **74**(6), WCC1–WCC26.
- White, D. & Clowes, R., 1994. Seismic attenuation structure beneath the Juan de Fuca Ridge from tomographic inversion of amplitudes, *Journal of geophysical research*, **99**(B2), 3043–3056.
- Williamson, P. R. & Pratt, R. G., 1995. A critical review of acoustic wave modeling procedures in 2.5 dimensions, *Geophysics*, **60**(2), 591–595.
- Williamson, P. R. & Worthington, M. H., 1993. Resolution limits in ray tomography due to wave behavior: Numerical experiments, *Geophysics*, **58**(5), 727–735.
- Woodward, M. J., 1992. Wave-equation tomography, *Geophysics*, **57**(1), 15–26.
- Woodward, M. J., Nichols, D., Zdraveva, O., Whitfield, P., & Johns, T., 2008. A decade of tomography, *Geophysics*, **73**(5), VE5–VE11.
- Wu, R., Araújo, F., & Huang, L., 1994. Multifrequency backscattering tomography for constant and vertically varying backgrounds, *International Journal of Imaging*, **5**, 7–21.
- Wu, R.-S. & Toksoz, M. N., 1987. Diffraction tomography and multisource holography applied to seismic imaging, *Geophysics*, **52**(1), 11–25.
- Xie, X., Jin, S., & Wu, R., 2006. Wave-equation-based seismic illumination analysis, *Geophysics*, **71**(5), S169–S177.
- Xu, K. & Greenhalgh, S., 2010. Ore-body imaging by crosswell seismic waveform inversion: A case study from Kambalda, Western Australia, *Journal of Applied Geophysics*, **70**(1), 38–45.
- Yilmaz, O., 2001. *Seismic data analysis*, Society of Exploration Geophysicists Tulsa.
- Zelt, C. & Ellis, R., 1990. Crust and upper mantle Q from seismic refraction data: Peace River region, *Canadian Journal of Earth Sciences*, **27**, 1040–1047.
- Zelt, C. a. & Barton, P. J., 1998. Three-dimensional seismic refraction tomography: A comparison of two methods applied to data from the Faeroe Basin, *Geophysical Journal International*, **103**(B4), 7187–7210.
- Zelt, C. A. & Smith, R. B., 1992. Seismic travelttime inversion for 2-D crustal velocity structure, *Geophysical Journal International*, **108**(1), 16–34.
- Zhang, J. & Toksoz, M. N., 1998. Nonlinear refraction travelttime tomography, *Geophysics*, **63**(5), 1726–1737.

# Chapter 2

## Waveform tomography imaging of a mega-splay fault system in the seismogenic Nankai subduction zone

A version of the chapter was published in *Earth and Planetary Science Letters* as: Kamei, R., Pratt, R.G., and Tsuji, T., “Waveform Tomography Imaging of a Megasplay Fault System in the Seismogenic Nankai Subduction Zone”

### 2.1 Introduction

Megathrust earthquakes in subduction zones have claimed a large number of casualties, and have caused devastating damage to human lives and to social infrastructure. The accompanying tsunamis have led to further destruction, especially in coastal regions (Ando, 1975; Lay et al., 2005). To understand the mechanism of megathrust earthquakes, it is critical to reveal the history of fault systems, and to characterize their geo-mechanical, thermal and hydrological properties (Hyndman & Wang, 1993; Oleskevich et al., 1999; Moore & Saffer, 2001). Direct measurements of such properties have been carried out through in-situ measurements, and laboratory experiments of core samples (Hashimoto et al., 2010; Tsuji et al., 2006; Saffer et al., 2009). However a full spatial characterization requires an understanding of detailed crustal structures. A key element in such characterization is controlled source seismic experiments, which have been extensively employed to illustrate two dimensional (2D) and/or three-dimensional (3D) crustal structures (Biju-Duval et al., 1982; Davis et al., 1990; Park et al., 2002a), and to estimate physical properties of subduction zones such as seismic velocities, porosity and pore-pressure (Bangs et al., 1990; Kodaira et al., 2004; Calahorrano B et al., 2008; Tobin & Saffer, 2009b).

Reflection seismic surveys are particularly useful in generating subsurface images that respond to impedance contrasts in the subsurface, and are commonly referred to as *reflectivity* images (see for example Biju-Duval et al., 1982; Davis et al., 1990; Park et al., 2002a; Moore et al., 2009). Seismic reflectivity images require extensive data processing using the methods of Common-Mid-Point (CMP) stacking and seismic migration (see Yilmaz, 2001 for a comprehensive summary). Reflectivity images are well suited for delineating complex fault systems, and the resulting images have resolutions of a wavelength (typically on the order of tens to hundreds of meters). Such high-resolution reflectivity images have enabled detailed analysis of complicated fault systems, especially when combined with direct observations from core-logs and core samples (e.g. Strasser et al., 2009).

However, reflectivity images do not provide enough information to analyze the mechanical properties of fault systems; instead quantitative images of seismic velocities are essential for the analysis of fault mechanics. In order to make use of seismic velocities, the relationship between velocity and other physical properties (e.g. porosity and pore pressure) must be established by adopting empirical relationships constrained from well-log data (Bangs et al., 1990; Calahorrano B et al., 2008; Tobin & Saffer, 2009a) and/or rock physics (Tsuji et al., 2008). The required velocity images can be generated from reflection seismic data by Normal Moveout (NMO) velocity analysis (Bangs et al., 1990; Cochrane et al., 1994; von Huene et al., 1998) or more accurately by migration velocity analysis (MVA, Calahorrano B et al., 2008; Park et al., 2002b, 2010). These velocity analysis methods generate velocity models that provide optimally focused reflectivity images. Typically a simple layered structure is assumed for NMO analysis, but more detailed models may be produced using tomographic approaches for MVA (e.g. Stork, 1992). In either case, the resulting velocity images are restricted in resolution when compared to reflectivity sections, since velocity imaging techniques typically rely on discrete arrivals and on asymptotic ray theory (Chen & Schuster, 1999; Woodward et al., 2008).

Velocity structures can also be reliably extracted from other type of seismic surveys, e.g. refraction seismic surveys, primarily through travelttime tomography (Dessa et al., 2004; Nakanishi et al., 2002, 2008; Kodaira et al., 2004). Travelttime tomography is the process of reconstructing subsurface velocity variation based on distinct arrivals using asymptotic ray theory (Williamson & Worthington, 1993). The combination of the asymptotic assumption and the significantly lower frequency signals employed in crustal refraction surveys than in reflection surveys hinder the resolution of travelttime tomography (typically to the order of kilometres).

To overcome the resolution limits of the conventional velocity imaging techniques

described above, we utilize frequency-domain waveform tomography, an alternative velocity imaging method based on a numerical solution to the full wave equation. Waveform tomography is a development of the waveform inversion methods which attempt to fit seismic waveforms beyond first arrivals. The method was first proposed by Lailly (1983) and Tarantola (1984); recently Virieux & Operto (2009) provided a full review of these methods, and characterized the frequency-domain approach as a powerful and practical velocity imaging technique in terms of the computational costs and stability. The frequency-domain approach was originally proposed by Pratt & Worthington (1990), it was suggested for crustal imaging by Pratt et al. (1996), and it was further developed by Pratt et al. (1998) and Sirgue & Pratt (2004). Like travelttime tomography, Waveform tomography focuses on transmission (refraction) energy, but the use of seismic waveforms rather than first arrivals lead to an improved potential for providing quantitative images at resolution scales of a half-wavelength or less (Wu & Toksoz, 1987; Mora, 1989; Pratt, 1999): The theoretical resolution of waveform tomography is thus compatible with that of seismic migration (provided that the frequency bandwidths are identical) (Sirgue et al., 2010).

The frequency-domain waveform tomography method used in this chapter was extensively validated in a blind test with synthetic elastic data by Brenders & Pratt (2007a,b), and has been successfully applied to the crustal scale imaging in complex environments including the Eastern Nankai subduction zone (Operto et al., 2006), the Queen Charlotte Basin (Takougang & Calvert, 2011), the Southern Apennines (Ravaut et al., 2004), the San Andreas Fault (Bleibinhaus et al., 2007), and the Polish Basin (Malinowski & Operto, 2008; Malinowski et al., 2011). In this chapter, we apply waveform tomography to refraction data obtained using Ocean Bottom Seismographs (OBSs) in the central Nankai subduction zone, and demonstrate that waveform tomography produces quantitative high-resolution velocity images. The images merge the fine-scale characteristics of migration methods with the quantitative aspects of tomographic velocity imaging, allowing an improved interpretation of the mega-splay fault system.

## 2.2 Geological background

The Nankai subduction zone is located southwest of Japan, where the Philippine Sea Plate is subducting beneath the Eurasia Plate. Episodic megathrust earthquakes in this region are typically tsunamigenic, and have caused devastation most recently in 1944 and in 1946 (Ando, 1975). In the central Nankai subduction zone off the Kii Peninsula (Fig. 2.1), migrated reflection seismic sections (Park et al., 2002a; Moore et al.,

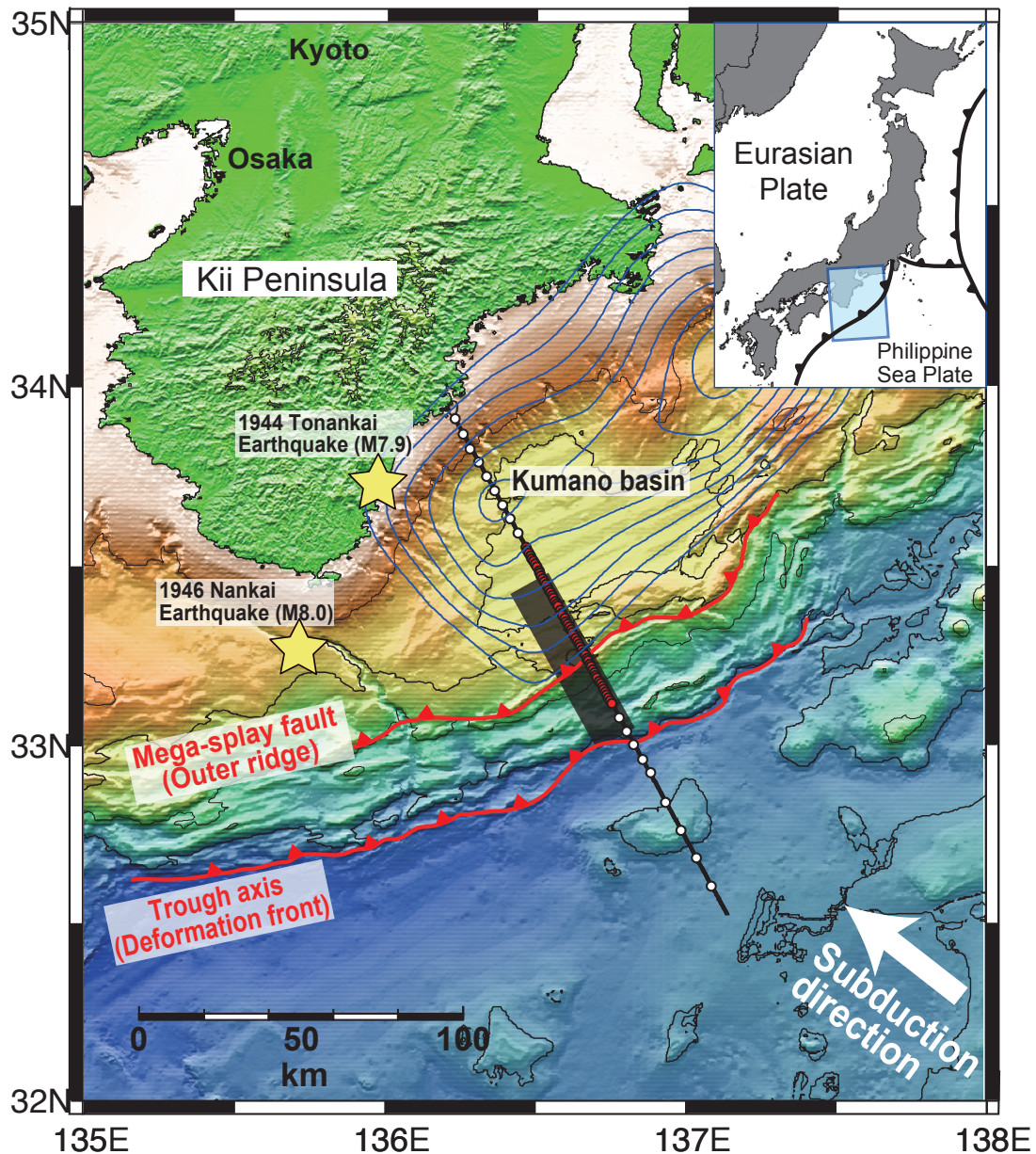


Figure 2.1: Maps of southwest Japan and the Nankai Trough. An ocean bottom seismograph (OBS) survey was conducted in 2004 (solid black line). Circles indicate OBS positions; red circles indicate OBS positions used for waveform tomography in this chapter. The 3D reflection survey area used by Moore et al. (2009) is shown as a grey-shaded area. Dark blue contours show the coseismic slip distribution of the 1944 Tonankai earthquake (Kikuchi et al., 2003). The subduction direction of the Philippine Sea Plate is based on the MORVEL vector of DeMets et al. (2010).

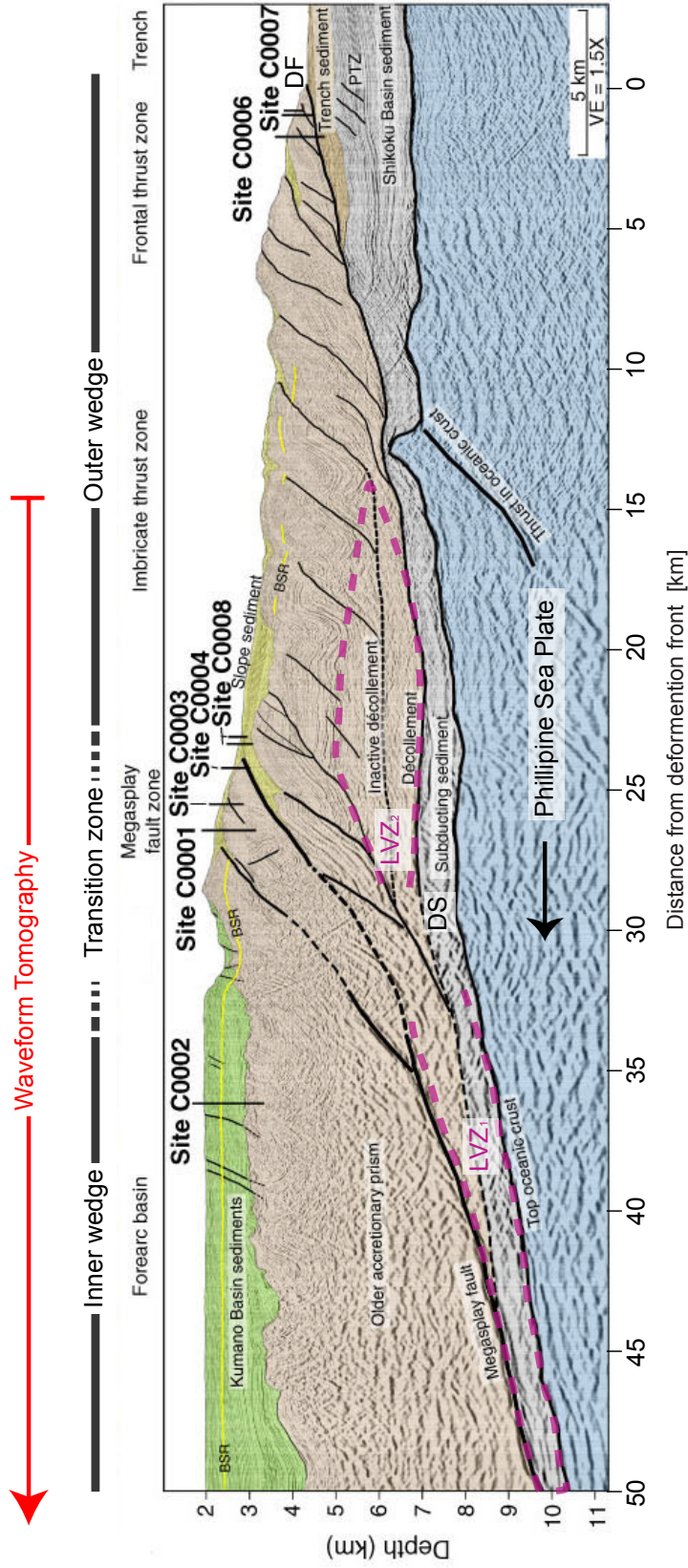


Figure 2.2: Interpreted pre-stack migration section (after Figure F6B in Moore et al., 2009). Two low velocity zones identified by previous researchers are outlined in magenta and identified as LVZ<sub>1</sub> (Bangs et al., 2009) and LVZ<sub>2</sub> (Park et al., 2010). PTZ stands for protothrust zone, BSR for bottom simulating reflector, DF for deformation front, and VE for vertical exaggeration. DS represents the décollement stepdown interpreted in Park et al. (2002a). Large black arrow indicates subduction direction of the Philippine Sea Plate.



2007, 2009) revealed a characteristic out-of-sequence thrust, known as a mega-splay fault (Tobin & Kinoshita, 2006). Park et al. (2002a) correlated the location of the fault to the coseismic rupture zones of 1944 Tonankai earthquake (Kikuchi et al., 2003; Tanioka & Satake, 2001), and interpreted the mega-splay fault as a critical structure for rupture propagation and tsunami generation. The mega-splay fault is believed to branch from the main subduction plate interface (the megathrust) of the subducting Philippine Sea Plate, and cut through the inner accretionary wedge (Park et al., 2002a; Moore et al., 2007, 2009). Near the sea bottom, the mega-splay fault splits further due to reduced confining pressures, and some of the splays reach the seafloor (Moore et al., 2007). The mechanical and frictional properties of the mega-splay fault are strongly influenced by pore-fluid pressures, which reduce effective stress and friction coefficients (Moore & Saffer, 2001; Wang & Hu, 2006; Tobin & Saffer, 2009b). Over-pressured regions typically show weak rigidity, and result in low-velocity and low-density materials. Potentially over-pressured low velocity zones have been identified in the vicinity of the mega-splay fault using reflection and refraction seismic surveys (Park et al., 2002a, 2010). A low velocity zone (LVZ<sub>1</sub> in Fig. 2.2) in the inner accretionary wedge directly underneath the mega-splay fault was identified from the reverse polarity of the reflection from the mega-splay fault (Park et al., 2002a; Bangs et al., 2009). LVZ<sub>1</sub> is associated with fluid migration along the fault (Park et al., 2002a), and/or the existence of over-pressured underthrust sediments as the extended portion of the underthrust sediments in the outer accretionary wedge (Bangs et al., 2009). Another low velocity zone (LVZ<sub>2</sub> in Fig. 2.2) was suggested in the transition zone between the inner and outer wedge by Park et al. (2010). LVZ<sub>2</sub> may be abundant in pore fluids due to the compaction of pore space and the dehydration of clay minerals in unconsolidated sediments, and may have been formed by underplating of the accretionary prism by underthrust sediments (Park et al., 2010). Park et al. (2010) further speculated that the geometrical proximity of the mega-splay fault and LVZ<sub>2</sub> may imply fluid migration between them. However previous migration images are poorly resolved in the area between these low velocity zones due to the influence of the sea bottom topographic relief on the images. Furthermore, the velocity images from conventional travelttime tomography have not yielded sufficient resolution to resolve the connection between these zones (Nakanishi et al., 2008). These technical disadvantages have left an ambiguous geometrical relationship of the two over-pressured layers (LVZ<sub>1</sub> and LVZ<sub>2</sub>) and the mega-splay fault, precluding a complete image of the mega-splay fault system.

## 2.3 Long offset OBS data

In order to generate waveform tomography images, we used waveforms from Ocean Bottom Seismograph (OBS) data acquired in the southeast offshore of the Kii Peninsula (Fig. 2.1) by the Japan Agency for Marine Earth Science and Technology (JAMSTEC) in 2004 (Nakanishi et al., 2008). The OBSs were located at 1 km intervals near the outer ridge, and in 5-10 km intervals elsewhere. A large air gun array with a total volume of about 200 l and a pressure of 14 MPa was employed at 10 m water depths, at 200 m intervals. 74 OBSs were deployed at the sea bottom over a total interval of 175 km. The OBSs recorded 4 motion components (3 orthogonal particle velocities, and the pressure field).

Our goal was to image a sub-surface section 60 km wide and 15 km deep in the area of the active mega-splay (Fig. 2.2). This section was analyzed using a subset of the original data: 54 OBSs at 1 km spacing, with 285 air gun sources distributed regularly over the entire 65 km profile. Using conventional traveltime tomography and handpicked arrival times, Nakanishi et al. (2008) recovered a velocity model with a spatial resolution of approximately 2.5 km. This velocity model is shown in Fig. 2.3a; it predicts arrival times to an RMS misfit of 60 ms, which is comparable to the error levels for the original traveltime picks.

## 2.4 Frequency-domain acoustic waveform tomography

We applied frequency-domain acoustic waveform tomography (Pratt & Worthington, 1990; Pratt et al., 1998; Sirgue & Pratt, 2004; Brenders & Pratt, 2007a,b) to the original waveform data recorded at these 54 OBSs, in order to obtain a quantitative, high-resolution P-wave velocity image. In this approach, the required forward simulations use a frequency-domain finite difference method for the 2D visco-acoustic wave equation developed by Pratt & Worthington (1990), with further modifications by Jo et al. (1996). For our purposes of forming P-wave velocity images, we employed only the vertical component records from the OBSs. This is a plausible approximate approach for P-velocity imaging, because our pressure sources were excited in acoustic environment (i.e. the ocean), and because P-wave energy dominates the early part of the vertical components of our OBS data. This methodology is consistent with that tested by Brenders & Pratt (2007a) on synthetic elastic data.

Waveform tomography employs a local gradient method for model optimization, in

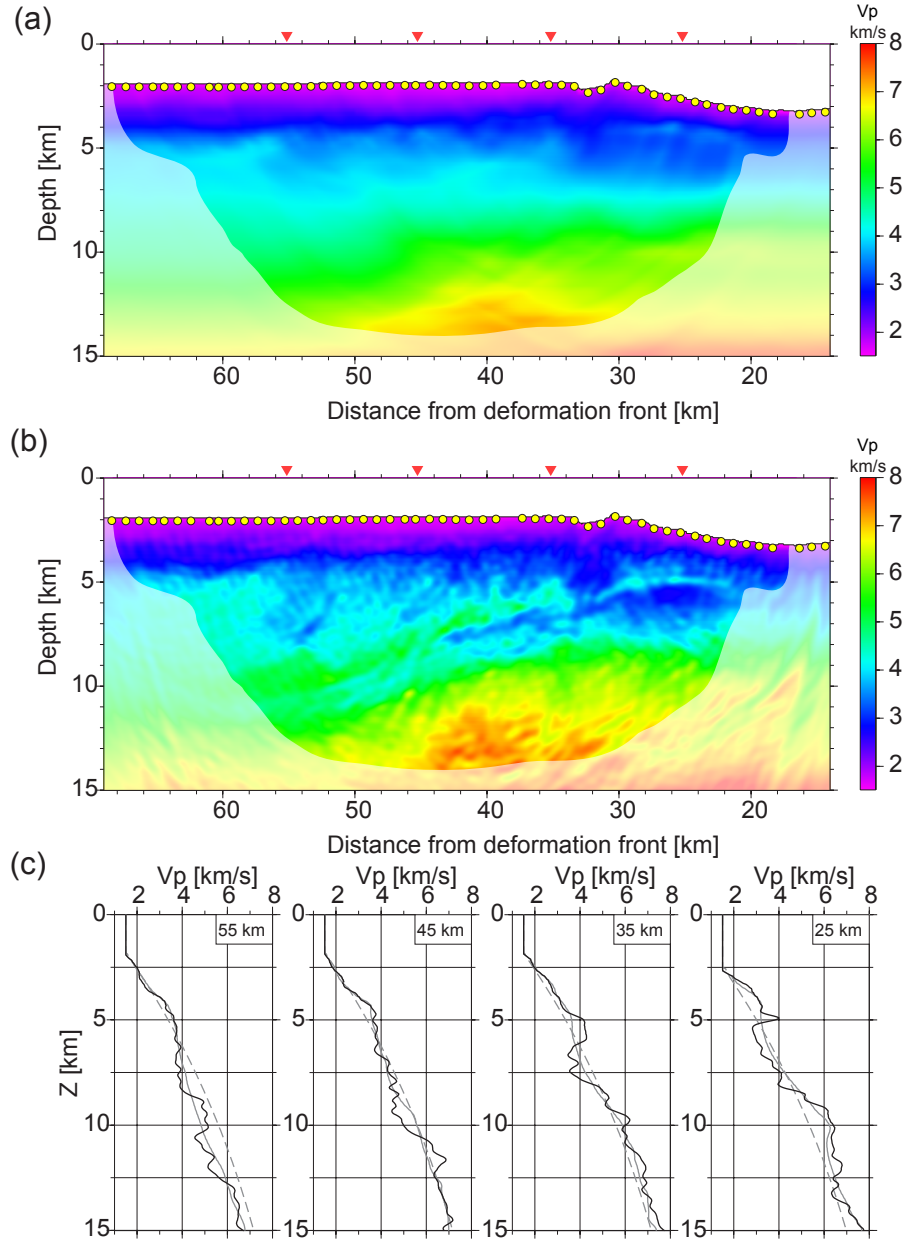


Figure 2.3: (a) P-wave velocity model obtained by travelt ime tomography (Nakanishi et al., 2008), and used as a starting model for waveform tomography in this chapter. Areas with poor wavepath coverage are shaded. The horizontal axis is the landward distance from the deformation front (see Fig. 2.2). Yellow circles show the location of the OBS used for analysis in this study. (b) Velocity structure after waveform tomography. (c) Vertical profiles of the velocity structures at the distances of 25, 35, 45, and 55 km from the deformation front (red triangles in (a) and (b)). Grey lines in (c) represent the velocities in the starting model in (a), the black lines correspond to the waveform tomography results in (b), and the dashed lines correspond to the background model as the 3rd order polynomial  $V_o(x, z) = a(z - z_0(x))^3 + b(z - z_0(x))^2 + c(z - z_0(x)) + d$ , best fitting the travelt ime tomography result (Fig. 2.5a).

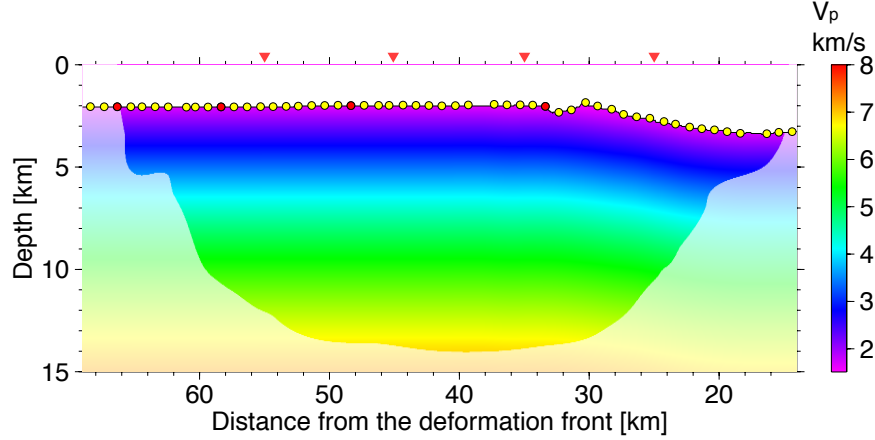


Figure 2.4: Background velocity model defined by  $V_o(x, z) = a(z - z_0(x))^3 + b(z - z_0(x))^2 + c(z - z_0(x)) + d$ , where  $z_0$  is the depth of the seafloor. Red triangles indicate the locations of the vertical profiles shown in Figs 2.3c and 2.5c.

which the gradients (the update images) are calculated using an adjoint operator (after Lailly, 1983 and Tarantola, 1984, and fully described for the frequency domain by Pratt et al. (1998)). We minimize the logarithmic Least Squares misfit functional, which allows a straightforward separation of phase and amplitude information (Shin & Min, 2006) (Details are discussed in Chapter 3 and 4). Since waveform tomography is a strongly non-linear inverse problem (Sirgue & Pratt, 2004), the traveltime tomography result of Nakanishi et al. (2008) shown in Fig. 2.3a was used as a starting model for the process; this model provides an excellent fit of the picked traveltimes. The inversions were conducted in the frequency domain, facilitating a multiscale approach to increase stability and convergence (Bunks et al., 1995). Initial results were generated using low frequencies (starting at 2.5 Hz), and constrained to low wavenumbers, following which higher frequencies (up to 8.5 Hz) and higher wavenumbers were reconstructed (see Bunks et al. (1995), Pratt et al. (1998) and Sirgue & Pratt (2004) for further discussion of the multiscale approach). The final velocity models were verified by observing the decreases in the logarithmic Least Squares misfit functional, by visual comparison of time-domain synthetic wavefields with the observed data, and by comparison with previous migration images. These validation methods provide the required confidence in our results to allow us to proceed.

In order to use an acoustic waveform tomography algorithm with field data, a series of data preprocessing steps are required (Brenders & Pratt, 2007a): Following deconvolution (spectral whitening) performed by Nakanishi et al. (2008), a bandpass filter was applied to limit data frequencies to between 2.0-8.5 Hz. The waveforms were then time-

windowed to exclude late arrivals as these are contaminated with surface multiples and S-wave arrivals. The near offset data (from 0 to 5 km) were also eliminated due to the observed amplitude saturation of early arrivals. Finally, the amplitude behaviour of the data with respect to the offset was calibrated to fit acoustic wavefield modelling following Brenders & Pratt (2007a). Throughout the modelling and inversions, exponential time damping was applied to avoid temporal aliasing, and to preferentially weight early arrivals in the data (Sirgue & Pratt, 2003; Brenders & Pratt, 2007a); this approach is easily implemented in frequency-domain algorithms through the use of complex-valued frequencies (see for example Shin & Cha, 2009). Wavenumber filtering (Sirgue & Pratt, 2003, 2004) was applied to each successive gradient image, in order to mitigate receiver-side spatial aliasing, and also to enhance the recovery of low spatial wavenumbers in the images at early stages of the inversion process. The source wavelet was repeatedly re-estimated from the data after each velocity update step using the linear optimization method described in Pratt (1999).

## 2.5 Results

Our final waveform tomography results represent a waveform inversion of data between 2.25 Hz and 8.5 Hz, and are presented in Fig. 2.3b (the final P-wave velocity waveform tomography image), and in Fig. 2.3c (a series of velocity profiles). The final waveform tomography P-wave velocity images in Fig. 2.3b have a large dynamic range in velocity, from velocities of soft sediments, close to 1.5 km/s at the sea bottom, to velocities of approximately 8 km/s within the Philippine Sea Plate. In order to further evaluate these results we removed the background velocity trend from the images. This background (shown in Fig. 2.3c) was defined as the dominant vertical trend below the sea floor by the 3rd order polynomial  $V_o(x, z) = a(z - z_0(x))^3 + b(z - z_0(x))^2 + c(z - z_0(x)) + d$  which best fit the original 2D traveltime tomography result in Fig. 2.3a, where  $z_0(x)$  is the depth of a sea floor. The order of the polynomial was chosen to simultaneously represent shallow accretionary prisms where the velocity is rapidly increasing, and the deep oceanic crust where the velocity increase is relatively gentle. We show the background velocity model in Fig. 2.4. The de-trended velocity image is then defined by  $\Delta V(x, z) = V(x, z) - V_o(x, z)$ . We show the de-trended P-wave velocity image in Fig. 2.5a and b in both colour and grey scale, and we show selected profiles of the de-trended velocities in Fig. 2.5c. The colour image illustrates the quantitative velocity values, while the grey scale version highlights the high-resolution fabric evident on the results. We also show the same de-trended velocity image with an overlay obtained from the nearest 2D slice from the 3D

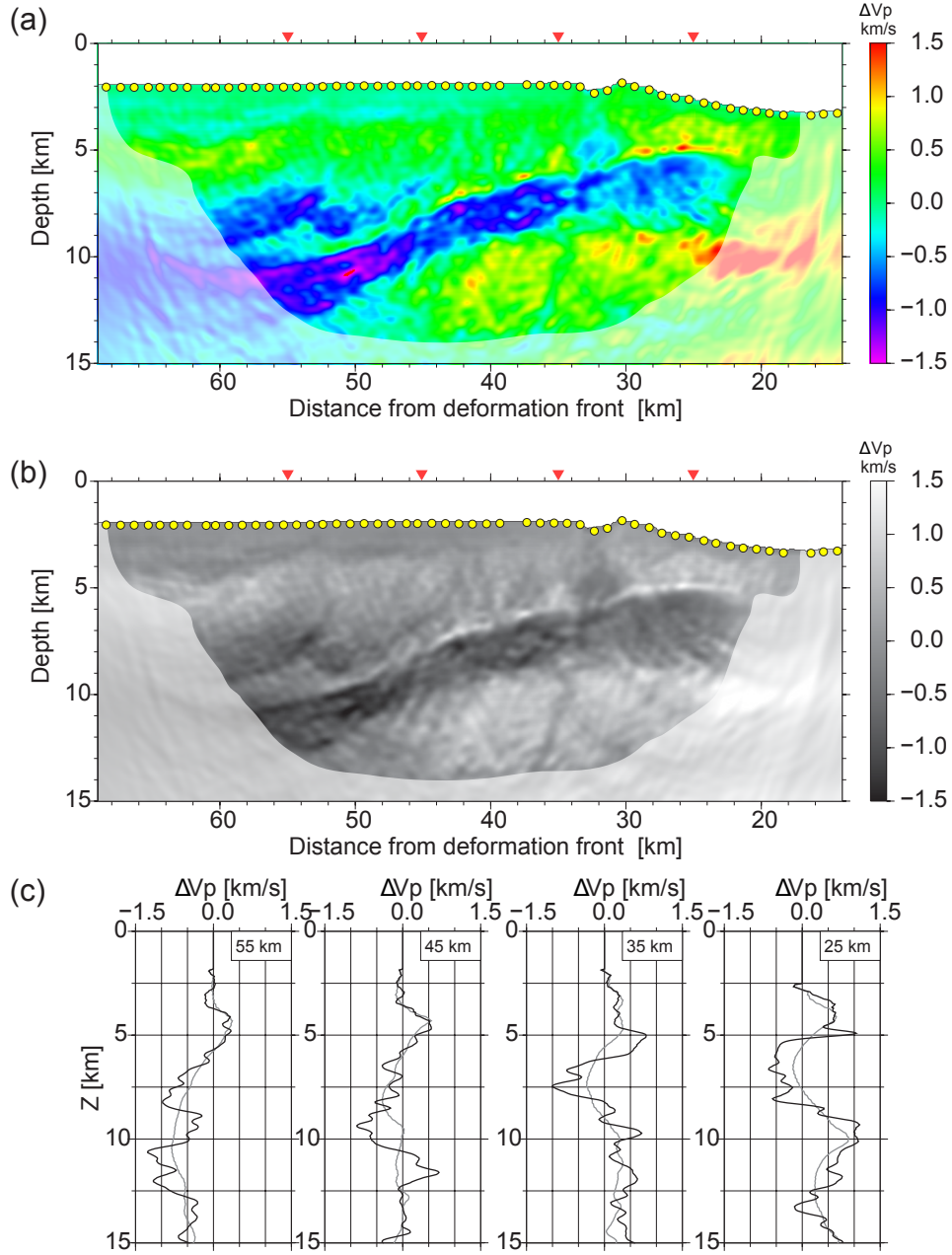


Figure 2.5: De-trended  $\Delta V(x,z)$  velocity structures obtained by removing the best-fit  $V_o(x,z)$  background velocity of the analyzed area displayed in Fig. 2.4. (a) The de-trended waveform tomography result shown in colour. The horizontal axis represents the landward distance from the deformation front (see Fig. 2.2). Yellow circles show the location of the OBSs. (b) The same model as (a), depicted in grey scale. (c) Vertical profiles of the de-trended velocity structures at distances of 25, 35, 45, and 55km from the deformation front, (red triangles in (a) and (b)). Grey lines in (c) represent de-trended velocities from the starting model in Fig. 2.3a, and the black lines represent de-trended velocities from the waveform tomography results in Fig. 2.3b.

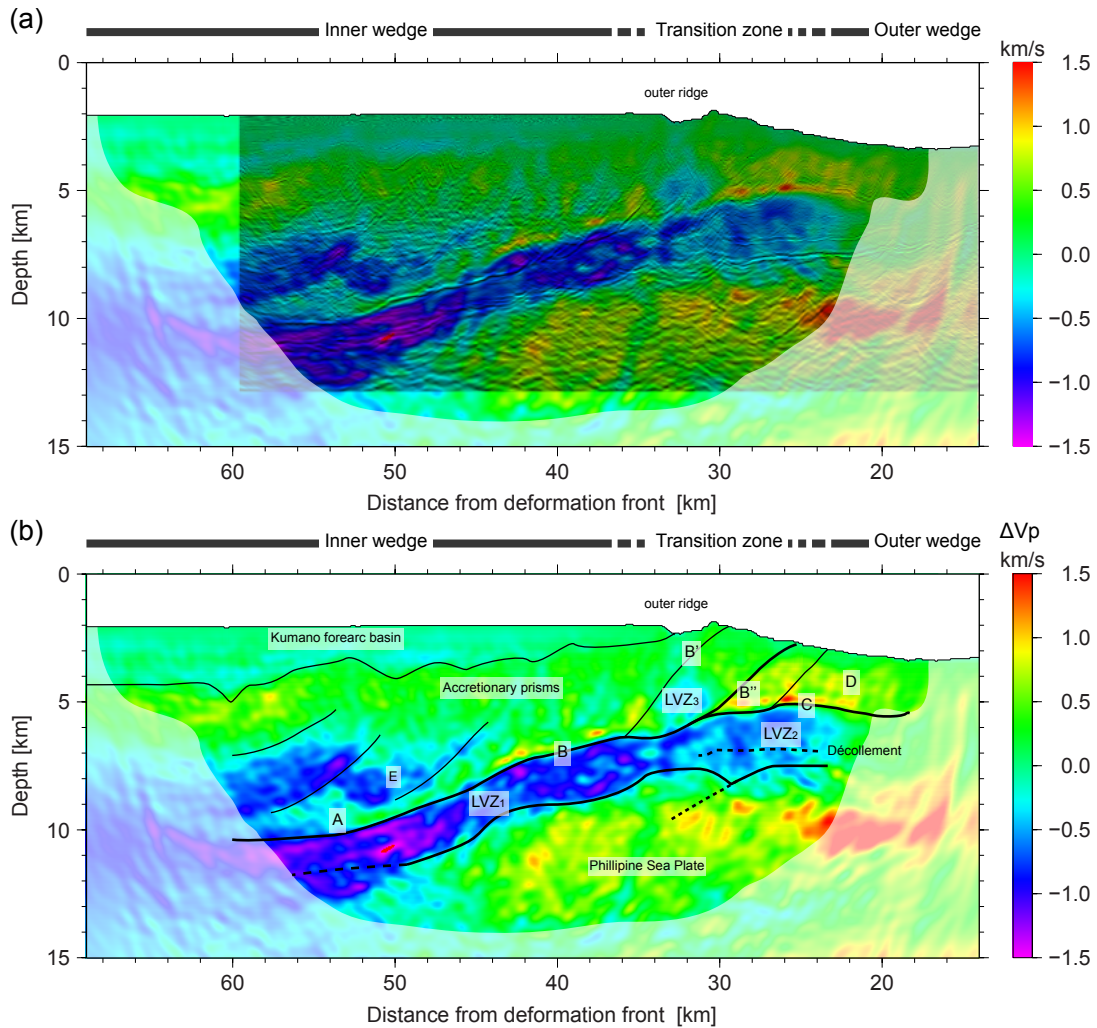


Figure 2.6: (a) The de-trended waveform tomography result with an overlay taken from the nearest 2D slice of the 3D migration volume (Moore et al., 2009). (b) The de-trended waveform tomography result with a geological interpretation. The strong velocity discontinuity appearing along the mega-splay fault between 20-60 km distance was divided into lines A, B and C. Lines B' and B'' represents the most seaward branching of the mega-splay fault. The low velocity zones are labelled LVZ<sub>1</sub> (landward), LVZ<sub>2</sub> (seaward), and LVZ<sub>3</sub> (under the outer ridge). Dashed line represents lithology boundaries unclear in waveform tomography, and interpreted in conjunction with the reflectors evident on the migration image in (a). Area D indicates the accretionary prisms which exhibit higher velocity values with respect to the  $V_o(x, z)$  background model. Area E shows a fourth low velocity layer within the older accretionary prisms in the inner wedge.

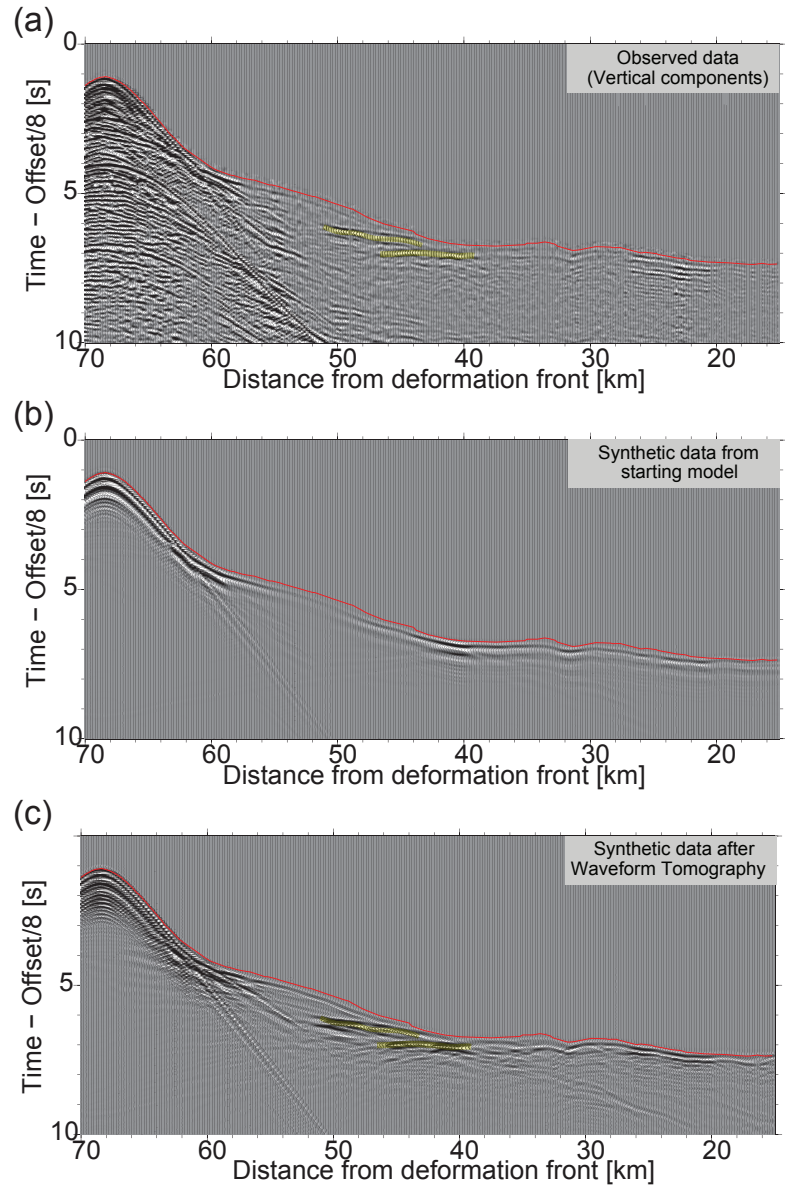


Figure 2.7: (a) Representative vertical component seismic waveforms recorded at the OBS located 65 km landward of the deformation front (Fig. 2.2). The red line indicates the picked first arrivals, and the yellow overlay indicates the interpreted wide angle reflection from the mega-splay fault. (b) Synthetic waveforms predicted in the starting velocity model (Fig. 2.3a) at the same OBS location, computed with a visco-acoustic finite difference method. Early arrival times in (b) correspond well with the observed data in (a), but the gather lacks the wide-angle reflections from the mega-splay fault. (c) Synthetic waveforms computed in the final waveform tomography result (Fig. 2.3b); these successfully reproduce the wide-angle reflections in the observed data in (a).



migration volume of Moore et al. (2009) in Fig. 2.6a. Note that here the spatial resolution differs between our waveform tomography results and the migration image, since the Waveform Tomography result was generated using a frequency bandwidth of 2.25 - 8.5 Hz, significantly lower than that of the reflection survey (which contained frequencies up to 80 Hz). In Fig. 2.6b, we identify major velocity discontinuities and anomalies visible in waveform tomography results: Solid black lines indicate velocity discontinuities clearly observed in the waveform tomography image, independent of their appearance in the migration sections. Black dashed lines indicate velocity discontinuities not clear in waveform tomography, but may be interpretable as lithology boundaries and/or faults in conjunction with the overlaid migrated reflectivity image in Fig. 2.6a. We identified three low velocity zones in Fig. 2.5, and labelled the zones as LVZ<sub>1</sub> – LVZ<sub>3</sub> in Fig. 2.6b. The other distinct velocity anomalies were indicated as area D and E. All interpretations and discussions below are made with reference to Fig. 2.5 and Fig. 2.6. The structures inside the Philippine Sea Plate are not interpreted, as extensive chequerboard testing (see Chapter 3) indicated the poor resolution in these area.

## 2.5.1 Interpretation

The increased resolution in the final waveform tomography result is evident when compared with the original traveltimes tomography images; velocity anomalies as small as 700 m horizontally and 350 m vertically in size can now be discerned (see Section 3.6.3.1 for a resolution analysis using chequerboard tests). The waveform tomography method produced a high-resolution quantitative velocity image that extends as deep as 12 km in places. Most major lithological boundaries are well depicted, including the mega-splay fault, the fore-arc basin, and the plate boundaries. Our image reveals the extensive distribution and the detailed geometry of the low velocity zones, and also illustrates the previously obscured geological structure beneath the outer ridge.

### 2.5.1.1 Mega-splay fault and velocity discontinuities

The mega-splay fault is imaged as a sharp velocity discontinuity (see especially line B) delineating the upper surface of a significant velocity reduction of approximately 0.5 km/s to 1 km/s with respect to the  $V_o(x, z)$  trend. The boundary of this discontinuity is mostly coincident with a major reflector evident on the migration images. Interestingly, the velocity discontinuity is not limited to the previously identified location (lines A and B), but appears to extend continuously throughout the entire region we analyzed. Beginning at the most landward portion of the velocity discontinuity, line A ( $X = 50 - 60$  km) is

nearly parallel to the seafloor at 10 km depth. Line A is closest to the plate boundary around  $X = 44$  km; unfortunately it is difficult to clearly locate the branching point of the mega-splay fault from the top of the oceanic crust on the waveform tomography image. Moving seaward, the velocity discontinuity turns upward into a steeper angle (line B). Several additional splay faults appear to branch from the mega-splay fault in the shallow subsurface (lines B' and B''). The velocity discontinuity appears to continue seawards (line C). Due to the limited coverage at the ends of the section, our images do not resolve the seaward termination of the velocity discontinuity.

### 2.5.1.2 Low velocity zones

The velocity discontinuities at lines A-C represent the upper boundaries of extensive low velocity zones. LVZ<sub>1</sub> is bounded at the top by lines A and B, and at the bottom by the oceanic crust of the Philippine Sea Plate. LVZ<sub>1</sub> is apparently 2 km thick or thicker, and extends at least 25 km landward of the outer ridge, although the landward termination is obscured by the limited coverage at the end of the section. The velocity distribution inside LVZ<sub>1</sub> is heterogeneous, with variations in velocity of up to 1 km/s. We observe the velocity reduction most prominently along the top and bottom boundaries. LVZ<sub>2</sub> is bounded at the top by line C of the velocity discontinuity; the layer directly above (area D) shows a velocity higher than expected from the velocity trend. The lower bound of LVZ<sub>2</sub> is poorly defined. There is little apparent velocity contrast between the presumably underplated sediments and the subducting underthrust sediments as suggested by Park et al. (2010). The décollement is primarily identifiable from its expression on the migration image with a positive reflectivity shown in Fig. 2.6a, and indicated as a dashed line in Fig. 2.6b. LVZ<sub>2</sub> appears to contain a fairly homogeneous velocity distribution.

### 2.5.1.3 Structures underneath the outer ridge

Line B of the mega-splay fault branches into line B' and B'', and we observe a small low velocity zone (LVZ<sub>3</sub>) occupying the region between the two splay branches. The two low velocity zones, LVZ<sub>1</sub> and LVZ<sub>2</sub> appear to be connected at  $X=33$  km underneath the outer ridge. The thickness of the connection zone is approximately 1.5 km, narrower than the average widths of LVZ<sub>1</sub> and LVZ<sub>2</sub>. Underneath the connected zone, we observe an apparent 1 km vertical relief in the oceanic crust.

## 2.5.2 Verification

As with any inversion method, the final result should provide a demonstrable improvement in data fit. Data fit is qualified by the level of data residuals, i.e. the differences between the observed data and the synthetic data from a given velocity model. During the inversion process, the frequency domain data residuals were reduced by 30% as compared with those observed from the starting traveltime velocity model. We also observed significant improvements in the fit of more conventional time domain simulations: Fig. 2.7 shows representative seismic waveforms from the OBS at  $X = 68$  km. In Fig. 2.7a, we depict the original recorded data waveforms. Clear wide-angle reflections from the mega-splay fault are evident between  $X = 40 - 52$  km, in conjunction with refractions travelling through the accretionary prisms ( $X = 15 - 40$  km), and the oceanic crust ( $X = 46 - 56$  km). Fig. 2.7b illustrates synthetic acoustic wavefields from the same OBS, simulated in the starting velocity model (i.e., in the traveltime tomography result shown in Fig. 2.3a). The synthetic wavefields show excellent agreement with the first arrival times from the observed wavefields, demonstrating the accuracy of the traveltime tomography velocity model, but the corresponding wavefields lack the wide-angle reflections from the mega-splay fault. Fig. 2.7c illustrates synthetic data computed in the final waveform tomography velocity structure of Fig. 2.3b; these wavefield data reproduce the wide-angle reflections from the mega-splay fault successfully, and also show an improved fit of amplitude variations in the waveforms. These substantial improvements in waveform fit provide significant confidence in the velocity reconstructions of Fig. 2.3b and c.

## 2.5.3 Comparison with the pre-stack migration section

The notable agreement of apparent lithological boundaries evident on the waveform tomography with corresponding reflectors on the migration image (Fig. 2.6a) provides further confidence in the validity of the waveform tomography approach. We note a slight discrepancy in the depth of the mega-splay fault (line A) and the plate boundary between our image and the migration image; this can be attributed to the fact that velocity values in the inner wedge seen for the waveform tomography result are approximately 0.5 km/s slower than the velocity model used for the seismic migration. This discrepancy is partly due to large uncertainties in the migration velocity caused by the short length (4.6 km) of the streamer cable employed in the 3D reflection survey (Moore et al., 2009). Other discrepancies may have arisen due to velocity anisotropy, as the two methods rely on significantly different directions of wave propagation. The upper bound of LVZ<sub>2</sub>

(line C) corresponds to a weak discontinuous reflector in the migration image, in spite of the strong and continuous velocity reduction of approximately 0.8 km/s apparent in the waveform tomography results. This same apparent discrepancy was also noted by Park et al. (2010) between the migration velocity analysis and the migration image. The discrepancy is likely to arise for technical reasons: If line C has an irregular surface, the reflection energy (5-80Hz) may be scattered in 3D, making it difficult to migrate the reflector effectively. However the low-frequency refraction energy (2.25-8.5Hz) used in waveform tomography is less sensitive to the detailed structure of the boundary, leading to a more continuous reconstruction of the boundary.

Waveform tomography has also yielded a superior recovery of the area underneath the outer ridge ( $X = 33$  km) in comparison with the migration images, and the new images suggest the existence of a low velocity zone connecting LVZ<sub>1</sub> and LVZ<sub>2</sub>. We attribute this improvement to the differences in the forward modelling algorithms embedded in each imaging method: The seismic Kirchhoff pre-stack migration algorithm adopted in Moore et al. (2009) and Park et al. (2010), uses pre-stack asymptotic ray theory, while waveform tomography in this study uses a numerical solution for the full acoustic wave equation. Furthermore, the absence of LVZ<sub>3</sub> in the migration velocity model may have prevented an effective migration of the reflectors below. Migration images can theoretically be improved by using more elaborate algorithms like Reverse Time Migration (Baysal et al., 1983; Chang & McMechan, 1986), or possibly by re-migration of the reflection data using the velocity model obtained in this study.

The décollement was not clearly depicted in the waveform tomography result, although a possible signature can possibly be discerned on the grey-scale de-trended velocity image. This may imply that the impedance contrasts at the décollement seen in the migration images are mainly due to density changes which do not follow the Gardner's relationship assumed in the inversion, and that in this specific region of the image the velocity changes are not significant enough to be recovered by waveform tomography.

## 2.6 Discussions

Waveform tomography was used to provide a quantitative P-wave velocity section of the entire mega-splay fault system. This reconstruction filled in parts of the structures that were poorly resolved on earlier migration images, and provided quantitative high resolution velocity information. The improvement is prominent in the inner wedge, and in the illustration of the over-pressured low velocity zones including LVZ<sub>1</sub> and LVZ<sub>2</sub>.

The low velocity zones have been interpreted as representing the distribution of over-

pressured unconsolidated sediments which are much younger than the overlying accretionary prisms (Bangs et al., 2009; Park et al., 2010). In our area of study, we observe a low velocity zone (LVZ<sub>2</sub>) at 15 - 33 km landward of the deformation front, located in the transition zone between the inner and outer wedge, and also close to the updip limit of the coseismic slip (Ichinose et al., 2003; Baba et al., 2006; Wang & Hu, 2006). LVZ<sub>2</sub> is significantly thicker than the seaward portion of the underthrust sediments, and is characterized at the top by a sharp velocity discontinuity but weak reflectivity. The location of LVZ<sub>2</sub> coincides with the segments suggested by Park et al. (2010) as underplated sediments. Park et al. (2010) suggested that underplated sediments exist above the décollement, separated from the underthrust sediments (although the décollement is ambiguous in terms of velocity discontinuities in our P-wave velocity image). Bangs et al. (2009) have suggested that the décollement has previously stepped down into underthrusting sediments (their Figure 4c), implying that the top of the current low velocity zone marks the location of the previous décollement. The accretionary wedge above LVZ<sub>2</sub> (area D in Fig. 2.6b) exhibits a higher velocity than expected, and the migration image suggests a relatively undeformed layered structure. Direct observation of core samples has also inferred relatively undeformed sediments composed of unconsolidated sand and mud materials (Screaton et al., 2009). Hence, we suggest that area D may possess a permeability lower than LVZ<sub>2</sub>, because younger LVZ<sub>2</sub> should possess high porosity. Thus area D may act as a structural seal for upward movement of excess water in LVZ<sub>2</sub>. While fluids may be transferred to the sea bottom along the décollement below this area, the coincidence with interseismic low frequency tremors (Obana & Kodaira, 2009) may indicate that accumulated pore fluids also possibly elevate pore-pressures in LVZ<sub>2</sub>, and may require episodic release through conduits such as the shallow mega-splay branches, as inferred by (Obana & Kodaira, 2009).

Underneath the outer ridge, the waveform tomography image indicates apparent low velocity materials below the mega-splay fault (line B), and these connect the low velocity zones between the inner and outer wedges. The fault structures display complexities possibly related to the mega-splay fault movement, or to plate bending. LVZ<sub>3</sub> between the two splay fault branches (line B' and B'') may indicate the destruction of fabric due to the repetitive displacement of both line B' and B''. The topographic relief on the oceanic crust may be related to activity of the reverse fault as suggested by Tsuji et al. (2009).

Further landward, LVZ<sub>1</sub> may be inferred again to represent over-pressured unconsolidated sediments contacting the low velocity zones in the outer wedge; either underplating (Ikesawa et al., 2005; Kitamura et al., 2005; Kondo et al., 2005) or underthrusting (Bangs

et al., 2009). If we accept the décollement step down inferred in Park et al. (2002a), and identified as DS in Fig. 2.2, then underplating may be a plausible cause for LVZ<sub>1</sub>. Alternatively, LVZ<sub>1</sub> may be interpreted as being primarily composed of a continuous portion of the underthrust sediments appearing in the outer wedge as suggested by Bangs et al. (2009), and the mega-splay fault may mark the top of the underthrust sediments. This is supported by the continuous appearance of low velocity zones in the inner and outer wedge. The existence of unusually deep underthrust sediments have been associated with delayed dehydration, and also have been suggested to cause the unusually deep updip limit of the seismogenic zone (Bangs et al., 2009). Unfortunately neither our waveform tomography images nor previous seismic migration images have the required resolution to strongly support either hypothesis of underplating, or underthrusting. waveform tomography also indicates a prominent low velocity area at the top of LVZ<sub>1</sub> (line B), which may represent the shear zone of the mega-splay fault. This is potentially a fluid conduit transporting pore-fluid water from deeper sources (Park et al., 2002a) or from in-situ dehydration in the underthrust sediments moving fluids to the shallower splay faults (Bangs et al., 2009), or possibly moving fluids to LVZ<sub>2</sub> as suggested by Park et al. (2010). The velocity decrease in LVZ<sub>1</sub> gradually diminishes landward, indicating continuous lithification within the sediments: the landward termination of LVZ<sub>1</sub> was not resolved on the waveform tomography image.

## 2.7 Conclusions

We have used waveform tomography to successfully image the mega-splay fault system in the Nankai subduction zone, and to illustrate potential pathways for large-scale fluid migration. The velocity images provide a significant improvement in waveform data fit compared to conventional travelttime tomography, and show excellent agreement with previous migration images. The results provide greater insight into the distribution of underthrust sediments and the relationship with the mega-splay fault.

Future analysis of these data with additional waveform tomography methods may prove fruitful. Waveform tomography is potentially able to image attenuation (Pratt et al., 2004; Malinowski et al., 2011), and elastic implementations can illustrate S-wave velocity structures (Brossier et al., 2009). These additional images will help to further constrain the geomechanical properties of the mega-splay fault system,

## Acknowledgements

The authors thank the Institute For Research on Earth Evolution (IFREE) of the Japan Agency for Marine-Earth Science and Technology (JAMSTEC) for providing the OBS data, G. Moore for giving permission to access the migration volume, S. Kodaira for help improving our manuscript, A. Nakanishi for providing the traveltime inversion result, Y. Kido for the help in data processing, D. Jiang, and A. Miyakawa for discussions about the geology, and A. Brenders and B. Smithyman for discussion of our waveform tomography results.

## References

- Ando, M., 1975. Source mechanisms and tectonic significance of historical earthquakes along the Nankai trough, Japan, *Tectonophysics*, **27**(2), 119–140.
- Baba, T., Cummins, P. R., Hori, T., & Kaneda, Y., 2006. High precision slip distribution of the 1944 Tonankai earthquake inferred from tsunami waveforms: Possible slip on a splay fault, *Tectonophysics*, **426**(1-2), 119–134.
- Bangs, N. L. B., Westbrook, G. K., Ladd, J. W., & Buhl, P., 1990. Seismic Velocities From the Barbados Ridge Complex: Indicators of High Pore Fluid Pressures in an Accretionary Complex, *J. Geophys. Res.*, **95**(B6), 8767–8782.
- Bangs, N. L. B., Moore, G. F., Gulick, S. P. S., Pangborn, E. M., Tobin, H. J., Kuramoto, S., & Taira, A., 2009. Broad, weak regions of the {N}ankai {M}egathrust and implications for shallow coseismic slip, *Earth and Planetary Science Letters*, **284**(1-2), 44–49.
- Baysal, E., Kosloff, D. D., & Sherwood, J. W., 1983. Reverse time migration, *Geophysics*, **48**(11), 1514–1524.
- Biju-Duval, B., Le Quellec, P., Mascle, A., Renard, V., & Valery, P., 1982. Multibeam bathymetric survey and high resolution seismic investigations on the Barbados Ridge complex (Eastern Caribbean): A key to the knowledge and interpretation of an accretionary wedge, *Tectonophysics*, **86**(1-3), 275–304.
- Bleibinhaus, F., Hole, J. A., Ryberg, T., & Fuis, G. S., 2007. Structure of the California Coast Ranges and San Andreas Fault at SAFOD from seismic waveform inversion and reflection imaging, *Journal of Geophysical Research*, **112**, B0631.
- Brenders, A. J. & Pratt, R. G., 2007a. Full waveform tomography for lithospheric imaging: results from a blind test in a realistic crustal model, *Geophysical Journal International*, **168**(1), 133–151.

- Brenders, A. J. & Pratt, R. G., 2007b. Efficient waveform tomography for lithospheric imaging: implications for realistic, two-dimensional acquisition geometries and low-frequency data, *Geophysical Journal International*, **168**(1), 152–170.
- Brossier, R., Operto, S., & Virieux, J., 2009. Seismic imaging of complex onshore structures by 2D elastic frequency-domain full-waveform inversion, *Geophysics*, **74**(6), WCC105–WCC118.
- Bunks, C., Saleck, F. M., Zaleski, S., & Chavent, G., 1995. Multiscale seismic waveform inversion, *Geophysics*, **60**(5), 1457–1473.
- Calahorrano B, A., Sallares, V., Collot, J., Sage, F., & Ranero, C., 2008. Nonlinear variations of the physical properties along the southern Ecuador subduction channel: Results from depth-migrated seismic data, *Earth and Planetary Science Letters*, **267**(3–4), 453–467.
- Chang, W.-F. & McMechan, G. A., 1986. Reverse-time migration of offset vertical seismic profiling data using the excitation-time imaging condition, *Geophysics*, **51**(1), 67.
- Chen, J. & Schuster, G. T., 1999. Resolution limits of migrated images, *Geophysics*, **64**(4), 1046–1053.
- Cochrane, G. R., Moore, J. C., MacKay, M. E., & Moore, G. F., 1994. Velocity and inferred porosity model of the Oregon accretionary prism from multichannel seismic reflection data: Implications on sediment dewatering and overpressure, *J. Geophys. Res.*, **99**(B4), 7033–7043.
- Davis, E. E., Hyndman, R. D., & Villinger, H., 1990. Rates of Fluid Expulsion Across the Northern Cascadia Accretionary Prism: Constraints From New Heat Flow and Multichannel Seismic Reflection Data, *J. Geophys. Res.*, **95**(B6), 8869–8889.
- DeMets, C., Gordon, R. G., & Argus, D. F., 2010. Geologically current plate motions, *Geophysical Journal International*, **181**(1), 1–80.
- Dessa, J.-X., Operto, S., Kodaira, S., Nakanishi, A., Pascal, G., Uhira, K., & Kaneda, Y., 2004. Deep seismic imaging of the eastern Nankai trough, Japan, from multifold ocean bottom seismometer data by combined travel time tomography and prestack depth migrations, *J. Geophys. Res.*, **109**, B02111.
- Hashimoto, Y., Tobin, H. J., & Knuth, M., 2010. Velocity-porosity relationships for slope apron and accreted sediments in the Nankai Trough Seismogenic Zone Experiment, Integrated Ocean Drilling Program Expedition 315 Site C0001, *Geochemistry Geophysics Geosystems*, **11**(May).
- Hyndman, R. D. & Wang, K., 1993. Thermal Constraints on the Zone of Major Thrust Earthquake Failure: The Cascadia Subduction Zone, *J. Geophys. Res.*, **98**(B2), 2039–2060.



- Ichinose, G. A., Thio, H. K., Somerville, P. G., Sato, T., & Ishii, T., 2003. Rupture process of the 1944 Tonankai earthquake (Ms 8.1) from the inversion of teleseismic and regional seismograms, *J. Geophys. Res.*, **108**(B10), 2497.
- Ikesawa, E., Kimura, G., Sato, K., Ikehara-Ohmori, K., Kitamura, Y., Yamaguchi, A., Ujiie, K., & Hashimoto, Y., 2005. Tectonic incorporation of the upper part of oceanic crust to overriding plate of a convergent margin: An example from the Cretaceous-early Tertiary Mugi Mlange, the Shimanto Belt, Japan, *Tectonophysics*, **401**(3-4), 217–230.
- Jo, C.-h., Shin, C., & Suh, J. H., 1996. 2-D scalar wave extrapolator, **61**(2), 529–537.
- Kikuchi, M., Nakamura, M., & Yoshikawa, K., 2003. Source rupture processes of the 1944 Tonankai earthquake and the 1945 Mikawa earthquake derived from low-gain seismograms, *Earth Planets and Space*, **55**(4), 159–172.
- Kitamura, Y., Sato, K., Ikesawa, E., Ikehara-Ohmori, K., Kimura, G., Kondo, H., Ujiie, K., Onishi, C. T., Kawabata, K., Hashimoto, Y., Mukoyoshi, H., & Masago, H., 2005. Mlange and its seismogenic roof dcollement: A plate boundary fault rock in the subduction zone — An example from the Shimanto Belt, Japan, *Tectonics*, **24**(5), TC5012—.
- Kodaira, S., Iidaka, T., Kato, A., Park, J.-O., Iwasaki, T., & Kaneda, Y., 2004. High pore fluid pressure may cause silent slip in the Nankai Trough, *Science*, **304**(5675), 1295–1298.
- Kondo, H., Kimura, G., Masago, H., Ohmori-Ikehara, K., Kitamura, Y., Ikesawa, E., Sakaguchi, A., Yamaguchi, A., & Okamoto, S., 2005. Deformation and fluid flow of a major out-of-sequence thrust located at seismogenic depth in an accretionary complex: Nobeoka Thrust in the Shimanto Belt, Kyushu, Japan, *Tectonics*, **24**(6), TC6008.
- Lailly, P., 1983. The seismic inverse problem as a sequence of before stack migrations, in *Conference on inverse scattering: theory and application*, pp. 206–220, SIAM, Soc. Industr. appl. Math., Philadelphia, PA.
- Lay, T., Kanamori, H., Ammon, C. J., Nettles, M., Ward, S. N., Aster, R. C., Beck, S. L., Bilek, S. L., Brudzinski, M. R., Butler, R., DeShon, H. R., Ekström, G., Satake, K., & Sipkin, S., 2005. The Great Sumatra-Andaman Earthquake of 26 December 2004, *Science*, **308**(5725), 1127–1133.
- Malinowski, M. & Operto, S., 2008. Quantitative imaging of the Permo-Mesozoic complex and its basement by frequency domain waveform tomography of wide-aperture seismic data from the Polish Basin, *Geophysical Prospecting*, **56**(6), 805–825.
- Malinowski, M., Operto, S., & Ribodetti, a., 2011. High-resolution seismic attenuation imaging from wide-aperture onshore data by visco-acoustic frequency-domain full-waveform inversion, *Geophysical Journal International*, **186**(3), 1179–1204.
- Moore, G. F., Bangs, N. L., Taira, A., Kuramoto, S., Pangborn, E., & Tobin, H. J., 2007.

- Three-Dimensional Splay Fault Geometry and Implications for Tsunami Generation, *Science*, **318**(5853), 1128–1131.
- Moore, G. F., Park, J., Bangs, N. L., Gulick, S. P., Tobin, H. J., Nakamura, Y., Sato, S., Tsuji, T., Yoro, T., Tanaka, H., Uraki, S., Kido, Y., Sanada, Y., & Kuramoto, S., 2009. Structural and seismic stratigraphic framework of the NanTroSEIZE Stage 1 transect, in *Proc.IODP, 314/315/316*, vol. 314, Integrated Ocean Drilling Program Management International, Inc.
- Moore, J. C. & Saffer, D., 2001. Updip limit of the seismogenic zone beneath the accretionary prism of southwest Japan: An effect of diagenetic to low-grade metamorphic processes and increasing effective stress, *Geology*, **29**(2), 183.
- Mora, P., 1989. Inversion = migration + tomography, *Geophysics*, **54**(12), 1575–1586.
- Nakanishi, A., Takahashi, N., Park, J.-O., Miura, S., Kodaira, S., Kaneda, Y., Hirata, N., Iwasaki, T., & Nakamura, M., 2002. Crustal structure across the coseismic rupture zone of the 1944 Tonankai earthquake, the central Nankai Trough seismogenic zone, *Journal of Geophysical Research*, **107**(B1).
- Nakanishi, A., Kodaira, S., Miura, S., Ito, A., Sato, T., Park, J.-O., Kido, Y., & Kaneda, Y., 2008. Detailed structural image around splay-fault branching in the Nankai subduction seismogenic zone: Results from a high-density ocean bottom seismic survey, *J. Geophys. Res.*, **113**, B03105.
- Obana, K. & Kodaira, S., 2009. Low-frequency tremors associated with reverse faults in a shallow accretionary prism, *Earth and Planetary Science Letters*, **287**(1-2), 168–174.
- Oleskevich, D. A., Hyndman, R. D., & Wang, K., 1999. The updip and downdip limits to great subduction earthquakes: Thermal and structural models of Cascadia, south Alaska, SW Japan, and Chile, *J. Geophys. Res.*, **104**(B7), 14965–14991.
- Operto, S., Virieux, J., Dessa, J.-X., & Pascal, G., 2006. Crustal seismic imaging from multifold ocean bottom seismometer data by frequency domain full waveform tomography: Application to the eastern Nankai trough, *J. Geophys. Res.*, **111**, B09306.
- Park, J.-O., Tsuru, T., Kodaira, S., Cummins, P. R., & Kaneda, Y., 2002a. Splay Fault Branching Along the Nankai Subduction Zone, *Science*, **297**(5584), 1157–1160.
- Park, J.-O., Tsuru, T., Takahashi, N., Hori, T., Kodaira, S., Nakanishi, A., Miura, S., & Kaneda, Y., 2002b. A deep strong reflector in the Nankai accretionary wedge from multichannel seismic data: Implications for underplating and interseismic shear stress release, *J. Geophys. Res.*, **107**(B4), 2061.
- Park, J.-O., Fujie, G., Wijerathne, L., Hori, T., Kodaira, S., Fukao, Y., Moore, G. F., Bangs, N. L., Kuramoto, S., & Taira, A., 2010. A low-velocity zone with weak reflectivity along the Nankai subduction zone, *Geology*, **38**(3), 283–286.

- Pratt, R. G., 1999. Seismic waveform inversion in the frequency domain, Part 1: Theory and verification in a physical scale models, *Geophysics*, **64**(3), 888–901.
- Pratt, R. G. & Worthington, M. H., 1990. Inverse theory applied to multi-source cross-hole tomography. Part 1: Acoustic wave-equation method, *Geophysical Prospecting*, **38**(3), 287–310.
- Pratt, R. G., Song, Z.-M., Williamson, P., & Warner, M., 1996. Two-dimensional velocity models from wide-angle seismic data by wavefield inversion, *Geophysical Journal International*, **124**(2), 323–340.
- Pratt, R. G., Shin, C., & Hicks, G., 1998. Gauss-Newton and full Newton methods in frequency-space seismic waveform inversions, *Geophysical Journal International*, **133**(2), 341–362.
- Pratt, R. G., Hou, F., Bauer, K., & Weber, M. H., 2004. Waveform tomography images of velocity and inelastic attenuation from the Mallik 2002 Crosshole Seismic Surveys, in *Scientific results from the Mallik 2002 Gas Hydrate Production Research Well Program, Mackenzie Delta, North Territories, Canada*, vol. 585, pp. 1–14, eds Dallimore, S. R. & Collet, T. S., Geological Survey of Canada.
- Ravaut, C., Operto, S., Imbrota, L., Virieux, J., Herrero, A., & Dell’Aversana, P., 2004. Multiscale imaging of complex structures from multifold wide-aperture seismic data by frequency-domain full-waveform tomography: application to a thrust belt, *Geophysical Journal International*, **159**(3), 1032–1056.
- Saffer, D., McNeill, L., Araki, E., Byrne, T., Eguchi, N., Toczko, S., Takahashi, K., & Scientists, t. E. ., 2009. NanTroSEIZE Stage2: NanTroSEIZE riser/riserless observatory, *IODP Prel.Rept.*, **319**.
- Screaton, E., Kimura, G., Curewitz, D., & the Expedition 316 Scientists, 2009. Expedition 316 summary, in *Proc. IODP, 314/315/316*, Integrated Ocean Drilling Program Management International, Inc., Washington, DC.
- Shin, C. & Cha, Y. H., 2009. Waveform inversion in the Laplace-Fourier domains, *Geophysical Journal International*, **177**(3), 1067–1079.
- Shin, C. & Min, D.-J., 2006. Waveform inversion using a logarithmic wavefield, *Geophysics*, **71**(3), R31–R42.
- Sirgue, L. & Pratt, R. G., 2003. Waveform inversion under realistic conditions: Mitigation of non-linearity, *SEG Technical Program Expanded Abstracts*, **22**(1), 694–697.
- Sirgue, L. & Pratt, R. G., 2004. Efficient waveform inversion and imaging: A strategy for selecting temporal frequencies, *Geophysics*, **69**(1), 231–248.
- Sirgue, L., Barkved, O. I., Dellinger, J., Etgen, J., Albertin, U., & Kommedal, J. H., 2010. Full waveform inversion : the next leap forward in imaging at Valhall, *First*

- Break*, **28**(April), 65–70.
- Stork, C., 1992. Reflection tomography in the postmigrated domain, *Geophysics*, **57**(5), 680.
- Strasser, M., Moore, G. F., Kimura, G., Kitamura, Y., Kopf, A. J., Lallemand, S., Park, J.-O., Sreaton, E. J., Su, X., Underwood, M. B., & Zhao, X., 2009. Origin and evolution of a splay fault in the Nankai accretionary wedge, *Nature Geosci*, **2**(9), 648–652.
- Takougang, E. M. T. & Calvert, A. J., 2011. Application of waveform tomography to marine seismic reflection data from the Queen Charlotte Basin of western Canada, *Geophysics*, **76**(2), B55–B70.
- Tanioka, Y. & Satake, K., 2001. Detailed coseismic slip distribution of the 1944 Tonankai Earthquake estimated from tsunami waveforms, *Geophys. Res. Lett.*, **28**(6), 1075–1078.
- Tarantola, A., 1984. Inversion of seismic reflection data in the acoustic approximation, *Geophysics*, **49**(8), 1259–1266.
- Tobin, H. J. & Kinoshita, M., 2006. NanTroSEIZE: the IODP Nankai Trough seismogenic zone experiment, *Scientific Drilling*, **2**(2, March 2006), 23–27.
- Tobin, H. J. & Saffer, D. M., 2009a. Elevated fluid pressure and extreme mechanical weakness of a plate boundary thrust, Nankai Trough subduction zone, *Geology*, **37**(8), 679–682.
- Tobin, H. J. & Saffer, D. M., 2009b. Elevated fluid pressure and extreme mechanical weakness of a plate boundary thrust, Nankai Trough subduction zone, *Geology*, **37**(8), 679–682.
- Tsuji, T., Kimura, G., Okamoto, S., Kono, F., Mochinaga, H., Saeki, T., & Tokuyama, H., 2006. Modern and ancient seismogenic out-of-sequence thrusts in the Nankai accretionary prism: Comparison of laboratory-derived physical properties and seismic reflection data, *Geophysical Research Letters*, **33**(18), L18309.
- Tsuji, T., Tokuyama, H., Costa Pisani, P., & Moore, G., 2008. Effective stress and pore pressure in the Nankai accretionary prism off the Muroto Peninsula, southwestern Japan, *J. Geophys. Res.*, **113**(B11), B11401.
- Tsuji, T., Park, J.-O., Moore, G., Kodaira, S., Fukao, Y., Kuramoto, S., & Bangs, N., 2009. Intraoceanic thrusts in the Nankai Trough off the Kii Peninsula: Implications for intraplate earthquakes, *Geophysical Research Letters*, **36**(6), L06303.
- Virieux, J. & Operto, S., 2009. An overview of full-waveform inversion in exploration geophysics, *Geophysics*, **74**(6), WCC1–WCC26.
- von Huene, R., Klaeschen, D., Gutscher, M., & Fruehn, J., 1998. Mass and fluid flux during accretion at the Alaskan margin, *Geological Society of America Bulletin*, **110**(4),

468–482.

- Wang, K. & Hu, Y., 2006. Accretionary prisms in subduction earthquake cycles: The theory of dynamic Coulomb wedge, *J. Geophys. Res.*, **111**(B6), B06410.
- Williamson, P. R. & Worthington, M. H., 1993. Resolution limits in ray tomography due to wave behavior: Numerical experiments, *Geophysics*, **58**(5), 727–735.
- Woodward, M. J., Nichols, D., Zdraveva, O., Whitfield, P., & Johns, T., 2008. A decade of tomography, *Geophysics*, **73**(5), VE5–VE11.
- Wu, R.-S. & Toksoz, M. N., 1987. Diffraction tomography and multisource holography applied to seismic imaging, *Geophysics*, **52**(1), 11–25.
- Yilmaz, O., 2001. *Seismic data analysis*, Society of Exploration Geophysicists Tulsa.

# Chapter 3

## On acoustic waveform tomography of wide-angle OBS data — Strategies for preconditioning and inversion

A version of the chapter was submitted for publication to *Geophysical Journal International* as: Kamei, R., Pratt, R.G., and Tsuji, T., “ On Acoustic Waveform Tomography of wide-angle OBS data — Strategies for preconditioning and inversion”

### 3.1 Introduction

In this chapter we develop a suite of preprocessing, data conditioning, imaging conditioning and inversion strategies for acoustic Waveform Tomography of deep water, densely sampled Ocean Bottom Seismograph (OBS) data. These strategies are developed, tested and applied to a data set acquired in the Nankai subduction zone (Nakanishi et al., 2008). Waveform tomography images from these data were described in Chapter 2, and published by Kamei et al. (2012); the purpose of this chapter is to describe in detail the strategies that were required in the production of those images. Our processing and inversion strategies are critical in optimizing the images, and in mitigating several issues: i) The well known non-linearities in the waveform inversion problem, ii) the challenges arising from crustal-survey design, and iii) modelling errors due to the use of an acoustic implementation. A key component of the strategies is that the final velocity structures are subjected to extensive quality control by scrutiny of synthetic waveforms, coherency of source estimates, and careful comparison with three-dimensional (3D) pre-stack depth

Table 3.1: List of mathematical symbols used in this chapter

Symbol	Type	Dimension	Description
$\mathbf{x}$	real		spatial location
$f$	real		frequency
$\omega$	real		angular frequency
$\Omega$	complex		complex angular frequency
$\omega_o$	real		reference frequency for attenuative models
$\tau$	real		characteristic time for exponential time-damping
$\sigma$	real		Laplace constant
$s$	complex		complex Laplace constant
$c$	complex		P-wave velocity
$c_R, c_I$	real		real or imaginary part of P-wave velocity
$\rho$	real		density
$Q$	real		quality factor
$N_d$	integer		number of data
$N_l$	integer		number of nodes in finite difference model
$N_m$	integer		number of model parameters
$\mathbf{S}$	complex	$N_l \times N_l$	frequency-domain finite difference matrix
$\mathbf{f}$	complex	$N_l \times 1$	pressure source vector
$\mathbf{d}$	complex	$N_d \times 1$	observed data vector
$\mathbf{u}$	complex	$N_l \times 1$	predicted data vector
$A_d, \theta_d$	real		amplitude and phase of observed data
$A_u, \theta_u$	real		amplitude and phase of predicted data
$\mathbf{F}$	complex	$N_l \times N_m$	virtual source matrix
$\mathbf{w}$	complex	$N_d \times 1$	re-weighted residual vector
$\mathbf{m}$	complex	$N_m \times 1$	model parameter vector
$\mathbf{m}_o$	complex	$N_m \times 1$	starting model parameter vector
$\delta\mathbf{m}$	complex	$N_m \times 1$	update model parameter vector
$E(\mathbf{m}, \mathbf{m}_o; \mathbf{d})$	real		objective function
$\mathbf{J}$	complex	$N_m \times N_m$	Fréchet matrix of partial derivatives
$\alpha$	real		steplength
$\gamma$	real	$N_m \times 1$	conjugate gradient or steepest descent direction
$\beta$	real		small number used for perturbations
$\Delta$	real		spatial size of finite difference grid cells
$s_f$	complex		source update
$\Delta_s, \Delta_r$	real		source and OBS intervals
$\Delta_{N_y}$	real		maximum unaliased interval
$N_{A_s}, N_{A_r}$	real		sparsity of source and receiver intervals
$\kappa_x, \kappa_z$	real		horizontal and vertical wavenumber
$\kappa_{x_c}, \kappa_{z_c}$	real		horizontal and vertical cut-off wavenumbers
$\Re, \Im$	function		real and imaginary part of complex numbers

migrations.

From wide-angle refraction data, velocity structures have conventionally been extracted through traveltimes tomography (Dessa et al., 2004; Nakanishi et al., 2002, 2008; Kodaira et al., 2004). Unfortunately, traveltimes tomography results are restricted in resolution (to the size of Fresnel zone), since the method relies on distinct arrival times and on asymptotic ray theory (Williamson & Worthington, 1993; Chen & Schuster, 1999; Woodward et al., 2008). However, seismic waveforms are richer in velocity information when the full waveform is considered beyond the arrival time. Full waveform inversion methods were introduced to potentially access the full information content of seismic records, ideally including all P-waves, S-waves as well as surface waves (Lailly, 1983; Tarantola, 1984). Such methods are able to include all potential wave modes by virtue of being based on numerical wave equation solvers (for example, the finite difference methods of Levander (1988) and Pratt (1990), the finite element methods of Shin & Cha (2008), the spectral element methods of Tromp et al. (2005), or the discontinuous Galerkin methods of Brossier et al. (2008)).

The full waveform inversion approach does demand significant computational resources due to the costs of repeated numerical modelling. More seriously, waveform inversions often elude the goal of the complete exploitation of waveforms due to the strongly non-linear nature of the problem. For controlled seismic surveys of crustal structures, most 2D or 3D inversions have been conducted with refracted P-wave components, and inversions have typically assumed acoustic waveform propagation. Pratt et al. (1996) inverted simple synthetic models of crustal refraction surveys using acoustic data, and Brenders & Pratt (2007a,b) extensively tested the validity of the acoustic assumptions, and developed strategies for handling the associated limitations in a blind test with third-party synthetic elastic data.

Real data applications for crustal investigations have demonstrated the potential for imaging structurally complex P-wave velocity structures both in marine and land experiments, including the Eastern Nankai subduction zone (Operto et al., 2006), the Queen Charlotte Basin (Takam Takougang & Calvert, 2011), the Southern Apennines (Ravaut et al., 2004), the San Andreas Fault (Bleibinhaus et al., 2007, 2009), the Polish Basin (Malinowski & Operto, 2008), and the Canadian Foothills (Brenders et al., 2010). Additionally, P-wave attenuation structures have also been imaged in the Queen Charlotte Basin (Takam Takougang & Calvert, 2011) and the Polish Basin (Malinowski et al., 2011). Wide-angle crustal surveys typically deploy large explosive sources, and large source-receiver offset to penetrate the deep crust. The availability of low-frequency components, and the abundance of wide-angle refraction arrivals benefit waveform inversion.



However the acquisition geometry is typically challenging; either sources or receivers are sparsely located, and the inversion requires adequate model preconditioning strategies (Bleibinhaus et al., 2009).

The acoustic method described above ignores many elastic effects, most notably P-SV mode conversions. These omissions lead to incorrect modelling of reflectivity coefficients, amplitude-versus-offset effects, and focusing/defocusing errors. As a result concerns remain regarding the reliability of the acoustic implementation. In particular, Barnes et al. (2008) pointed out the underestimation of sharp velocity contrasts when using the acoustic assumption. Barnes et al. (2008) and Choi et al. (2008) demonstrated through synthetic examples that the use of elastic forward modelling code may improve P-wave imaging. Shipp & Singh (2002) used the elastic wave-equation to carry out S-wave velocity inversion of field data from the Faroe-Shetland basin; similarly Sears et al. (2010) carried out S-wave velocity inversion for a hydrocarbon reservoir in the North Sea.

The conventional implementation of waveform inversion is an exploration of an elastic parameter model space to minimize specific “objective functions” (Tarantola, 1984; Pratt et al., 1998). Objective functions have typically been based on  $L_2$  or  $L_1$  data residuals formed from a simple subtraction of predicted data from observed data (Tarantola, 1984; Pratt et al., 1998; Brossier et al., 2010), but Shin & Min (2006) proposed a subtraction of logarithmic wavefields to stabilize the optimization process. Amplitude information may be discarded to reduce the effects of modelling errors and to stabilize waveform inversion (Bleibinhaus et al., 2007; Brenders, 2011).

Minimization can be approached either globally or locally from an appropriate starting point. The application of global search techniques, while desirable for such a highly non-linear problem, is still elusive due to the expense of repeated forward modelling, although some simple 1D problems have been tested by Sen & Stoffa (1991, 1992). In contrast, local optimization methods can be formulated to optimally reduce the computational cost by taking advantage of the adjoint method to compute gradients efficiently (as originally formulated by Lailly (1983) and Tarantola (1984) for the time domain, and by Pratt & Worthington (1990) for the frequency domain). Local optimizations can be either varieties of the steepest descent method, including the conjugate gradient method (Pratt et al., 1996; Ravaut et al., 2004; Operto et al., 2006; Bleibinhaus et al., 2007; Takam Takougang & Calvert, 2011), or varieties of the Newton method requiring the calculation of the exact or approximate Hessian matrix (Hicks & Pratt, 2001; Brossier et al., 2009). Pratt et al. (1998) has provided detailed descriptions and interpretations of these optimization methods. The gradient-based approaches of the conjugate gradient and steepest descent methods have been popular for waveform inversion due to its

computational efficiency achieved by the adjoint computation. The Newton methods formally require the expensive Fréchet derivatives (one forward modelling per each model parameter), but can be approximated by computationally affordable L-BFGS (Brossier et al., 2009), truncated Gaussian (Métivier et al., 2012), or implicit Jacobian methods (Abubakar et al., 2012).

The strong non-linearity of the full waveform inversion problem (even when only P-wave velocity imaging is the goal) requires that considerable attention be paid to the starting model, and to appropriate inversion strategies (Mora, 1989; Bunks et al., 1995; Pratt et al., 1998; Sirgue, 2003). Critically, when observed data and predicted data in the starting model are out of phase by more than a half cycle, local waveform inversions will likely fail because of the existence of local minima in the objective function. This “cycle-skipping problem” therefore demands that the starting model be highly accurate, and thus a first arrival tomography method such as those of Zelt & Smith (1992) and Zhang & Toksoz (1998), or a reflection tomography approach such as that summarized in Woodward et al. (2008) have typically been employed to generate starting models for waveform inversion (Brenders & Pratt, 2007a; Brenders et al., 2010; Operto et al., 2006; Ravaut et al., 2004). Brenders & Pratt (2007a) and Pratt (2008) have referred to this hierarchical sequence of traveltimes tomography followed by waveform inversion as “Waveform Tomography”, since the whole inversion process aims to extend the use of first arrival tomography to obtain high resolution subsurface models that fit the refracted (i.e. transmitted) parts of the seismic records.

A multiscale approach (Bunks et al., 1995) is often applied to further mitigate the non-linearity; initially inverting large-scale features, and sequentially refining the spatial scale. As the resolution of waveform inversion is roughly proportional to the highest temporal frequency of the data (Wu & Toksoz, 1987), the multiscale method can be applied by starting inversions at low temporal frequencies and sequentially fitting higher frequency components. The approach has the highly desirable effect of reducing the cycle-skipping between observed and predicted data, which is less severe at lower temporal frequencies (Sirgue, 2003).

In addition to using the frequency selection strategies of the previous paragraph, the multiscale approach can also be implemented using time selection strategies by first restricting waveform inversion to early arrivals, and sequentially incorporating later arrivals: The early part of refracted seismic waveforms are primarily sensitive to large-scale velocity structures, and are relatively linear in comparison with later arrivals (i.e. scattered or diffracted waves which are more sensitive to small-scale features and to the deeper parts of the model) (Sirgue & Pratt, 2004; Brenders & Pratt, 2007a).

It is advantageous to implement both frequency and time selection strategies when considering multiscale inversions. In the time domain, these may be implemented by the combination of convolutional bandpass filters and time-windowing functions (Sears et al., 2010). In the frequency domain, while the hierarchical usage of frequency windows is trivial, simple time windowing approaches will require a convolutional operator over frequencies. However, an exponential time-damping function may be introduced to rigorously extract early arrivals without a convolutional operator (Sirgue & Pratt, 2004; Brenders & Pratt, 2007a). This approach was reformulated by Shin & Cha (2009) as “Laplace-Fourier domain” waveform inversion in which the Laplace constant is the inverse of the characteristic time of the exponential time-damping function. The initial employment of lower frequencies and larger Laplace constants (smaller time-damping constants) minimizes non-linearities. A hierarchical approach in which these initial parameter choices are followed by higher frequencies and smaller Laplace constants (larger damping constants) then maximizes the model illumination in terms of wavenumber spectrum and depth coverage (Sirgue & Pratt, 2004; Brenders & Pratt, 2007c; Shin & Cha, 2009; Brenders, 2011).

Further enforcement of the multiscale approach involves initially restricting the roughness and the depth recovery of the models. Model space gradients of the objective function are typically preconditioned by using smoothing operators to suppress undesirable oscillations in the image (Sirgue, 2003; Ravaut et al., 2004; Brenders & Pratt, 2007b), and offset weighting of data can further constrain the depth recovery of waveform inversion (Brenders & Pratt, 2007a; Sears et al., 2010)

### **3.1.1 Outline of the chapter**

In Section 3.2 of this chapter, we review the geological background of the survey area, and give a description of the survey data used in the chapter. We also review the previous traveltimes tomography work of Nakanishi et al. (2008) conducted for the data. We then briefly summarize the theory underlying Laplace-Fourier waveform inversion in Section 3.3. Following this, we describe the OBS data used in the study, and further present a detailed description of our preprocessing workflow in Section 3.4. The inversion strategy is extensively reviewed in Section 3.5 of the chapter, followed by a full description and interpretation of inversion results in Section 3.6. The chapter concludes with a discussion of inversion strategies, illustrating critical components which contributed the successful waveform inversion for the wide-angle OBS data. A list of mathematical symbols used in this chapter is provided in Table 3.1.

## 3.2 Geological background, survey description, and traveltimes tomography result

### 3.2.1 Geological background

The seismogenic Nankai subduction zone is located southwest of Japan, where the Philippine Sea Plate is subducting beneath the Eurasia Plate. The area has been the subject of a number of seismic experiments to characterize crustal structures, and to understand the seismogenesis (Moore et al., 2001; Nakanishi et al., 2002; Kodaira et al., 2004; Moore et al., 2007). In the central Nankai subduction zone off the Kii Peninsula (Figs. 2.1 and 2.2), migrated reflection seismic sections (Park et al., 2002a; Moore et al., 2007, 2009) revealed a characteristic out-of-sequence thrust, known as a mega-splay fault (Tobin & Kinoshita, 2006), which has been suggested as a critical structure for rupture propagation and tsunami generation. The mega-splay fault is believed to branch from the megathrust fault above the subducting Philippine Sea Plate, and cut through the inner accretionary wedge (Park et al., 2002b; Moore et al., 2007, 2009). Near the sea bottom, the mega-splay fault splits further due to reduced confining pressures, and some of the splays reach the seafloor (Moore et al., 2007).

Two potentially over-pressured low velocity layers have been identified in the vicinity of the mega-splay fault using reflection and refraction seismic surveys (Park et al., 2002a; Bangs et al., 2009; Park et al., 2010): One low velocity zone (LVZ<sub>1</sub> in Fig. 2.2) is in the inner accretionary wedge directly underneath the mega-splay fault (Park et al., 2002a; Bangs et al., 2009), and a second low velocity zone (LVZ<sub>2</sub> in Fig. 2.2) is in the transition zone between the inner and outer wedge (Park et al., 2010). LVZ<sub>1</sub> is characterized by the reverse polarity of the reflection from the mega-splay fault, and is associated with fluid migration along the fault (Park et al., 2002a), and/or the existence of fluid-rich underthrust sediments (Bangs et al., 2009). LVZ<sub>2</sub> was recognized during migration velocity analysis and through shadow zone analysis of refraction data. The geometrical proximity of the two low velocity zones may imply fluid migration between the inner and outer wedge. However previous migration images are poorly resolved in the area connecting these low velocity zones due to the influence of the sea bottom topographic relief on the images. Furthermore, the velocity images from conventional first-arrival refraction tomography (Nakanishi et al., 2008) have not yielded sufficient resolution to resolve the connection between these zones. These technical disadvantages have left an ambiguous geometrical relationship of the two fluid rich layers (LVZ<sub>1</sub> and LVZ<sub>2</sub>), precluding a complete image of the mega-splay fault system.

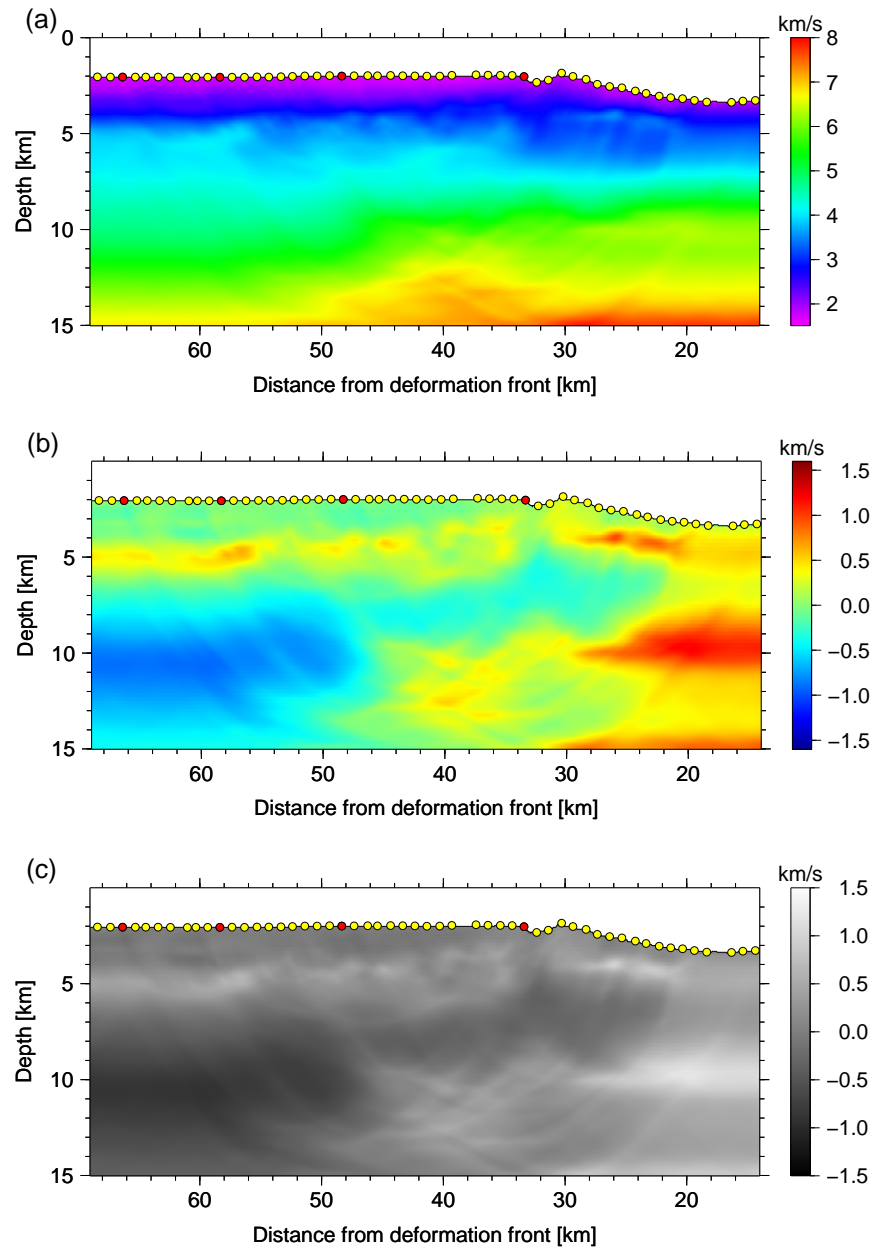


Figure 3.1: (a) Traveltime tomography result of Nakanishi et al. (2008), also used as a starting model for our waveform inversion, (b) de-trended model of (a) in colour, and (c) same as (b) in grey scale. The horizontal axis is the distance from the deformation front (see Fig. 2.2). Yellow circles show the location of the 16 bit OBS instruments, and red circles show the location of the 24 bit OBS instruments used in this study.

### 3.2.2 Survey description

In order to generate the waveform tomography images described in this chapter, we used waveforms from Ocean Bottom Seismographs (OBS) data acquired in the southeast offshore of the Kii Peninsula (Fig. 2.1) by the Japan Agency for Marine Earth Science and Technology (JAMSTEC) in 2004 (Nakanishi et al., 2008). A total of 74 OBS sensors described in Shinohara et al. (1993) were deployed at the sea bottom over a total interval of 175 km. Each OBS has a three-component, gimbal-mounted geophone system with a 4.5 Hz natural frequency and a hydrophone. The digital recorder had either 16-bit or 24-bit A/D converters, and signals were digitized with a 10 ms sampling rate. 54 OBSs were located at 1 km intervals near the outer ridge, and 20 OBSs were located in 5-10 km intervals elsewhere. A large air gun array with a total volume of 197 L ( $8 \times 25$  L BOLT 1500LL airguns) and a pressure of 14 MPa was deployed by JAMSTEC's R/V Kaiyo at 10 m water depths, at 200 m intervals.

### 3.2.3 Traveltime tomography result

Using these data, and the traveltime tomography approach by Zhang & Toksoz (1998), Nakanishi et al. (2008) recovered the velocity model depicted in Fig. 3.1, and concluded through checkerboard testing that their result had a spatial resolution of approximately 2.5 km. Nakanishi et al. (2008) conducted the tomography in two stages: First, they recovered a 175 km wide and 30 km depth section with a grid spacing 0.2 km x 0.2 km (Figure 4(a) in Nakanishi et al., 2008). They then refined the analysis to an area 65 km wide and 15 km deep in the vicinity of the outer ridge, with a new grid spacing 0.05 km x 0.05 km. The velocity structure in the refined area is shown in Fig. 3.1a.

The subsurface structure in Fig. 3.1a exhibits a large dynamic range in velocity, from velocities of soft sediments close to 1.5 km/s at the sea bottom, to velocities of approximately 8 km/s within the Philippine Sea Plate. In order to better visualize local velocity changes, we removed the background model from this image. The background model was defined as a one-dimensional trend below the sea floor by the 3rd order polynomial  $V_o(x, z) = a(z - z_0(x))^3 + b(z - z_0(x))^2 + c(z - z_0(x)) + d$  which best fit the 2D traveltime tomography result, and where  $z_0(x)$  is the depth of a sea floor. The order of the polynomial was chosen to simultaneously represent shallow accretionary prisms where the velocity is rapidly increasing, and the deep oceanic crust where the velocity increase is relatively gentle. The de-trended velocity image was then defined by  $\Delta V(x, z) = V(x, z) - V_o(x, z)$ . The background model is shown in Fig. 2.4. The resultant de-trended velocity structure is shown in Fig. 3.1b in colour and in Fig. 3.1c in grey.

These traveltimes tomography images appear to show the existence of low velocity zones, but the lithological boundaries are not obvious. This deficiency can be attributed to the fundamental limitations of the methodology, since the asymptotic assumption inherent in ray theory imposes a resolution restriction based on the Fresnel zone width, leading to a smooth final velocity model (e.g., Williamson & Worthington, 1993). In order to supplement the information on the locations of the apparent lithological structures, Nakanishi et al. (2008) conducted further analysis: The reflection traveltimes mapping method (Fujie et al., 2006) was adopted to migrate pre-picked secondary reflection arrivals to their original locations. However their method required the manual picking of distinct reflection arrivals, and thus they were unable to provide detailed structure maps.

### 3.3 Theory

Any approach to geophysical inversion necessarily comprises two steps: i) A forward modelling step in which geophysical data are simulated (“forward modelled”) in a manner consistent with the survey geometry and physical principles, and ii) an optimization process in which model parameters themselves are progressively updated in such a manner as to optimize the fit between the simulated and observed (true) data. The choice of forward-modelling theory determines the basic assumptions underlying the inverse problem, and implicitly characterizes the modelling error. In this study, following the approach of Brenders & Pratt (2007a), we assume 2D visco-acoustic wave propagation, and we ignore elastic effects and anisotropy. Following the approach of Pratt et al. (1998), Brenders & Pratt (2007a) and Shin & Cha (2009), we conduct forward modelling and inversion in the Laplace-Fourier domain. We use non-linear gradient-based optimization methods to iteratively update the model.

#### 3.3.1 The Laplace-Fourier domain

Following Shin & Cha (2009), the complex Laplace transform of the time-domain wavefield  $u(\mathbf{x}; t)$  is

$$u(\mathbf{x}; s) = \int_0^{\infty} u(\mathbf{x}; t) \exp[-st] dt, \quad (3.1)$$

where  $s$  is the complex-valued Laplace parameter. If we write

$$s = \sigma + i\omega, \quad (3.2)$$

with a real-valued Laplace constant  $\sigma$  and a real-valued angular frequency  $\omega$ , then

$$u(\mathbf{x}; s) = \int_0^{\infty} \{u(\mathbf{x}; t) \exp[-\sigma t]\} \exp[-i\omega t] dt. \quad (3.3)$$

Consider a characteristic decay time

$$\tau = 1/\sigma, \quad (3.4)$$

and  $u(\mathbf{x}; t < 0) = 0$ . Eq.(3.3) then becomes

$$u(\mathbf{x}; s) = \int_{-\infty}^{\infty} \left[ u(\mathbf{x}; t) \exp\left[-\frac{t}{\tau}\right] \right] \exp[-i\omega t] dt, \quad (3.5)$$

which is the Fourier transform of the original time-domain wavefield multiplied by a time-damping function,  $\exp[-t/\tau]$ . As is apparent from Eqs 3.3 and (3.5), the damping function acts as a data preconditioning operator (Sirgue, 2003; Brenders & Pratt, 2007a) in that smaller values of  $\tau$  (larger values of  $s$ ) preferentially weight early arrivals, and suppress later arrivals. We further rewrite Eq.(3.5) as

$$\begin{aligned} u(\mathbf{x}; s) &= \int_{-\infty}^{\infty} u(\mathbf{x}; t) \exp[-i\Omega t] dt, \\ &= u(\mathbf{x}; \Omega), \end{aligned} \quad (3.6)$$

where

$$\Omega = \omega - i/\tau, \quad (3.7)$$

is a complex-valued frequency. Eq.(3.7) is the Fourier domain wavefield at complex-valued frequency  $\Omega = \omega - i/\tau$  (as in Phinney (1965); Mallick & Frazer (1987); Sirgue (2003)). The equivalence of the complex Laplace and Fourier transforms leads us to refer to  $u(\mathbf{x}; s) = u(\mathbf{x}; \sigma, \omega) = u(\mathbf{x}; \omega, \tau) = u(\mathbf{x}; \Omega)$  as the ‘‘Laplace-Fourier domain wavefield’’ following Shin & Cha (2009). Hereafter we use  $\omega$  and  $\tau$  as our parametrization because of the intuitive connection of  $\omega$  and  $\tau$  to the physical quantities of frequency and decay time.

### 3.3.2 Forward modelling

The visco-acoustic wave equation in the Laplace-Fourier domain is

$$\nabla \left( \frac{1}{\rho(\mathbf{x})} \nabla u(\mathbf{x}; \Omega) \right) + \frac{\Omega^2}{\rho(\mathbf{x})c(\mathbf{x}; \omega)^2} u(\mathbf{x}; \Omega) = f(\mathbf{x}; \Omega), \quad (3.8)$$



where  $\rho(\mathbf{x})$  is the density,  $u(\mathbf{x}; \Omega)$  is the pressure field, and  $f(\mathbf{x}; \Omega)$  is the source term describing both the spatial distribution of the source(s), and the Laplace-Fourier component of the source time function. Attenuative media can be included by utilizing a complex-valued velocity field  $c$ , in which the attenuation factor

$$Q^{-1} = -\frac{c_I(\mathbf{x}; \omega)}{2c_R(\mathbf{x}; \omega)}, \quad (3.9)$$

where  $c_R(\mathbf{x}; \omega) = \Re[c(\mathbf{x}; \omega)]$  and  $c_I(\mathbf{x}; \omega) = \Im[c(\mathbf{x}; \omega)]$  (Song et al., 1995). We assume a frequency independent  $Q$ , and the dispersion relationship

$$\frac{1}{c_R(\mathbf{x}; \omega)} = \frac{1}{c_R(\mathbf{x}; \omega_o)} \left( 1 + \frac{1}{\pi Q} \ln \left( \frac{\omega_o}{\omega} \right) \right), \quad (3.10)$$

where  $\omega_o$  is a reference frequency (Aki & Richards, 1980).

A numerical solution of the wave equation in Eq.(3.8) for arbitrary velocity, density and attenuation distributions requires a discretization of the model. If we assume that the 2D P-wave subsurface velocity, density and attenuation structure may be described by a set of model parameters,  $\mathbf{m}$ , at  $N_m$  nodal points, Eq.(3.8), then leads to the matrix form

$$\mathbf{S}(\mathbf{m})\mathbf{u} = \mathbf{f}, \quad (3.11)$$

(Pratt et al., 1998), where  $\mathbf{u}$  represents the discrete solutions to the wave equation at  $N_l$  grid points,  $\mathbf{m}$  is the model parameter vector representing in discrete form the spatial distributions of  $N_m$  model parameters,  $\mathbf{f}$  represents the discrete distribution of source terms at  $N_l$  grid points, and  $\mathbf{S}$  is the  $N_l \times N_l$  impedance matrix. In this study we adopt the finite difference approach for the matrix elements in Eq.(3.11) developed by Pratt & Worthington (1988) and Jo et al. (1996), but we implement an absorbing boundary condition using the perfectly matched layer method (Hustedt et al., 2004; Zeng et al., 2001). Note that Eq.(3.11) and all results below are dependent on the complex angular frequency,  $\Omega = \omega - i/\tau$ , although we shall omit this specific dependence unless required.

### 3.3.3 Optimization

As before we assume the subsurface is described by a set of model parameters,  $\mathbf{m}$ , at  $N_m$  nodal points, and we now assume that observed data,  $\mathbf{d}$ , are available at  $N_d$  points. These data will necessarily be extracted from seismic recordings, and transformed into discrete Laplace-Fourier components prior to the inversion. We seek to iteratively update the model to fit the set of Laplace-Fourier components using a local optimization via the

conjugate gradient method, as this is one of most popular and computationally efficient methods for waveform inversion (e.g. (Song et al., 1995; Bleibinhaus et al., 2007; Brenders & Pratt, 2007a)).

We define an objective function  $E(\mathbf{d}, \mathbf{m})$  using the  $L_2$  norm such that

$$2E = \sum_{\omega} \delta \mathbf{d}^T \delta \mathbf{d}, \quad (3.12)$$

where  $\delta \mathbf{d}$  is the residual, and  $^T$  indicates the Hermitian conjugate of the vector. Conventionally the residual is defined simply as

$$\delta d_j = u_j - d_j, \quad j = 1, \dots, N_d, \quad (3.13)$$

(e.g., Pratt et al., 1998). In this work, instead of the conventional residual, we employ the ‘‘logarithmic residual’’

$$\delta d_j = \ln \left( \frac{u_j}{d_j} \right). \quad (3.14)$$

(as originally introduced by Shin & Min, 2006). Now denote

$$\begin{aligned} u_j &= A_{u_j} \exp [i\theta_{u_j}], \\ d_j &= A_{d_j} \exp [i\theta_{d_j}], \end{aligned} \quad (3.15)$$

and assume no cycle skipping between the observed and estimated data, i.e.  $|\theta_{u_j} - \theta_{d_j}| \leq \pi$ . Then

$$\delta d_j = \ln \left( \frac{A_{u_j}}{A_{d_j}} \right) + i (\theta_{u_j} - \theta_{d_j}), \quad (3.16)$$

Eq.(3.16) illustrates two main advantages of the logarithmic implementation over the conventional approach: i) the natural separation of amplitude and phase information into real and imaginary parts of the misfit, and ii) the scaling of amplitudes in the real part leads to a reduced dynamic range of residuals. As the phase represents the kinematics, and the amplitude represents the dynamics of wave propagation, it is trivial to form a misfit functional focusing on kinematics by eliminating the real part of Eq.(3.16),

$$\delta d_j = \Im \left[ \ln \left( \frac{u_j}{d_j} \right) \right] = (\theta_{u_j} - \theta_{d_j}), \quad (3.17)$$

which will be referred to as the ‘logarithmic phase-only residual’. To distinguish Eq.(3.14) from Eq.(3.17), we refer Eq.(3.14) as the ‘‘logarithmic phase-amplitude residual’’.

In order to reduce the objective function, we adopt a local conjugate gradient method,

with model update at the  $k$ th iteration

$$\delta \mathbf{m}^{(k)} = -\alpha^{(k)} \boldsymbol{\gamma}^{(k)}, \quad (3.18)$$

where  $\alpha^{(k)}$  is the steplength, and  $\boldsymbol{\gamma}^{(k)}$  is the conjugate gradient direction, available at each iteration through a linear combination of preconditioned model gradients at past iterations (Polak & Ribière, 1969). The model gradient itself  $\nabla_{\mathbf{m}} E$  is obtained at each iteration by the adjoint method (Lailly, 1983; Tarantola, 1984; Pratt et al., 1998), so that the computationally expensive Fréchet kernel is not required in explicit form. Following Pratt et al. (1998), the gradient of  $E$  takes the form

$$\nabla_{\mathbf{m}} E = \Re [\mathbf{F}^t \mathbf{S}^{-1} \mathbf{w}^*], \quad (3.19)$$

where  $\mathbf{F}$  is a matrix containing the virtual sources for each model parameter,  $\mathbf{w}$  is the “re-weighted residual vector”, and  $*$  indicates the complex conjugate. Note that the virtual sources,  $\mathbf{F}$ , are independent of the definition of the residual, and the  $l$ -th column of  $\mathbf{F}$  is given by

$$\mathbf{F}_l = -\frac{\partial \mathbf{S}}{\partial m_l} \mathbf{u}. \quad (3.20)$$

The re-weighted residuals,  $\mathbf{w}$ , however, depend on the definition of the residuals: For logarithmic residual

$$w_j = \frac{1}{u_j^*} \ln \frac{u_j}{d_j}, \quad (3.21)$$

while for logarithmic phase-only residuals

$$w_j = \frac{i}{u_j} \Im \left( \ln \frac{u_j}{d_j} \right). \quad (3.22)$$

The final requirement in Eq.(3.18) is  $\alpha$ , the “step length”. By assuming the model parameters are approximately linear in the vicinity of  $\mathbf{m}$ ,

$$\alpha \sim -\frac{(\nabla_{\mathbf{m}} E)^T \boldsymbol{\gamma}}{(\mathbf{J}^T \boldsymbol{\gamma})^T (\mathbf{J}^T \boldsymbol{\gamma})}, \quad (3.23)$$

where  $\mathbf{J}$  is the Fréchet derivative kernel (Song, 1994; Song et al., 1995; Pratt et al., 1998). The term  $\mathbf{J}^T \boldsymbol{\gamma}$  may be approximated by the finite-difference calculation

$$\mathbf{J}^T \boldsymbol{\gamma} \sim \frac{\mathbf{d}(\mathbf{m} + \beta \boldsymbol{\gamma}) - \mathbf{d}(\mathbf{m})}{\beta}, \quad (3.24)$$

where  $\beta$  is a small perturbation constant.

### 3.3.4 Source estimation

The inverse method described above assumes that the forward problem can be solved through Eq.(3.11), in which the source terms  $\mathbf{f}$  are assumed known. However, these terms need to be provided. Fortunately, under the assumption of a known subsurface structure the source wavelet in the Laplace-Fourier domain can easily be estimated as a linear inverse problem (Pratt, 1999). Following Pratt (1999), we may compute an optimal source signature by the multiplication of the current wavelet,  $\mathbf{f}$ , by a complex-valued scalar,  $s_f$ . Using this, Eq.(3.11) becomes

$$\mathbf{S}\mathbf{u} = s_f\mathbf{f}. \quad (3.25)$$

(Each source location may possess an independent source wavelet, and to handle this we may assume different scalars,  $s_{f_1}, s_{f_1}, \dots, s_{f_{N_s}}$ ). Thus the source wavelet estimation problem is re-cast by the Laplace-Fourier domain optimization problem with respect to a scalar,  $s_f$  or a number of scalars. If we assume our estimated subsurface structure is correct,  $\mathbf{u}$  becomes independent of  $\mathbf{m}$ , and  $s_f$  can be found by a linear optimization algorithm, since  $\mathbf{u}$  is a linear function of  $s_f$ . In practise, the velocity model used in Eq.(3.25) will not be precise, and the source inversion should be updated after each update of the velocity structure.

The objective function for the source estimation can be the  $L_2$  norm of either the conventional residuals in Eq.(3.13) (Pratt, 1999), or the logarithmic residuals in Eq.(3.14) (Shin et al., 2007). Shin et al. (2007) have compared the accuracies in source wavelet estimation between two misfit definitions through synthetic tests, and have concluded the discrepancies between the estimated wavelet are not substantial. In this study, we apply the conventional misfit in Eq.(3.13), and  $s_f$  can be found by

$$s_f = \frac{\mathbf{u}^t \mathbf{d}^*}{\mathbf{u}^t \mathbf{u}^*}. \quad (3.26)$$

Note that the linear inverse method converges in one iteration (Pratt, 1999).

Source wavelet estimates can also be used to detect the divergence of the estimated model from the true model (Pratt & Symes, 2002; Gao et al., 2007; Smithyman et al., 2009; Malinowski et al., 2011). Suppose all sources excited an identical wavelet, and all receivers shared identical receiver coupling effects. Then consider estimating a source wavelet for each source location: When the “true” velocity structure is given, the esti-

estimated source waveforms will be identical, but if an estimated model is imperfect, the estimated source signals will differ from each other, especially where strong discrepancies remain between estimated and true models. Thus the coherency of source wavelets informs the validity of velocity models. Pratt & Symes (2002) demonstrated that the semblance and differential semblance of the source waveforms may provide a robust indicator of model validity.

## 3.4 Data and Preprocessing

### 3.4.1 Data description

The OBS data we use in this study and the traveltimes tomography results carried out previously are described above in Section 3.2. In order to avoid under-sampling artifacts arising from sparse OBS intervals, we conducted our waveform tomography study on a subsurface section 65 km wide and 15 km deep in the area of the active mega-splay. This section corresponds to the refined area of the traveltimes tomography result in Nakanishi et al. (2008), and comprises a subset of the original data: 54 OBS's at 1 km spacing, with 285 air gun sources. Four OBSs have 24 bit A/D converters (indicated by red circles in Fig. 3.1), and the rest of the OBSs have 16 bit A/D converters (indicated by yellow circles in Fig. 3.1). Although pressure component data are desirable (since the pressure is the direct output of our acoustic forward modelling), poor signal-to-noise ratios precluded their usage. Instead we employed the vertical component records from the OBSs. The application of the vertical components is a plausible approximate approach for P-velocity imaging, because our pressure sources were excited in acoustic environment (i.e. the ocean), and because P-wave energy dominates the early part of the vertical components of our OBS data. Strictly speaking, a conversion of velocity components to pressure is required (Operto et al., 2006), but Brenders & Pratt (2007a) and Brossier et al. (2009) demonstrated by using synthetic and real elastic data that vertical components can be treated as pressure components, and can provide reliable velocity structures.

Representative waveforms from OBS 47 (located 65 km landward of the deformation front DF) are depicted in Fig. 3.2a with the application of a reduction velocity of 8 km/s. The amplitude spectrum from the same OBS gather is presented as a solid black line in Fig. 3.2b. A strong bubble reverberation is apparent throughout the OBS gather, however relatively clear seismic signals were available. Refracted waves from the shallower subsurface are observed at distances between 45 km and 60 km, and from deeper structures at distances 15 km and 45 km, and two wide-angle reflections are evident at

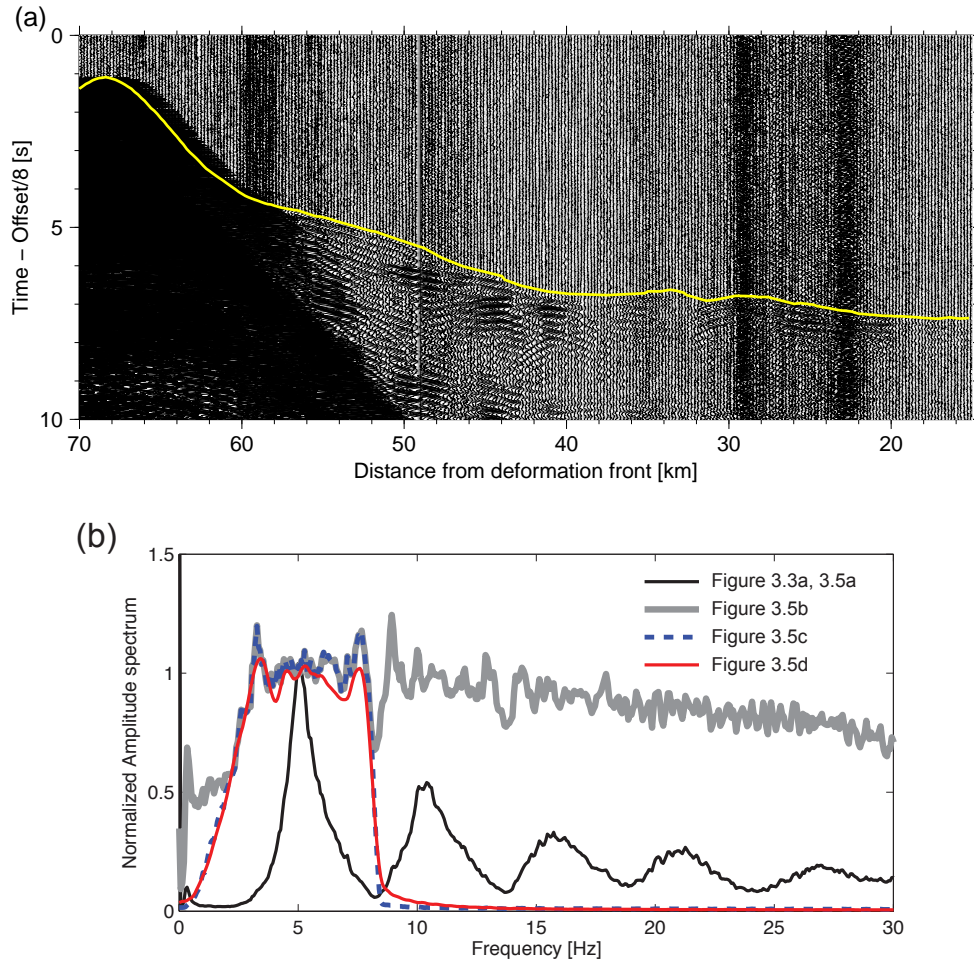


Figure 3.2: (a) Representative vertical component seismic waveforms recorded at OBS 47, located 65 km landward of the deformation front. The yellow line indicates the picked first arrivals. (b) RMS amplitude spectra from OBS 47. Amplitudes are normalized to the value at 5 Hz. The black line shows the amplitude spectrum of (a), the grey line after deconvolution (Fig. 3.4b), the dashed blue line shows the spectrum after bandpass filter (Fig. 3.4c), and the red line shows the spectrum after all preprocessing (Fig. 3.4d).

distances 38 km and 52 km.

### 3.4.2 Preprocessing

Data preprocessing is essential for successful acoustic waveform inversion. We designed a pre-processing flow with the objectives of enhancing the signal to noise ratio (especially at lowest frequencies), and eliminating undesirable (non-acoustic) arrivals. Fig. 3.3 schematically illustrates the approximate preprocessing workflow followed prior to waveform inversion. Fig. 3.4 displays the gather from OBS 47 after each step in the preprocessing flow; the corresponding amplitude spectra are shown in Fig. 3.2b.

Predictive deconvolution with a gap of 24 ms and operator lengths of 750 ms was performed in order to remove the air gun bubble reverberation (Nakanishi et al., 2008). The deconvolved waveforms in Fig. 3.4b exhibit sharper and more distinct arrivals, but residual bubble effects remain as secondary arrivals at 400 ms after the first arrivals. The corresponding amplitude spectrum (the red line in Fig. 3.2b), exhibits the general flattening of the spectrum and the enhancement of high frequency components. Following deconvolution, an Ormsby minimum-phase bandpass filter was applied with corner frequencies of 0.1 - 2.5 - 8.0 - 8.5 Hz (Fig. 3.4c), designed to accept the first two peaks in the amplitude spectrum of the raw data (the dashed line in Fig. 3.2b). We eliminated higher frequencies due to the severe under-sampling in the OBSs.

A time window of 1.8 sec was then applied to the waveforms, in order to exclude early ambient noise, shear arrivals, and multiples. The start of the time window is controlled by first arrival time picks; if there is no available pick for a given trace it is discarded from the inversion. The hand-picked arrivals used by Nakanishi et al. (2008) for traveltome tomography were adjusted and augmented where necessary in order to allow a full set of traces to contribute to the waveform inversions. Since acoustic waveform modelling cannot reproduce converted shear waves, shear modes can cause systematic errors in our waveform inversion. Although we can simulate surface-related multiples with the application of a free surface condition in the forward modelling code, we consider the multiples represent redundant information (repetitive of the first arrivals) that potentially increases the level of artifacts in our velocity image due to increased non-linearity.

The next step was to process the signal amplitudes. We first normalized the RMS amplitudes of each OBS gather, primarily because the two types of A/D converters used resulted in a different dynamic range in the observed waveforms, but also because the elastic coupling to the sea floor differs between the OBSs. Next the observed (elastic) amplitude versus offset (AVO) effects were compensated to fit synthetic (acoustic) AVO

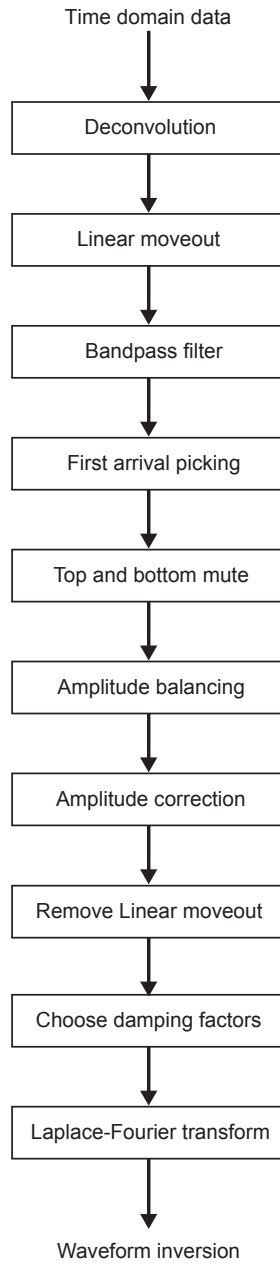


Figure 3.3: The preprocessing flow used to bring time-domain data through to Laplace-Fourier domain waveform inversion



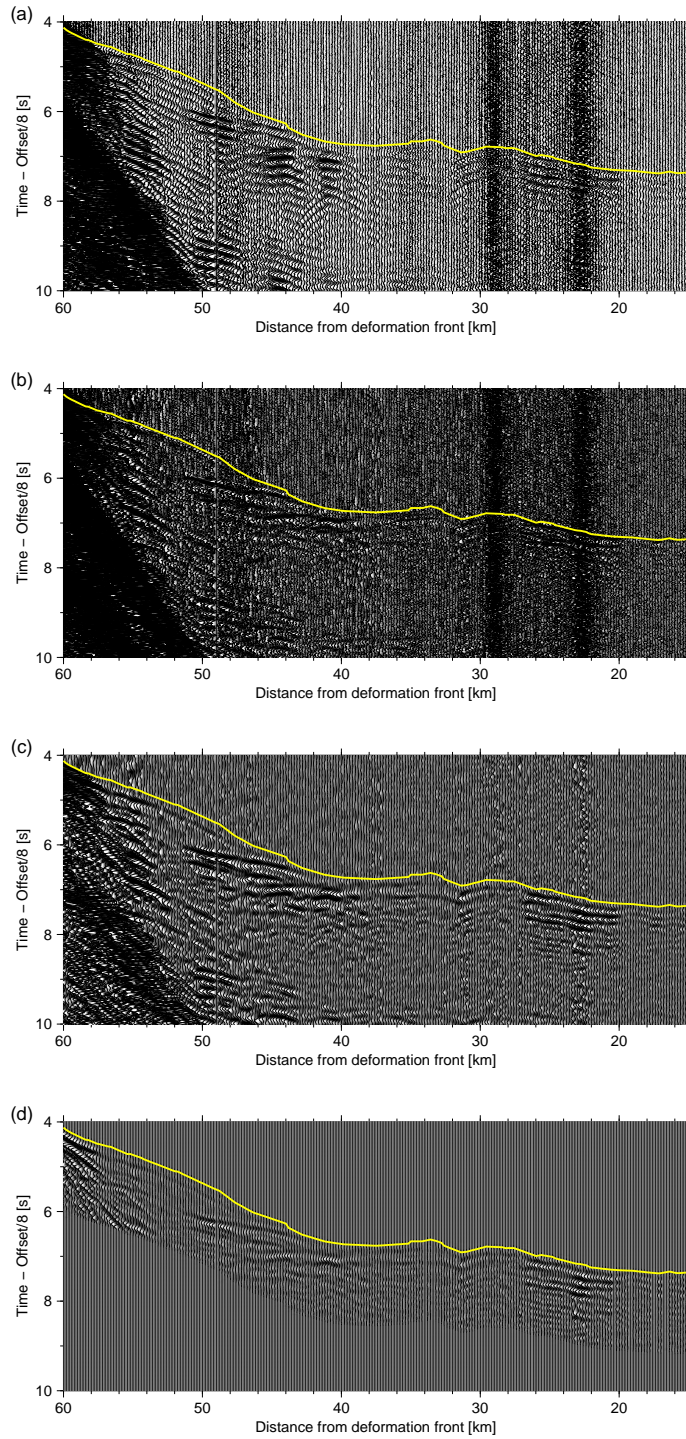


Figure 3.4: Processing of vertical component seismic waveforms from OBS 47. The yellow line indicates the picked first arrivals. (a) Raw data (b) Deconvolved wavefield (c) After band pass filter (2.5-8.0 Hz) (d) After Time-windowing and amplitude correction

effects following the methodology described in Brenders & Pratt (2007a). This procedure also calibrated the vertical components in the observed data to simulate the pressure component output from the acoustic modelling code. The reference acoustic wavefield was computed by the frequency domain visco-acoustic modelling code using the traveltimes tomography result shown in Fig. 3.1 as a velocity model. The attenuation model was set using  $Q_p = 100$  beneath the sea floor, and  $Q_p = 10,000$  for the seawater brine. The amplitude-corrected waveforms are displayed in Fig. 3.4d, with the corresponding RMS amplitude spectrum shown in Fig. 3.2b as a red curve.

As a final pre-processing step, we eliminated all traces with offsets less than 5.0 km, because the observed wavefields exhibited amplitude saturation, and because the wavefields consist primarily of direct arrivals propagating solely through the ocean. Eliminating these data may degrade the resolution of very shallow surface structures, but such structures are probably not invertible due to the severe artifacts arising from the under-sampled OBS intervals (see Section 3.5.4).

### 3.5 Inversion Strategies

We chose to invert the preprocessed waveforms for the P-wave velocity structure of the subsurface, with a starting model derived from the traveltimes tomography results described in Section 3.2.3 and shown in Fig. 3.1. A flowchart outlining the overall Laplace-Fourier waveform inversion strategy is displayed in Fig. 3.5. As in the amplitude compensation step described in Section 3.4.2, the attenuation model was set at  $Q_p = 100$  beneath the sea floor, and  $Q_p = 10,000$  for the brine; this model was kept constant during the inversion process. Density was computed from the velocity model at each iteration by applying Gardner’s relationship (Gardner et al., 1974).

A primary choice in waveform inversion is the choice of objective function. We defined logarithmic phase-amplitude and phase-only objective functions in Section 3.3.3. To first order, the P-wave velocity is constrained by the kinematics of the early arriving waveforms. By contrast, the dynamic properties of seismic wavefields (i.e., the amplitudes) are responsive to second order terms in the velocity distribution (Snieder & Lomax, 1996). Moreover the amplitudes are strongly affected by various factors other than P-wave velocity structure: They are more vulnerable to 3D wave propagation effects, source/receiver coupling effects, source radiation patterns, P-SV converted waves, impedance contrasts, and so on. Although we have attempted to mitigate these non-acoustic or 3D effects through preprocessing (especially through amplitude correction and time-windowing), a phase-only approach provides more stable and reliable P-wave velocity images. Thus we

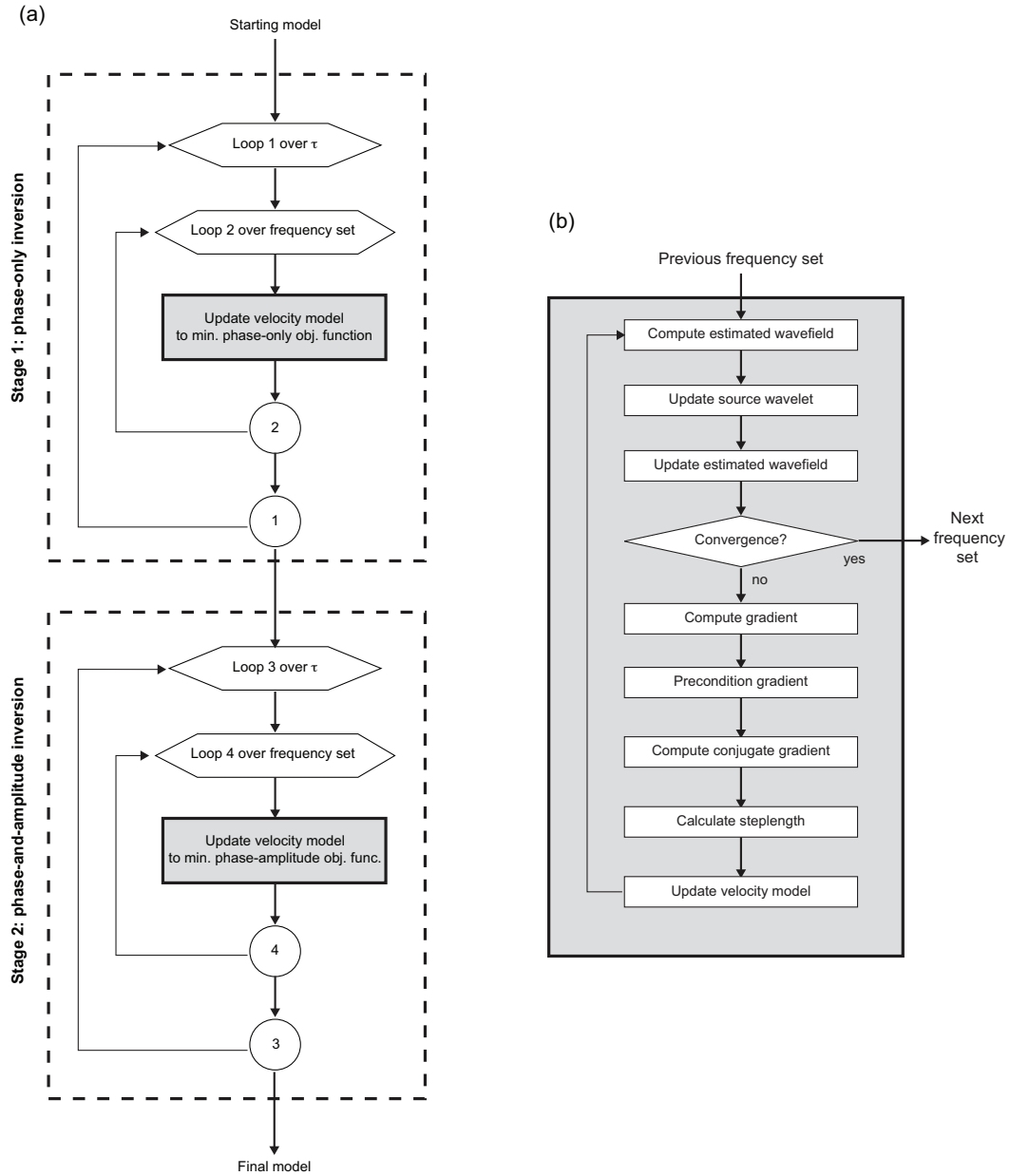


Figure 3.5: (a) Flowchart outlining waveform inversion. (b) Details of update step used in both stages in (a), corresponding to grey shaded boxes in (a)

adopted a two-stage approach: First we began with the logarithmic phase-only objective function in Eq.(3.17). Then in a second stage, we used the logarithmic phase-amplitude objective function in Eq.(3.14) to incorporate the amplitude information into waveform inversion. This strategy is reflected in the flowcharts in Fig. 3.5.

At each stage, the multiscale method was primarily facilitated by appropriately scheduling the same Laplace-Fourier parameters,  $\omega$  and  $\tau$ . The model update was calculated as described in Section 3.3.3, and the model gradient was preconditioned by wavenumber filtering (see Section 3.5.4 below) to remove unacceptable oscillations. The source wavelet was updated after each iteration following the method described in Section 3.3.4.

### 3.5.1 Waveform inversion parameter choices

Forward modelling of visco-acoustic wave propagation was carried out in the Laplace-Fourier domain following the methods described in Section 3.3.2. In order to avoid numerical dispersion, the finite difference cell size,  $\Delta$ , was chosen to approximately satisfy

$$\Delta \leq \frac{\lambda_{min}}{4} = \frac{v_{min}}{4f_{max}}, \quad (3.27)$$

(Jo et al., 1996) where  $\lambda_{min}$  is the minimum wavelength,  $v_{min}$  is the minimum velocity, and  $f_{max}$  is the maximum modelling frequency. As the minimum velocity in the medium is that of brine (1500 m/s), and as  $f_{max} = 8.5$  Hz, a strict implementation requires

$$\Delta \leq \frac{1500}{4 \times 8.5} = 44.4 \text{ [m]}. \quad (3.28)$$

However we used the original 50 m square cell sizes from the travelttime tomography settings, which satisfies Eq.(3.28) at all but the highest frequencies ( $>7.5$  Hz) and the lowest velocities ( $<1700$  m/s). (The choice of  $\Delta = 50$  m was confirmed not to cause significant waveform distortion by conducting a forward modelling test.) Our choice of  $\Delta = 50$  m corresponds to  $1161 \times 393$  grid points for the  $58.0 \text{ km} \times 19.65 \text{ km}$  tomographic section we are using.

Because we did not use an explicit free surface condition, we simulated a source ghost by locating image sources at mirror locations with respect to the sea surface. A virtual water layer of 10 grid points was added to the top of the model for the source ghost simulation. An additional 10 grid points were then added to all model edges as a damping zone for the absorbing boundary condition. Thus the total model dimension is  $1181 (1161 + 2 \times 10) \times 423 (393 + 10 + 2 \times 10)$  grid points.

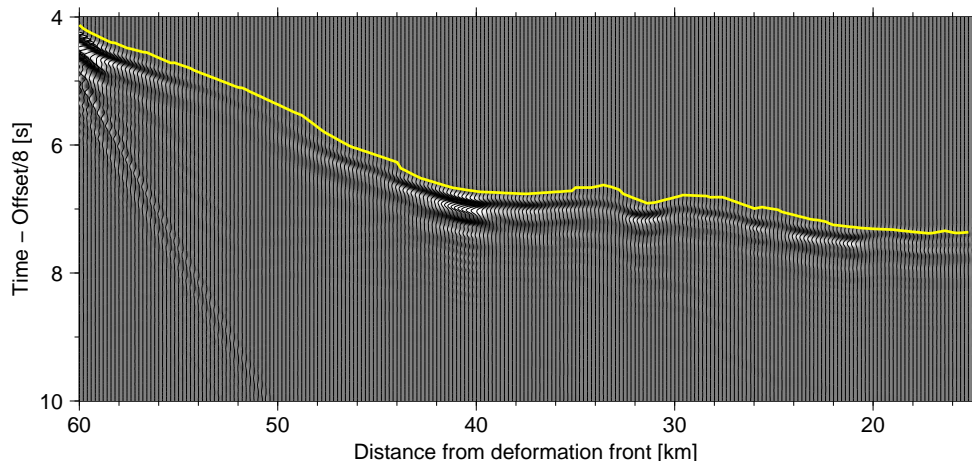


Figure 3.6: Synthetic OBS gather from the starting model (Fig. 3.1) at OBS 47, computed using a visco-acoustic forward modelling code. Picked first arrivals from the comparable real data are shown in yellow.

Since the number of sources ( $N_s = 258$ ) outnumbered the number of receivers ( $N_R = 54$ ), reciprocity was employed in the forward wavefield calculation to save computational costs: A source signature was excited at each OBS location, and responses were recorded at locations corresponding to the airgun shot locations. A single common source signature was estimated for OBSs, employing the method described above in Section 3.3.4. We assumed all OBSs excite the same signature, and share the same coupling effect. The source signature was re-estimated after each iteration to reflect the changed velocity structures.

### 3.5.2 Starting model

Waveform inversion, a highly non-linear inverse problem, necessitates the use of a particularly good starting model: The usual criterion is that the starting model should predict waveforms that are within a half-cycle of the observed data. In this study, we employed the traveltime tomography result of Nakanishi et al. (2008) shown in Fig. 3.1. This result predicts picked times to within a 60 millisecond RMS error in traveltime (Nakanishi et al., 2008), corresponding to 13.5 % of a period at 2.25 Hz (the lowest frequency used for waveform inversion as described in Section 3.5.3). Thus, at least on average we are well within the half-cycle criteria at the lowest frequency available for waveform inversion. To validate our starting model, we computed time domain synthetic waveforms using the forward modelling code used for our inversion. The synthetic wavefields displayed

Table 3.2: Damping factors,  $\tau$ , the equivalent Laplace constants employed for phase-only and phase-amplitude inversions respectively.

Objective function	$\tau$ [sec]	$s$ [sec <sup>-1</sup> ]
phase-only	0.167, 0.2, 0.25, 0.333, 0.5, 1.0, 2.0	6, 5, 4, 3, 2, 1, 0.5
phase-amplitude	0.333, 0.5, 1.0, 2.0	3, 2, 1, 0.5

in Fig. 3.6 show good agreement in the vicinity of the picked first arrivals (shown in yellow) when compared to the preprocessed wavefields in Fig. 3.4c, demonstrating the accuracy of the traveltome tomography velocity model. However the simulated waveforms lack the later, wide-angle reflections from the mega-splay fault, indicating the potential improvement in waveform fit to be gained by inverting the high-wavenumber features of the velocity model.

### 3.5.3 Scheduling of Laplace-Fourier domain parameters

As described in Section 3.3, the Laplace-Fourier domain wavefield is governed by two individual parameters, the frequency ( $\omega$ ) and the damping factor ( $\tau$ ). These parameters control the spatial scale of the images, the depth extent of the inversion, and the linearity of the inversion. In order to fully characterize seismic waveforms and stabilize the inversion, waveform inversion needs to start from low  $\omega$  and  $\tau$ , and move progressively to higher values of  $\omega$  and  $\tau$ . Earlier studies comparing alternative strategic schedules for  $\omega$  and  $\tau$  selection were inconclusive (Shin et al., 2010; Brenders, 2011). In this chapter, we adopted the conventional approach used by Sirgue & Pratt (2004) and Brenders & Pratt (2007a): At each  $\tau$ , all frequency sets are evaluated, before increasing the  $\tau$  values. Phenomenologically, as  $\tau$  increases the inversions become sensitive to deeper structures. Thus we can interpret this strategy as the adoption of a “layer stripping method” as characterized by Shin et al. (2010).

#### 3.5.3.1 Frequency sampling

We conducted waveform inversion using frequencies between 2.25 and 8.5 Hz. The frequency range was determined visually by selecting the lowest frequency with usable signal-to-noise ratios of Laplace-Fourier domain wavefields, and the highest frequency that avoids any serious artifacts in the gradients arising from the spatial aliasing due to the coarse OBS intervals. Laplace-Fourier waveform inversion does not impose a need for regular sampling in frequency: For example, Sirgue & Pratt (2004) proposed an optimal frequency-selection strategy designed to achieve continuous vertical wavenumber coverage of velocity structure (based on the plane-wave diffraction tomography theory of Wu

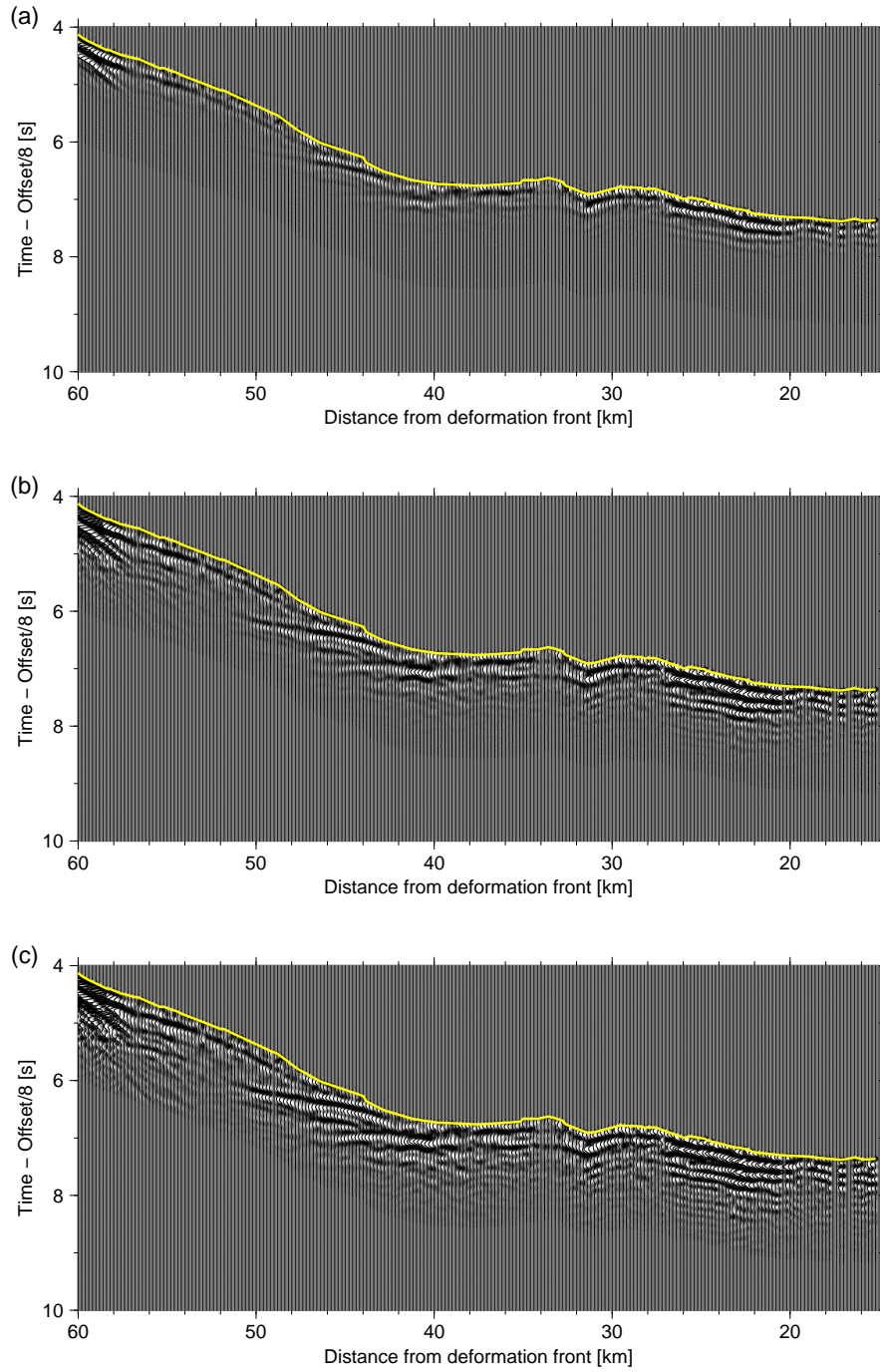


Figure 3.7: Observed wavefield with  $\tau =$  (a) 0.167, (b) 0.333, and (c) 0.5 sec. The damped wavefields are displayed with the application of  $\exp(t_0/\tau)$  to compensate for the amplitude loss, where  $t_0$  is the picked arrival times.

& Toksoz, 1987). However, Mulder & Plessix (2004) suggested that smaller frequency intervals are required in the presence of noise, and also showed that a set of multiple frequencies help stabilize the inversion as utilized for example by Pratt (1999), Bleibinhaus et al. (2007), and Brossier et al. (2009). With our wide-angle data of 55 km maximum source-receiver offset, the selection strategy of Sirgue & Pratt (2004) would only require the end-members of the frequency range we used, i.e., 2.25 Hz and 8.5 Hz. Instead of using this extreme choice, we employed a group of 4 frequencies in 0.25 Hz interval (e.g. [2.25, 2.5, 2.75 3.0] Hz) at each iteration. After 5 iterations, the next group of 4 frequency components were inverted, while allowing 2 of them to overlap with the previous group (e.g. the next group is [2.75 3.0 3.25 3.5] Hz). The above frequency intervals and increments were chosen by conducting several experiments, and subjectively selecting the combination yielding the best results in the reasonable time.

### 3.5.3.2 Decay constant sampling

Rigorous sampling strategies for selecting values of the characteristic decay time,  $\tau$  have not been developed. Typically, inversions have used regularly sampled values for  $\tau$  (Brenders & Pratt, 2007a; Brenders, 2011) or  $\sigma$  (Shin et al., 2010). In our inversions, characteristic times of  $\tau = 0.167, 0.2, 0.25, 0.333, 0.5, 1.0, 2.0$  sec were selected, corresponding to nearly-regularly sampled values of the decay constant  $\sigma = 6, 5, 4, 3, 2, 1, 0.5 \text{ sec}^{-1}$ . The smallest  $\tau$  value was selected visually by examining the signal-to-noise ratio of the damped wavefield, and the largest  $\tau$  value was selected by avoiding higher  $\tau$  values once the velocity update became negligible. The full schedule for Stages 1 and 2 of our Laplace-Fourier waveform inversion is shown in Table 3.2. Examples of time-damped waveforms are shown in Fig. 3.7 for  $\tau = 0.167, 0.333, 0.5$  sec, in which the suppression of later arrivals is evident as  $\tau$  values decrease. At  $\tau = 0.167$  sec, our input data for waveform inversion consist largely of first arrival energy, and the ambient noise between the opening of the data window and the actual arrival time becomes amplified unacceptably, preventing the use of smaller  $\tau$  values.

### 3.5.4 Gradient preconditioning

A key computation in waveform inversion is the gradient of the objective function (described above in Section 3.3.3). The gradient represents an image of the updates to be applied to the velocity model, but normally requires preconditioning. The gradient of waveform inversion tends to be sensitive to the high-wavenumber components of the earth (Mora, 1989; Sirgue, 2003), and often is contaminated by a visible "acquisition footprint"



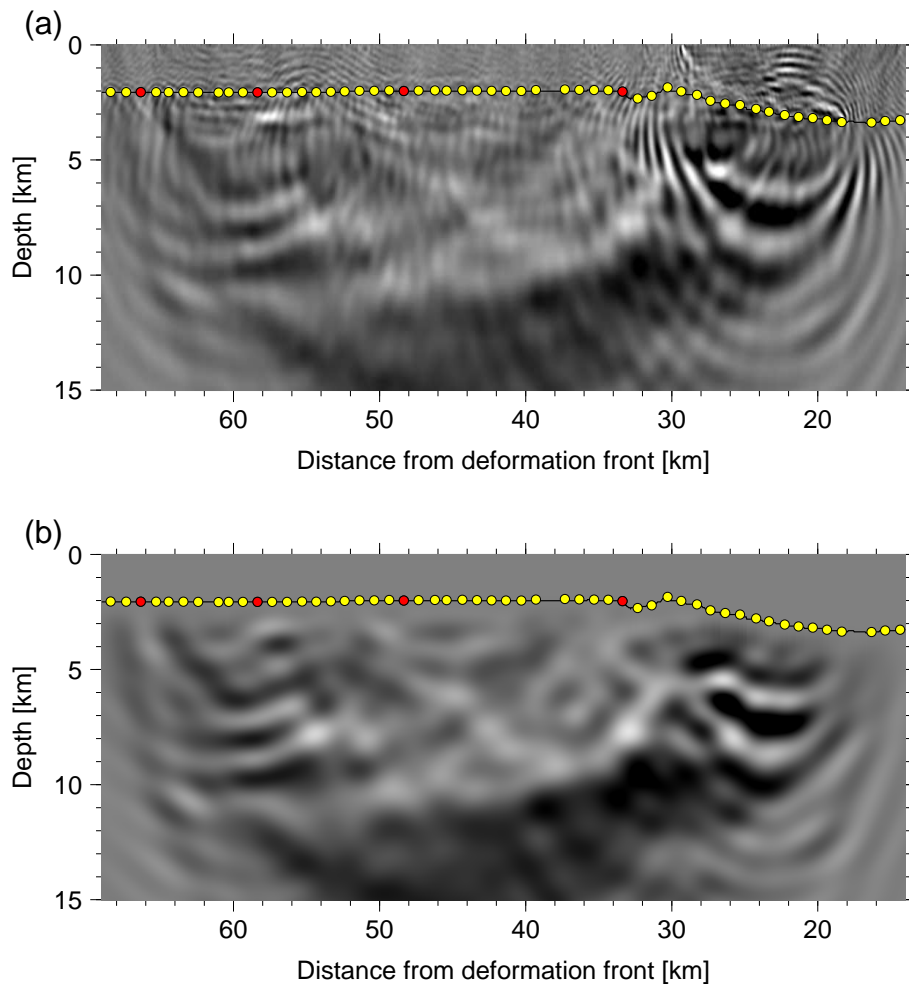


Figure 3.8: Effects of gradient filtering. (a) Raw P-wave gradient for the starting model, obtained with  $f = 2.25, 2.50, 2.75, 3.00$  Hz, and  $\tau = 2.0$  sec, and (b) the same gradient after the application of wavenumber filtering, and gradient masking. The logarithmic phase-only objective function (Eq.(3.13)) was used. Yellow circles show the location of the 16 bit OBS instruments, and red circles show the location of the 24 bit OBS instruments used in this study.

due to sparse survey geometry. Thus the gradient needs to be preconditioned to remove artifacts, and to enhance the smoothness of the resulting models (Sirgue, 2003; Ravaut et al., 2004; Brenders & Pratt, 2007b). We adopted a low-pass wavenumber filter (Sirgue, 2003) which passes the components of wavenumber spectra inside the ellipse defined by

$$\frac{\kappa_x^2}{\kappa_{x_c}^2} + \frac{\kappa_z^2}{\kappa_{z_c}^2} = 1, \quad (3.29)$$

where  $\kappa_{x_c}$  and  $\kappa_{z_c}$  are the cut-off wavenumbers. To minimize artifacts from sharp edges of the filter, a cosine taper zone is introduced outside the ellipses defined by Eq.(3.29).

We designed the wavenumber filter based on the theoretical resolution limit of waveform inversion derived by Wu & Toksoz (1987)

$$\kappa_o = \frac{2\omega}{c}, \quad (3.30)$$

where  $c$  is the velocity. The velocity  $c$  is conventionally selected to be the minimum velocity inside the medium, and is the 1.5 km/s velocity of seawater in our case. However our imaging targets are the low velocity zones and the mega-splay fault, with velocities of approximately 4 km/s, significantly higher than the velocity of seawater. Therefore, in order to optimize resolution, the wavenumber filter was designed for our targets rather than for the sea water and the shallow soft sediments. After extensive testing, we chose to use

$$\begin{aligned} \kappa_{c_x} &= \frac{1}{2} \kappa_o \Big|_{c=4 \text{ kms}^{-1}}, \\ \kappa_{c_z} &= \kappa_o \Big|_{c=4 \text{ kms}^{-1}}, \end{aligned} \quad (3.31)$$

to obtain the best result. Stronger smoothing constraints were adopted for the horizontal direction in order to enhance horizontal features in the models, a recognition of a priori expectation of the geological nature of the target.

We show an example of the raw gradient from the lowest frequency set used for waveform inversion in Fig. 3.8a; the gradient is overprinted by excess high-wavenumber oscillation and artifacts arising due to the sparsity of the OBSs. As the acquisition footprint is particularly strong in the near-field, we masked the gradient in the sea water, and applied a cosine taper just beneath the sea floor. The same gradient after the application of the masking and the low-pass wavenumber filter (Fig. 3.8b) shows that these artifacts have been successfully suppressed without degrading the resolution at our target depths. Note that some fine-scale features just below the sea floor have been sacrificed.

## 3.6 Results and validation

We first present the waveform tomography results in Section 3.6.1, and then describe the evaluation and verification of these results in Section 3.6.2. As a final verification step, we also present the results of checkerboard testing and a set of approximate point-scatter responses in Section 3.6.3.

### 3.6.1 Waveform tomography results

The velocity images obtained from waveform tomography are displayed in Fig. 3.9 (an intermediate result after Stage 1), and Fig. 3.10 (the final model after Stage 2); the de-trended velocity models are shown both in colour and grey scales. A series of 1D velocity profiles are shown in Fig. 3.11. During waveform inversion, the objective function decreased monotonically during the inversion about 5-10 percent per frequency set. The differences between the Stage 1 (intermediate) and Stage 2 (final) models are not substantial: The final velocity structure exhibits sharper lithological boundaries, particularly at the bottom of the low velocity zones, and contains less artifacts inside the oceanic crust. The overall resemblance between two models indicates the significant resolving power of the phase-only inversion used to form the Stage 1 results.

Fig. 3.12 depicts the final Waveform Tomography result with an interpretative overlay following Chapter 2. We identify a number of visible velocity anomalies and velocity discontinuities in Fig. 3.12: Solid black lines indicate velocity discontinuities clearly observed in the waveform tomography image, independently of their appearance in the previous migration images. Black dashed lines indicate velocity discontinuities not clear in waveform tomography, but possibly interpretable as lithological boundaries and/or faults in conjunction with the migrated reflectivity image of Moore et al. (2009) (shown in Fig. 3.13; discussed in Section 3.6.2.1).

Our intermediate and final velocity structures show significant improvement from the traveltimes tomography result displayed in Fig. 3.1. The velocity structure down to 12 km depth is better determined over most of the model, with clear delineations of lithological boundaries including the fore-arc basin, the plate boundaries, the mega-splay fault (line A-B-B',B''), and two low velocity zones (LVZ<sub>1</sub> and LVZ<sub>2</sub>). The mega-splay fault is identified as a sharp 1 km/s velocity reduction between distances 33 km and 55 km (line A-B). The fault splits into two branches at the seaward end (distance 33 km at 6.5 km depth, line B' and B''). A continuous low velocity region is recognizable both in the inner wedge and in the outer wedge: LVZ<sub>1</sub> is well defined by the mega-splay fault at the top, and the plate boundary at the bottom. LVZ<sub>2</sub> is also clearly resolved

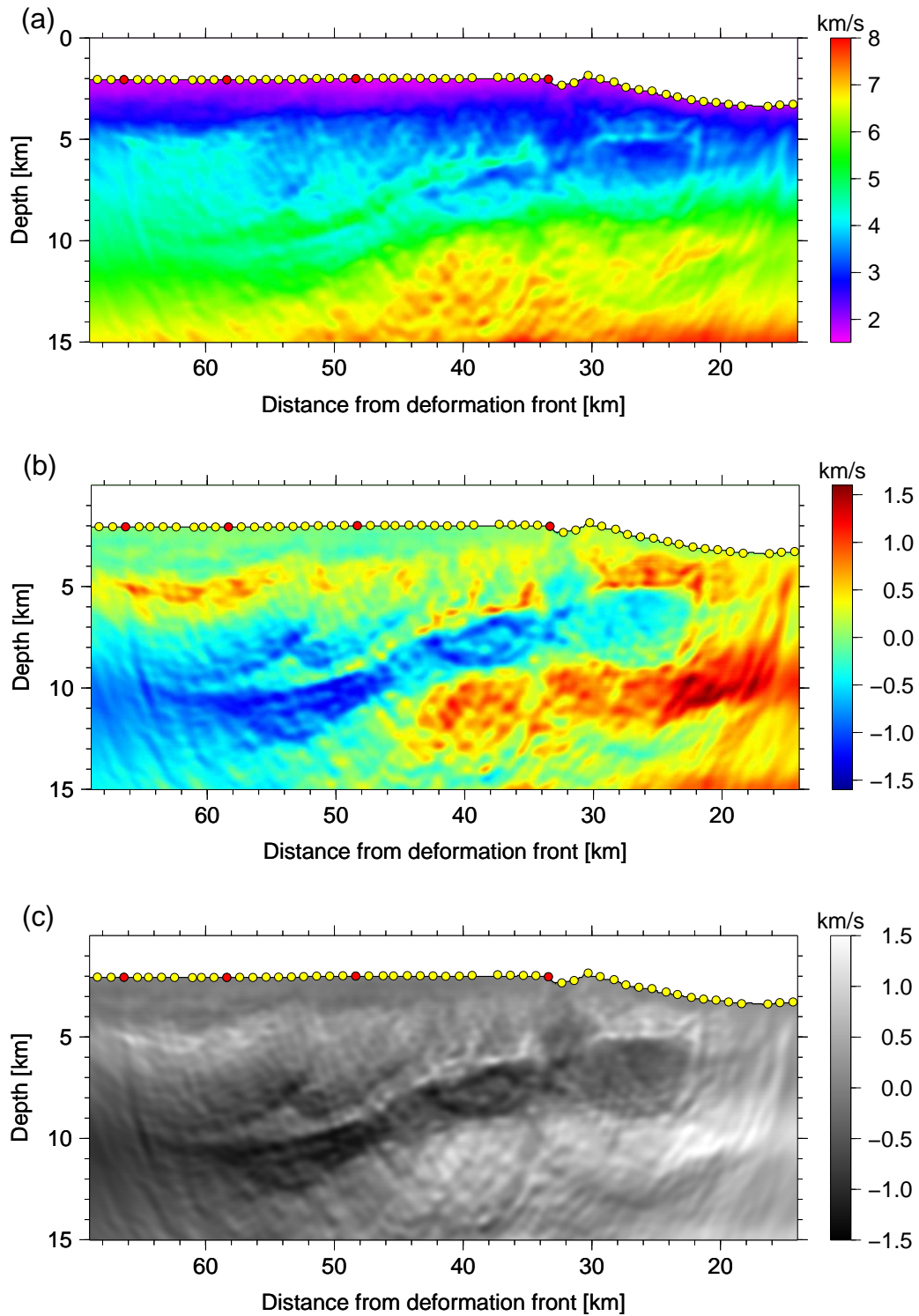


Figure 3.9: P-wave velocity structure after Stage 1 of waveform inversion. (a)  $V_p$  model, (b) de-trended model of (a) in colour, and (c) same as (b) but shown in greyscale.

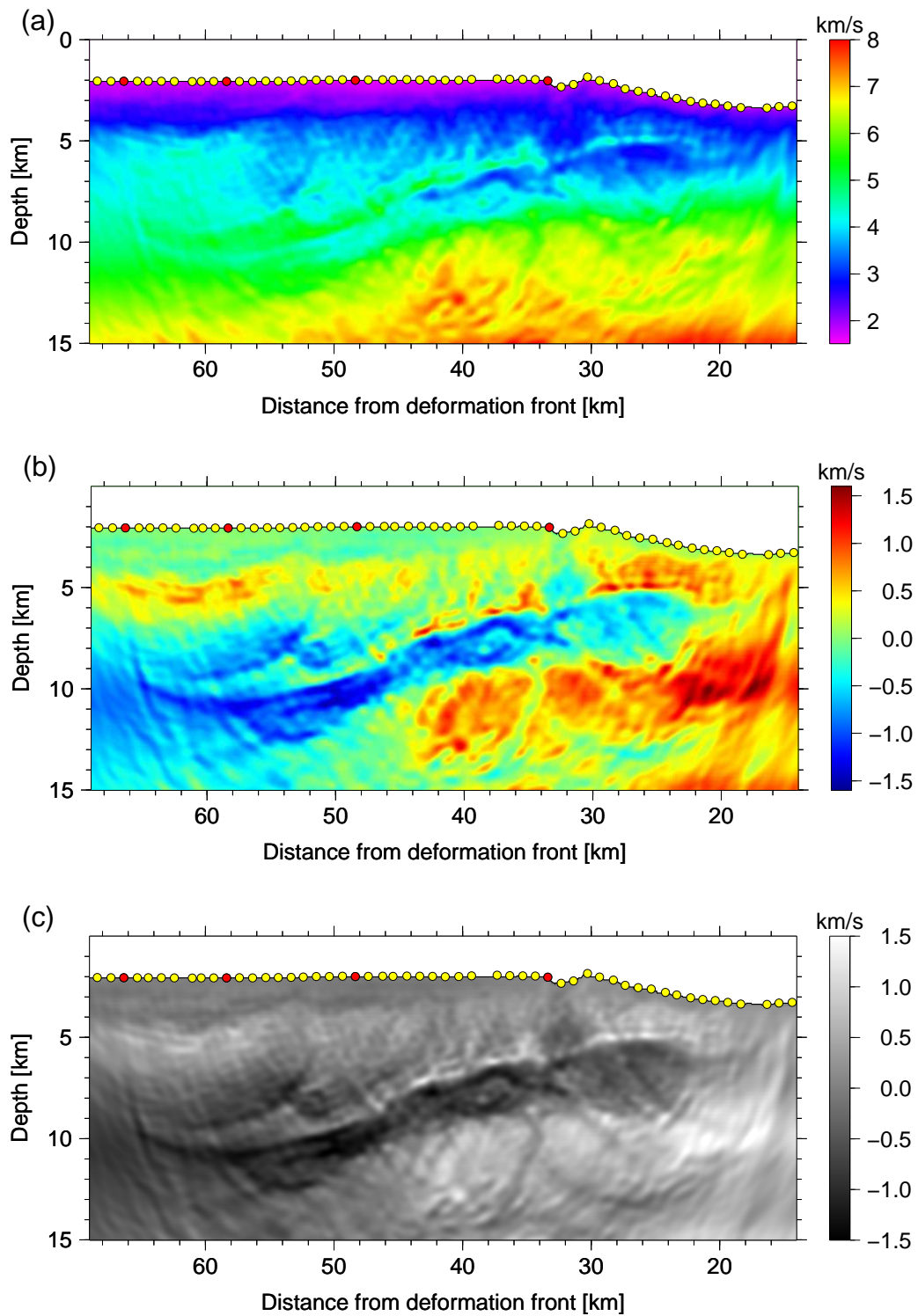


Figure 3.10: P-wave velocity structure after Stage 2 of waveform inversion. (a)  $V_p$  model, (b) de-trended model of (a) in colour, and (c) same as (b) but shown in greyscale.

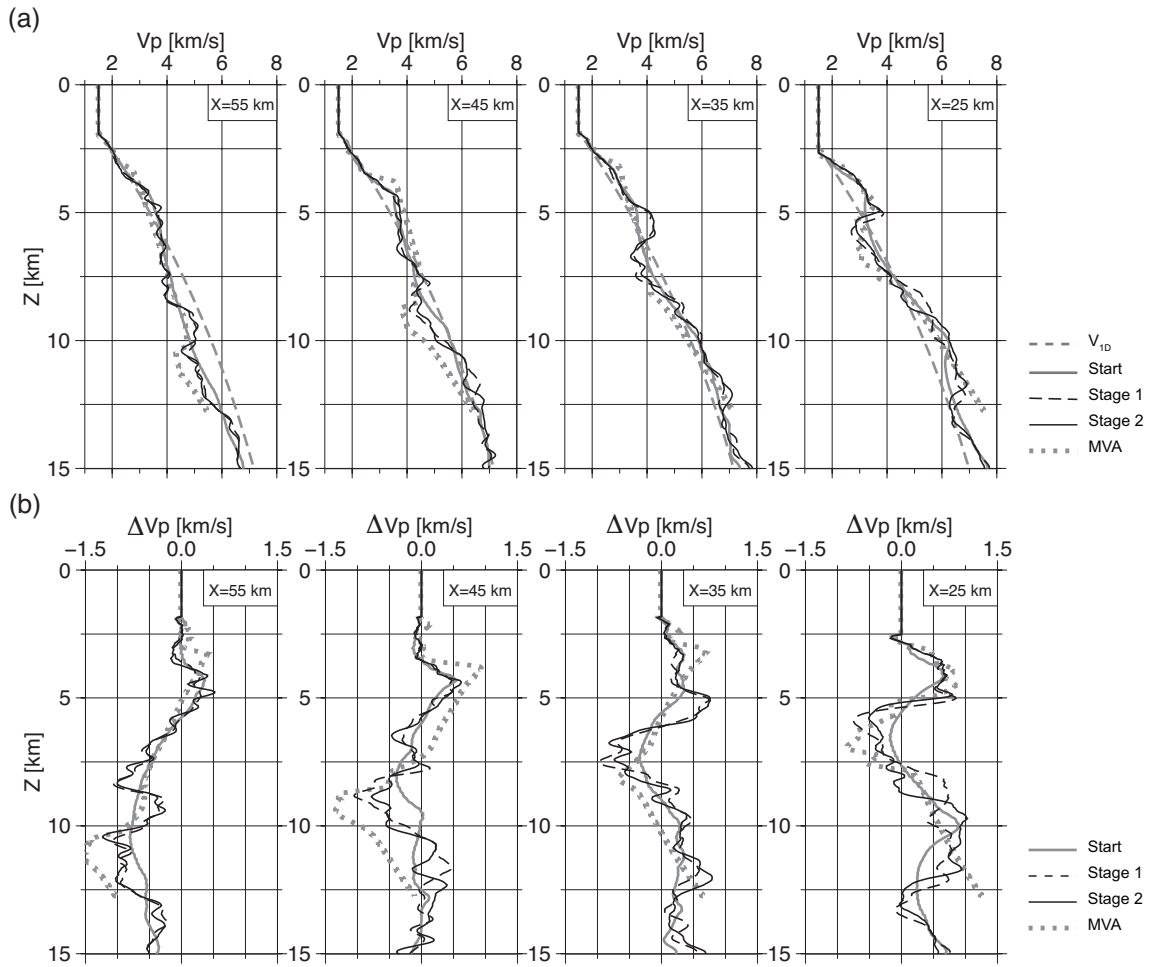


Figure 3.11: (a) Vertical velocity profiles and (b) de-trended velocity profiles at distances 55, 45, 35, 25 km (from left to right). Dashed grey lines show the velocity trend before removal  $V_o(z)$  (only present in (a)), grey lines the starting model, dashed black lines the intermediate velocity models after Stage 1, black lines the final velocity, and grey dotted lines the velocities from the MVA of Park et al. (2010).

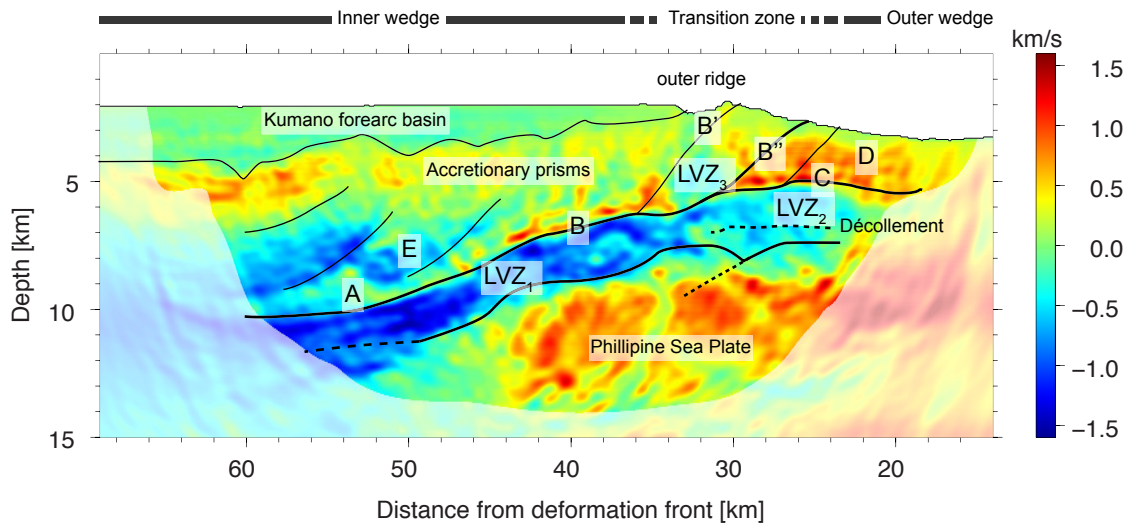


Figure 3.12: De-trended final waveform tomography result with interpretation. The strong velocity discontinuity appearing at depths of 5 - 11 km between distances between 20 km and 60 km is identified as lines A, B and C. Lines B' and B'' represent the seaward branching of the mega splay fault. The low velocity zones are labelled LVZ<sub>1</sub> (landward), LVZ<sub>2</sub> (seaward), and LVZ<sub>3</sub> (under the outer ridge). Dashed lines represent lithological boundaries as interpreted in conjunction with the reflectors evident on the migration image in Fig. 3.13. Area D indicates the seaward accretionary prism, exhibiting higher velocity values with respect to the  $V_o(x, z)$  trend. Area E shows a fourth low velocity layer within the older accretionary prisms in the inner wedge.

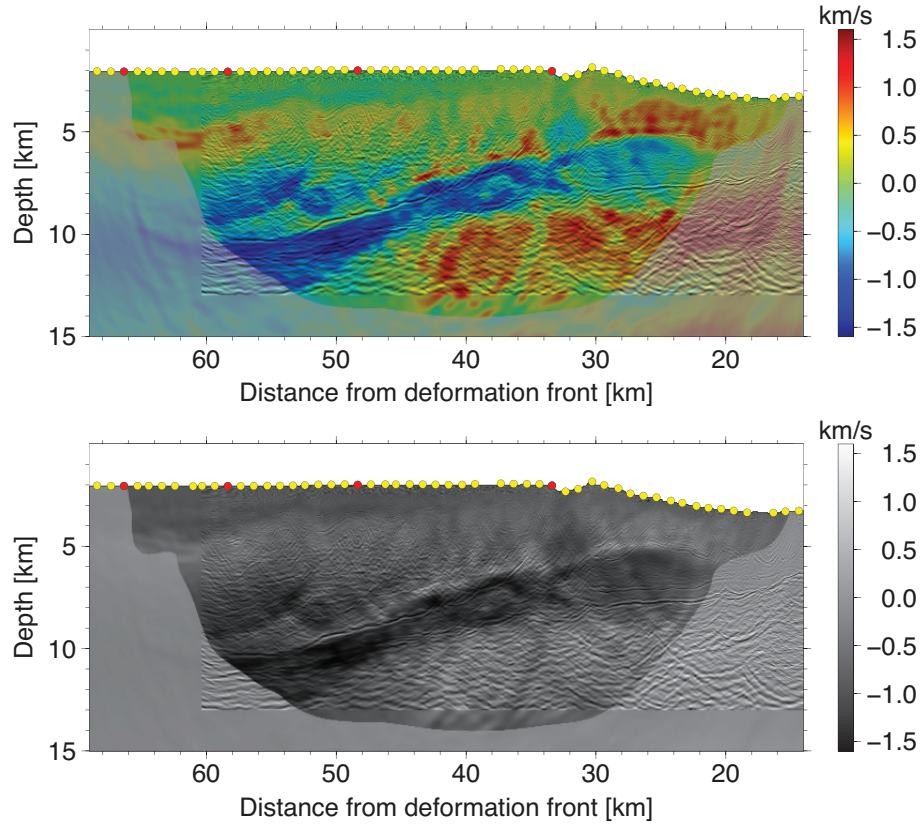


Figure 3.13: De-trended final waveform tomography velocity model overlaid by the nearest 2D slice of 3D PSDM results in Moore et al. (2009), (a) in colour and (b) in grey scale

between distances 20 km and 30 km, and is apparently connected to  $LVZ_1$ . The seaward termination of  $LVZ_2$  is ambiguous due to the limited wavepath coverage.  $LVZ_2$  is overlaid by the layer whose velocity is about 1 km/s higher than the trend function  $V_o(x, z)$  (area D). Underneath the outer ridge at distance 33 km between the splays  $B'$  and  $B''$ , there is a third low velocity zone ( $LVZ_3$ ) above the main fault. In the inner wedge, the last low velocity zone is marked as area E. Area E contains several lineations, which may represent a large fault structure, although these particular velocity discontinuities may in fact be artifacts associated with the anomalously sparse OBS intervals between distances 38 km and 40 km.



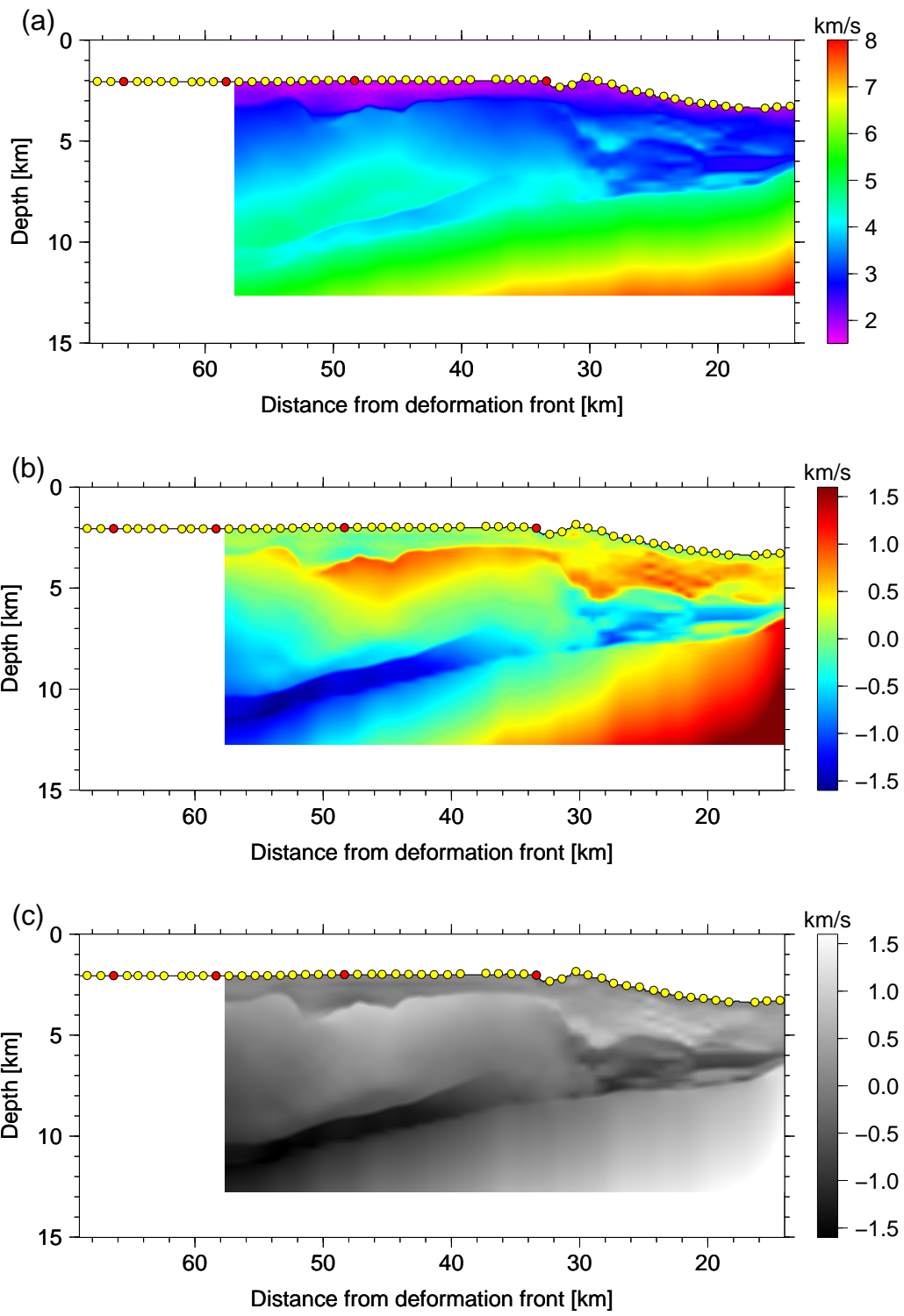


Figure 3.14: (a) The nearest 2D slice of the 3D migration velocity model presented in Park et al. (2010), (b) de-trended velocity model of (a) in colour and (c) the de-trended velocity model in grey-scale.

## 3.6.2 Evaluation and verification of waveform tomography results

### 3.6.2.1 Comparison with a Pre-stack migration image

Velocity structures obtained from waveform tomography can resolve geological features at a spatial scale comparable to migration images, provided that similar frequency bandwidths are employed (Sirgue et al., 2010). Therefore a visual comparison of waveform tomography images and migration images has been a common approach to validate the reliability of the apparent geological boundaries (e.g., Ravaut et al., 2004; Operto et al., 2006; Smithyman et al., 2009; Takam Takougang & Calvert, 2011). In Fig. 3.13, we compare our P-wave velocity images to the nearest 2D slice from the 3D anisotropic Kirchhoff pre-stack depth migration (PSDM) volume described by Moore et al. (2009) and Park et al. (2010). Note that here the spatial resolution differs between our waveform tomography results and PSDM, since the Waveform Tomography result was generated using a frequency bandwidth of 2.25 - 8.5 Hz, significantly lower than that of the reflection survey (which contained frequencies up to 80 Hz).

The 3D reflection survey was conducted in the same area as the OBS survey (see the grey shaded area in Fig. 2.1). The survey was conducted by the Integrated Ocean Drilling Program (IODP) as a part of Nankai Trough Seismogenic Zone Experiment (NanTro-SEIZE) (Moore et al., 2007, 2009; Park et al., 2010). Detailed survey geometry and processing flows can be found in Moore et al. (2009) and Park et al. (2010): The migration velocity model was iteratively updated by applying 3D horizon-based tomography (Kosloff, 1996) and 3D grid-based tomography (Stork, 1992) to obtain the best focused, anisotropic, Kirchhoff PSDM image. The traveltime tomography result of Nakanishi et al. (2008), (also used here as a starting model) guided the migration velocity analysis (MVA) particularly in the inner wedge to compensate for the lack of major reflectors in the thick accretionary prism. The resulting MVA model is shown in Fig. 3.14, and is also shown with the background velocity profiles in Fig. 3.11.

The comparison in Fig. 3.13 depicts a convincing agreement of apparent lithological boundaries evident on the waveform tomography image with the corresponding reflectors on the PSDM images. The MVA result in Fig. 3.14 and the waveform tomography velocity model also show similar values in the outer wedge, where the MVA model apparently shows higher resolution than elsewhere. These similarities provide further confidence in the validity of the waveform tomography result.

Waveform tomography yielded superior results in the area underneath the outer ridge around distance 33 km down to 9 km depth in comparison with the migration images.

We attribute the evident improvement in the waveform tomography velocity model over the MVA velocities in Fig. 3.14 to the employment of refraction data and wide-angle reflection data in waveform tomography, while the MVA only utilized the narrow-angle reflection components. Note that the absence of LVZ<sub>3</sub> in the MVA velocity model may have prevented an effective migration of the reflectors below (i.e. the mega-splay fault and the plate boundary). Furthermore, the seismic Kirchhoff pre-stack migration algorithm adopted in Moore et al. (2009) and Park et al. (2010) uses asymptotic ray theory, while waveform tomography uses a numerical solution for the full acoustic wave equation.

We note a discrepancy in Fig. 3.13 in the depth of the mega-splay fault of about 800 m between distances 35 km and 45 km. The shallower depths on the waveform tomography result can be attributed to the fact that velocity values in the inner wedge are approximately 0.5 km/s slower for the waveform tomography result than for the MVA model. Considering the large uncertainties in the MVA velocity due to the short 4.6 km length of the streamer cable and the strong feathering in the 3D reflection survey (Moore et al., 2009), the mega-splay fault depth from waveform tomography may be considered to be more reliable. However seismic velocity anisotropy may also have contributed to discrepancies in estimated velocity values: MVA utilizes reflection waves which propagate vertically, while Waveform Tomography primarily inverts refraction and wide-angle reflections which propagate horizontally.

A further discrepancy between the waveform tomography result and the PSDM image is evident at the upper bound of LVZ<sub>2</sub>, which corresponds to a weak discontinuous reflector in the migration image, in spite of the strong and continuous velocity reduction of approximately 0.8 km/s apparent in the waveform tomography results. This same apparent discrepancy was also noted by Park et al. (2010) between the MVA model and the PSDM image. Although a strong positive density contrast could reduce the impedance contrast by compensating for the velocity reduction, the discrepancy is more likely to arise for technical reasons: If line C has an irregular surface, the reflection energy (5-80Hz) will likely be scattered in a complicated manner, making it difficult to migrate the reflector effectively with the Kirchhoff migration. By contrast, the low-frequency refraction energy (2.25-8.5Hz) used in waveform tomography is less sensitive to the detailed structure of the boundary, leading to a more continuous reconstruction of the boundary.

A further discrepancy between the waveform tomography and PSDM results is evident at the location of the décollement in Fig. 3.12 and 3.13. The décollement is not clearly depicted in the waveform tomography result, although a possible signature can be discerned on the greyscale de-trended velocity image. This may imply that the impedance contrasts at the décollement seen in the migration images are mainly due to density changes, and

that in this specific region of the image the velocity changes are not significant enough to be recovered by waveform tomography.

We observe splay-like features on Fig. 3.12 in area E in the waveform tomography images that are less recognizable in the PSDM. Although we cannot rule out the possibility that these structures arise from the irregular OBS geometries as suggested in Section 3.6.1, these features are also geologically plausible as imbricated thrusts by correlating their angle with the topographic relief at the base of the fore-arc basin. A future re-migration of the reflection data with the waveform tomography velocity model may be useful in resolving this issue.

### 3.6.2.2 Time-domain waveforms

The primary, independent, quality-control tool for seismic waveform inverse method is a comparison between synthetic and observed waveforms in either the time-domain or the frequency domain, or both (e.g., Ravaut et al., 2004; Bleibinhaus et al., 2007; Brenders & Pratt, 2007a; Takam Takougang & Calvert, 2011). The sparse OBS intervals in our data set preclude the visualization of frequency domain waveforms due to spatial under-sampling in the OBS domain, and thus we focus on time-domain evaluations. We used the visco-acoustic waveform modelling code described in Section 3.3.2, and synthesized waveforms for the intermediate velocity model after Stage 1 (Fig. 3.9) and the final model after Stage 2 (Fig. 3.10). The source signature was estimated for each velocity result using the methodology described in Section 3.3.4, assuming all sources excited an identical wavelet. The observed waveforms for OBS 47 are shown in Fig. 3.15a with the application of the data preprocessing described in Section 3.4.2 (apart from bottom muting, so that later waveforms may be compared). The synthesized waveforms from the same OBS are displayed in Fig. 3.15b and c. Our intermediate and final waveform tomography results yield virtually identical synthetic waveforms, as might be expected from the similar appearances of the respective velocity models. Both results show significant improvement in the fit of the synthetic waveforms when compared with those of the starting model (Fig. 3.6). Most notably, these synthetic waveforms successfully reproduce many of the characteristics of the observed waveforms: The first arrival refractions match well, as do the amplitudes variations from trace to trace; significantly, the wide-angle reflections are clearly visible between distances 40 km and 44 km.

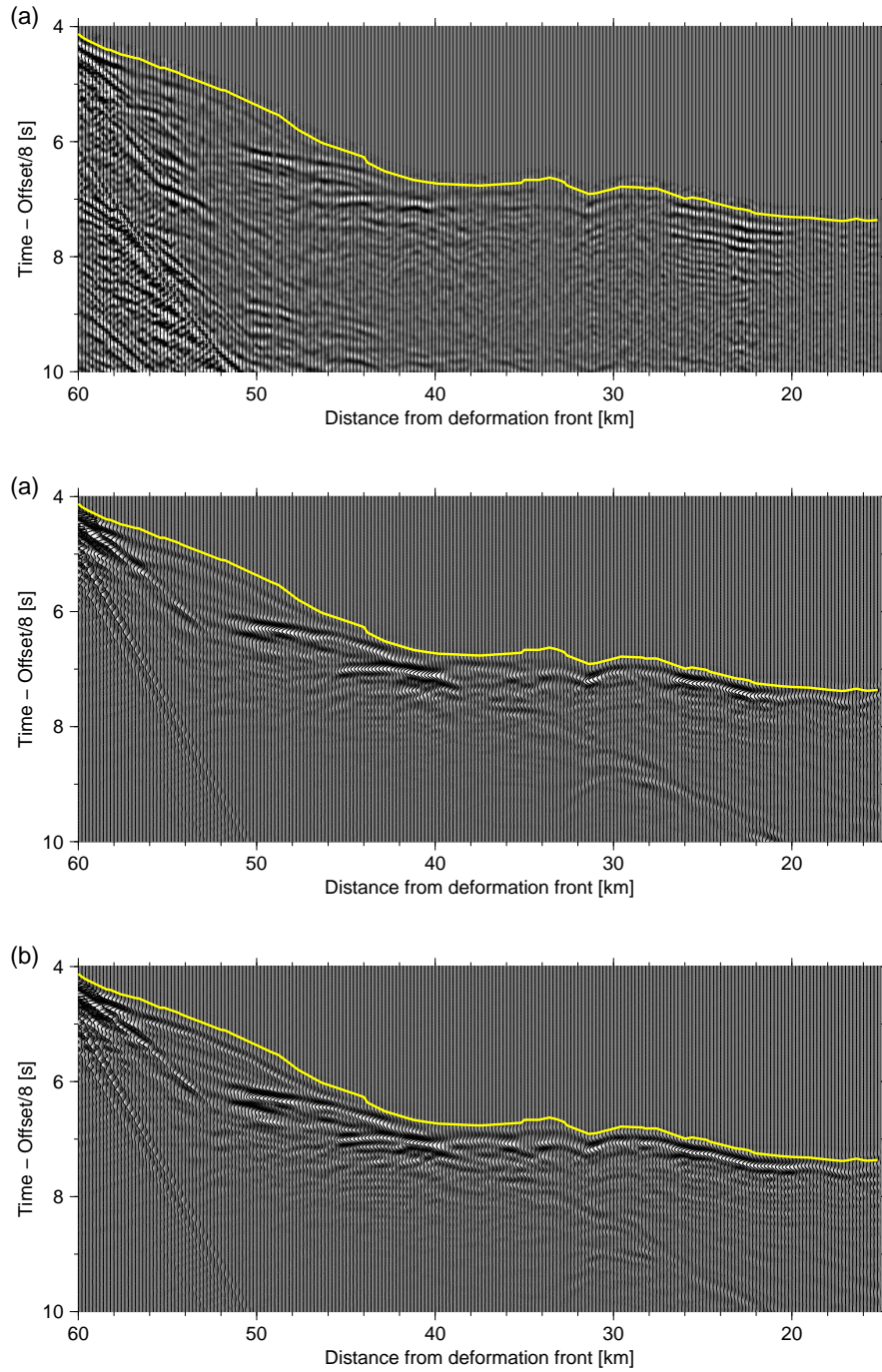


Figure 3.15: (a) Representative vertical component seismic waveforms recorded at OBS 47. Data preprocessing was applied although bottom muting is omitted here so that later waveforms may be compared. (b) Predicted pressure wavefield at OBS 47 computed from the intermediate velocity model after Stage 1, and (c) from the final velocity model. The yellow lines indicate the picked first arrivals.

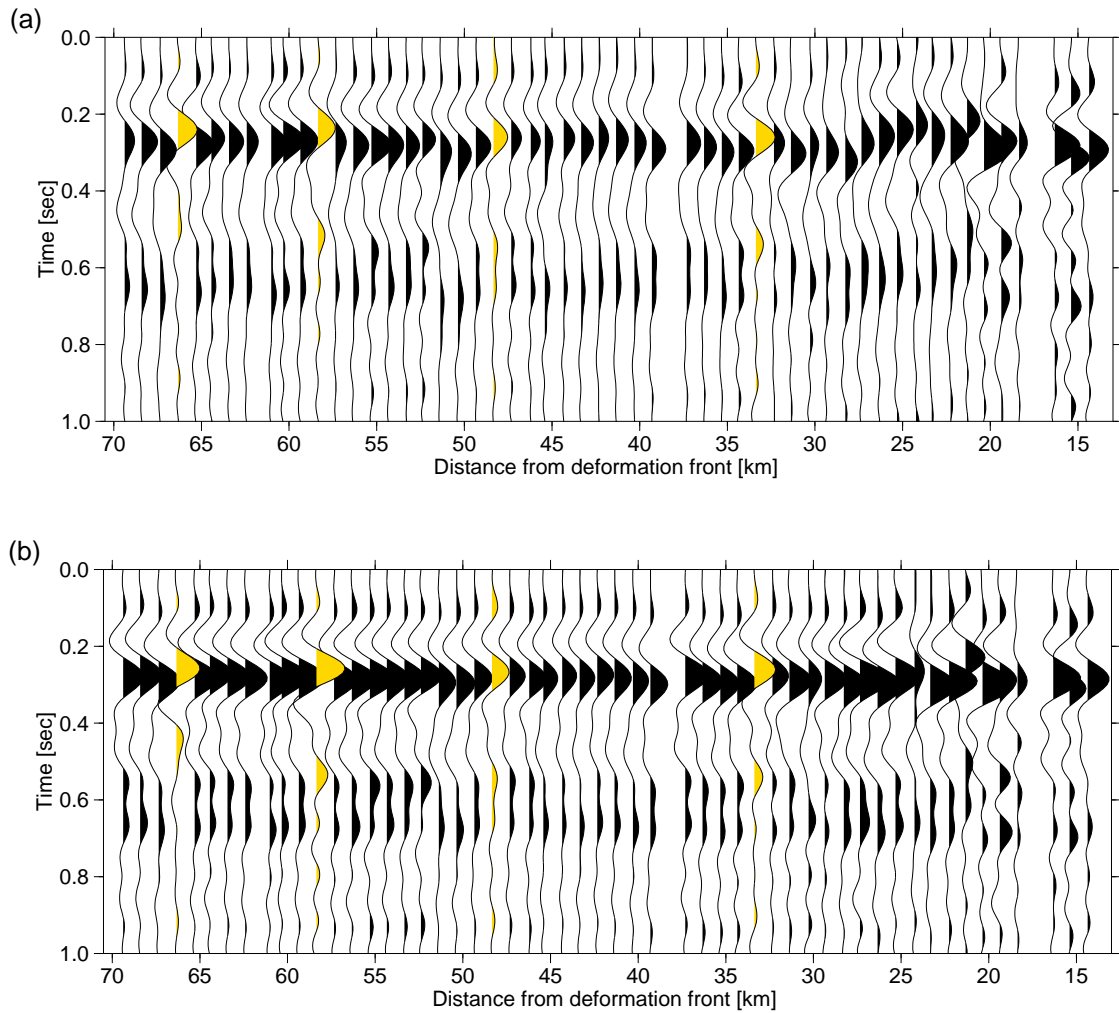


Figure 3.16: Source waveforms estimated individually at each OBSs for (a) the starting model, and (b) the final velocity models. Source estimates from the OBSs with a 24bit A/D converter are shown in yellow. There is an evident improvement in the coherence of the source wavelets estimated in the final model.

### 3.6.2.3 Improvement in source estimation coherency

As described in Section 3.3.4, we can also utilize the coherency of the source estimates to evaluate the quality of our obtained velocity models. As described in Section 3.3.4, we invoke reciprocity to qualitatively evaluate the similarity of “source” waveforms at 54 OBS locations (instead of actual shot locations). The estimated source waveforms for the starting model and the final velocity model are displayed in Fig. 3.16. A 20 ms phase-shift is evident in the source waveforms at the 24 bit OBSs (shown in yellow colour in Fig. 3.16), when compared to the other 16 bit OBSs. This suggests the existence of different instrumental filtering effects between the two types of the OBSs.

Fig. 3.16a illustrates that the starting model already provided coherent waveforms over most of the OBSs. This indicates a sufficiently accurate starting model over most of the inverted area. The exception is the incoherency in source waveforms at OBSs between distances 14 km and 28 km, suggesting an erroneous velocity structure in the outer wedge over this interval. After waveform inversion, the estimated source waveforms became visibly more consistent (Fig. 3.16b), but slight incoherencies remain at a few OBSs around distance 20 km. The visible improvement in the source estimation coherency provides confidence in the validity of the velocity update. The remaining inconsistencies may be a result of a receiver coupling problem, since these OBSs were located on a slope consisting of soft sediments which have experienced multiple landslides (Moore et al., 2011).

### 3.6.3 Resolution tests

The final appraisal of our waveform tomography result is provided by characterizing the model resolution, model uncertainties and modelization errors (i.e. acoustic assumption). The upper resolution limit of waveform inversion is imposed by the wavenumber filter at the highest frequency used in the inversion (as described in Section 3.5.4), which limits the results to a resolution of 0.7 km horizontally and 0.35 km vertically. The spatial coverage of waveform tomography can be roughly approximated by the ray coverage of the model, which we use throughout the figures in this chapter to mask the waveform tomography images.

In this study, we employed conventional chequerboard tests and point-spread function tests. These approaches enable us to explore modelization errors arising due to the use of the acoustic wave assumption. We synthesized both acoustic and elastic waveforms for the chequerboard and point-spread function models, and compared the acoustic waveform inversion images from both wavefields.

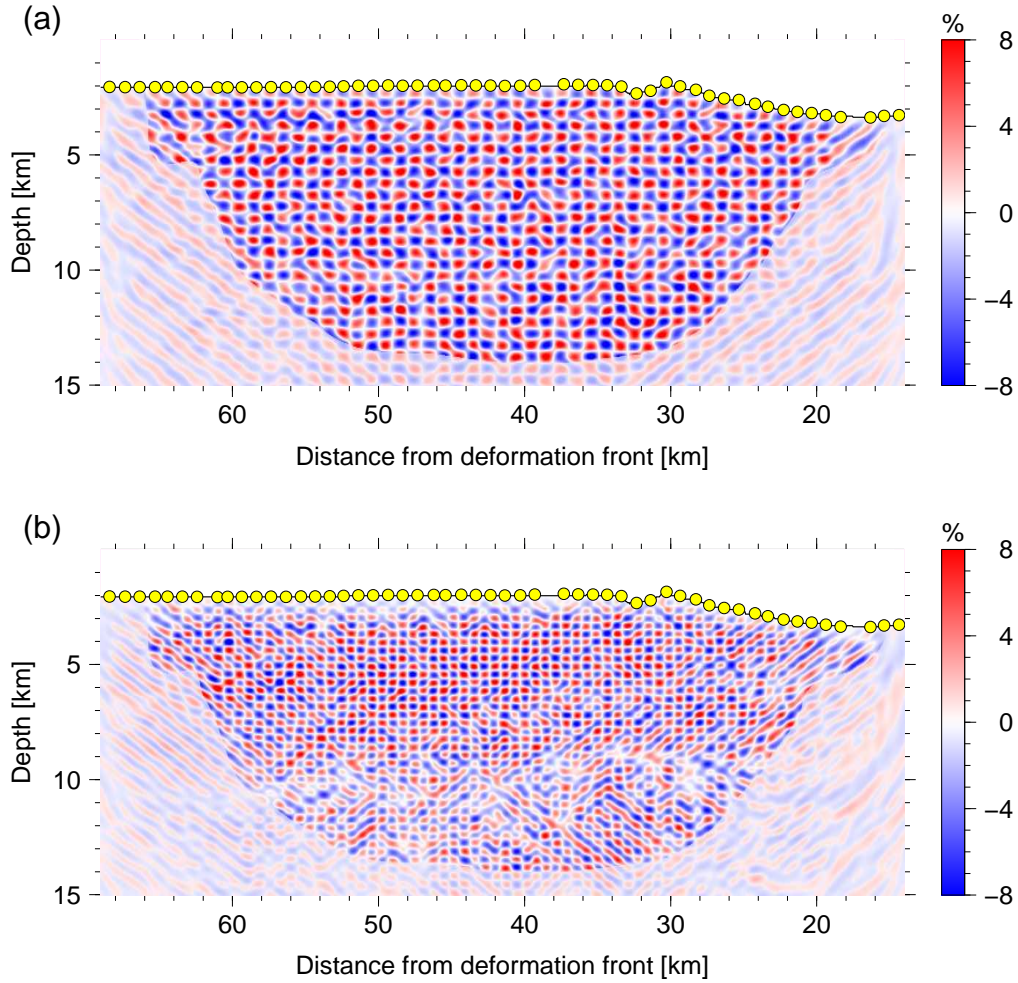


Figure 3.17: Acoustic chequerboard test results. Acoustic waveform inversion results of acoustic wavefields are shown for (a)  $1.0 \text{ km} \times 0.5 \text{ km}$  and (b)  $0.7 \text{ km} \times 0.35 \text{ km}$  chequerboard patterns.

### 3.6.3.1 Chequerboard testing

Chequerboard tests have conventionally been used to estimate the spatial resolution of travelt ime tomography results (e.g., Zelt & Barton, 1998; Nakanishi et al., 2008); more recently chequerboard tests have also been applied to waveform inversion results (Smithyman et al., 2009; Malinowski et al., 2011). In this study, we assigned chequerboard perturbations to the reference P-wave structures of spatial dimension i)  $1.0 \text{ km} \times 0.5 \text{ km}$ , and ii)  $0.7 \text{ km} \times 0.35 \text{ km}$  (the latter representing theoretical upper resolution limit). As a reference model, we used the final P-wave velocity model shown in Fig. 3.10, and we perturbed the velocities by plus-and-minus 5 %. The corresponding density model was generated by applying Gardner’s relationship to the perturbed P-wave velocity model,



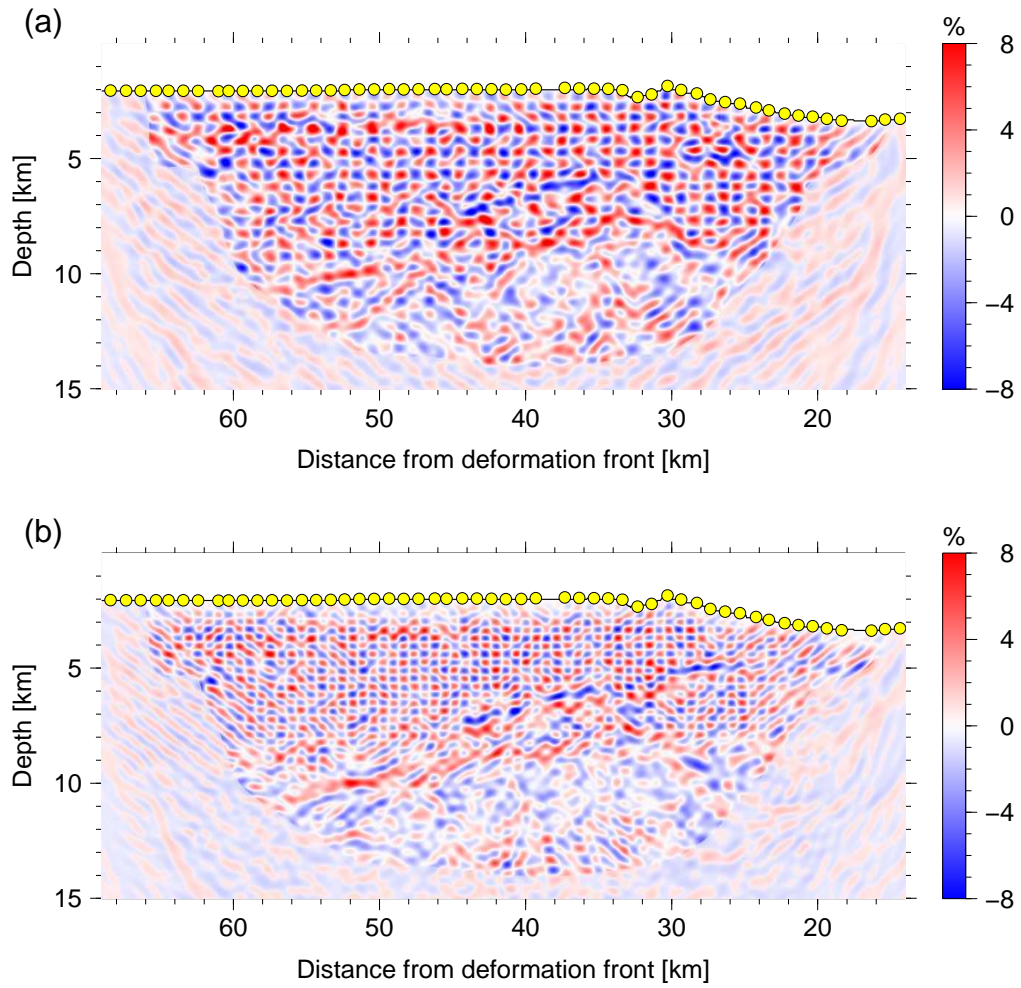


Figure 3.18: Elastic checkerboard test results. Acoustic waveform inversion results of elastic wavefields are shown for (a)  $1.0 \text{ km} \times 0.5 \text{ km}$  and (b)  $0.7 \text{ km} \times 0.35 \text{ km}$  checkerboard patterns.

while the corresponding S-wave velocity model was generated from the perturbed P-wave velocity model by assuming a Poisson’s ratio of 0.28. We set the P-wave and S-wave attenuation ( $Q_p$  and  $Q_s$ ) structures to be same as the  $Q_p$  model of the real-data waveform inversion:  $Q_p = Q_s = 500$  for the sub-sea bottom lithologies, and  $Q_p = 10,000$  for the seawater brine.

Using the perturbed P-wave, density and  $Q_p$  structures, acoustic waveforms were generated by the forward modelling code described in Section 3.3.2. The acoustic inversion results of the resulting acoustic wavefields are displayed in Fig. 3.17a for the  $1.0 \text{ km} \times 0.5 \text{ km}$  chequerboard patterns and Fig. 3.17b for the  $0.7 \text{ km} \times 0.35 \text{ km}$  patterns (note that we display only the perturbations recovered from the waveforms). Waveform inversion of the acoustic perturbations successfully resolved the chequerboard patterns down to 12 km depth for the  $1.0 \text{ km} \times 0.5 \text{ km}$  model, and down to 9 km depth for the  $0.7 \text{ km} \times 0.35 \text{ km}$  model. These purely acoustic test results apparently suggest that acoustic waveform inversion can achieve the theoretical resolution throughout the model, with some losses in resolution in the deeper part.

Following evaluation of the chequerboard patterns within the acoustic assumption, we then moved on to an evaluation of the elastic modelization errors embedded in that assumption. We generated full elastic waveforms for both the reference model and the perturbed velocity models by using the elastic time-domain finite-difference code of Robertsson et al. (1994). A free-surface boundary condition was applied to the top of the model (i.e. the sea surface), and an absorbing boundary condition to the rest of the model boundaries. Synthesized vertical velocity components were preprocessed using the identical procedure as the real OBS data (as described in Section 3.4.2). The acoustic waveform inversion result of the elastic wavefields are depicted in Fig. 3.18a for the  $1.0 \text{ km} \times 0.5 \text{ km}$  patterns and in Fig. 3.18b for the  $0.7 \text{ km} \times 0.35 \text{ km}$  patterns. The acoustic waveform inversion of these elastic data resolved both sizes of the chequerboard patterns above the mega-splay fault in the inner wedge, and above the oceanic crust in the outer wedge. In the inner wedge, underneath the mega-splay fault, the chequerboard patterns recovered from the elastic waveforms became ambiguous, particularly for the smaller  $0.7 \text{ km} \times 0.35 \text{ km}$  patterns, and the patterns are almost indistinguishable below the plate-boundary. This degradation apparently coincides with the lack of structures inside the oceanic crust in the actual waveform tomography result from the real data (as seen in Fig. 3.10).

The imprints of the reference model are apparent at sharp velocity discontinuities, such as that located at the bottom of the fore-arc basin and at the mega-splay fault. We consider that this degradation is due to the failure of the acoustic assumption in

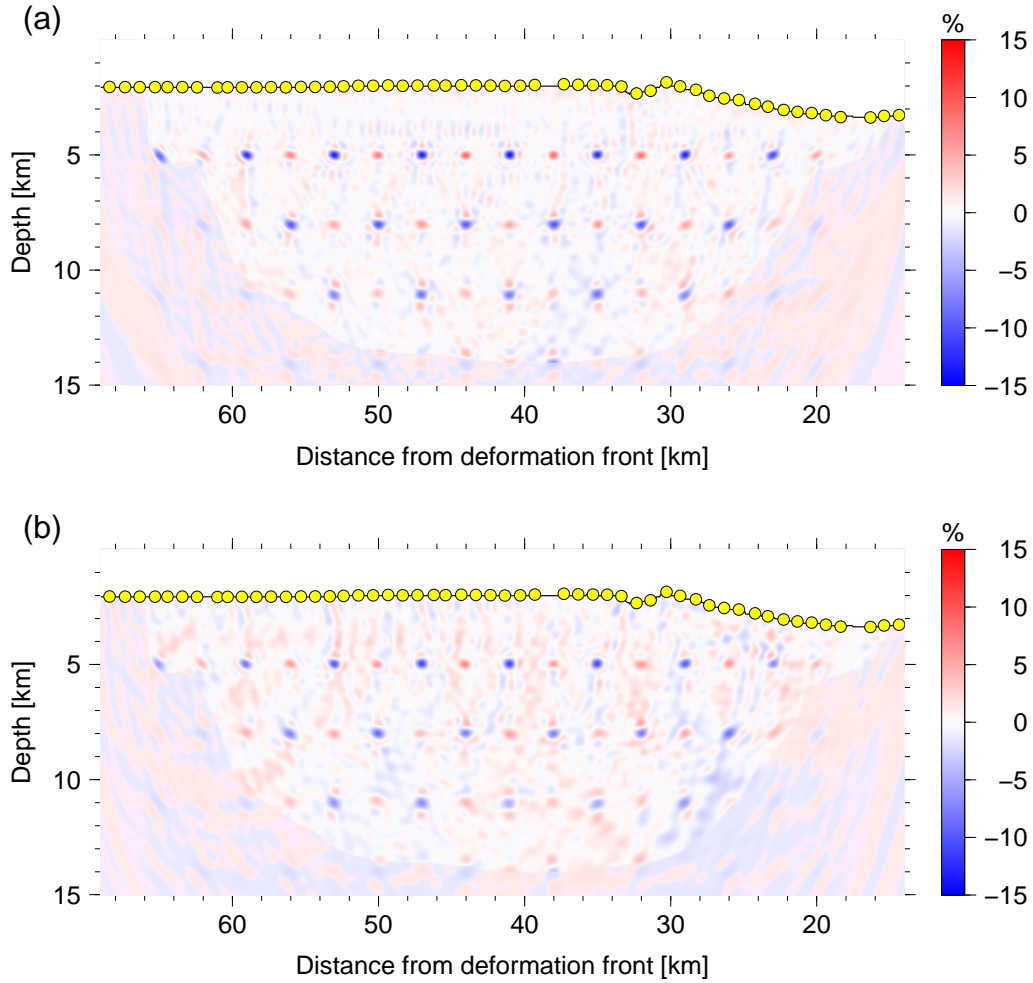


Figure 3.19: Point scatter test results. Acoustic waveform inversion of (a) acoustic wavefields, and (b) elastic wavefields.

treating P-SV conversions, leading to incorrectly modelled reflectivity at these lithological boundaries. For the same reason, the elastic surface scattering effects at the sea floor may degrade the velocity image underneath the topographic relief at the outer ridge at distance 33 km (as illustrated by Bleibinhaus & Rondenay, 2009, for a land survey). However soft sediments at the sea bottom probably limited the influence of mode conversions in this case, and chequerboard patterns were recovered satisfactorily down to the base of the mega-splay fault. This test implies that acoustic waveform inversion is able to fulfil the theoretical resolution only above the oceanic crust, and that this limitation arises due to the failure of the acoustic approximation.

### 3.6.3.2 Point-scatter testing

Point-scatter tests have been used in the resolution analysis of imaging techniques utilizing diffraction energy (Chen & Schuster, 1999; Spetzler & Snieder, 2004). The uncertainty and resolution of the imaging methods can be analyzed by quantifying broadening of a point scatterer, cross-talk between point scatterers, and size of the smallest recognizable scatterers (Chen & Schuster, 1999; Fichtner & Trampert, 2011b). To test these, we distributed square scatterers 250 m (corresponding to 5 grid intervals) on a side at 2.5 km horizontal and vertical intervals throughout the reference model. We used this relatively sparse distribution of scatterers in order to limit the occurrence of non-linearity arising from multiple scattering. In this test, we chose the background velocity model defined in Section 3.2.3 as the reference model since fine-scale structures present in the final velocity model induced excessive artifacts. We perturbed P-wave velocity by plus-and-minus 25 % at the locations of the scatterers. The density model and S-wave velocity structures were generated from the perturbed P-wave velocity model as in the chequerboard testing, and we assigned the same P-wave and S-wave attenuation ( $Q_p$  and  $Q_s$ ) structures in the same way as the chequerboard tests. We simulated and preprocessed both acoustic and elastic waveforms following the procedure used in the chequerboard testing.

The acoustic inversion result of the acoustic wavefields are displayed in Fig. 3.19a: The individual scattering points are well resolved down to 12 km, but we could not fully recover the true 25 % perturbation values. We interpret this as a manifestation of the fact that the spike perturbations are spatially smaller than the resolving power of the survey.

The acoustic inversion result of the elastic wavefields are displayed in Fig. 3.19b. In this case, we terminated the inversion after Stage 1, as the elastic AVO effects related to the sub-resolution scatterers were difficult to correct properly for, and thus the inversion rather degraded the velocity image during Stage 2. In contrast with the chequerboard tests, point scatterers down to 12 km are resolved since the reference model of the point-scatter test does not contain sharp velocity discontinuities. The retrieved values at the centre of the assigned point-scatterers are much smaller than for the acoustic test, indicating the degradation induced by P-SV convergence as seen in the chequerboard testing in Section 3.6.3.1. The point scatter test results above suggest that our waveform inversion was sensitive to velocity perturbation as small as a 250 m diameter in size, but that we may not be able to fully recover true velocity values for such small scatter.

## 3.7 Discussion and conclusions

Waveform tomography provided reliable and high-resolution P-wave velocity images of the mega-splay fault system in the central Nankai subduction zone. Our velocity image successfully delineated most of the previously identified geological features (e.g. the fore-arc basin, the mega-splay fault, and the plate boundary). Moreover waveform tomography delineated features not previously identified in the migration images of Moore et al. (2007, 2009): Substantial improvements were recognized for the structures underneath the outer ridge, and the inner wedge. Our results were extensively validated by a comparison of the de-trended velocity model with the 3D PSDM image from Moore et al. (2009) and Park et al. (2010), by a comparison of the synthetic time-domain waveforms and the observed waveforms, and by a scrutiny in the coherency of the source estimations. Using the checkerboard tests and point-scatter tests, we estimated that the waveform tomography image resolution is 0.7 km horizontally and 0.35 km vertically above the plate boundary fault, but we also concluded that the internal structures of the deeper oceanic crust were unresolvable due to the limit of the acoustic assumption.

In this section, we first discuss key inversion strategies for successful waveform tomography: 1) the data acquisition design, 2) the quality of the starting model, 3) the mitigation of non-linearity, and 4) the treatment of elastic data using the acoustic assumption. We then comment on our quality control tools.

### 3.7.1 Data acquisition

In crustal-scale refraction surveys, large explosive sources and large source-receiver offsets are typically employed to penetrate deep crustal structures. The resulting availability of low frequency signals and large offset data benefits waveform tomography by mitigating non-linearity, and by illuminating deep and long-wavelength velocity structures (Sirgue & Pratt, 2004). On the other hand, often the source or receiver intervals are sparse enough to induce subsampling artifacts in velocity images, and thus preclude achieving the theoretical resolution derived by Wu & Toksoz (1987).

In our OBS data set, the lowest frequency component available was 2.25 Hz, and the largest offset available was 55 km, which enabled us to retrieve velocity features above the top of the oceanic crust. The source and OBS intervals were 200 m and 1 km respectively. While these intervals are relatively dense in terms of crustal refraction surveys, the under-sampled OBS distribution required the use of carefully designed wavenumber filtering of the gradients.

Following Bleibinhaus et al. (2009), we define the measure of the sparsity for the

source distribution

$$N_{A_s} = \frac{\Delta_s}{\Delta_{N_y}}, \quad (3.32)$$

and for the receiver distribution

$$N_{A_r} = \frac{\Delta_r}{\Delta_{N_y}}, \quad (3.33)$$

where  $\Delta_s(\Delta_r)$  is the source (receiver) interval, and

$$\Delta_{N_y} = \frac{\pi c}{\omega}, \quad (3.34)$$

is the maximum unaliased interval for a velocity  $c$  (Takam Takougang & Calvert, 2011). A summary of  $\max(N_{A_s}, N_{A_r})$  for some past waveform inversion studies was given in Table 1 of Bleibinhaus et al. (2009) and Table 1 of Takam Takougang & Calvert (2011). In our study, the values of  $N_{A_r}$  are between 3 (2.25 Hz) and 11 (8.5 Hz), and the values of  $N_{A_s}$  are between 0.6 (2.25 Hz) and 2.7 (8.5 Hz), in the seawater, with  $c = c_{min} = 1.5$  km/s. These values are comparable to those from Operto et al. (2006), Brenders & Pratt (2007a), and Bleibinhaus et al. (2009). The condition  $N_{A_s} \leq 1$  indicates there is no aliasing in receiver gathers, and  $N_{A_s} \leq 1$  in source gathers. As  $N_{A_r} > 1$ , strong under-sampling artifacts were observed in raw gradients as shown in Fig. 3.8a, but reliable velocity structures were also retrieved in gradients thanks to the fact that  $N_{A_s} < 1$  for most of the inverted frequencies. In such a case, as demonstrated by Brenders & Pratt (2007b) and Bleibinhaus et al. (2007), a carefully designed low-pass wavenumber filter successfully eliminates most of the acquisition footprint and stabilizes waveform inversion, by sacrificing some resolution in the shallow sediments. As an alternative to wavenumber filtering, Malinowski et al. (2011) utilized a Gaussian filter with a characteristic length that varied depending on local velocity value, and Guitton & Díaz (2011) proposed a Laplace filter based on local dip of migration images, which can suppress features with geological dips that are inconsistent with the migration images. For our data set, the poor resolution of the PSDM image below the outer ridge and in the inner wedge may prevent the efficient design of such a dip filter.

Our OBS data presented challenges due to some of the instrument settings of the OBSs and the airgun arrays. We employed the vertical components of the OBS data due to the insufficient signal-to-noise ratios in the pressure components. Instead of converting to pressure components (as in Ravaut et al., 2004; Operto et al., 2006), we handled the discrepancies between vertical and pressure components i) by the AVO correction described in Section 3.4.2, and ii) by the source estimation step which generated a source wavelet suitable for the vertical component of the data. This is consistent with the

approach extensively tested by Brenders & Pratt (2007a) on elastic, vertical component, synthetic data.

Two types of A/D converters (24 bit and 16 bit) were used in the OBS survey, which caused the dynamic range to vary between OBSs. As described in Section 3.4.2, we normalized RMS amplitudes between OBS gathers to handle this problem. The source inversion results further suggested the different A/D converters may have had a 20 ms phase shift between them (Section 3.6.2.3). We did not estimate individual source wavelets for the two types of OBSs during the inversion, since a synthetic test (not shown) indicated little degradation would occur.

The untuned airgun array induced strong bubble reverberations in the observed waveforms, much of which could be mitigated during the preprocessing. Nevertheless, the pre-processed waveforms contained arrivals around 200 ms after the first break which are the remainders of the bubble effects. The source estimation process again played a critical role by including the extra reverberations.

### **3.7.2 Starting model and geological complexity**

Our starting model, the traveltimes tomography result of Nakanishi et al. (2008), was highly accurate, as demonstrated by the synthetic waveforms and the source inversion coherence discussed in Section 3.6.2.3. Furthermore the geological setting in the analyzed area is relatively simple when compared with other areas, such as the eastern Nankai subduction zone (Operto et al., 2006) or thrust-fold belts (Ravaut et al., 2004; Brenders, 2011). In our data set, the strong wide-angle reflection from the mega-splay fault was the dominant feature in the data, and our strategies could readily be evaluated with reference to this feature in the waveforms. The combination of an accurate starting model, and a clear waveform feature to focus on meant that it was relatively easy to evaluate the success of a wide variety of inversion strategies.

### **3.7.3 Hierarchical inversion strategies to mitigate non-linearity**

We implemented a hierarchical inversion strategy for waveform tomography, in which the inversion starts from an accurate traveltimes tomography result, then moves on to fitting the most linear components of the data, and gradually incorporates the more non-linear components. We proceeded by implementing a two-stage inversion using the Laplace-Fourier domain approach: We first minimized the logarithmic phase-only objective function to fit the kinematic portion of the seismic wavefields (Stage 1), and only then was the logarithmic phase-and-amplitude objective function used to fit both phase

and amplitude components (Stage 2). Within each stage, a multiscale, layer-stripping approach was adopted by selecting appropriate  $\omega$  and  $\tau$  schedules in the Laplace-Fourier domain waveform inversion. The multi-scale approach resulted in the recovery of large-scale and shallow structures in the early stages.

The phase-only inversion (Stage 1) retrieved much of the detailed velocity structure, and the dynamic component of the waveforms contributed to a final, limited improvement of the model (Stage 2). The results confirm that kinematic information is primarily sensitive to velocity perturbations as also suggested by Brenders (2011), and hence the kinematic inversion is rich in velocity information. Because the phase-only objective function ignores all trace-to-trace amplitude variations, the preprocessing of data amplitudes does not affect the phase-only inversion stage.

### 3.7.4 Acoustic waveform inversion of elastic field data

The acoustic assumption conventionally employed in waveform inversion and used in this study does not fully describe real-world elastic wave propagation. Thus, elastic effects, in particular P-SV converted waveforms and elastic AVO effects are not accounted for. However the waveform tomography P-wave velocity structure we obtained delineates the subsurface structure surprisingly well, including several sharp boundaries. This result confirms the acceptability of the acoustic assumption in inverting (elastic) real data (as also demonstrated by e.g., Ravaut et al., 2004; Brenders & Pratt, 2007a; Brenders, 2011; Takam Takougang & Calvert, 2011). The phase-only inversion during Stage 1 is an effective approach for reducing artifacts from elastic effects. For the phase-amplitude inversions of Stage 2, we compensated the elastic AVO effects by amplitude corrections.

In spite of the notable success of acoustic waveform tomography, the chequerboard tests and the point-scatter tests in Section 3.6.3 reveal some of the limitations of the acoustic assumption. The chequerboard tests show that the velocity structure is substantially degraded underneath the sharper discontinuities (the mega-splay fault and the plate boundary); in particular there is no visible structure inside the oceanic crust on the waveform tomography results. The point scatter tests also demonstrated the degradation of deeper scatterers when using the elastic wave data. These observations are consistent with the appearance of our final model, which also indicates a degradation underneath the mega-splay fault, and has a lack of visible structures in the oceanic crust (as described in Section 3.6.1). We suggest the failure of acoustic forward modelling to account for P-SV converted waveforms is the primary reason for these deficiencies. By using elastic waveform modelling code with these data in the future, P-wave velocity imaging should



be improved (as has been demonstrated through synthetic tests by Barnes et al. (2008) and Choi et al. (2008)).

### 3.7.5 Appraisal of results

One of most challenging themes in waveform tomography has been the validation of the resulting models. Waveform inversion results have historically been evaluated through:

- i A comparison of the synthetic waveforms with the observed data in the time domain (e.g., Ravaut et al., 2004; Brenders & Pratt, 2007a; Brenders, 2011) or in the frequency domain (Bleibinhaus et al., 2009; Brenders, 2011; Malinowski & Operto, 2008),
- ii An examination of the coherency in the source estimates (Gao et al., 2007; Smithyman et al., 2009; Malinowski et al., 2011),
- iii A consideration of the consistency of a velocity structure with past geological interpretations (e.g., Ravaut et al., 2004; Operto et al., 2006; Bleibinhaus et al., 2007; Brenders, 2011),
- iv A comparison of a velocity image with a reflection image, typically a migration images (e.g., Ravaut et al., 2004; Operto et al., 2006; Smithyman et al., 2009; Takam Takougang & Calvert, 2011),
- v A comparison of 1D vertical profiles with sonic log data (e.g., Ravaut et al., 2004; Malinowski et al., 2011; Takam Takougang & Calvert, 2011),
- vi Re-migration of the reflection seismic data (Sirgue et al., 2010; Plessix et al., 2012).

We have employed methods i) through iv), and thereby confirmed the reliability of the final waveform tomography velocity model (Section 3.6.2.1, 3.6.2.2, and 3.6.2.3). We were not able to evaluate the frequency-domain waveforms because of the spatial aliasing in the shot domain, which precluded a visual comparison as done by Malinowski & Operto (2008) and Brenders (2011). Although sonic log data were obtained along our line during the NanTroSEIZE project (indicated as C0002 in Fig. 2.2) (Screaton et al., 2009), the maximum depth was only 2 km from the sea floor. A comparison of just 40 grid points at shallow depths would not be particularly meaningful.

In this study we did not re-migrate the previous 2D or 3D reflection seismic data. The visual comparison of the PSDM image with our velocity model in Section 3.6.2.1 showed good agreement at most lithological boundaries. However we observed some discrepancies in the depths of the mega-splay fault at distances 33 - 44 km, and moreover using waveform tomography, we retrieved several structures not identified in the PSDM

image (most notably LVZ<sub>3</sub>, and structures inside the accretionary prism in the inner wedge). Large uncertainties in the MVA model suggest that the waveform tomography image may be the more reliable of the two. To further confirm the validity of the waveform tomography result, it will be useful to eventually remigrate the previous reflection data using the waveform tomography velocity model.

In addition to using the methods described above, we conducted checkerboard tests and point-scatter tests to illustrate the model resolution and the modelling error (Section 3.6.3). The elastic tests provided substantial insights into the realistic spatial resolution in the presence of modelization errors. The acoustic checkerboard tests, however, overestimated the resolving power, and indicated the limitations of the “inverse crime” (Colton & Kress, 1998; Wirgin, 2004) implied by these tests.

More complete resolution and uncertainty analysis can be carried out by estimating a resolution matrix or posterior model-covariance matrix (Tarantola, 2005). Although the computational cost of repeated forward modelling precludes this, Fichtner & Trampert (2011a,b) introduced a computationally efficient way of calculating the action of the Hessian matrix. Nevertheless, a rigorous uncertainty analysis would require methods from Bayesian inference, and a comprehensive sampling of the model space.

### 3.7.6 Conclusions

We successfully applied acoustic waveform tomography to the wide-angle OBS data acquired in the Nankai subduction zone. We illustrated waveform inversion is a challenging inverse problem, due to the non-linearity, the modelling errors, as well as the acquisition parameters for the wide-angle crustal surveys. We conclude that a six-fold set of strategies are key to our success: i) Availability of low-frequency components, and long-offset refraction arrivals to mitigate the non-linearity, and to increase the depth penetration, ii) a highly accurate starting model to mitigate the non-linearity, iii) the hierarchical inversion of phase-components first, and amplitude components later to reduce artifacts from the acoustic assumption, iv) A Laplace-Fourier domain approach that facilitates a multi-scale approach, v) careful preconditioning of the gradient to eliminate undesirable high-wavenumber components, and vi) a strategy for source estimation that reduces the influence of the acquisition design. The inversion parameters (choice of frequencies, decay constants, the number of iterations and so on) may depend on each specific inversion problem, however the strategies to choose parameters described in the thesis are generic.

## Acknowledgements

The authors thank the Institute For Research on Earth Evolution (IFREE) of the Japan Agency for Marine-Earth Science and Technology (JAMSTEC) for providing the OBS data, G. Moore for giving permission to access the migration volume, A. Nakanishi for providing the travelttime inversion result, Y. Kido for the help in data processing, J. O. A. Robertsson for providing his elastic finite difference program, F. Bleibinhaus for help conducting elastic waveform simulation, and A. Brenders and B. Smithyman for discussion of our waveform tomography results.

## References

- Abubakar, A., Li, M., Lin, Y., & Habashy, T. M., 2012. Compressed implicit Jacobian scheme for elastic full-waveform inversion, *Geophysical Journal International*, **189**(3), 1626–1634.
- Aki, K. & Richards, P. C., 1980. *Quantitative seismology*, W. H. Freeman & Co.
- Bangs, N. L. B., Moore, G. F., Gulick, S. P. S., Pangborn, E. M., Tobin, H. J., Kuramoto, S., & Taira, A., 2009. Broad, weak regions of the Nankai Megathrust and implications for shallow coseismic slip, *Earth and Planetary Science Letters*, **284**(1-2), 44–49.
- Barnes, C., Charara, M., & Tsuchiya, T., 2008. Feasibility study for an anisotropic full waveform inversion of cross-well seismic data, *Geophysical Prospecting*, **56**(6), 897–906.
- Bleibinhaus, F. & Rondenay, S., 2009. Effects of surface scattering in full-waveform inversion, *Geophysics*, **74**(6), WCC69–WCC77.
- Bleibinhaus, F., Hole, J. A., Ryberg, T., & Fuis, G. S., 2007. Structure of the California Coast Ranges and San Andreas Fault at SAFOD from seismic waveform inversion and reflection imaging, *Journal of Geophysical Research*, **112**, B0631.
- Bleibinhaus, F., Lester, R. W., & Hole, J. A., 2009. Applying waveform inversion to wide-angle seismic surveys, *Tectonophysics*, **472**(1-4), 238–248.
- Brenders, A. J., 2011. *Strategies For Waveform Tomography of Long-offset, 2-D Exploration Seismic Data*, Ph.D. thesis, University of Western Ontario.
- Brenders, A. J. & Pratt, R. G., 2007a. Full waveform tomography for lithospheric imaging: results from a blind test in a realistic crustal model, *Geophysical Journal International*, **168**(1), 133–151.
- Brenders, A. J. & Pratt, R. G., 2007b. Efficient waveform tomography for lithospheric imaging: implications for realistic, two-dimensional acquisition geometries and low-frequency data, *Geophysical Journal International*, **168**(1), 152–170.

- Brenders, A. J. & Pratt, R. G., 2007c. Waveform tomography of marine seismic data: What can limited offset offer?, *SEG Technical Program Expanded Abstracts*, **26**(1), 3024–3028.
- Brenders, A. J., Pratt, R. G., & Charles, S., 2010. Evaluation of preconditioning strategies on waveform tomography of field data: Success with long offset seismic data in a thrust-fold belt, *SEG Technical Program Expanded Abstracts*, **29**(1), 4348–4353.
- Brossier, R., Virieux, J., & Operto, S., 2008. Parsimonious finite-volume frequency-domain method for 2-D P-SV-wave modelling, *Geophysical Journal International*, **175**(2), 541–559.
- Brossier, R., Operto, S., & Virieux, J., 2009. Seismic imaging of complex onshore structures by 2D elastic frequency-domain full-waveform inversion, *Geophysics*, **74**(6), WCC105–WCC118.
- Brossier, R., Operto, S., & Virieux, J., 2010. Which data residual norm for robust elastic frequency-domain full waveform inversion?, *Geophysics*, **75**(3), R37–R46.
- Bunks, C., Saleck, F. M., Zaleski, S., & Chavent, G., 1995. Multiscale seismic waveform inversion, *Geophysics*, **60**(5), 1457–1473.
- Chen, J. & Schuster, G. T., 1999. Resolution limits of migrated images, *Geophysics*, **64**(4), 1046–1053.
- Choi, Y., Min, D.-J., & Shin, C., 2008. Two-dimensional waveform inversion of multi-component data in acoustic-elastic coupled media, *Geophysical Prospecting*, **56**(6), 863–881.
- Colton, D. & Kress, R., 1998. *Inverse Acoustic and Electromagnetic Scattering Theory*, Springer, Berlin.
- Dessa, J.-X., Operto, S., Kodaira, S., Nakanishi, A., Pascal, G., Uhira, K., & Kaneda, Y., 2004. Deep seismic imaging of the eastern Nankai trough, Japan, from multifold ocean bottom seismometer data by combined travel time tomography and prestack depth migrations, *Journal of Geophysical Research*, **109**, B02111.
- Fichtner, A. & Trampert, J., 2011a. Hessian kernels of seismic data functionals based upon adjoint techniques, *Geophysical Journal International*, **185**(2), 775–798.
- Fichtner, A. & Trampert, J., 2011b. Resolution analysis in full waveform inversion, *Geophysical Journal International*, **187**(3), 1604–1624.
- Fujie, G., Ito, A., Kodaira, S., Takahashi, N., & Kaneda, Y., 2006. Confirming sharp bending of the Pacific plate in the northern Japan trench subduction zone by applying a travelttime mapping method, *Physics of The Earth and Planetary Interiors*, **157**(1-2), 72–85.
- Gao, F., Levander, A., Pratt, R. G., Zelt, C. A., & Fradelizio, G.-L., 2007. Waveform

- tomography at a groundwater contamination site: Surface reflection data, *Geophysics*, **72**(5), G45–G55.
- Gardner, G. H. F., Gardner, L. W., & Gregory, A. R., 1974. Formation velocity and density —The diagnostic basics for stratigraphic traps, *Geophysics*, **39**(6), 770–780.
- Guillon, A. & Díaz, E., 2011. Attenuating crosstalk noise with simultaneous source full waveform inversion, *Geophysical Prospecting*, **60**(4), 759–768.
- Hicks, G. J. & Pratt, R. G., 2001. Reflection waveform inversion using local descent methods: Estimating attenuation and velocity over a gas-sand deposit, *Geophysics*, **66**(2), 598–612.
- Hustedt, B., Operto, S., & Virieux, J., 2004. Mixed-grid and staggered-grid finite-difference methods for frequency-domain acoustic wave modelling, *Geophysical Journal International*, **157**(3), 1269–1296.
- Jo, C.-H., Shin, C., & Suh, J. H., 1996. An optimal 9-point, finite-difference, frequency-space, 2-D scalar wave extrapolator, *Geophysics*, **61**(2), 529–537.
- Kamei, R., Pratt, R. G., & Tsuji, T., 2012. Waveform tomography imaging of a megasplay fault system in the seismogenic Nankai subduction zone, *Earth and Planetary Science Letters*, **317–318**, 343–353.
- Kodaira, S., Iidaka, T., Kato, A., Park, J.-O., Iwasaki, T., & Kaneda, Y., 2004. High pore fluid pressure may cause silent slip in the Nankai Trough, *Science*, **304**(5675), 1295–1298.
- Kosloff, D., 1996. Velocity and interface depth determination by tomography of depth migrated gathers, *Geophysics*, **61**(5), 1511–1523.
- Lailly, P., 1983. The seismic inverse problem as a sequence of before stack migrations, in *Conference on inverse scattering: theory and application*, pp. 206–220, SIAM, Soc. Industr. appl. Math., Philadelphia, PA.
- Levander, A. R., 1988. Fourth-order finite-difference P-SV seismograms, *Geophysics*, **53**(11), 1425–1436.
- Malinowski, M. & Operto, S., 2008. Quantitative imaging of the Permo-Mesozoic complex and its basement by frequency domain waveform tomography of wide-aperture seismic data from the Polish Basin, *Geophysical Prospecting*, **56**(6), 805–825.
- Malinowski, M., Operto, S., & Ribodetti, A., 2011. High-resolution seismic attenuation imaging from wide-aperture onshore data by visco-acoustic frequency-domain full-waveform inversion, *Geophysical Journal International*, **186**(3), 1179–1204.
- Mallick, S. & Frazer, L. N., 1987. Practical aspects of reflectivity modeling, *Geophysics*, **52**(10), 1355–1364.
- Métivier, L., Brossier, R. J., & Operto, S., 2012. Towards gauss-newton and exact newton

- optimization for full waveform inversion., *EAGE Conference & Exhibition incorporating SPE EUROPEC 2012 Copenhagen, Denmark, 4 - 7 June 2012*, p. P016.
- Moore, G. F., Taira, A., Klaus, A., Becker, L., Boeckel, B., Cragg, B. A., Dean, A., Ferguson, C. L., Henry, P., Hirano, S., Hisamitsu, T., Hunze, S., Kastner, M., Maltman, A. J., Morgan, J. K., Murakami, Y., Saffer, D. M., Snchez-Gmez, M., Sreaton, E. J., Smith, D. C., Spivack, A. J., Steurer, J., Tobin, H. J., Ujiie, K., Underwood, M. B., & Wilson, M., 2001. New insights into deformation and fluid flow processes in the Nankai Trough accretionary prism: Results of Ocean Drilling Program Leg 190, *Geochemistry Geophysics Geosystems*, **2**(10), 1058.
- Moore, G. F., Bangs, N. L., Taira, A., Kuramoto, S., Pangborn, E., & Tobin, H. J., 2007. Three-Dimensional Splay Fault Geometry and Implications for Tsunami Generation, *Science*, **318**(5853), 1128–1131.
- Moore, G. F., Park, J., Bangs, N. L., Gulick, S. P., Tobin, H. J., Nakamura, Y., Sato, S., Tsuji, T., Yoro, T., Tanaka, H., Uraki, S., Kido, Y., Sanada, Y., & Kuramoto, S., 2009. Structural and seismic stratigraphic framework of the NanTroSEIZE Stage 1 transect, in *Proc.IODP, 314/315/316*, vol. 314, Integrated Ocean Drilling Program Management International, Inc.
- Moore, G. F., Saffer, D., Studer, M., & Costa Pisani, P., 2011. Structural restoration of thrusts at the toe of the Nankai Trough accretionary prism off Shikoku Island, Japan: Implications for dewatering processes, *Geochemistry Geophysics Geosystems*, **12**(5), Q0AD12.
- Mora, P., 1989. Inversion = migration + tomography, *Geophysics*, **54**(12), 1575–1586.
- Mulder, W. A. & Plessix, R.-E., 2004. How to choose a subset of frequencies in frequency-domain finite-difference migration, *Geophysical Journal International*, **158**(3), 801–812.
- Nakanishi, A., Takahashi, N., Park, J.-O., Miura, S., Kodaira, S., Kaneda, Y., Hirata, N., Iwasaki, T., & Nakamura, M., 2002. Crustal structure across the coseismic rupture zone of the 1944 Tonankai earthquake, the central Nankai Trough seismogenic zone, *Journal of Geophysical Research*, **107**(B1), 2326.
- Nakanishi, A., Kodaira, S., Miura, S., Ito, A., Sato, T., Park, J.-O., Kido, Y., & Kaneda, Y., 2008. Detailed structural image around splay-fault branching in the Nankai subduction seismogenic zone: Results from a high-density ocean bottom seismic survey, *Journal of Geophysical Research*, **113**, B03105.
- Operto, S., Virieux, J., Dessa, J.-X., & Pascal, G., 2006. Crustal seismic imaging from multifold ocean bottom seismometer data by frequency domain full waveform tomography: Application to the eastern Nankai trough, *Journal of Geophysical Research*,

111, B09306.

- Park, J.-O., Tsuru, T., Kodaira, S., Cummins, P. R., & Kaneda, Y., 2002a. Splay Fault Branching Along the Nankai Subduction Zone, *Science*, **297**(5584), 1157–1160.
- Park, J.-O., Tsuru, T., Takahashi, N., Hori, T., Kodaira, S., Nakanishi, A., Miura, S., & Kaneda, Y., 2002b. A deep strong reflector in the Nankai accretionary wedge from multichannel seismic data: Implications for underplating and interseismic shear stress release, *Journal of Geophysical Research*, **107**(B4), 2061.
- Park, J.-O., Fujie, G., Wijerathne, L., Hori, T., Kodaira, S., Fukao, Y., Moore, G. F., Bangs, N. L., Kuramoto, S., & Taira, A., 2010. A low-velocity zone with weak reflectivity along the Nankai subduction zone, *Geology*, **38**(3), 283–286.
- Phinney, R. A., 1965. Theoretical Calculation of the Spectrum of First Arrivals in Layered Elastic Mediums, *Journal of Geophysical Research*, **70**(20), 5107–5123.
- Plessix, R.-E., Baeten, G., de Maag, J. W., ten Kroode, F., & Rujie, Z., 2012. Full waveform inversion and distance separated simultaneous sweeping: a study with a land seismic data set, *Geophysical Prospecting*, **60**(4), 733–747.
- Polak, E. & Ribière, G., 1969. Note sur la convergence de méthodes de directions conjuguées, *Revue Fr. Inf. Rech. Oper.*, **16-R1**, 35–43.
- Pratt, R. & Symes, W., 2002. Semblance and differential semblance optimisation for waveform tomography: a frequency domain implementation, in *Sub-basalt imaging*, *Journal of Conference Abstracts*, vol. 7, pp. 183–184.
- Pratt, R. G., 1990. Frequency-domain elastic wave modeling by finite differences: A tool for crosshole seismic imaging, *Geophysics*, **55**(5), 626–632.
- Pratt, R. G., 1999. Seismic waveform inversion in the frequency domain, Part 1: Theory and verification in a physical scale models, *Geophysics*, **64**(3), 888–901.
- Pratt, R. G., 2008. Waveform Tomography - Successes, cautionary tales, and future directions, *the 69th Conference and Exhibition of the EAGE, Rome, Italy (Workshop 11, "Full Waveform Inversion - Current Status and Perspectives"*.
- Pratt, R. G. & Worthington, M. H., 1988. The application of diffraction tomography to cross-hole seismic data, *Geophysics*, **53**(10), 1284–1294.
- Pratt, R. G. & Worthington, M. H., 1990. Inverse theory applied to multi-source cross-hole tomography. Part 1: Acoustic wave-equation method, *Geophysical Prospecting*, **38**(3), 287–310.
- Pratt, R. G., Song, Z.-M., Williamson, P., & Warner, M., 1996. Two-dimensional velocity models from wide-angle seismic data by wavefield inversion, *Geophysical Journal International*, **124**(2), 323–340.
- Pratt, R. G., Shin, C., & Hicks, G., 1998. Gauss-Newton and full Newton methods

- in frequency-space seismic waveform inversions, *Geophysical Journal International*, **133**(2), 341–362.
- Ravaut, C., Operto, S., Improta, L., Virieux, J., Herrero, A., & Dell’Aversana, P., 2004. Multiscale imaging of complex structures from multifold wide-aperture seismic data by frequency-domain full-waveform tomography: application to a thrust belt, *Geophysical Journal International*, **159**(3), 1032–1056.
- Robertsson, J. O. A., Blanch, J. O., & Symes, W. W., 1994. Viscoelastic finite-difference modeling, *Geophysics*, **59**(9), 1444–1456.
- Screaton, E., Kimura, G., Curewitz, D., & the Expedition 316 Scientists, 2009. Expedition 316 summary, in *Proc. IODP, 314/315/316*, Integrated Ocean Drilling Program Management International, Inc., Washington, DC.
- Sears, T. J., Barton, P. J., & Singh, S. C., 2010. Elastic full waveform inversion of multicomponent ocean-bottom cable seismic data: Application to Alba Field, U. K. North Sea, *Geophysics*, **75**(6), R109–R119.
- Sen, M. K. & Stoffa, P. L., 1991. Nonlinear one-dimensional seismic waveform inversion using simulated annealing, *Geophysics*, **56**(10), 1624–1638.
- Sen, M. K. & Stoffa, P. L., 1992. Rapid sampling of model space using genetic algorithms: examples from seismic waveform inversion, *Geophysical Journal International*, **108**(1), 281–292.
- Shin, C. & Cha, Y. H., 2008. Waveform inversion in the Laplace domain, *Geophysical Journal International*, **173**(3), 922–931.
- Shin, C. & Cha, Y. H., 2009. Waveform inversion in the Laplace-Fourier domains, *Geophysical Journal International*, **177**(3), 1067–1079.
- Shin, C. & Min, D.-J., 2006. Waveform inversion using a logarithmic wavefield, *Geophysics*, **71**(3), R31–R42.
- Shin, C., Pyun, S., & Bednar, J. B., 2007. Comparison of waveform inversion, Part 1: conventional wavefield vs logarithmic wavefield, *Geophysical Prospecting*, **55**(4), 449–464.
- Shin, C., Koo, N.-H., Cha, Y. H., & Park, K.-P., 2010. Sequentially ordered single-frequency 2-D acoustic waveform inversion in the Laplace-Fourier domains, *Geophysical Journal International*, **181**(2), 933–950.
- Shinohara, M., Suyehiro, K., Matsuda, S., & Ozawa, K., 1993. Digital recording ocean bottom seismometer using portable digital audio tape recorder, *Journal of the Japanese Society of Marine Survey and Technology*, **5**, 21–31.
- Shipp, R. M. & Singh, S. C., 2002. Two-dimensional full wavefield inversion of wide-aperture marine seismic streamer data, *Geophysical Journal International*, **151**(2),



325–344.

- Sirgue, L., 2003. *Inversion de la forme d'onde dans le domaine frequential de donnees sismiques grands offsets.*, Ph.D. thesis, l'Ecole Normale Superieure de Paris.
- Sirgue, L. & Pratt, R. G., 2004. Efficient waveform inversion and imaging: A strategy for selecting temporal frequencies, *Geophysics*, **69**(1), 231–248.
- Sirgue, L., Barkved, O. I., Dellinger, J., Etgen, J., Albertin, U., & Kommedal, J. H., 2010. Full waveform inversion : the next leap forward in imaging at Valhall, *First Break*, **28**, 65–70.
- Smithyman, B., Pratt, R. G., Hayles, J., & Wittebolle, R., 2009. Detecting near-surface objects with seismic waveform tomography, *Geophysics*, **74**(6), WCC119–WCC127.
- Snieder, R. & Lomax, A., 1996. Wavefield smoothing and the effect of rough velocity perturbations on arrival times and amplitudes, *Geophysical Journal International*, **125**(3), 796–812.
- Song, Z.-M., 1994. *Frequency domain wave equation crosshole modeling and inversion*, Ph.D. thesis, Imperial College of Science Technology and Medicine.
- Song, Z.-M., Williamson, P. R., & Pratt, R. G., 1995. Frequency-domain acoustic-wave modeling and inversion of crosshole data: Part II—Inversion method, synthetic experiments and real-data results, *Geophysics*, **60**(3), 796–809.
- Spetzler, J. & Snieder, R., 2004. The Fresnel volume and transmitted waves, *Geophysics*, **69**(3), 653 – 663.
- Stork, C., 1992. Reflection tomography in the postmigrated domain, *Geophysics*, **57**(5), 680–692.
- Takam Takougang, E. M. & Calvert, A. J., 2011. Application of waveform tomography to marine seismic reflection data from the Queen Charlotte Basin of western Canada, *Geophysics*, **76**(2), B55–B70.
- Tarantola, A., 1984. Inversion of seismic reflection data in the acoustic approximation, *Geophysics*, **49**(8), 1259–1266.
- Tarantola, A., 2005. *Inverse problem theory and methods for model parameter estimation*, Society of Industrial and Applied Mathematics, Philadelphia, 2nd edn.
- Tobin, H. J. & Kinoshita, M., 2006. NanTroSEIZE: the IODP Nankai Trough seismogenic zone experiment, *Scientific Drilling*, **2**(2), 23–27.
- Tromp, J., Tape, C., & Liu, Q., 2005. Seismic tomography, adjoint methods, time reversal and banana-doughnut kernels, *Geophysical Journal International*, **160**(1), 195–216.
- Williamson, P. R. & Worthington, M. H., 1993. Resolution limits in ray tomography due to wave behavior: Numerical experiments, *Geophysics*, **58**(5), 727–735.
- Wirgin, A., 2004. The inverse crime, *Arxiv preprint math-ph/0401050*, pp. 1–10.

- Woodward, M. J., Nichols, D., Zdraveva, O., Whitfield, P., & Johns, T., 2008. A decade of tomography, *Geophysics*, **73**(5), VE5–VE11.
- Wu, R.-S. & Toksoz, M. N., 1987. Diffraction tomography and multisource holography applied to seismic imaging, *Geophysics*, **52**(1), 11–25.
- Zelt, C. a. & Barton, P. J., 1998. Three-dimensional seismic refraction tomography: A comparison of two methods applied to data from the Faeroe Basin, *Geophysical Journal International*, **103**(B4), 7187–7210.
- Zelt, C. A. & Smith, R. B., 1992. Seismic travelttime inversion for 2-D crustal velocity structure, *Geophysical Journal International*, **108**(1), 16–34.
- Zeng, Y. Q., He, J. Q., & Liu, Q. H., 2001. The application of the perfectly matched layer in numerical modeling of wave propagation in poroelastic media, *Geophysics*, **66**(4), 1258–1266.
- Zhang, J. & Toksoz, M. N., 1998. Nonlinear refraction travelttime tomography, *Geophysics*, **63**(5), 1726–1737.

# Chapter 4

## On misfit functionals in waveform inversion, with application to wide-angle OBS data

A version of the chapter was submitted for publication to *Geophysical Prospecting* as: Kamei, R., Pratt, R.G., and Tsuji, T., “On misfit functionals in waveform inversion, with application to wide-angle OBS data”

### 4.1 Introduction

Waveform inversion methods have the potential to fully utilize seismic records, incorporating all wave types including P-wave, S-wave and surface waves. The emergence of waveform inversion began with Lailly (1983) and Tarantola (1984) who adopted numerical wave equation solutions, and developed innovative methods for calculating the gradient of the objective function. A complete solution to the waveform inversion problem would require a full exploration of elastic parameter model space to ultimately develop a probability distribution for elastic tensors (Tarantola, 1988). In exploration seismology, the inversion problem is typically reduced to a local optimization problem of determining P-wave velocity structure, using an acoustic implementation (Pratt & Shipp, 1999; Ravaut et al., 2004; Bleibinhaus et al., 2007; Kamei et al., 2012b).

The main difficulty encountered in waveform inversion is the strongly non-linear and non-unique nature of the inverse problem. Even when simply inverting for a P-wave velocity model, the problem of non-linearity and non-uniqueness forces us to carefully design inversion strategies that mitigate non-linearity. For example, the multi-scale method (Bunks et al., 1995; Sirgue & Pratt, 2004) is a hierarchical approach that is designed to

Table 4.1: List of mathematical symbols used in this chapter

Symbol	Type	Dimension	Description
$\mathbf{x}$	real		spatial location
$f$	real		frequency
$\omega$	real		angular frequency
$\Omega$	complex		complex angular frequency
$\tau$	real		characteristic time for exponential time-damping
$\sigma$	real		Laplace constant
$s$	complex		complex Laplace constant
$c$	complex		P-wave velocity
$\rho$	real		density
$Q$	real		quality factor
$N_d$	integer		number of data
$N_l$	integer		number of nodes in finite difference model
$N_m$	integer		total number of model parameters
$\mathbf{S}$	complex	$N_l \times N_l$	frequency-domain finite difference matrix
$\mathbf{f}$	complex	$N_l \times 1$	pressure source vector
$\mathbf{d}$	complex	$N_d \times 1$	observed data vector
$\mathbf{u}$	complex	$N_l \times 1$	predicted data vector
$A_d, \theta_d$	real		amplitude and phase of observed data
$A_u, \theta_u$	real		amplitude and phase of predicted data
$\mathbf{F}$	complex	$N_l \times N_m$	virtual source matrix
$\mathbf{w}$	complex	$N_d \times 1$	re-weighted residual vector
$\mathbf{m}$	complex	$N_m \times 1$	model parameter vector
$\mathbf{m}_o$	complex	$N_m \times 1$	starting model parameter vector
$\delta\mathbf{m}$	complex	$N_m \times 1$	update model parameter vector
$E(\mathbf{m}, \mathbf{m}_o; \mathbf{d})$	real		objective function
$\mathbf{J}$	complex	$N_m \times N_m$	Fréchet matrix of partial derivatives
$\alpha$	real		steplength
$\gamma$	real	$N_m \times 1$	conjugate gradient or steepest descent direction

approach the most linear and robust aspects of the problem first. Thus we begin the inversion with the smoothest model and shallowest model components, and sequentially increase both the model resolution, and the depth of illumination. This same strategy may be enforced in the data space by inverting i) from low-frequency components to high-frequency components (Pratt & Worthington, 1990; Sirgue, 2003; Shin et al., 2010), ii) from early direct arrivals to later scattered waveforms and reflection waveforms (Luo & Schuster, 1991; Sirgue, 2003; Shin et al., 2010), iii) from short offset refraction waveforms to large offset refraction waveforms (Sirgue, 2003; Brenders & Pratt, 2007). We may further mitigate non-linearity by phase and amplitude decomposition: For velocity imaging, kinematic (phase) information is relatively linear and robust when compared to amplitude information, pointing to a strategy that utilizes iv) phase information before using amplitude information.

Our implementation of the hierarchical approach starts with a decomposition of the model parameters and the data space into appropriate subsets, and determining the inversion order of the subsets in accordance with the degree of non-linearity. For each subset, we define a suitable misfit functional that restricts the topography of the objective function. We then select an appropriate data domain for waveform inversion. The data subsets can be a set of frequencies for frequency-domain inversion, a time window for time domain inversion, etc., and may be further refined by data preconditioning operations such as bandpass-filtering, time-windowing, time-damping and offset-weighting. The extracted data subsets implicitly specify a set of model subsets since different data components will be sensitive to different components of the model. Additionally, gradient preconditioning can further restrict the model space by adopting, for example, wavenumber filtering (Sirgue & Pratt, 2004), spatial weighting (Kamei et al., 2012b), or dip filtering (Guitton & Díaz, 2011).

Waveform misfit is conventionally defined using the  $L_2$  misfit functional (e.g. Tarantola, 1984; Pratt et al., 1998). More robust  $L_1$  norms, and mixed norms of  $L_1$  and  $L_2$  norms (such as Cauchy and Huber criterion) have been suggested to provide stable waveform inversion results when non-Gaussian data noise is present (Cruse et al., 1990; Shin & Ha, 2008; Brossier et al., 2010). Both  $L_1$  and  $L_2$  norms have been typically formulated using simple data residuals (i.e. subtraction of predicted data from observed data). This simple formulation has two main disadvantages: First, kinematic and dynamic information are inextricably mingled, and second the objective functions are highly weighted by data amplitudes. The amplitude effects can be mitigated by the preconditioning of model gradients based on a Hessian or approximate Hessian matrix (Ravaut et al., 2004; Shin & Min, 2006; Operto et al., 2006; Shin & Cha, 2009), or by data preconditioning to

compensate for offset dependencies (Zhou & Greenhalgh, 2003; Bleibinhaus et al., 2007; Brossier et al., 2009).

Alternatively, other definitions for data residuals can be utilized to suppress the over sensitivity to amplitude effects (Shin & Min, 2006; Leeuwen & Mulder, 2010). Shin & Min (2006) proposed logarithmic residuals, which decompose data residuals as logarithmic relative amplitude in the real part, and phase residual in the imaginary part of the residuals. They demonstrated a better conditioned topography of the misfit functional constructed from the logarithmic residuals when compared the functional constructed from the conventional residuals. Moreover the effects of the large dynamic range of seismic amplitudes are mitigated by the amplitude scaling implicit in the definition of the logarithmic residuals. Most importantly, it is trivial to construct the logarithmic phase-only misfit functional by extracting the imaginary part of the logarithmic residual, and also to construct the amplitude-only misfit functional by extracting the real part of the logarithmic residual (Shin & Min, 2006; Bednar et al., 2007; Pyun et al., 2007). Note that the phase-only logarithmic misfit functional is equivalent to the cross-correlation based misfit functionals advocated by Leeuwen & Mulder (2010) and Choi & Alkhalifah (2011).

In Shin & Min (2006), and a series of three papers in 2007 (Shin et al., 2007; Bednar et al., 2007; Pyun et al., 2007), Shin’s group examined the conventional and logarithmic residuals for each of phase-amplitude and phase-only, amplitude-only formulations using both synthetic and field data sets. From the synthetic tests, they concluded that the logarithmic residuals provided more reliable structures than the conventional definition of the residual. Between the three types of the logarithmic residuals, the logarithmic phase-amplitude and phase-only residuals yield comparative results, but the logarithmic phase-amplitude residuals are restricted in resolution. Unfortunately the superiority of logarithmic formulations were not clearly demonstrated in their the short-offset real data examples, and moreover the use of the pseudo Hessian as a gradient preconditioner make it difficult to carry out direct comparisons of the conventional and logarithmic residuals.

In this chapter, we seek optimal misfit functionals for the hierarchical inversion approach. We only consider the misfit functionals based on the  $L_2$  norm. We employ a wide-angle field data set, and evaluate four types of residuals; i.e. the conventional phase-amplitude, conventional phase-only, logarithmic phase-amplitude, and logarithmic phase-only residuals. We apply minimum preconditioning to the model gradient, and demonstrate the distinct performance of each of the residuals. Our results are largely in accordance with the results of Shin’s group. However we emphasize the importance of kinematic information for the building velocity model which is partially discussed in

Shin et al. (2007), and develop two-stage hierarchical waveform inversion, in which the phase information is inverted first, and the amplitude information is incorporated in the later stage. We advocate the Laplace-Fourier domain for waveform inversion (Shin & Cha, 2009), and use Ocean Bottom Seismograph (OBS) data from the seismogenic Nankai subduction zone following Chapter 2. A 2-D acoustic approximation is employed throughout our inversion tests.

### 4.1.1 Outline of the chapter

In Section 4.2 we review the theory of the Laplace-Fourier domain waveform inversion, and define four misfit functionals employed in this research. In Section 4.3, we introduce the OBS data from the Nankai subduction, and describe the general settings of waveform inversion. In Section 4.4 we conduct a series of inversion tests and compare the robustness and stability of misfit functionals. Finally we discuss our results, and provide conclusions in Section 4.5.

## 4.2 Theory

### 4.2.1 The Laplace-Fourier domain

Following Shin & Cha (2009), the complex Laplace transform of the time-domain wavefield  $u(\mathbf{x}; t)$  is

$$u(\mathbf{x}; s) = \int_0^{\infty} u(\mathbf{x}; t) \exp[-st] dt, \quad (4.1)$$

where  $s$  is the complex-valued Laplace parameter

$$s = \sigma + i\omega, \quad (4.2)$$

with a real-valued Laplace constant  $\sigma$  and a real-valued angular frequency,  $\omega$ . Consider a characteristic decay time

$$\tau = 1/\sigma, \quad (4.3)$$

and  $u(\mathbf{x}; t < 0) = 0$ , and then

$$u(\mathbf{x}; s) = \int_{-\infty}^{\infty} \left[ u(\mathbf{x}; t) \exp \left[ -\frac{t}{\tau} \right] \right] \exp [-i\omega t] dt, \quad (4.4)$$

$$= \int_{-\infty}^{\infty} u(\mathbf{x}; t) \exp [-i(\omega - i/\tau)t] dt, \quad (4.5)$$

$$= u(\mathbf{x}; \Omega), \quad (4.6)$$

is the complex-valued Fourier transform with

$$\Omega = \omega - i/\tau. \quad (4.7)$$

Eq.(4.4) is the Fourier domain wavefield at a complex-valued frequency  $\Omega = \omega - i/\tau$  (as in Phinney, 1965; Mallick & Frazer, 1987; Sirgue, 2003). The equivalence of the complex Laplace and Fourier transforms leads us to refer to  $u(\mathbf{x}; s) = u(\mathbf{x}; \sigma, \omega) = u(\mathbf{x}; \omega, \tau) = u(\mathbf{x}; \Omega)$  as the ‘‘Laplace-Fourier domain wavefield’’ following Shin & Cha (2009). Hereafter we use  $\Omega = \omega - i/\tau$  as our parametrization because of the intuitive connection of  $\omega$  and  $\tau$  to the physical quantities of frequency and decay time.

## 4.2.2 Forward modelling

The visco-acoustic wave equation in the Laplace-Fourier domain is

$$\nabla \left( \frac{1}{\rho(\mathbf{x})} \nabla u(\mathbf{x}; \Omega) \right) + \frac{\Omega^2}{\rho(\mathbf{x})c(\mathbf{x}; \omega)^2} u(\mathbf{x}; \Omega) = f(\mathbf{x}; \Omega), \quad (4.8)$$

where  $\rho(\mathbf{x})$  is the density,  $u(\mathbf{x}; \Omega)$  is the pressure field, and  $f(\mathbf{x}; \Omega)$  is the source term describing both the spatial distribution of the source(s), and the Laplace-Fourier component of the source time function. Attenuative media are implemented by utilizing a complex-valued velocity field  $c$  and introducing an appropriate dispersion relationship such as that found in Aki & Richards (1980) (as used by Song et al. (1995)).

A numerical solution of the wave equation in Eq.(4.8) for arbitrary velocity, density and attenuation distributions requires the discretization of the model. If we assume that the P-wave and density subsurface velocity may be described by a set of model parameters,  $\mathbf{m}$ , at  $N_m$  nodal points, Eq.(4.8) then leads to the matrix form

$$\mathbf{S}(\mathbf{m})\mathbf{u} = \mathbf{f}, \quad (4.9)$$

(Pratt et al., 1998), where  $\mathbf{u}$  represents the discrete solutions to the wave equation at  $N_l$



grid points,  $\mathbf{m}$  is the model parameter vector representing in discrete form the spatial distributions of velocity at  $N_l$  grid points, and  $\mathbf{f}$  represents the discrete distribution of source terms at  $N_l$  grid points. In this study we adopt the 2D finite difference approach for the matrix elements in Eq.(4.9) developed by Pratt & Worthington (1988) and Jo et al. (1996), but implemented the absorbing boundary condition using the perfectly matched layer method (Hustedt et al., 2004; Zeng et al., 2001). Note that Eq.(4.9) and all results below are dependent on the complex angular frequency,  $\Omega = \omega - i/\tau$ , but we shall omit the specific dependence unless required.

### 4.2.3 Optimization

As before we assume the subsurface is described by a set of model parameters,  $\mathbf{m}$ , at  $N_m$  nodal points. We now assume that observed data in the Laplace-Fourier domain,  $\mathbf{d}$ , are available at  $N_d$  points. We seek to iteratively update the model parameters to fit the set of data components using a local conjugate gradient optimization method, as this is one of most popular and computationally efficient methods for waveform inversion (e.g. (Song et al., 1995; Bleibinhaus et al., 2007; Brenders & Pratt, 2007)). . For simplicity, we assume that the only unknowns in the model are the seismic slowness (inverse of the seismic velocities); the density parameters are determined from the velocities using Gardner’s relationship (Gardner et al., 1974).

#### 4.2.3.1 Misfit functionals - four alternative definitions

We define a misfit functional  $E^l(\mathbf{d}, \mathbf{m})$  using the  $L_2$  norm such that

$$2E^l = \sum_{\omega} \delta \mathbf{d}^{lT} \delta \mathbf{d}^l, \quad (4.10)$$

where  $\delta \mathbf{d}^l$  is the residual vector, and superscript  $l = 1, \dots, 4$  indicates the four types of residuals we will examine in this chapter, and  $^T$  indicates the Hermitian of the vector. Note that we construct  $E^l(\mathbf{d}, \mathbf{m})$  from multiple frequency components, but only one decay constant. Conventionally the  $j$ th element of residual is defined simply as

$$\delta d_j^1 = u_j - d_j, \quad j = 1, \dots, N_d, \quad (4.11)$$

(Pratt et al., 1998) - this is the first of our four definitions for the residual. We call this the “conventional phase-amplitude residual”, and refer to the corresponding misfit

functional  $E^1$  as the conventional phase-amplitude misfit functional. Now denote

$$u_j = A_{u_j} \exp [i\theta_{u_j}], \quad (4.12)$$

$$d_j = A_{d_j} \exp [i\theta_{d_j}]. \quad (4.13)$$

Then from Eq.(4.11),

$$\delta d_j^1 = A_{u_j} \exp [i\theta_{u_j}] - A_{d_j} \exp [i\theta_{d_j}], \quad (4.14)$$

which illustrates that the magnitudes of the data residuals vary between traces depending on the data amplitudes errors, effectively weighting the inversions to emphasize large amplitudes in the data. In Laplace-Fourier waveform inversion, such amplitude effects are further exaggerated by the exponential decay function in Eq.(4.4), although we can compensate the latter effect following Brenders & Pratt (2007) by rescaling the residual as

$$\delta \hat{d}_j^1 = (u_j - d_j) \exp(\tau/t_o), \quad (4.15)$$

where  $t_o$  is the first arrival time.

We may normalize the trace-to-trace amplitude variations by

$$\delta d_j^2 = \frac{u_j}{|u_j|} - \frac{d_j}{|d_j|}, \quad (4.16)$$

$$= \exp [i\theta_{u_j}] - \exp [i\theta_{d_j}] \quad (4.17)$$

and we refer to this second alternative as the ‘‘conventional phase-only’’ residual (the second of our four definitions), and  $E^2$  as the corresponding conventional phase-only misfit functional. Note that Bednar et al. (2007) defined the phase-only residual, in a slightly different manner as

$$\delta d_j^{2'} = u_j - \frac{|u_j|}{|d_j|} d_j, \quad (4.18)$$

$$= A_{u_j} (\exp [i\theta_{u_j}] - \exp [i\theta_{d_j}]), \quad (4.19)$$

and thus their residual was still weighted with respect to the amplitude of the observed wavefields.

Shin & Min (2006) introduced the “logarithmic residual”,

$$\delta d_j^3 = \ln \left( \frac{u_j}{d_j} \right) \quad (4.20)$$

$$= \ln \left( \frac{A_{uj}}{A_{dj}} \right) + i (\theta_{uj} - \theta_{dj}), \quad (4.21)$$

(our third definition). We refer to  $E^3$  as the logarithmic phase-amplitude misfit functional. Eq.(4.17) was derived by assuming no cycle skipping between the observed and estimated data, i.e.  $|\theta_{uj} - \theta_{dj}| \leq \pi$ . This logarithmic phase-amplitude residual utilizes both amplitude and phase. However, amplitude and phase information is separated into the real and imaginary part of the residuals, and the scaling of amplitudes in the real part leads to a smaller influence arising from the dynamic range in seismic amplitudes. It is trivial to form a residual extracting phase-only information:

$$\delta d_j^4 = \Im \left[ \ln \left( \frac{u_j}{d_j} \right) \right] = (\theta_{uj} - \theta_{dj}) \quad (4.22)$$

after Bednar et al. (2007). We refer to the above definition as the “logarithmic phase-only residual”, and the corresponding misfit functional  $E^4$  as the logarithmic phase-only misfit functional; this is the fourth of our four definitions.

#### 4.2.3.2 Optimization algorithms

We adopt a local conjugate gradient method in which the model update with respect to the misfit functional  $E^l$  is

$$\delta \mathbf{m}^l = -\alpha^l \boldsymbol{\gamma}^l, \quad (4.23)$$

where  $\boldsymbol{\gamma}^l$  is the conjugate gradient direction. The steplength  $\alpha^l$  may be approximately computed by using a linear assumption (Pratt et al., 1998; Kamei et al., 2012a). The conjugate gradient direction is obtained by a linear combination of model gradients (Polak & Ribière, 1969). The model gradient  $\nabla_{\mathbf{m}} E^l$  itself is obtained by the adjoint method (Lailly, 1983; Tarantola, 1984; Pratt et al., 1998), so that the computationally expensive Fréchet kernel is not required in explicit form.

Following Pratt et al. (1998), the gradient of  $E$  takes the form

$$\nabla_{\mathbf{m}} E^l = \Re [\mathbf{F}^t \mathbf{S}^{-1} \mathbf{w}^{l*}], \quad (4.24)$$

where  $\mathbf{F}$  is a matrix containing the virtual sources for each model parameter,  $\mathbf{w}^l$  is the “re-weighted residual”, and  $*$  is the complex conjugate. Note that the virtual sources,  $\mathbf{F}$ ,

are independent of the definition of the residual, and the  $k$ -th column of  $\mathbf{F}$  is given by

$$\mathbf{F}_k = -\frac{\partial \mathbf{S}}{\partial m_k} \mathbf{u}. \quad (4.25)$$

The re-weighted residuals in Eq.(4.24),  $\mathbf{w}^l$ , however, depend on which of the definitions of the residuals given in the previous section is implemented. First, for the conventional phase-amplitude misfit functional

$$w_j^1 = \delta d_j^1; \quad (4.26)$$

second, for the conventional phase-only misfit functional

$$w_j^2 = \frac{-1}{2u_j} \left( \frac{u_j^*}{|u_j|} + \frac{d_j^*}{|d_j|} \right) \delta d_j^2; \quad (4.27)$$

third, for the logarithmic phase-amplitude misfit functional

$$w_j^3 = \frac{1}{u_j^*} \delta d_j^3; \quad (4.28)$$

and finally, for the logarithmic phase-only misfit functional

$$w_j^4 = \frac{i}{u_j} \delta d_j^4. \quad (4.29)$$

Bednar et al. (2007) formulated the gradient of  $E$  for the logarithmic phase-only residuals in a different form;

$$\nabla_{\mathbf{m}} E = \Im \left[ \mathbf{F}^t \mathbf{S}^{-1} \mathbf{w}^{4'} \right], \quad (4.30)$$

instead of Eq.(4.24), but it is trivial to show both definitions are equivalent, and

$$w_j^{4'} = -i w_j^4 = \frac{1}{u_j} \delta d_j^4, \quad (4.31)$$

which is Eq 20 in Bednar et al. (2007).

Each of these re-weighted residuals appears in Eq.(4.25) as the conjugate of a source term for the backpropagated wavefield  $\mathbf{v}^l = \mathbf{S}^{-1} \mathbf{w}^{l*}$ . For the conventional misfit functional  $E^1$ ,  $\mathbf{w}^1$  is the residual  $\delta \mathbf{d}^1$  itself, and the gradient  $\nabla_{\mathbf{m}} E^1$  is most sensitive only to the traces which have large amplitudes (i.e. the near-offset traces). This may lead to a poor subsurface illumination, and may make the inversion ill-conditioned. On contrary, the re-weighted residuals for  $E^{2,3,4}$  include a term  $u_j^{-1}$  or  $u_j^{*-1}$ . As the residuals are either independent ( $\delta \mathbf{d}^{2,4}$ ) or weakly dependent ( $\delta \mathbf{d}^3$ ) on the amplitude of waveforms,

$w^{2,3,4}$  will be larger for weak-amplitude traces (i.e. far-offset traces). This allows larger contribution to the gradient from these traces than when using the conventional misfit functional  $E^1$ , and thus improves the subsurface illumination naturally.

### 4.3 Waveform inversion of OBS data from the Nankai subduction zone

In Section 4.4 to follow, we present a series of waveform inversion tests to evaluate the robustness and stability of the four misfit functionals  $E^{1,\dots,4}$  defined in Section 4.2.3. We carried out these comparisons by forming and validating P-wave velocity images from Ocean Bottom Seismograph (OBS) data acquired in the central part of the Nankai subduction zone by the Japan Agency for Marine Earth Science and Technology (JAMSTEC) (Nakanishi et al., 2008; Kamei et al., 2012a,b). The analyzed area is characterized by an active large out-of-sequence thrust, known as a mega-splay fault (Tobin & Kinoshita, 2006). In Chapter 2 and 3, we successfully applied Laplace-Fourier waveform inversion to the OBS data, and obtained a high-resolution P-wave velocity model. In this chapter, we follow the approaches of Chapters 2 and 3 to preprocess the recorded OBS waveforms, and to select the basic parameters of Laplace-Fourier waveform inversion before carrying out our numerical tests. In this section, we briefly summarize below the acquisition and preprocessing of the OBS data, and the basic settings for Laplace-Fourier waveform inversion tests.

#### 4.3.1 Data acquisition and preprocessing

We performed all waveform inversion tests for a subsurface section 65 km wide and 15 km deep in the area of the active mega-splay. The area comprises 54 OBSs at 1 km spacing, with 285 air gun sources at 200 m spacing. We employed the vertical component records from the OBSs instead of the pressure component, due to the poor signal-to-noise ratio of the pressure components. The application of the vertical components is a plausible approximate approach for P-velocity imaging (Brenders & Pratt, 2007; Brossier et al., 2009), because our pressure sources were excited in acoustic environment (i.e. the ocean), and because P-wave energy dominates the early part of the vertical components of our OBS data.

We preprocessed the recorded OBS waveforms in order to enhance the signal to noise ratio, to suppress the bubble reverberation, and to eliminate late arrivals. Predictive deconvolution was performed in order to remove the bubble reverberation (Nakanishi et al.,

2008). An Ormsby minimum-phase bandpass filter was applied with corner frequencies of 0.1 - 2.5 - 8.0 - 8.5 Hz. Time windowing of 1.8 sec was applied to the waveforms beginning at the first arrivals in order to exclude early ambient noise, and late phases such as shear arrivals and multiples, inconsistent with the acoustic equation (note that we used absorbing boundary conditions rather than a free surface). We then normalized RMS amplitudes across each of the OBS gathers, in order to compensate for the different dynamic ranges and for any receiver coupling effects. The observed (elastic) amplitude versus offset (AVO) effects were then compensated to fit synthetic, acoustic AVO effects following the methodology described in Brenders & Pratt (2007). Finally, because the observed wavefields exhibit amplitude saturation at near offsets, traces of less than 5.0 km offset were eliminated from our waveform inversion.

### 4.3.2 Inversion settings

We inverted the preprocessed seismic waveforms using temporal frequencies from 2.25 to 8.5 Hz. The grid size,  $\Delta$ , was set to 50 m in order to avoid the numerical dispersion, and was consistent both in the forward modelling and during the optimization process. Since the number of sources ( $N_S = 258$ ) outnumbers the number of receivers ( $N_R = 54$ ), reciprocity was used in the forward wavefield calculation to save computational costs.

We employed the traveltimes tomography result of Nakanishi et al. (2008) shown in Fig. 4.1 as a starting model. The attenuation model was set at  $Q_p = 100$  beneath the sea floor, and  $Q_p = 10,000$  for the water layer; the  $Q_p$  model was kept constant during the inversion process. Density was computed from the velocity model at each iteration by applying Gardner’s relationship (Gardner et al., 1974). The source wavelet was updated after each iteration following the method described in Pratt (1999).

The subsurface structure exhibits a large dynamic range in velocity, from velocities of soft sediments, nearly 1.5 km/s at the sea bottom, to velocities of approximately 8 km/s within the Philippine Sea Plate. In order to visualize the local velocity change, we removed the dominant quasi one-dimensional trend from the images. This trend was defined by the 3rd order polynomial  $V_o(x, z) = a(z - z_0(x))^3 + b(z - z_0(x))^2 + c(z - z_0) + d$  which best fit the 2D traveltimes tomography result, and where  $z_0(x)$  is the depth of a sea floor. The de-trended velocity image was then defined by  $\Delta V(x, z) = V(x, z) - V_o(x, z)$ . The resultant “de-trended”, or “residual” velocity structure is shown in Fig. 4.1b in colour and Fig. 4.1c in grey. The traveltimes tomography image indicates the existence of low velocity zones, but the lithology boundaries are not obvious, due to the well understood limitations of the asymptotic assumption of the ray theory requires

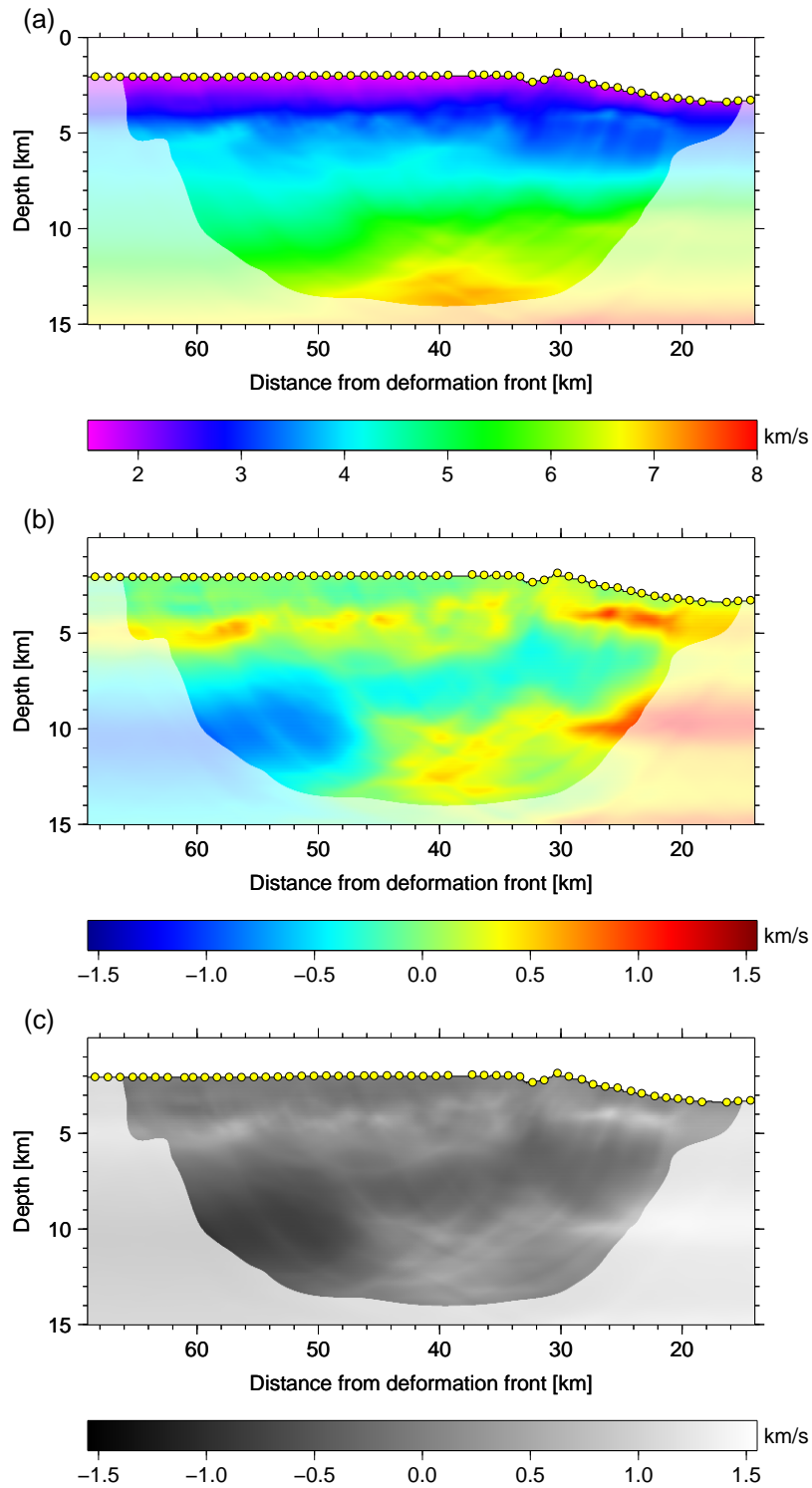


Figure 4.1: (a) Traveltime tomography result of Nakanishi et al. (2008), also used as a starting model for our waveform inversion, (b) de-trended model of (a) in colour, and (c) de-trended model of (a) in grey scale. The horizontal axis is the distance from the deformation front. Yellow circles show the location of the OBS instruments.

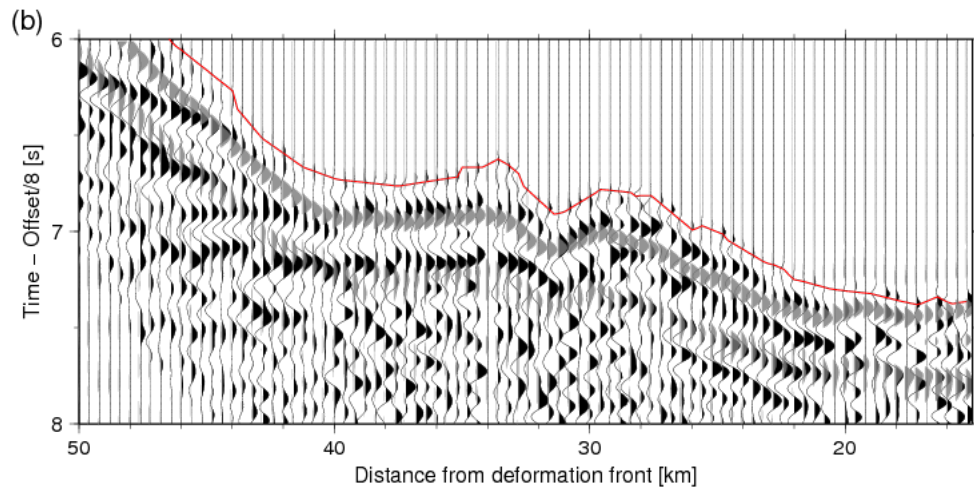
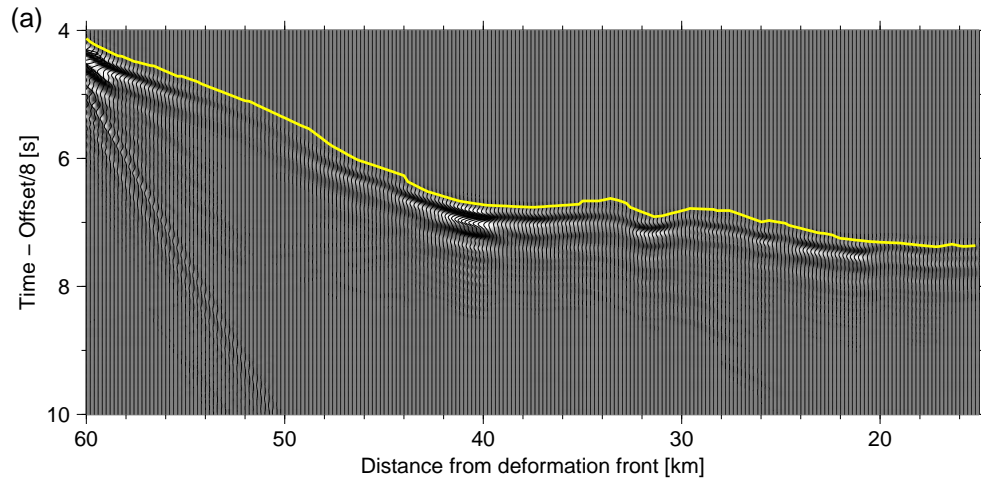


Figure 4.2: (a) Synthetic OBS gather of OBS 47 at distance 65 km, computed from the starting model by a visco-acoustic forward modelling code. (b) Overlay of (a) in grey on the observed OBS gather in black. Picked first arrivals from the comparable real data are shown (a) in yellow, and (b) in red.



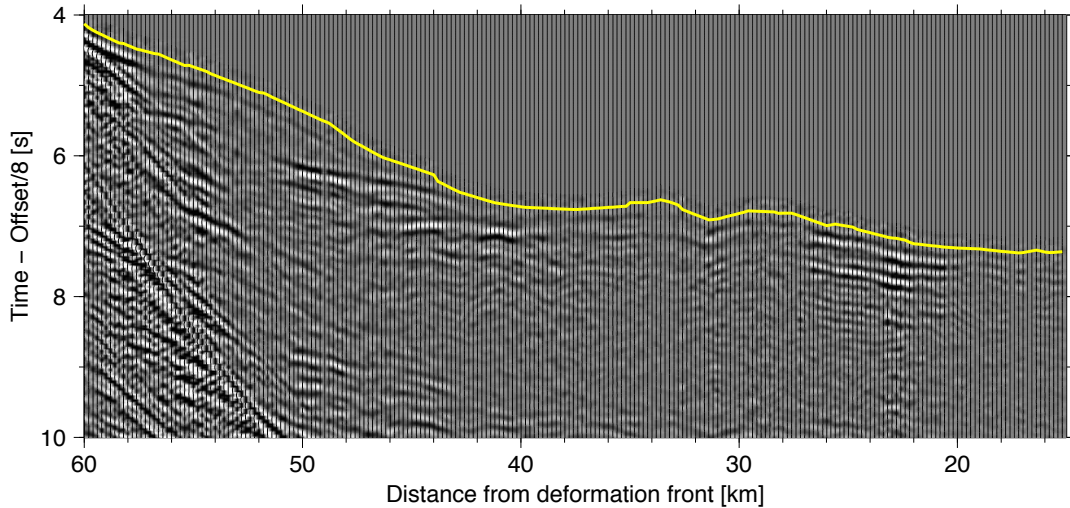


Figure 4.3: Representative vertical component seismic waveforms recorded at the OBS 47 located 65 km landward of the deformation front (Nakanishi et al., 2002). All data preprocessing was applied except for bottom muting. The yellow line indicates the picked first arrivals.

a smooth velocity model. Synthetic waveforms computed from the model (Fig. 4.2) show good agreement in the appearances of the first arrivals when compared to the observed wavefields displayed in Fig. 4.3, demonstrating the accuracy of the traveltime tomography velocity model. However the simulated waveforms show some discrepancies in phase at distances between 20 km and 40 km, and lack the wide-angle reflections from the megasplay fault, indicating a potential for improvement in both low- and high-wavenumber components of the subsurface image.

We used 12 groups of frequencies between 2.25 and 8.5 Hz, and 7 values of the damping constants,  $\tau$ . Each frequency group consists of 4 frequencies in 0.25 Hz interval, allowing two of the frequencies to overlap between the two consecutive groups to stabilize the inversion (e.g. the first two groups are [2.25, 2.5, 2.75, 3.0] Hz and [2.75, 3.0, 3.25, 3.5] Hz). We selected  $\tau = 0.167, 0.2, 0.25, 0.333, 0.5, 1.0, 2.0$  sec, correspondingly  $s = 6, 5, 4, 3, 2, 1, 0.5 \text{ sec}^{-1}$ . At  $\tau = 0.167$  sec, the damped wavefields are almost completely limited to the first arrivals, but any ambient noise between the arrival picks and the actual arrivals becomes amplified.

For each  $\tau - \omega$  set, we iteratively updated the velocity model five times using the optimization method described in Section 4.2.3. The model gradient was preconditioned by using a wavenumber filter (Sirgue & Pratt, 2004) and by masking changes in the ocean, in order to remove unacceptable high-wavenumber oscillations and to reduce the

artifacts arising from the sparsity in the OBS domain. The cut-off wavenumber for the wavenumber filter was selected to be the inverse of a wavelength for the horizontal direction, and the inverse of a half-wavelength for the vertical direction at a P-wave velocity value of 4 km/s.

## 4.4 Results

In Section 4.2.3, we defined four types of misfit functionals such as the conventional phase-amplitude misfit functional ( $E^1$ ) in Eq.(4.11), the conventional phase-only misfit functional ( $E^2$ ) in Eq.(4.16), the logarithmic phase-amplitude misfit functional ( $E^3$ ) in Eq.(4.20), and the logarithmic phase-only misfit functional ( $E^4$ ) in Eq.(4.22). In this section, we first evaluate these four misfit functionals by means of a qualitative examination of raw gradient images (Section 4.4.1), and the scrutiny of inverted velocity models (Section 4.4.2). We then investigate the significance of amplitude information on velocity imaging in Section 4.4.3.

### 4.4.1 Gradient images

The success and efficiency of gradient-based optimizations especially depend on the quality of a model gradient at early iterations. Although various preconditioning techniques are available to improve the quality of the gradient, it is informative to examine raw gradients.

In Fig. 4.4 we display the gradients from the starting model obtained for the proposed four misfit functionals. These images represent the gradient computed with the lowest frequency set ([2.25, 2.50, 2.75, 3.00] Hz), and with a decay constant of  $\tau = 0.333$  sec. The decay constant was the smallest time available for the conventional misfit  $E^1$ , since a decay constant less than 0.333 sec (i.e. 0.167 sec) does not illuminate an area beneath the sea floor.

The gradient from the conventional phase-amplitude misfit functional  $E^1$  is restricted in illumination to the shallowest 2 km from the sea floor (Fig. 4.4a), whereas the logarithmic phase-amplitude misfit  $E^3$  extends in illumination down to at least 12 km from the sea surface (Fig. 4.4b). The conventional and logarithmic phase-only misfit functionals  $E^2$  and  $E^4$  retrieve the deepest illuminations, extending close to 15 km from the sea surface (Fig. 4.4c and d).

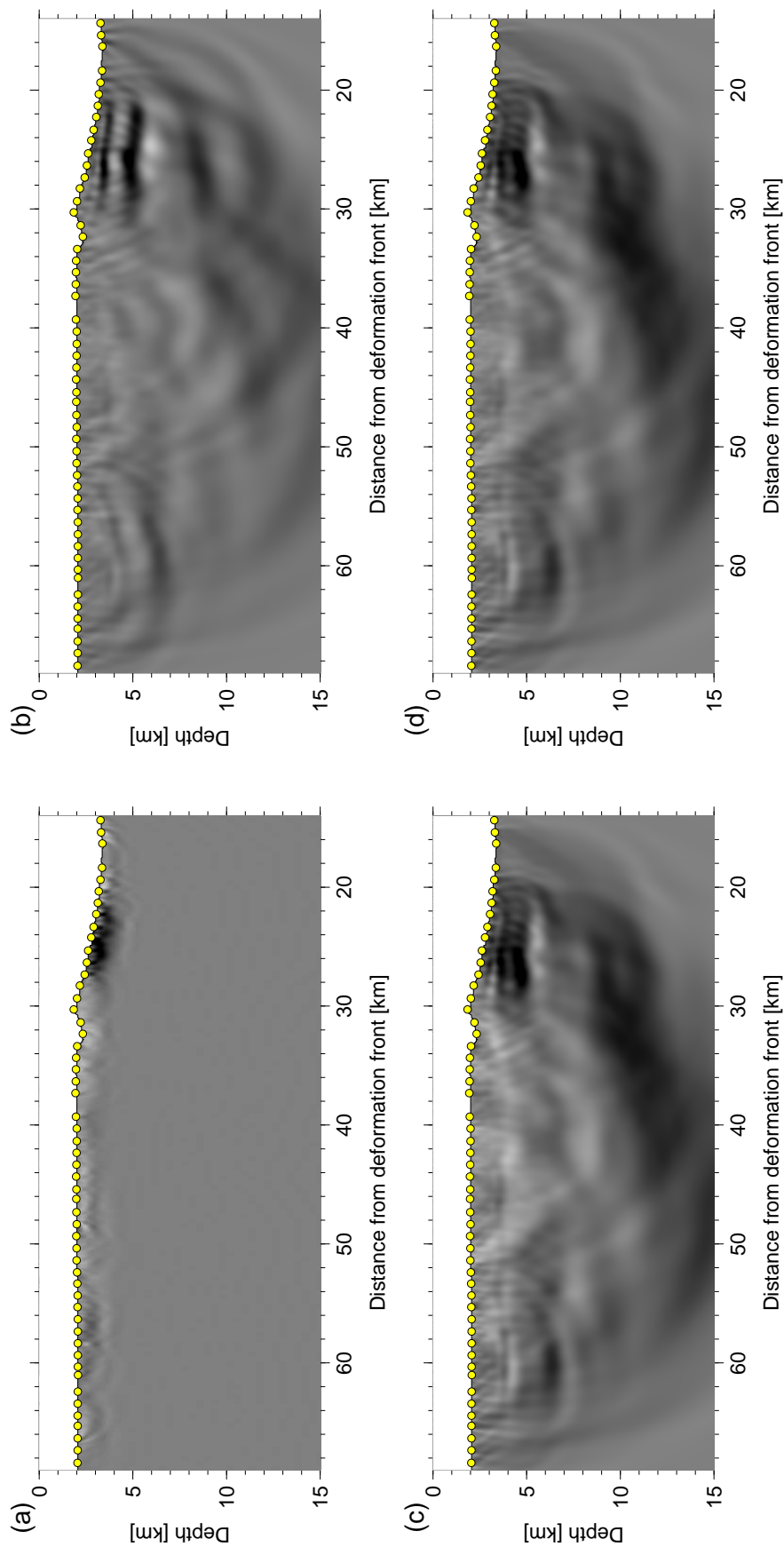


Figure 4.4: Gradient images at a frequency set of 2.25, 2.50, 2.75 and 3.0 Hz, and  $\tau = 0.333$  sec obtained using as the objective function, (a) the conventional phase-amplitude misfit functional  $E^1$ , (b) the logarithmic phase-amplitude misfit functional  $E^3$ , (c) the conventional phase-only misfit functional  $E^2$ , and (d) the logarithmic phase-only misfit functional  $E^4$ .

## 4.4.2 Comparison of velocity images

We conducted four waveform inversion tests. In each test, we employed one of the four misfit functionals as an objective function, and formed a P-wave velocity model. As suggested in Section 4.4.1, the minimum useful decay constant is  $\tau = 0.333$  sec for the conventional misfit functional. Thus we carried out the conventional and logarithmic phase-amplitude inversion by using 4 decay constants between 0.333 and 2.0 sec. However the logarithmic and conventional phase-only inversion was conducted by using all 7 decay constants between 0.167 and 2.0 sec. All four waveform inversion tests showed a good convergence in the objective functions, achieving about 5-10 % reduction for each  $\omega - \tau$  set.

### 4.4.2.1 Velocity images

We display the resulting de-trended velocity models from the four tests in Fig. 4.5 in colour and in Fig. 4.6 in grey-scale. Fig. 4.7 represents the de-trended velocity model from the logarithmic phase-only misfit functional  $E^4$  overlain by the geological interpretation modified from Fig. 3.12 presented in Chapter 3. The interpretation was guided by the pre stack migration image of Moore et al. (2009) (shown in Fig. 3.13). A series of 1D vertical profiles from the de-trended velocity models are shown in Fig. 4.8.

The conventional phase-amplitude inversion (minimizing  $E^1$ ) retrieves features to a maximum depth of approximately 10 km (Figs 4.5a and 4.6a). The long wavelength structure are altered from the starting model at depths shallower than 6 km, while high-wavenumber components are changed both above and below 6 km depth (e.g. and part of the mega-splay fault). In the shallower part, the conventional phase-amplitude inversion succeeds in characterizing the base of the fore-arc basin, and its internal structures. However high-wavenumber oscillations contaminate the area shallower 5 km throughout the model, (most obvious in the grey-scale de-trended model in Fig. 4.6a). Part of the mega-splay fault is visible as a mild velocity reduction ( $< 500$  m/s) at distances between 35 km and 50 km, although the continuity of the fault is not imaged clearly. The low velocity zone is depicted at distances between 30 km and 45 km above 10 km depths, while the changes from the travelttime homograph result is only evident above 6 km depths. The landward portion of the low velocity zone (LVZ<sub>1</sub>) is bounded at the top by the mega-splay fault (LVZ<sub>1</sub>), and contains many small fragmentary reflectors. The seaward portion of the low velocity zone (LVZ<sub>2</sub>) is clearly characterized by a sharp top boundary, but the bottom is ambiguous. P-wave velocities in a layer above LVZ<sub>2</sub> (area D) is 1.5 km/s higher than the background velocity trend.

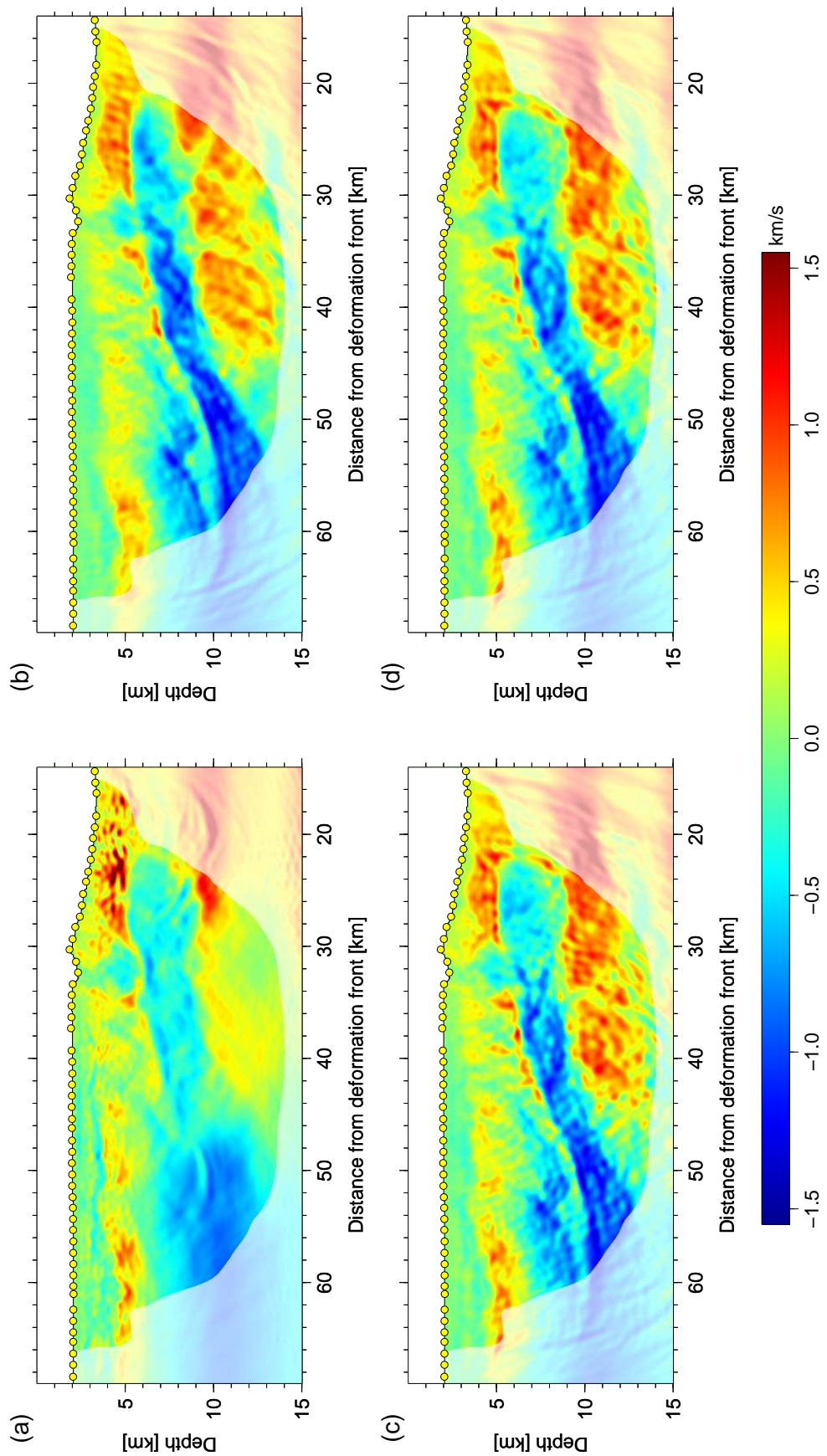


Figure 4.5: De-trended velocity models in colour obtained by (a) the conventional phase-amplitude inversion  $E^1$  ( $\tau \geq 0.333$  sec), (b) the logarithmic phase-amplitude inversion  $E^3$  ( $\tau \geq 0.333$  sec), (c) the conventional phase-only inversion  $E^2$  ( $\tau \geq 0.167$  sec), and (d) the logarithmic phase-only inversion  $E^4$  ( $\tau \geq 0.167$  sec).

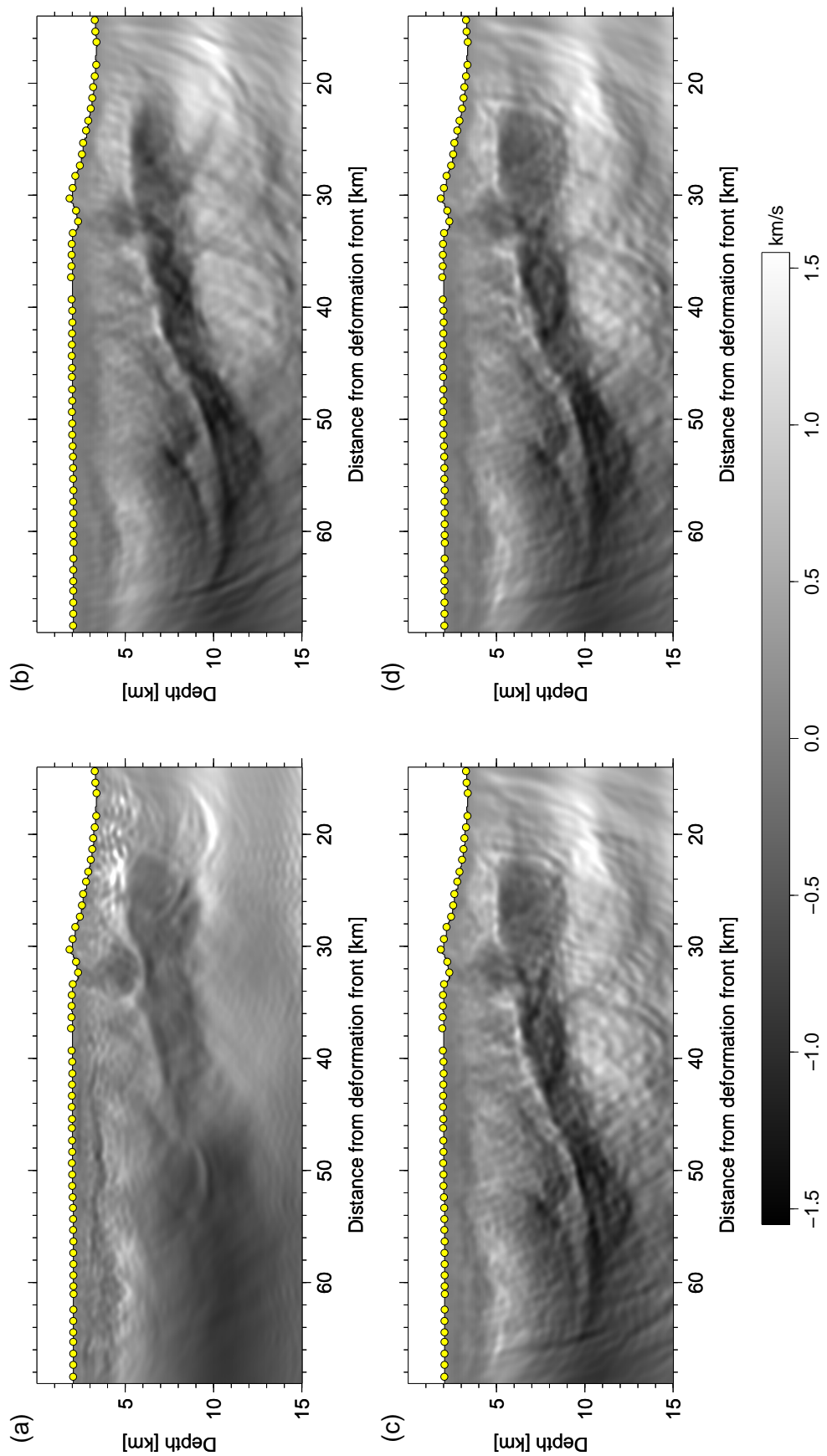


Figure 4.6: De-trended velocity models of Fig. 4.5 in grey-scale obtained by (a) the conventional phase-amplitude inversion  $E^1$  ( $\tau \geq 0.333$  sec), (b) the logarithmic phase-amplitude inversion  $E^3$  ( $\tau \geq 0.333$  sec), (c) the conventional phase-only inversion  $E^2$  ( $\tau \geq 0.167$  sec), and (d) the logarithmic phase-only inversion  $E^4$  ( $\tau \geq 0.167$  sec).

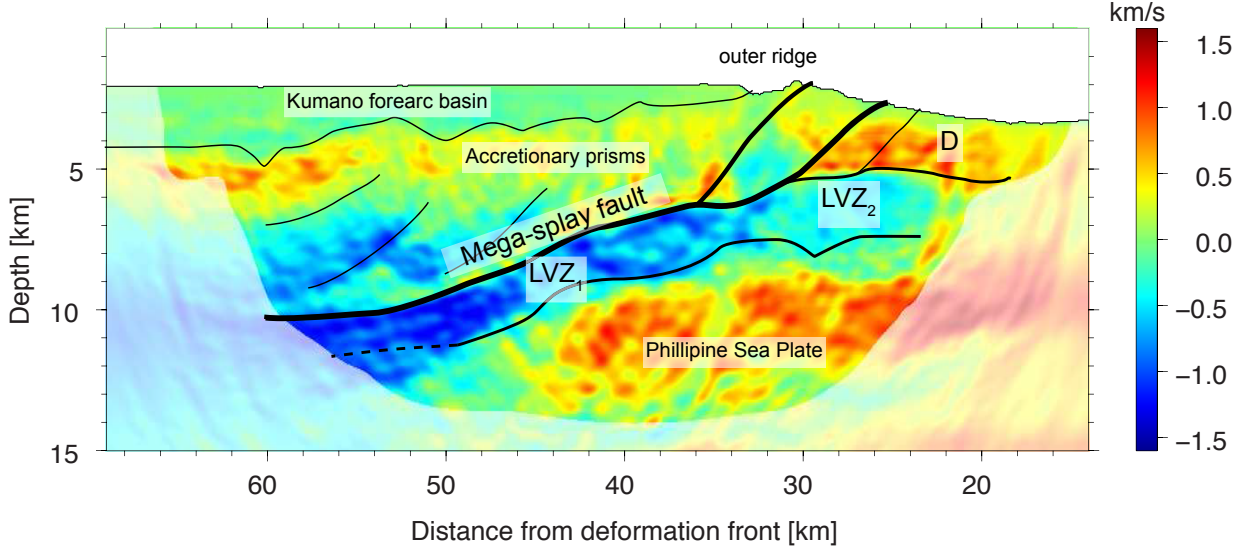


Figure 4.7: Geological interpretation overlaying the de-trended velocity model in Fig. 4.5c. The mega-splay fault and its branches are shown with thick black lines. The low velocity zones are labelled LVZ<sub>1</sub> (landward), and LVZ<sub>2</sub> (seaward). Area D indicates a seaward accretionary prism, exhibiting higher velocity values with respect to the  $V_o(z)$  trend.

The other three misfit functionals  $E^{2-4}$  retrieved detailed velocity structures down to 12 km with a clear delineation of lithology boundaries including the fore-arc basin, the plate boundaries, and the mega-splay fault (Figs 4.5b-d and 4.6b-d). The discrepancies between the three models are small. The oscillatory artifacts in the shallow area are significantly suppressed, in comparison with the conventional phase-amplitude inversion. In all three images, the mega-splay fault is identified as a sharp velocity reduction (of about 1 km/s) at distances between 33 km and 55 km, and splits into two branches in the shallower subsurface at a distance of 33 km, and depths of 6.5 km. LVZ<sub>1</sub> is well defined by the mega-splay fault at the top, and the plate boundary at the bottom. LVZ<sub>2</sub> is also clearly resolved at distances between 33 km and 20 km, and apparently connected to LVZ<sub>1</sub>. The seaward termination of LVZ<sub>2</sub> is ambiguous due to the limited wavepath coverage. The logarithmic phase-amplitude inversion delineated the top of LVZ<sub>2</sub> 300 m deeper and the bottom of LVZ<sub>2</sub> 500 m shallower than the phase-only inversions. As in the conventional phase-amplitude inversion, LVZ<sub>2</sub> for the phase-only results is overlain by a layer (area D) whose velocity is higher than the background trend, but the velocity contrasts are approximately 1 km/s, i.e. only two-thirds of the values obtained by the conventional phase-amplitude inversion.

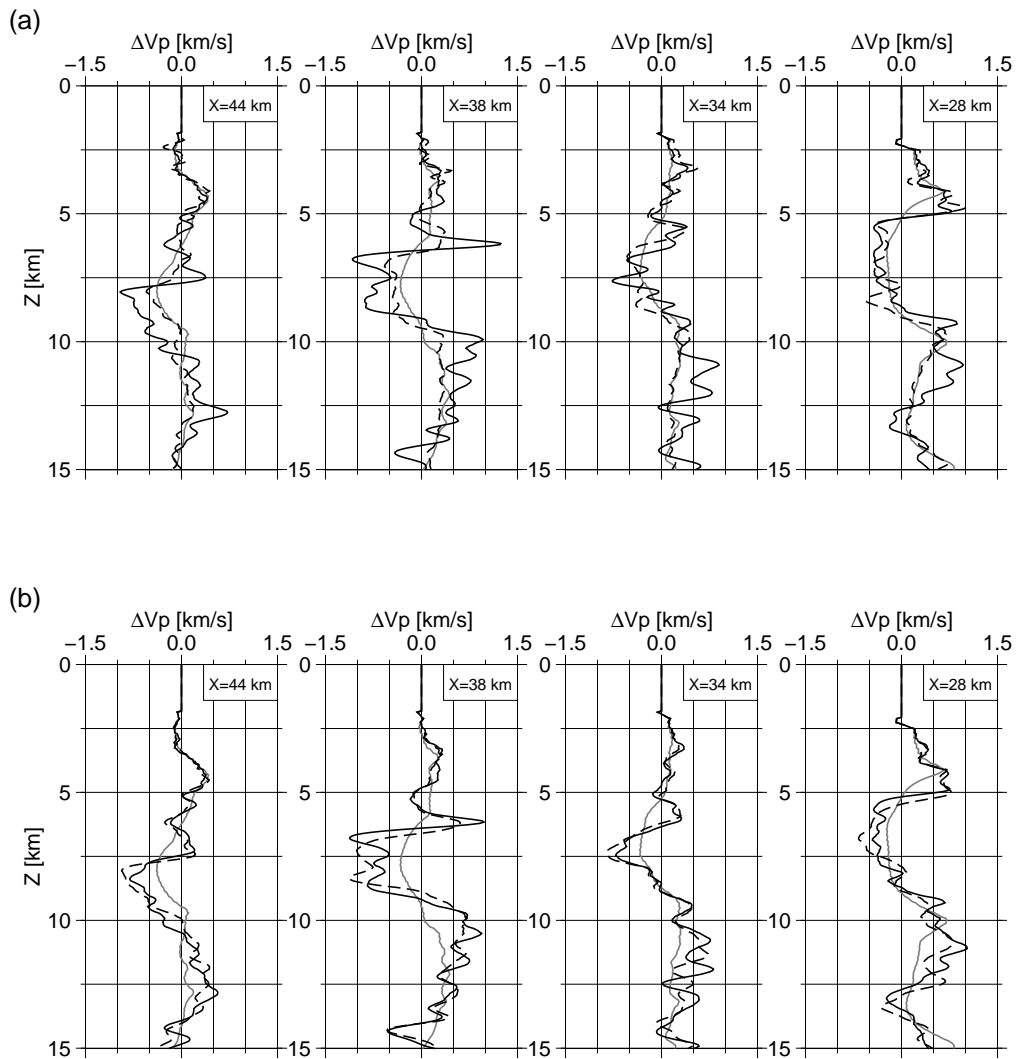


Figure 4.8: Vertical de-trended velocity profiles of Fig. 4.5 at distances 44, 38, 34, 28 km (from left to right). (a) The dashed black lines indicate the inversion results obtained by  $E^1$ , and the solid black lines by  $E^2$ , (b) the dashed black lines by  $E^3$ , and the solid black lines by  $E^4$ . In both (a) and (b), and solid grey lines the starting model.



#### 4.4.2.2 Synthetic waveforms

In order to further evaluate the four waveform inversion test results obtained in Section 4.4.2.1, we generated synthetic waveforms from each final velocity model by using the visco-acoustic finite-difference code described in Section 4.2.2, and compared the results with the observed waveforms. We show the observed waveforms at OBS 47 in Fig. 4.3, and the synthetic waveforms at the same OBS from the inverted velocity models in Fig. 4.9. In Fig. 4.10, we also display overlays of the same synthetic waveforms and the observed waveforms in order to examine waveform fits in detail.

The synthetic waveforms from the conventional phase-amplitude inversion results ( $E^1$ ) appear to show less agreement with the observed waveforms (Figs 4.9a and 4.10a) than those from the other velocity model obtained by  $E^{2-4}$ . The wide-angle reflection from the mega-splay fault is partially reproduced at distances between 45 km and 50 km, but is not delineated entirely; this corresponds to the discontinuity in the mega-splay fault in the velocity model shown in Fig. 4.5a. The predicted arrivals at large offsets show little improvements over those computed from the starting model shown in Fig. 4.2: The phase delay is still evident at distances between 8 km and 24 km, and indicates too slow velocities in the deeper part of the model. Moreover the refracted waveforms at distances less than 30 km are contaminated by small non-physical diffractions, which are probably induced by the oscillations in the velocity model.

The other inversion tests reproduced the characteristics of the observed waveforms significantly better than the conventional phase-amplitude inversion, as displayed in Fig. 4.9b-d, and in Fig. 4.10b-d. The first arrival refractions are in-phase with the observed wavefields at distances between 15 km and 40 km, although still slightly delayed. The wide-angle reflections at distances between 40 km and 55 km coincide well with the observed wavefields.

#### 4.4.2.3 Reduction of misfits during the inversion

We now examine the cumulative misfit functional

$$E_{total}^l = \sum_{f=2.5Hz}^{8.5Hz} \delta \mathbf{d}^{lT} \delta \mathbf{d}^l, \quad (4.32)$$

using all four definitions of data residuals in Section 4.2.3, in order to quantitatively evaluate the reliability of the waveform inversion results. For the purpose of these computations, we selected  $\tau = 2.8$  sec so that we can measure data fits over a large window of P-wave arrivals, and calculated the cumulative misfit functionals after each  $\omega - \tau$  set.

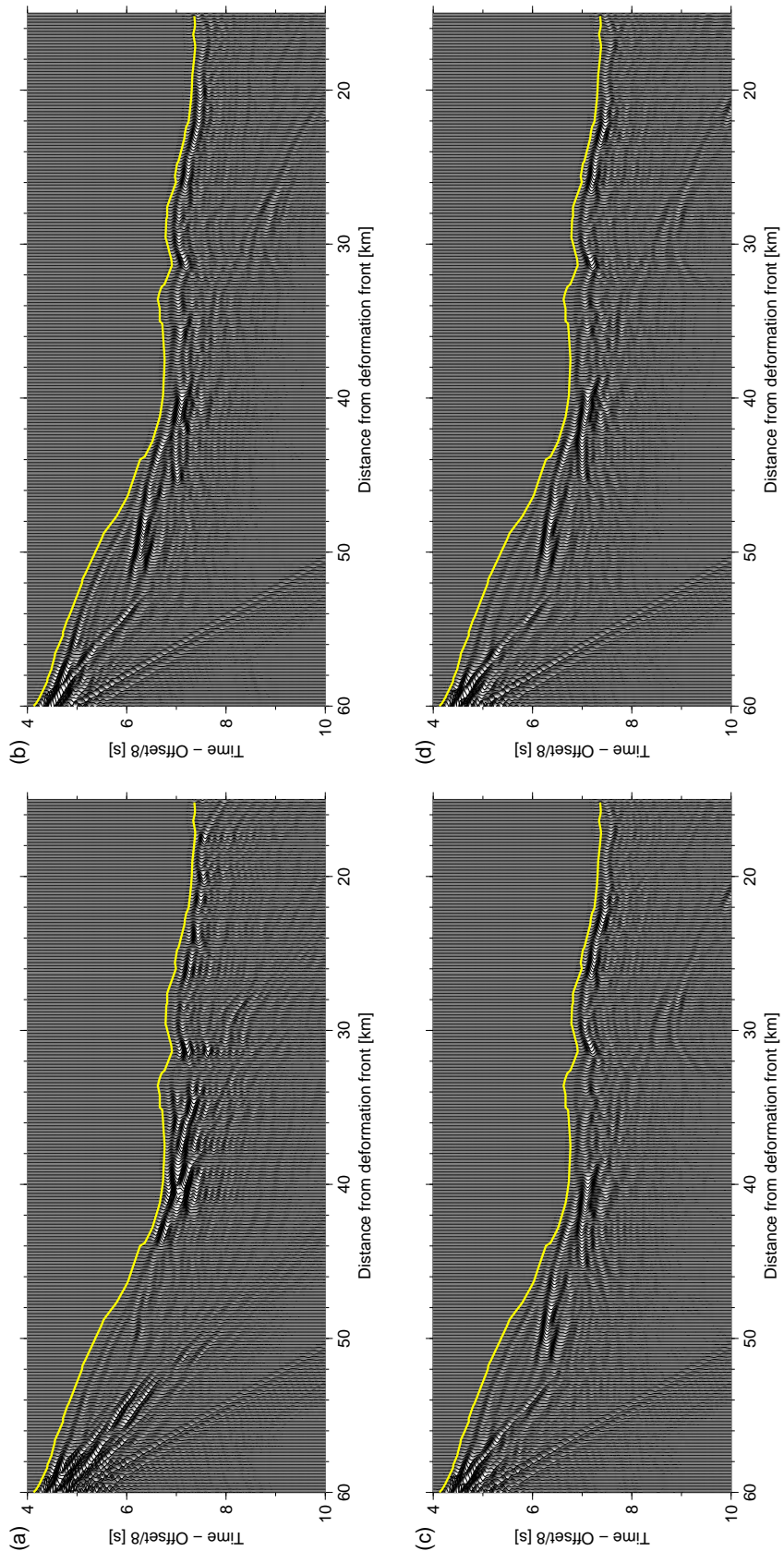


Figure 4.9: Predicted pressure wavefields at the OBS 47, computed from the velocity models shown in Fig. 4.5 retrieved by (a)  $E^1$ , (b)  $E^3$ , (c)  $E^2$ , and (d)  $E^4$ . The yellow curves indicate the picked first arrivals.

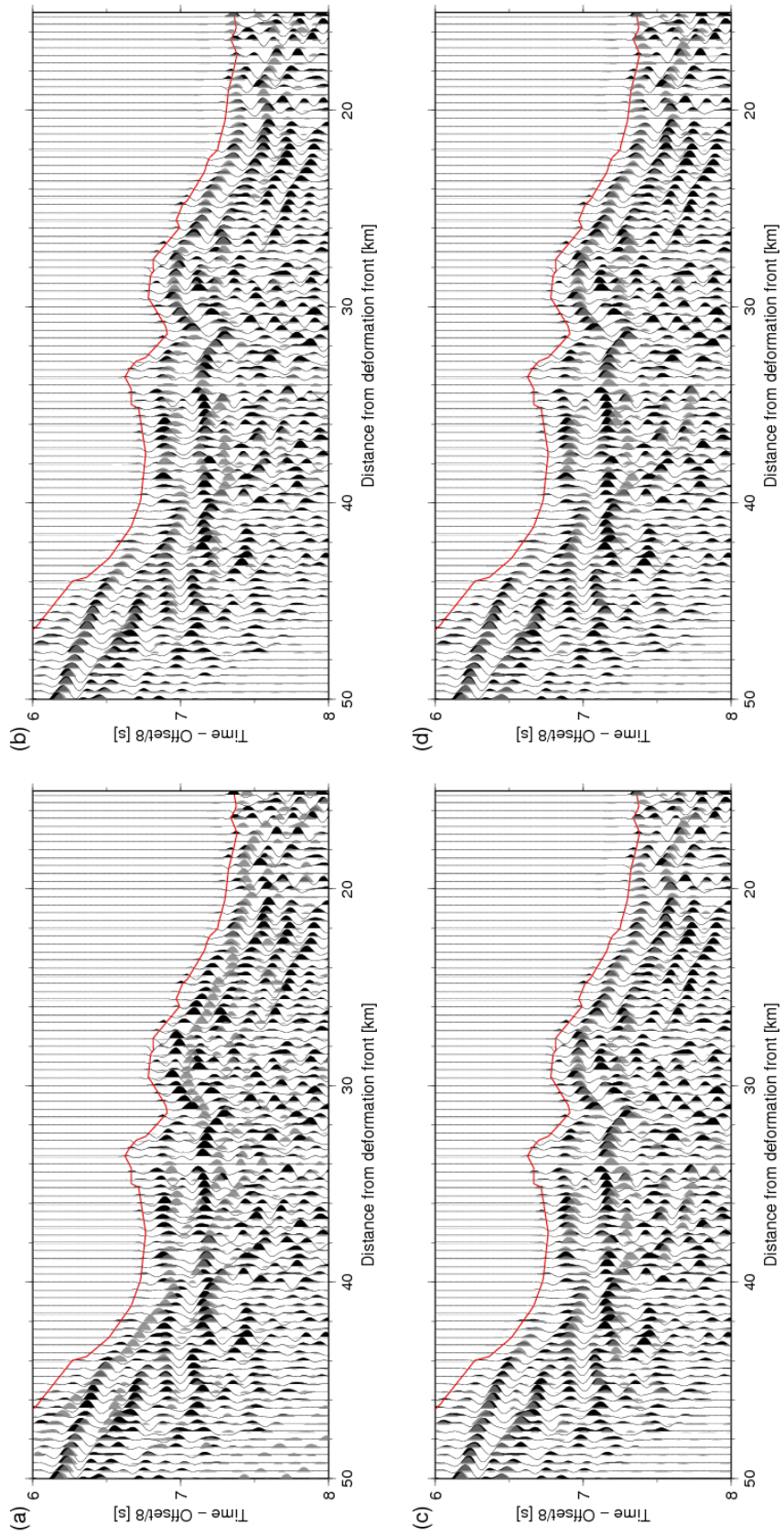


Figure 4.10: Predicted pressure wavefields overlaid by the observed wavefields at the OBS 47 computed from the velocity models shown in Fig. 4.5 retrieved by (a)  $E^1$ , (b)  $E^3$ , (c)  $E^2$ , and (d)  $E^4$ . Red lines indicate the picked first arrivals.

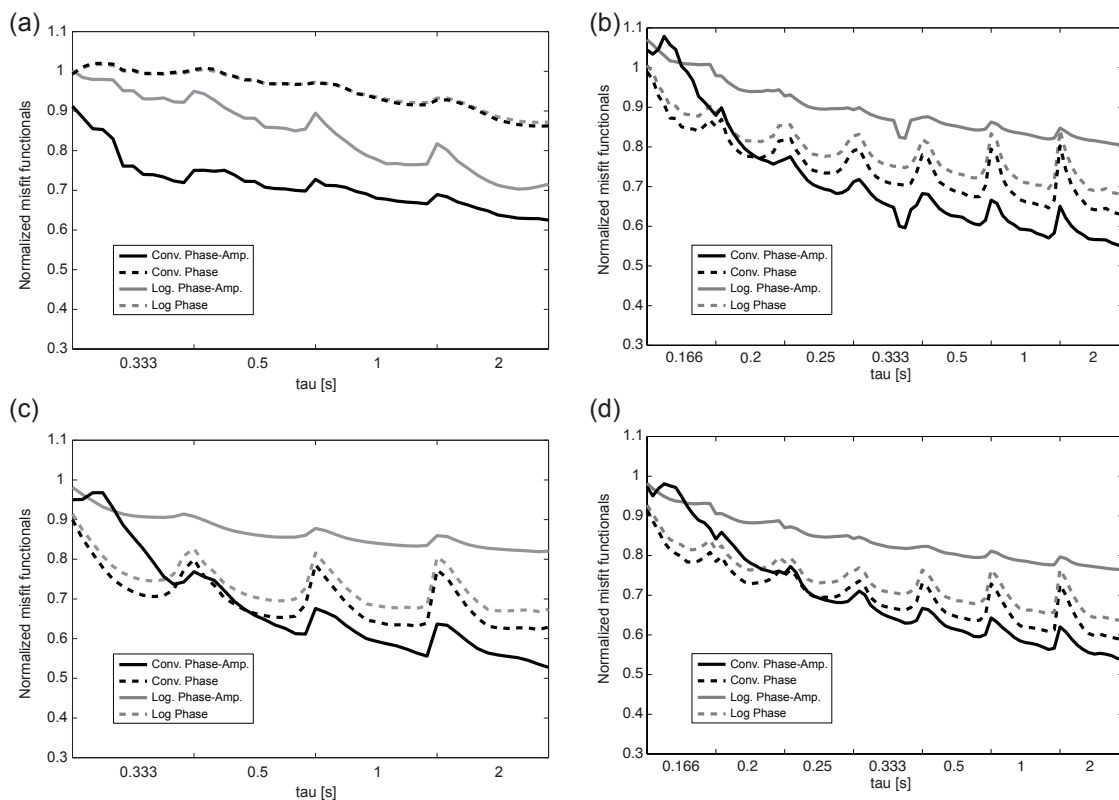


Figure 4.11: History of the misfit functionals through (a) the conventional phase-amplitude inversion b the logarithmic phase-amplitude inversion, (c) the conventional phase-only inversion, and (d) the logarithmic phase-only inversion. The conventional phase-amplitude misfit is shown as a grey solid line, the conventional phase-only misfit as a grey dashed line, the logarithmic phase-amplitude misfit is shown as a solid black line, the logarithmic phase-only misfit is as a dashed black line. The Y-axis indicates the  $\tau$  values employed during the velocity inversion. The misfit functionals show local increases each time  $\tau$  value in the inversion is changed.

We show the history of the misfit functionals during waveform inversion in Fig. 4.11 as a function of decay constants  $\tau$ ; within each  $\tau$  block, the frequency  $\omega$  increases from left to right.

In all four waveform inversion tests, the cumulative misfit functionals decrease regardless of which misfit functional was actually employed as an objective function. However the rate of convergence varies between the inversion tests and the type of the cumulative misfit functional. Note that discontinuities in the form of local increases in the misfit function are apparent on Fig. 4.11 each time  $\tau$  value used in the inversion is changed. This is because inverting for low frequencies with a new  $\tau$  value tends to cause a divergence of the unconstrained higher frequencies as discussed in Kamei & Pratt (2012). During the conventional phase-amplitude inversion (minimizing  $E^1$ ), the conventional and logarithmic phase-amplitude misfit functionals  $E_{total}^1$  and  $E_{total}^3$  were significantly reduced to approximately 60 % of the starting values, but the conventional and logarithmic phase-only misfit functionals  $E_{total}^2$  and  $E_{total}^4$  stayed above 80 %. This indicates that the conventional phase-amplitude inversion did not fit the phase information.

During the logarithmic phase-amplitude inversion (minimizing  $E^3$ ), however, the conventional and logarithmic phase-only misfit functionals  $E_{total}^2$  and  $E_{total}^4$  were successfully reduced to approximately 65 % of the starting values. In addition, we observe a 48 % reduction of the logarithmic phase-amplitude misfit functional  $E_{total}^3$ . The conventional phase-amplitude misfit  $E^1$  converged slowly, and ultimately was reduced to 80 % of the starting value for the final model.

During the conventional and logarithmic phase-only inversions (minimizing  $E^2$  and  $E^4$ ), the misfit functionals behaved in a similar manner as during the logarithmic phase-amplitude inversion (minimizing  $E^3$ ). Although the phase spectra were explicitly optimized, the phase-amplitude misfits show as much reduction as for the logarithmic phase-amplitude inversion. For the final model, the logarithmic phase-amplitude misfit  $E_{total}^3$  is 52 % of the starting value, although the conventional misfit  $E_{total}^1$  is approximately 80 %. This indicates that the velocity model obtained by phase-only inversions implicitly accounts for the amplitude effects in the data.

### 4.4.3 Amplitude information

Two of the velocity models in Section 4.4.2 were retrieved by minimizing phase-only misfit functionals  $E^2$  and  $E^4$  as an objective function, and thus amplitude spectra (representing the dynamic aspects of the problem) were left unused. We therefore tested the performance of additional phase-amplitude inversions starting from the final phase-only

inversion results. In this section, we evaluate improvements obtained by the secondary phase-amplitude inversions. We refer to the initial phase-only inversions conducted in Section 4.4.2 as Stage 1 of waveform inversion, and the secondary phase-amplitude inversions as Stage 2 of the inversion process. Two sets of Stage 2 waveform inversion were conducted: i) The conventional phase-amplitude misfit functional  $E^1$  was minimized starting from the conventional phase-only inversion result (which minimized  $E^2$ ) shown in Figs 4.5c and 4.6c (two-stage conventional waveform inversion), and ii) the logarithmic phase-amplitude misfit functional  $E^3$  was minimized starting from the logarithmic phase-only inversion result (which minimized  $E^4$  in Figs 4.5d and 4.6d (two-stage logarithmic waveform inversion)).

Stage 2 of the conventional waveform inversion was initially unstable: At  $\tau = 0.333$  sec, the objective function diverged at several frequency groups; in such case, we rolled back the model to the previous update, and moved to the next higher frequency group. At  $\tau = 0.5, 1.0, 2.0$  sec, the objective function decreased 3-5 % per each  $\omega - \tau$  set. During Stage 2 of the logarithmic waveform inversion, the objective function decreased about 5 % per each  $\omega - \tau$  set.

We display the resulting de-trended velocity models in Fig. 4.12a for the two-stage conventional waveform inversion, and in Fig. 4.12b for the two-stage logarithmic waveform inversion. We also show the spatial distribution of velocity updates during Stage 2 in Fig. 4.13. A series of de-trended vertical profiles are shown in Fig. 4.14.

The additional amplitude information did not yield substantial changes in low wavenumber components of the velocity models: The average velocity changes are approximately 80 m/s for both conventional and logarithmic inversions. In both images, the velocity updates are prominent in the high-wavenumber components, for example the top boundaries of LVZ<sub>1</sub> and LVZ<sub>2</sub> are apparently sharpened. The secondary conventional and logarithmic phase-amplitude inversions resolved different parts of the model. The conventional phase-amplitude inversion retrieved shallow velocity structures above 6 km depths, including horizontally layered structures in the fore-arc basin, but a substantial amount of oscillatory artifacts were induced near the sea floor (similar to those observed in the one-stage conventional phase-amplitude inversion in Figs 4.5a and 4.5a). Conversely, the logarithmic phase-amplitude inversion retrieved features in the deeper part of the model, and apparently smoothed the velocity structure.

#### 4.4.3.1 Synthetic waveforms

We generated synthetic waveforms from the velocity models obtained by the two-stage waveform inversion in Fig. 4.12, and display the synthetic waveforms at OBS 47 in

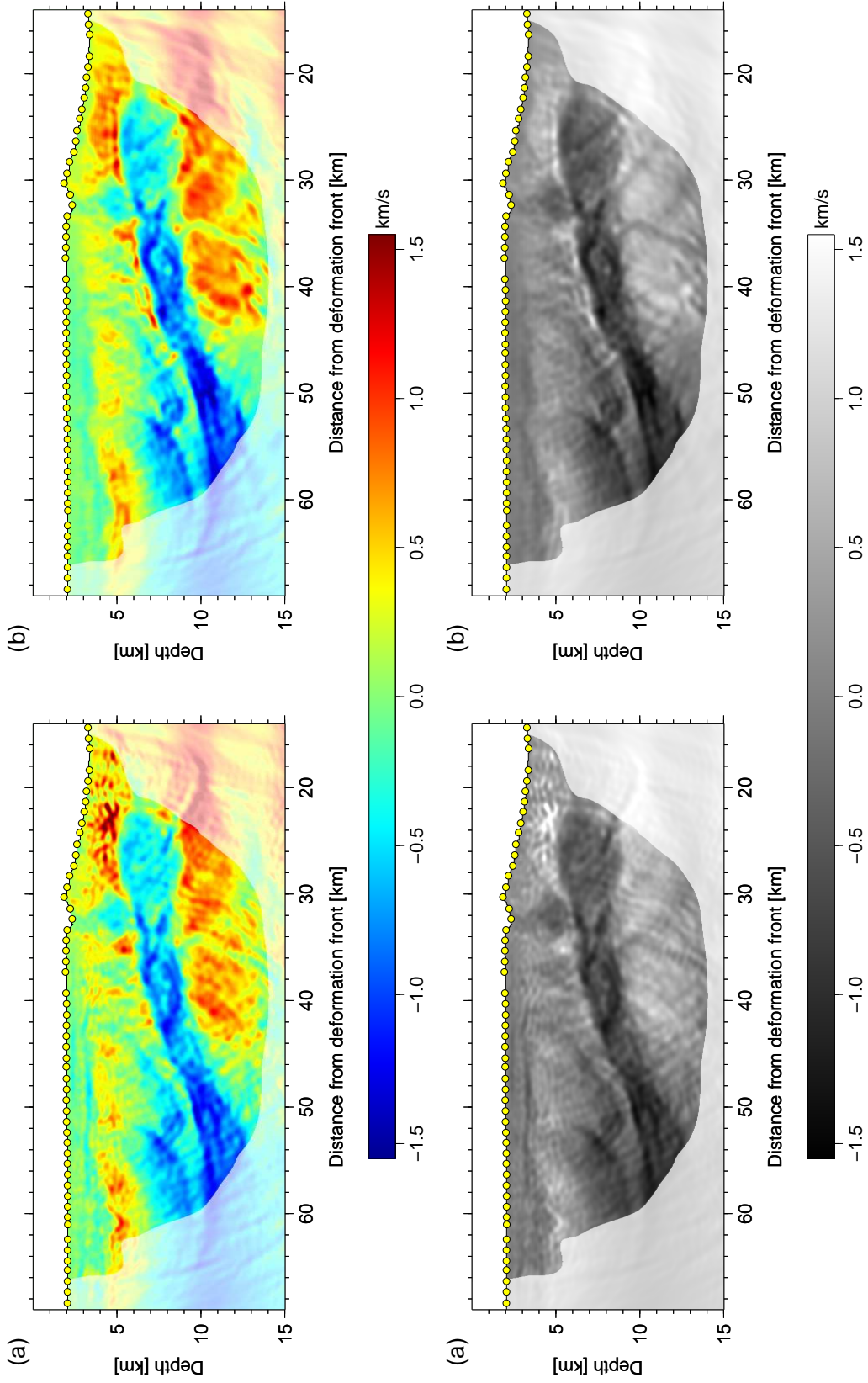


Figure 4.12: De-trended velocity models in colour (a) after Stage 2 of the two-stage conventional inversion (minimizing  $E^1$ ) and (b) after Stage 2 of the two-stage logarithmic inversion (minimizing  $E^4$ ). (c,d) are the same figures as in (a,b) but in grey scales.

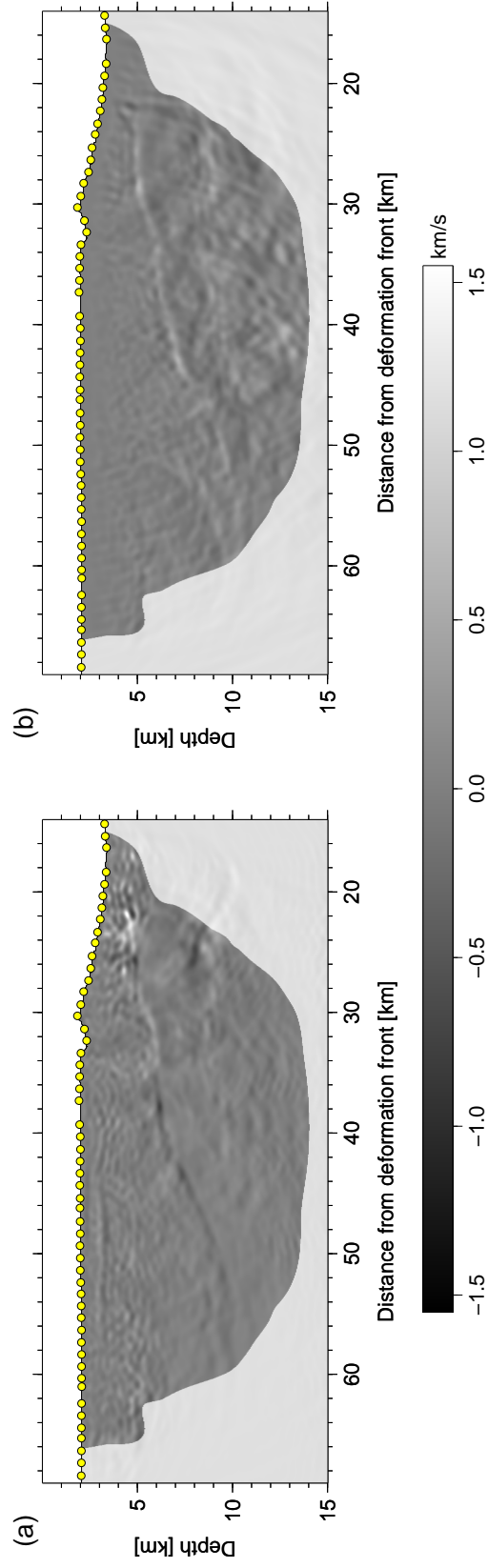


Figure 4.13: Velocity update from Stage 1 following Stage 2 of (a) the two-stage conventional waveform inversion, and of (b) the two-stage logarithmic waveform inversion.



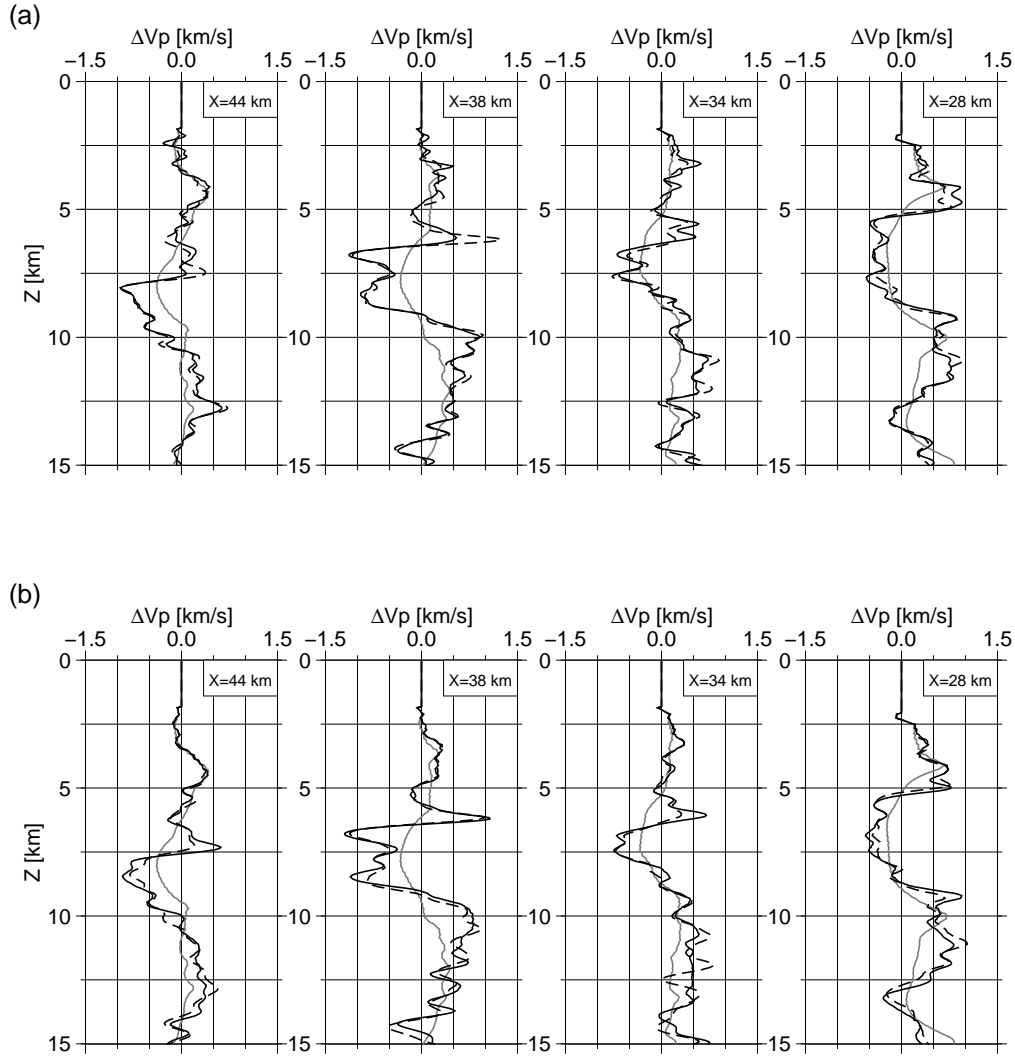


Figure 4.14: Vertical profiles of de-trended velocity model at  $X = 44, 38, 34, 28$  km (from left to right) after (a) the two-stage conventional waveform inversion, and (b) the two-stage logarithmic waveform inversions. Grey solid lines indicate the starting model, black dashed lines the de-trended velocity model after Stage 1, and black solid lines the de-trended velocity after Stage 2.

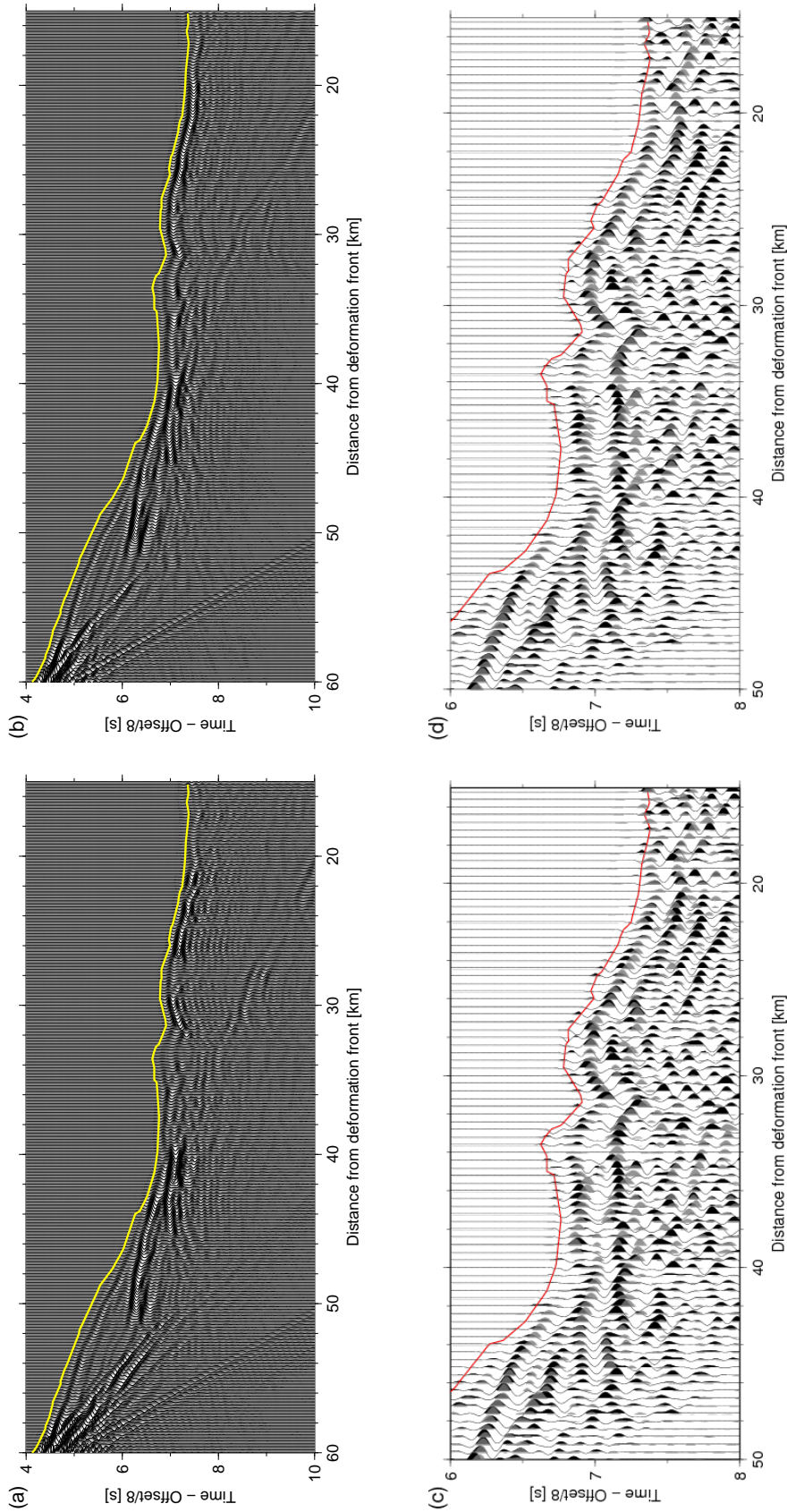


Figure 4.15: Predicted pressure wavefield at the OBS 47 generated from Fig. 4.12 after two-stage inversions using (a) the conventional misfit functionals, and (b) the logarithmic misfit functionals. (c,d) the same synthetic wavefields in grey as (a,b) overlaying the observed wavefields in black. Picked first arrivals from the comparable real data are shown (a) in yellow, and (b) in red.

Fig. 4.15a for the conventional waveform inversion, and in Fig. 4.15b for the logarithmic waveform inversion. In Figs 4.15c and 4.15c and d, we also overlay the same synthetic waveforms on the observed data.

We observe small changes in the appearance of synthetic waveforms when compared to the synthetic waveforms from the phase-only inversion results shown in Fig. 4.9 and 4.10. This is consistent with the minor changes in the final velocity structure from the Stage 1 results. The first arrivals of the synthetic waveforms after the two-stage conventional inversion are contaminated by diffractions at distances between 20 km and 27 km, which can be associated with the oscillatory artifacts in the shallow part of the velocity model (This is more obvious in the greyscale image in Fig. 4.15a than the overlay in Fig. 4.15c). In contrast, the synthetic waveform after the two-stage logarithmic inversion become slightly smoother than seismic waveforms generated from the Stage 1 velocity model in accordance with the smoother appearances in the velocity model.

#### 4.4.3.2 Misfit functionals

We evaluate the two-stage evolution of the cumulative misfit functionals defined in Eq.(4.32) as in Section 4.4.2. We calculated the four cumulative misfit functionals  $E_{total}^{1-4}$  defined in Section 4.2.3 after inverting every  $\omega - \tau$  set, and display their entire history during the two stage inversions in Fig. 4.16. Note that the misfit histories during Stage 1 are the same as in Fig. 4.11.

The Stage 2 conventional phase-amplitude inversion (minimizing  $E^1$ ) was apparently not stable, and the misfit functionals diverged at  $\tau = 0.333$  and 0.5 sec. The final conventional phase-amplitude misfit functional  $E_{total}^1$  is about 4.6 % smaller than that of after Stage 1. The conventional and logarithmic phase misfit functionals  $E_{total}^2$  and  $E_{total}^4$ , however, increased by 9.4 %. This suggest that the phase information was not well constrained during the conventional phase-amplitude inversion.

The Stage 2 logarithmic phase-amplitude inversion (minimizing  $E^3$ ) exhibits more stable behaviour. At the end of Stage 2, the logarithmic phase-amplitude misfit  $E_{total}^3$  was reduced by 7.4 %, and the conventional phase-amplitude misfit  $E_{total}^1$  by 1.4 %. The conventional and logarithmic phase-only misfit functionals  $E_{total}^2$  and  $E_{total}^4$  for the final model remain similar to those from the Stage 1 results, although perturbations are stronger than Stage 1 at transitions of  $\tau$  values. This may indicate that the Stage 2 logarithmic inversion may have successfully fitted amplitude misfits as a by-product of constraining phase-information.

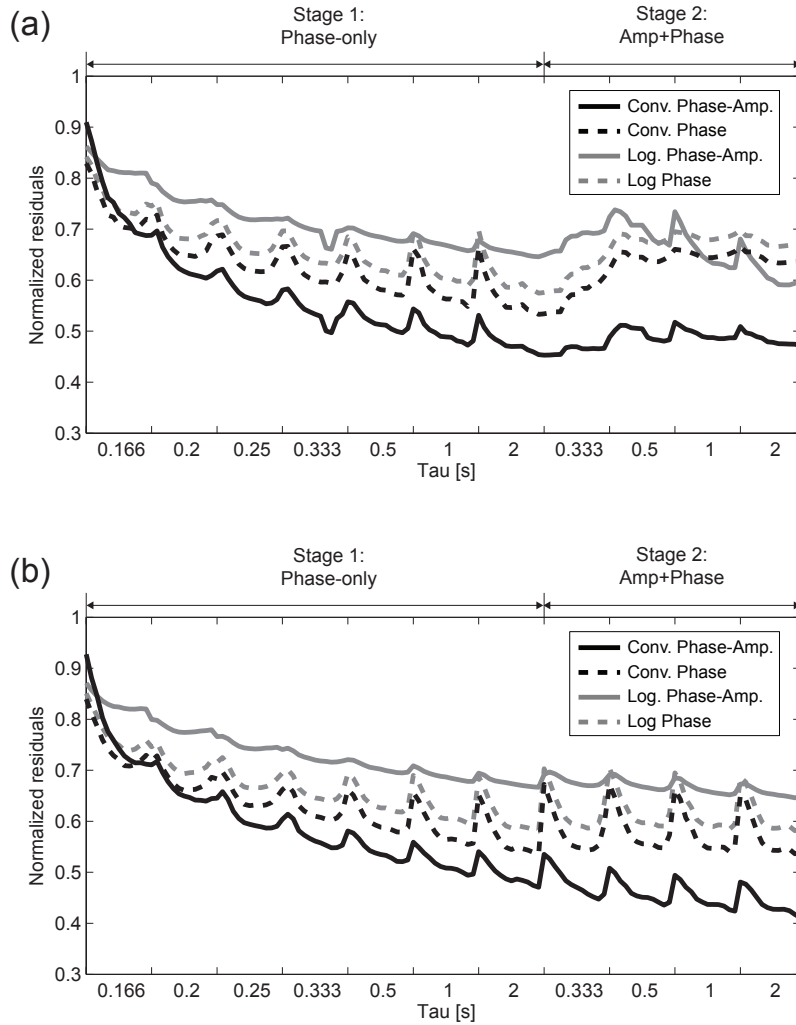


Figure 4.16: History of the cumulative misfit functionals through (a) the two-stage conventional inversion, and (b) the two-stage logarithmic inversion. Stage 1 results are the same as in Fig. 4.11c and d. The conventional phase-amplitude misfit is shown as a grey solid line, the conventional phase-only misfit as a grey dashed line, the logarithmic phase-amplitude misfit is shown as a solid black line, the logarithmic phase-only misfit is as a dashed black line. The y-axis indicates the  $\tau$  values employed during the velocity inversion. The misfit functionals show local increases each time  $\tau$  value in the inversion is changed.

## 4.5 Discussion and conclusions

Using the OBS data set from the Nankai subduction zone, we have investigated the four types of  $L_2$  misfit functionals  $E^{1-4}$  defined in Section 4.2.3: the conventional phase-amplitude residuals  $\delta\mathbf{d}^1$ , the conventional phase-only residuals  $\delta\mathbf{d}^2$ , the logarithmic phase-amplitude residuals  $\delta\mathbf{d}^3$ , and the logarithmic phase-only residuals  $\delta\mathbf{d}^4$ .

The examination of raw model gradients in Section 4.4.1 suggested the poor depth illumination of the conventional phase-amplitude misfit functional  $E^1$ , when compared to the other misfit functionals  $E^2$ ,  $E^3$  and  $E^4$ . The subsequent one-stage conventional phase-amplitude inversion in Section 4.4.2.1 retrieved only a limited region of the subsurface (i.e. shallow velocity features, and the mega-splay fault), and thus confirmed the illumination problem (Figs 4.5a and 4.6a). Furthermore, the comparisons of synthetic waveforms in Section 4.4.2.2 suggested the wide-angle reflections were partially recovered, but that the refraction waveforms at large offsets exhibited phase discrepancies. The examination of the misfit functionals indicated that the phase components of waveforms were not optimized, during the conventional phase-amplitude inversions.

The other three types of misfit functionals  $E^2$ ,  $E^3$ ,  $E^4$  illuminated velocity structures as deep as 12 km from the sea surface, and clearly delineated many velocity features including the fore-arc basin, the mega-splay fault, and the low velocity zones (Figs 4.5b-d and 4.6b-d). The three inversion results are similar, except that the logarithmic amplitude-phase inversion retrieved a narrower LVZ<sub>2</sub> than the others. The synthetic waveforms (Figs 4.9b-d and 4.10b-d) validated the velocity models by reproducing the wide-angle reflections, and substantially improving the waveform fit at large-offsets. The history of the misfit functionals (Figs 4.11b-d) confirms that dynamic components of wavefields can be reproduced by fitting simply phase spectra.

We also conducted Stage 2 phase-amplitude inversions subsequent to Stage 1 phase-only inversions in Section 4.4.3: The amplitude information did not appear to yield substantial improvements in the velocity models, and in the waveform fits. Moreover, Stage 2 conventional phase-amplitude inversion (minimizing  $E^1$ ) was not initially stable, and the phase misfit functionals  $E_{total}^2$  and  $E_{total}^4$  increased by nearly 10 % after Stage 2. The conventional phase-amplitude waveform inversion induced both geologically plausible and non-plausible high-wavenumber velocity features in the shallow part of the model. The Stage 2 logarithmic phase-amplitude inversion (minimizing  $E^3$ ) reduced the logarithmic phase-amplitude misfit  $E_{total}^3$  by 7 %, while the phase misfits  $E_{total}^2$  and  $E_{total}^4$  were largely unaffected. The logarithmic phase-amplitude functional updated the deeper part of the model, and also apparently resulted in smoother velocity images.

### 4.5.1 Dynamic range of data

We argue that discrepancies in the behaviours of the misfit functionals are primarily caused by the sensitivity of a model gradient to the dynamic range of the data, which is a well-known problem in gradient-based optimization (Nocedal & Wright, 1999). The conventional phase-amplitude misfit functional  $E^1$  is sensitive to magnitudes of observed data as described in Section 4.2.3. As our observed data amplitudes are dominated by the near-offset traces, and the wide-angle reflections, the conventional phase-amplitude inversion (minimizing  $E^1$ ) became ill-conditioned, and predominantly updated the shallow structures and the mega-splay fault. Conversely, the other misfit functionals eliminate the data amplitude naturally, and mitigate the excessive influence of data amplitudes in the model gradient. This effectively widens the offset range, and illuminates the deeper part of the model. The conventional and logarithmic phase-only misfit functionals  $E^2$  and  $E^4$  explicitly normalize data residuals, and thus near- and far-offset traces contribute equally to the computation of the gradients. The logarithmic phase-amplitude misfit functional  $E^3$  utilizes the amplitude information, however the logarithmic scaling of data amplitudes ( $\ln |A_u/A_d|$ ) suppresses the vulnerability to strong variations in amplitudes, and balances the contributions to the objective function from the phase components and the amplitude components. The term ( $\ln |A_u/A_d|$ ) may act as a regularization term, and may smooth the velocity structures as shown in Fig. 4.12, and described in Section 4.4.3.

Alternative preconditioning techniques are of course available to improve the poor behaviour of the conventional misfit functional  $E^1$ ; for example, an offset weighting function can be designed to boost amplitudes from large offset data (Operto et al., 2006; Brossier et al., 2009), and/or the gradient can be preconditioned by a pseudo-Hessian matrix (Shin et al., 2002), or by diagonal elements of an approximate Hessian from the starting model (Ravaut et al., 2004; Operto et al., 2006; Malinowski & Operto, 2008). However these approaches are approximate, and may not be as effective as the phase-only objective functions and the logarithmic phase-amplitude inversion when employed with the gradient-based methods (Shin et al., 2007). It will be interesting to compare the phase-only inversion results with the conventional inversion using quasi Newton method such as the L-BFGS methods advocated by Brossier et al. (2009) and Prioux et al. (2011), but this comparison is beyond the scope of this study.

### 4.5.2 Kinematic and dynamic components of wavefields

The results of the two stage inversions in Section 4.4.3 suggest that kinematic information is the primary source of velocity information, and that dynamic information is less

informative. Several researches have demonstrated that phase-only inversions can image detailed velocity structures: Brenders (2011) applied the logarithmic phase-only misfit functional  $E^4$  to Canadian Foothill data, and retrieved a geologically interpretable velocity model. Bednar et al. (2007) also demonstrated that the logarithmic phase misfit functional  $E^4$  provides a result comparative to the logarithmic phase-amplitude objective function  $E^3$ . Bleibinhaus et al. (2007) used a similar form of the conventional phase-only objective function by normalizing trace amplitudes, and successfully retrieved deep fault structures from the San Andreas Fault, California.

From these observations, we suggest that conventional or logarithmic phase-only inversion (minimizing  $E^2$  and  $E^4$ ) is sufficient to obtain robust and detailed velocity structures, and that the amplitude information is of secondary importance in constraining subsurface velocity models. Note that phase-only inversions only utilize phase-spectra, but this does not imply that we discard amplitude information entirely, as the relative amplitudes between first arrivals and later arrivals strongly influence the phase spectra. We may further motivate the use of kinematic information by the nature of these forms of information: Kinematics are less vulnerable than dynamics to source/receiver coupling problems, source radiation patterns, and elastic effects. While we attempt to minimize these by data preprocessing, we are unable to perfectly remove all these effects.

We further suggest that the two-stage logarithmic waveform inversion conducted in Section 4.4.3 is an effective and robust inversion approach for the gradient-based acoustic waveform inversion. Two-stage inversion respects the natural hierarchy of the phase and amplitude components, and allows the retrieval of deep velocity features during the early stages of the inversion. The initial phase-only inversion focuses on kinematics, thus reducing the need for data preconditioning efforts, and moreover minimizes the necessity of elaborate model preconditioning. The subsequent Stage 2 phase-amplitude inversion improves the velocity image by amplitude inversion, but the effects are apparently limited.

## Acknowledgement

The authors thank the Institute For Research on Earth Evolution (IFREE) of the Japan Agency for Marine-Earth Science and Technology (JAMSTEC) for providing the OBS data, A. Nakanishi for providing the traveltime inversion result, Y. Kido for the help in data processing, and A. Brenders and B. Smithyman for discussion of our Waveform Tomography results.

## References

- Aki, K. & Richards, P. C., 1980. *Quantitative seismology*, W. H. Freeman & Co.
- Bednar, J. B., Shin, C., & Pyun, S., 2007. Comparison of waveform inversion, part 2: phase approach, *Geophysical Prospecting*, **55**(4), 465–475.
- Bleibinhaus, F., Hole, J. A., Ryberg, T., & Fuis, G. S., 2007. Structure of the California Coast Ranges and San Andreas Fault at SAFOD from seismic waveform inversion and reflection imaging, *Journal of Geophysical Research*, **112**, B0631.
- Brenders, A. J., 2011. *Strategies For Waveform Tomography of Long-offset, 2-D Exploration Seismic Data*, Ph.D. thesis, University of Western Ontario.
- Brenders, A. J. & Pratt, R. G., 2007. Full waveform tomography for lithospheric imaging: results from a blind test in a realistic crustal model, *Geophysical Journal International*, **168**(1), 133–151.
- Brossier, R., Operto, S., & Virieux, J., 2009. Seismic imaging of complex onshore structures by 2D elastic frequency-domain full-waveform inversion, *Geophysics*, **74**(6), WCC105–WCC118.
- Brossier, R., Operto, S., & Virieux, J., 2010. Which data residual norm for robust elastic frequency-domain full waveform inversion?, *Geophysics*, **75**(3), R37–R46.
- Bunks, C., Saleck, F. M., Zaleski, S., & Chavent, G., 1995. Multiscale seismic waveform inversion, *Geophysics*, **60**(5), 1457–1473.
- Choi, Y. & Alkhalifah, T., 2011. Application of Encoded Multi-source Waveform Inversion to Marine-streamer Acquisition Based on the Global Correlation, *EAGE extended abstract*, pp. 23–26.
- Cruse, E., Pica, A., Noble, M., McDonald, J., & Tarantola, A., 1990. Robust elastic nonlinear waveform inversion: Application to real data, *Geophysics*, **55**(5), 527–538.
- Gardner, G. H. F., Gardner, L. W., & Gregory, A. R., 1974. Formation velocity and density —The diagnostic basics for stratigraphic traps, *Geophysics*, **39**(6), 770–780.
- Guillon, A. & Díaz, E., 2011. Attenuating crosstalk noise with simultaneous source full waveform inversion, *Geophysical Prospecting*, **60**(4), 759–768.
- Hustedt, B., Operto, S., & Virieux, J., 2004. Mixed-grid and staggered-grid finite-difference methods for frequency-domain acoustic wave modelling, *Geophysical Journal International*, **157**(3), 1269–1296.
- Jo, C.-H., Shin, C., & Suh, J. H., 1996. An optimal 9-point, finite-difference, frequency-space, 2-D scalar wave extrapolator, *Geophysics*, **61**(2), 529–537.
- Kamei, R. & Pratt, R. G., 2012. Wide-band multifrequency waveform inversion in the Laplace-Fourier domain, *SEG Technical Program Expanded Abstracts*, pp. 1–6.



- Kamei, R., Pratt, R., & Tsuji, T., 2012a. On Acoustic Waveform Tomography of wide-angle OBS data — Strategies for preconditioning and inversion, *Geophysical Journal International* (under review).
- Kamei, R., Pratt, R. G., & Tsuji, T., 2012b. Waveform tomography imaging of a megasplay fault system in the seismogenic Nankai subduction zone, *Earth and Planetary Science Letters*, **317-318**, 343–353.
- Lailly, P., 1983. The seismic inverse problem as a sequence of before stack migrations, in *Conference on inverse scattering: theory and application*, pp. 206–220, SIAM, Soc. Industr. appl. Math., Philadelphia, PA.
- Leeuwen, T. V. & Mulder, W. A., 2010. Waveform Tomography by Correlation Optimisation, *EAGE extended abstract*, pp. 14 – 17.
- Luo, Y. & Schuster, G. T., 1991. Wave-equation travelttime inversion, *Geophysics*, **56**(5), 645–653.
- Malinowski, M. & Operto, S., 2008. Quantitative imaging of the Permo-Mesozoic complex and its basement by frequency domain waveform tomography of wide-aperture seismic data from the Polish Basin, *Geophysical Prospecting*, **56**(6), 805–825.
- Mallick, S. & Frazer, L. N., 1987. Practical aspects of reflectivity modeling, *Geophysics*, **52**(10), 1355–1364.
- Moore, G. F., Park, J., Bangs, N. L., Gulick, S. P., Tobin, H. J., Nakamura, Y., Sato, S., Tsuji, T., Yoro, T., Tanaka, H., Uraki, S., Kido, Y., Sanada, Y., & Kuramoto, S., 2009. Structural and seismic stratigraphic framework of the NanTroSEIZE Stage 1 transect, in *Proc.IODP, 314/315/316*, vol. 314, Integrated Ocean Drilling Program Management International, Inc.
- Nakanishi, A., Takahashi, N., Park, J.-O., Miura, S., Kodaira, S., Kaneda, Y., Hirata, N., Iwasaki, T., & Nakamura, M., 2002. Crustal structure across the coseismic rupture zone of the 1944 Tonankai earthquake, the central Nankai Trough seismogenic zone, *Journal of Geophysical Research*, **107**(B1), 2326.
- Nakanishi, A., Kodaira, S., Miura, S., Ito, A., Sato, T., Park, J.-O., Kido, Y., & Kaneda, Y., 2008. Detailed structural image around splay-fault branching in the Nankai subduction seismogenic zone: Results from a high-density ocean bottom seismic survey, *Journal of Geophysical Research*, **113**, B03105.
- Nocedal, J. & Wright, S. J., 1999. *Numerical Optimization*, Springer.
- Operto, S., Virieux, J., Dessa, J.-X., & Pascal, G., 2006. Crustal seismic imaging from multifold ocean bottom seismometer data by frequency domain full waveform tomography: Application to the eastern Nankai trough, *Journal of Geophysical Research*, **111**, B09306.

- Phinney, R. A., 1965. Theoretical Calculation of the Spectrum of First Arrivals in Layered Elastic Mediums, *Journal of Geophysical Research*, **70**(20), 5107–5123.
- Polak, E. & Ribière, G., 1969. Note sur la convergence de méthodes de directions conjuguées,, *Revue Fr. Inf. Rech. Oper.*, **16-R1**, 35–43.
- Pratt, R. G., 1999. Seismic waveform inversion in the frequency domain, Part 1: Theory and verification in a physical scale models, *Geophysics*, **64**(3), 888–901.
- Pratt, R. G. & Shipp, R. M., 1999. Seismic waveform inversion in the frequency domain, Part 2: Fault delineation in sediments using crosshole data, *Geophysics*, **64**(3), 902–914.
- Pratt, R. G. & Worthington, M. H., 1988. The application of diffraction tomography to cross-hole seismic data, *Geophysics*, **53**(10), 1284–1294.
- Pratt, R. G. & Worthington, M. H., 1990. Inverse theory applied to multi-source cross-hole tomography. Part 1: Acoustic wave-equation method, *Geophysical Prospecting*, **38**(3), 287–310.
- Pratt, R. G., Shin, C., & Hicks, G., 1998. Gauss-Newton and full Newton methods in frequency-space seismic waveform inversions, *Geophysical Journal International*, **133**(2), 341–362.
- Prieux, V., Brossier, R., Gholami, Y., Operto, S., Virieux, J., Barkved, O. I., & Kommedal, J. H., 2011. On the footprint of anisotropy on isotropic full waveform inversion: the Valhall case study, *Geophysical Journal International*, **187**(3), 1495–1515.
- Pyun, S., Shin, C., & Bednar, J. B., 2007. Comparison of waveform inversion, part 3: amplitude approach, *Geophysical Prospecting*, **55**(4), 477–485.
- Ravaut, C., Operto, S., Imbrota, L., Virieux, J., Herrero, A., & Dell’Aversana, P., 2004. Multiscale imaging of complex structures from multifold wide-aperture seismic data by frequency-domain full-waveform tomography: application to a thrust belt, *Geophysical Journal International*, **159**(3), 1032–1056.
- Shin, C. & Cha, Y. H., 2009. Waveform inversion in the Laplace-Fourier domains, *Geophysical Journal International*, **177**(3), 1067–1079.
- Shin, C. & Ha, W., 2008. A comparison between the behavior of objective functions for waveform inversion in the frequency and Laplace domains, *Geophysics*, **73**(5), VE119–VE133.
- Shin, C. & Min, D.-J., 2006. Waveform inversion using a logarithmic wavefield, *Geophysics*, **71**(3), R31–R42.
- Shin, C., Marfurt, K. J., Park, K. G., Min, D.-J., Yoon, K., Yang, D., Ha, T., Ko, S., Kim, W., & Hong, S., 2002. Traveltime and amplitude calculation using a perturbation

- approach, *Geophysics*, **67**(5), 1648–1655.
- Shin, C., Pyun, S., & Bednar, J. B., 2007. Comparison of waveform inversion, Part 1: conventional wavefield vs logarithmic wavefield, *Geophysical Prospecting*, **55**(4), 449–464.
- Shin, C., Koo, N.-H., Cha, Y. H., & Park, K.-P., 2010. Sequentially ordered single-frequency 2-D acoustic waveform inversion in the Laplace-Fourier domains, *Geophysical Journal International*, **181**(2), 933–950.
- Sirgue, L., 2003. *Inversion de la forme d’onde dans le domaine frequential de donnees sismiques grands offsets.*, Ph.D. thesis, l’Ecole Normale Superieure de Paris.
- Sirgue, L. & Pratt, R. G., 2004. Efficient waveform inversion and imaging: A strategy for selecting temporal frequencies, *Geophysics*, **69**(1), 231–248.
- Song, Z.-M., Williamson, P. R., & Pratt, R. G., 1995. Frequency-domain acoustic-wave modeling and inversion of crosshole data: Part II—Inversion method, synthetic experiments and real-data results, *Geophysics*, **60**(3), 796–809.
- Tarantola, A., 1984. Inversion of seismic reflection data in the acoustic approximation, *Geophysics*, **49**(8), 1259–1266.
- Tarantola, A., 1988. Theoretical background for the inversion of seismic waveforms including elasticity and attenuation, *Pure and Applied Geophysics*, **128**(1-2), 365–399.
- Tobin, H. J. & Kinoshita, M., 2006. NanTroSEIZE: the IODP Nankai Trough seismogenic zone experiment, *Scientific Drilling*, **2**(2), 23–27.
- Zeng, Y. Q., He, J. Q., & Liu, Q. H., 2001. The application of the perfectly matched layer in numerical modeling of wave propagation in poroelastic media, *Geophysics*, **66**(4), 1258–1266.
- Zhou, B. & Greenhalgh, S. A., 2003. Crosshole seismic inversion with normalized full-waveform amplitude data, *Geophysics*, **68**(4), 1320–1330.

# Chapter 5

## Inversion strategies for visco-acoustic waveform inversion

A version of the chapter was submitted for publication to *Geophysical Journal International* as: Kamei, R., and Pratt, R.G., “Inversion strategies for visco-acoustic waveform inversion”

### 5.1 Introduction

Waveform inversion is a multiparameter non-linear problem with the goal of retrieving elastic parameters of the earth by exploiting recorded seismic waveform data (Tarantola, 1988). Waveform inversion has to date been almost exclusively implemented using local, gradient-based algorithms (e.g., Song et al., 1995; Pratt et al., 1998; Brossier et al., 2009). Although the problem is known to be highly non-linear (Mora, 1987; Sirgue & Pratt, 2004), more comprehensive solutions based on extensive global search methods (Sen & Stoffa, 1991; Mosegaard & Tarantola, 1995) are prohibitively expensive, due to the cost of forward simulations. Gradient-based methods are highly efficient, due to the ease of use of the adjoint method to compute the gradient (Lailly, 1983; Tarantola, 1984; Pratt & Worthington, 1990). In exploration seismology, while elastic waveform inversion is now emerging (Shipp & Singh, 2002; Brossier et al., 2009; Sears et al., 2010), acoustic or visco-acoustic waveform inversion has proven particularly useful in providing high-resolution P-wave velocity structures in a variety of applications (e.g., Song et al., 1995; Pratt et al., 2004; Ravaut et al., 2004; Gao et al., 2006; Sirgue et al., 2010; Kamei et al., 2012c). Intrinsic P-wave attenuation has also been of interest, since attenuation parameters can be directly related to rock and fluid properties (Mavko et al., 1998; Carcione, 2000; Chapman et al., 2006). However waveform inversion for attenuation has been recognized as more challenging than velocity inversion (Song et al., 1995; Liao &

Table 5.1: List of mathematical symbols used in this chapter. The superscript  $(j=1)$  indicates the velocity class, and  $(j=2)$  the attenuation class of the inversion parameter.

Symbol	Type	Dimension	Description
$\mathbf{x}$	real		spatial location
$\boldsymbol{\omega}$	real	$N_\Omega \times 1$	discrete angular frequencies
$\boldsymbol{\Omega}$	complex	$N_\Omega \times 1$	discrete complex angular frequencies
$\boldsymbol{\tau}$	real	$N_\Omega \times 1$	discrete characteristic times for exponential time-damping
$\omega_o$	real		reference angular frequency
$\kappa_o$	real		background wavenumber
$s$	complex		complex Laplace constant
$c$	complex		P-wave velocity
$\rho$	real		density
$\mathbf{Q}$	real	$N_l \times 1$	discrete quality factor
$N_s, N_r, N_\Omega$	integer		number of sources, receivers, complex frequencies
$N_m$	integer		number of model parameters
$\cdot N_l$	integer		number of nodes in finite difference model
$\mathbf{S}$	complex	$N_l \times N_l$	frequency-domain finite difference matrix
$\mathbf{f}$	complex	$N_l \times 1$	pressure source vector
$\mathbf{d}, \mathbf{u}$	complex	$N_l \times 1$	observed and predicted data vectors
$\delta\mathbf{d}, \delta\mathbf{d}^p, \delta\mathbf{d}^a$	complex	$N_r \times 1$	conventional, phase-only, logarithmic amplitude residual vectors
$\mathbf{F}$	complex	$N_l \times N_m$	virtual source matrix
$\mathbf{m}, \delta\mathbf{m}$	real	$N_m \times 1$	current model, and model update vectors
$E, E^p$	real		conventional, and logarithmic phase-only misfit functions
$\mathbf{K}$	complex	$N_m \times N_m$	Fréchet matrix of partial derivatives
$\alpha$	real		step length
$\boldsymbol{\gamma}$	real	$N_m \times 1$	conjugate gradient direction
$\mathbf{v}$	complex	$N_m \times 1$	back-propagated wavefields
$\boldsymbol{\eta}$	complex	$N_m \times 1$	inner product between $\mathbf{v}$ and $\mathbf{u}$
$\mathbf{P}$	real	$N_m \times 1$	preconditioning matrix
$\xi$	real		penalty term for attenuation parameter
$\mathbf{s}$	complex	$N_l \times 1$	slowness
$\mathbf{s}^{(r)}, \mathbf{s}^{(i)}$	real	$N_l \times 1$	real and imaginary part of $\mathbf{s}$
$\mathbf{s}_o^{(r)}, \mathbf{s}_o^{(i)}$	real	$N_l \times 1$	real and imaginary part of $\mathbf{s}$ at reference frequency
$\mathbf{J}$	real	$2 \times 2$	Jacobian matrix of coordinate change

McMechan, 1996; Pratt et al., 2004; Smithyman et al., 2009; Malinowski et al., 2011; Hak & Mulder, 2011; Takam Takougang & Calvert, 2012).

Waveform inversion of attenuation parameters was first formulated by Tarantola (1988) in the time domain as a part of a full visco-elastic waveform inversion theory. Song et al. (1995) later developed visco-acoustic waveform inversion in the frequency domain. The frequency-domain implementation has several advantages over the time-domain approach, particularly when considering attenuation: First, attenuation parameters (e.g.  $Q^{-1}$  values) and dispersive velocity relationships are easily incorporated into forward modelling by using complex-valued frequency-dependent velocities (Song et al., 1995), and both velocity and attenuation gradients can be computed simultaneously without extra cost (Song et al., 1995). Moreover, the frequency domain approach allows a natural implementation of a multi-scale approach to mitigate the non-linearity of waveform inversion (Bunks et al., 1995; Sirgue & Pratt, 2004): By starting the inversion from the lowest frequency components, and by sequentially inverting for higher frequency components, we can successively retrieve a wide range of features in the subsurface model.

Velocity parameters strongly influence the phase information in seismic data. In contrast, attenuation properties are most evident in amplitude information (Pratt et al., 2004). (Attenuation also changes the phase of seismic waveforms through velocity dispersion, but the effects on the phase are much smaller than those on the amplitudes, due to the limited bandwidth of available frequencies.) Unfortunately when compared to phase information, seismic amplitudes are easily contaminated by ambient noise, source and receiver coupling problem, source radiation patterns, and elastic (i.e. non-acoustic) effects. Thus careful pre-processing efforts are required to reduce such effects while preserving amplitude information (Pratt et al., 2004; Malinowski et al., 2011). Amplitude decay is caused by the combination of geometrical spreading, scattering, and intrinsic attenuation; the effects of geometrical spreading due to velocity structure are particularly significant (Kamei & Pratt, 2008). In frequency-domain waveform inversion, the model gradients (the steepest ascent direction of the objective function) for velocity and attenuation parameters are coupled, and the velocity and attenuation parameters are poorly resolved from each other (Song & Williamson, 1995; Mulder & Hak, 2009; Hak & Mulder, 2011); we refer to this lack of parameter resolution as “cross-talk”. Mulder & Hak (2009) studied the null space for reflection seismic data, and suggested that there exist many possible velocity and attenuation pairs for a given seismic data set if the dispersion relationship is not considered. Even when the frequency-dependent velocity is accounted for, many iterations are required to retrieve a true velocity and attenuation model (Hak & Mulder, 2011). Hak & Mulder (2010) suggested that the parameter res-

olution depends on survey geometry, and that with perfect subsurface illumination, the cross-talk problem is resolved. Nevertheless, a portion of the velocity perturbation will remain unresolved due to the finite frequency bandwidth, and this will also influence the cross-talk.

Because subsurface illumination is far from perfect, cross-talk remains a significant problem. Furthermore, simple gradient-based methods fail to account for the different sensitivity and scaling between classes of parameter, and specific parameters may dominate the inversions unless appropriate model covariance matrices are used. Additionally more complete, but computationally expensive optimization algorithms like the subspace method (Kennett et al., 1988) or Newton methods (Kennett & Sambridge, 1998) can further optimize the model update vector according to parameter classes.

As a result of the complications indicated in the previous paragraph, gradient-based attenuation imaging tends to suffer from artifacts when simultaneously inverting for both velocity and attenuation parameters (Song et al., 1995; Watanabe et al., 2004; Kamei & Pratt, 2008). Liao & McMechan (1996) and Hak & Mulder (2011) used synthetic studies to suggest that the cross-talk between velocity and attenuation parameters was particularly evident on images from the early stages of the inversion. Liao & McMechan (1996) also reported that model parameters need to be constrained to be within a certain range to retrieve a good attenuation model, and Hak & Mulder (2011) suggested the inversion may be accelerated by penalizing the attenuation component of the gradient based on the relative order of eigenvalues in two parameter classes. Malinowski et al. (2011) also applied a simultaneous inversion approach to real surface seismic data acquired in the Polish basin, and successfully retrieved an attenuation model consistent with available lithology information. They reported that stronger damping and strong smoothing constraints were required in order to recover attenuation parameters.

An alternative approach is to only attempt to invert for attenuation models after retrieving a sufficiently accurate velocity model, an approach we refer to as “sequential” inversion. This approach can potentially mitigate the cross-talk if we assume velocity structures are the first-order source of amplitude variation in the data. The initial velocity estimation is conducted by fixing a starting attenuation model (Pratt et al., 2004; Kamei & Pratt, 2008; Rao & Wang, 2008; Smithyman et al., 2009). Pratt et al. (2004) applied the sequential approach to a cross-well data set for a highly attenuative hydrate-bearing zone. They also used stronger smoothing constraints for attenuation parameters than for velocity parameters. The resulting attenuation model coincided well with independent estimates of attenuation from sonic waveform analysis. The sequential approach was also successfully adopted by Watanabe et al. (2004) for a laboratory experiment at

sonic frequencies, and by Smithyman et al. (2009) for the identification of near-surface objects. Watanabe et al. (2004) and Kamei & Pratt (2008) compared simultaneous and sequential approaches using synthetic data sets with a cross-well geometry, and favoured the sequential inversion method when regularization was not applied. Kamei & Pratt (2008) suggested the majority of amplitude variation in a given data set can be indeed explained by the distribution of velocity parameters.

In this chapter we explore robust inversion strategies to minimize the cross-talk and to yield highly resolved velocity and attenuation images using a synthetic cross-well model generated by Kamei & Pratt (2008). We seek to resolve these parameters both spatially, and from each other. We compare the simultaneous and sequential inversion approaches, and investigate the effects of a variety of gradient preconditioning schemes. We examine the attenuation imaging in the Laplace-Fourier domain, a natural and important generalization of the frequency domain (Sirgue & Pratt, 2004; Shin & Cha, 2009).

### 5.1.1 Outline of the chapter

In section 5.2, we formulate visco-acoustic waveform inversion in the Laplace-Fourier domain, and discuss the ill posedness of waveform inversion. We then describe a series of synthetic inversion experiments in section 5.3: We introduce our synthetic models in section 5.3.1, followed by the description of basic inversion methodology in section 5.3.2. After illustrating the cross-talk issue in section 5.3.3, we present the inversion test results in sections 5.3.4 - 5.3.7. The sensitivity of visco-acoustic waveform inversion to the synthetic noise is also examined in section 5.3.8. Finally in section 5.4, we discuss our results and explore robust inversion strategies for attenuation imaging.

## 5.2 Theory

### 5.2.1 Laplace-Fourier domain

Following Shin & Cha (2009), the complex Laplace transform of the time-domain wavefield  $u(\mathbf{x}; t)$  is

$$u(\mathbf{x}; s) = \int_0^{\infty} u(\mathbf{x}; t) \exp[-st] dt, \quad (5.1)$$

where  $s$  is the complex-valued Laplace parameter. If we write

$$s = 1/\tau + i\omega, \quad (5.2)$$



with a real-valued decay constant  $\tau$  and a real-valued angular frequency,  $\omega$ , then Eq.(5.1) becomes

$$u(\mathbf{x}; \tau, \omega) = \int_{-\infty}^{\infty} \left[ u(\mathbf{x}; t) \exp \left[ -\frac{t}{\tau} \right] \right] \exp [-i\omega t] dt, \quad (5.3)$$

which is the Fourier transform of the original time-domain wavefield multiplied by a time-damping function,  $\exp [-t/\tau]$ . The damping function acts as a data preconditioning operator (Sirgue, 2003; Brenders & Pratt, 2007) in that smaller values of  $\tau$  (larger values of  $s$ ) preferentially weight early arrivals, and suppress later arrivals. We further rewrite Eq.(5.3) as

$$\begin{aligned} u(\mathbf{x}; \tau, \omega) &= \int_{-\infty}^{\infty} u(\mathbf{x}; t) \exp [-i\Omega t] dt, \\ &= u(\mathbf{x}; \Omega), \end{aligned} \quad (5.4)$$

where

$$\Omega = \omega - i/\tau, \quad (5.5)$$

is a complex-valued frequency. Eq.(5.5) is the Fourier domain wavefield at a complex-valued frequency  $\Omega = \omega - i/\tau$  (as in Phinney, 1965; Mallick & Frazer, 1987; Sirgue, 2003), and the equivalence of the complex Laplace and complex Fourier transform leads us to refer waveform inversion in these domains a ‘‘Laplace-Fourier domain waveform inversion’’ following Shin & Cha (2009).

## 5.2.2 Forward modelling

The visco-acoustic wave equation in the Laplace-Fourier domain is

$$\nabla \left( \frac{1}{\rho(\mathbf{x})} \nabla u(\mathbf{x}; \Omega) \right) + \frac{\Omega^2}{\rho(\mathbf{x})c^2(\mathbf{x}; \omega)} u(\mathbf{x}; \Omega) = f(\mathbf{x}; \Omega), \quad (5.6)$$

where  $\rho(\mathbf{x})$  is the density,  $u(\mathbf{x})$  is the pressure field,  $f(\mathbf{x}; \Omega)$  is the source term. (Note that the velocity field may formally depend on the complex frequency  $\Omega$ , but the dependence of the velocity field on the imaginary part of  $\Omega$  (i.e. the decay constant  $\tau$ ) is assumed to be negligible.) Attenuative media can be included by utilizing a complex-valued velocity field  $c(\mathbf{x}; \omega)$ , in which the attenuation factor

$$Q^{-1} = -\frac{c^i(\mathbf{x}; \omega)}{2c^r(\mathbf{x}; \omega)}, \quad (5.7)$$

where  $c^r(\mathbf{x}; \omega) = \Re [c(\mathbf{x}; \omega)]$  and  $c^i(\mathbf{x}; \omega) = \Im [c(\mathbf{x}; \omega)]$  (Aki & Richards, 1980; Song et al., 1995). We define the complex-valued slowness field

$$s(\mathbf{x}; \omega) = \frac{1}{c(\mathbf{x}; \omega)}, \quad (5.8)$$

and

$$Q^{-1} = \frac{s^{(i)}(\mathbf{x}; \omega)}{2s^{(r)}(\mathbf{x}; \omega)}, \quad (5.9)$$

where  $s^{(r)}(\mathbf{x}; \omega) \equiv \Re [s(\mathbf{x}; \omega)]$  and  $s^{(i)}(\mathbf{x}; \omega) \equiv \Im [s(\mathbf{x}; \omega)]$ . We assume a frequency independent  $Q$ , and implement the dispersion relationship

$$s^{(r)}(\mathbf{x}; \omega) = s_o^{(r)}(\mathbf{x}) \left( 1 + \frac{1}{\pi Q} \ln \left( \frac{\omega_o}{\omega} \right) \right), \quad (5.10)$$

where  $s_o^{(r)}(\mathbf{x}) = \Re [s_o(\mathbf{x})]$ ,  $s_o(\mathbf{x}) = s(\mathbf{x}; \omega_o)$ , and  $\omega_o$  is the reference frequency (Aki & Richards, 1980; Song et al., 1995).

A numerical solution of the wave equation in Eq.(5.6) for arbitrary velocity, density and attenuation distributions requires a discretization of the model. If we assume that the 2D P-wave subsurface velocity, density and attenuation structure may be described by a set of  $N_m$  model parameters,  $\mathbf{m}$ , after appropriate discretization of the partial derivatives, Eq.(5.6) then leads to the matrix form

$$\mathbf{S}(\mathbf{m}; \Omega) \mathbf{u}(\Omega) = \mathbf{f}(\Omega), \quad (5.11)$$

(Pratt et al., 1998), where  $\mathbf{u}(\Omega)$  represents the discrete solutions to the wave equation at  $N_l$  grid points, and  $\mathbf{f}(\Omega)$  represents the discrete distribution of source terms at  $N_l$  grid points. In this study we adopt the finite difference approach for the matrix elements in Eq.(5.11) developed by Pratt & Worthington (1988) and Jo et al. (1996), but we implement an absorbing boundary condition using the perfectly matched layer method (Hustedt et al., 2004; Zeng et al., 2001).

### 5.2.3 Optimization

Instead of using complex-valued velocities as a single model parameter class as done by Song et al. (1995) and Liao & McMechan (1996), we assume two real-valued parameter classes to describe velocity and attenuation structures. The velocity structure is described by a set of real-valued parameters  $m_p^{(1)}$ , and the attenuation structure is described by a set of real-valued parameters  $m_p^{(2)}$  at each nodal point of the finite difference grid,  $\mathbf{x}_p$

( $p = 1 \dots N_l$ ). We assume the density model can be derived from the velocity model by a Gardner's relationship (Gardner et al., 1974). Therefore

$$\mathbf{m} = \begin{bmatrix} \mathbf{m}^{(1)} \\ \mathbf{m}^{(2)} \end{bmatrix}, \quad (5.12)$$

and the number of model parameters  $N_m = 2N_l$ . We also assume that observed data,  $\mathbf{d}(\Omega_l, \mathbf{x}_k^{\text{src}})$ , are available at  $N_r$  points for each source excitation at  $\mathbf{x}_k^{\text{src}}$  ( $k = 1, \dots, N_s$ ) and for a discrete set of complex-valued frequencies  $\Omega_l = \omega_l - i/\tau_l$  ( $l = 1, \dots, N_\Omega$ ). We seek to iteratively update the model to fit the Laplace-Fourier components using a local optimization based on the conjugate gradient method.

We define a misfit functional  $E(\mathbf{m}; \mathbf{d})$  using the  $L_2$  norm such that

$$2E(\mathbf{m}; \mathbf{d}) = \sum_{l=1}^{N_\Omega} E(\Omega_l) \quad (5.13)$$

$$= \sum_{l=1}^{N_\Omega} \sum_{k=1}^{N_s} \delta \mathbf{d}(\Omega_l, \mathbf{x}_k^{\text{src}})^T \delta \mathbf{d}(\Omega_l, \mathbf{x}_k^{\text{src}}), \quad (5.14)$$

where  $\delta \mathbf{d}$  is the residual, and  $^T$  indicates the Hermite conjugate of the vector. The residual is defined as

$$\delta d_j(\Omega_l, \mathbf{x}_k^{\text{src}}) = (u_j(\Omega_l, \mathbf{x}_k^{\text{src}}) - d_j(\Omega_l, \mathbf{x}_k^{\text{src}})) \exp [t_o/\tau_l], \quad j = 1, \dots, N_d, \quad (5.15)$$

where  $t_o$  is the picked arrival time, and the term  $\exp [t_o/\tau_l]$  is introduced to compensate for the extra amplitude loss caused by the exponential time damping in Eq.(5.3) (Brenders & Pratt, 2007). We refer to this definition of the residual as the ‘‘conventional’’ residual.

We also employ a logarithmic phase-only residual (Bednar et al., 2007)

$$\delta d_j^{\text{P}}(\Omega_l, \mathbf{x}_k^{\text{src}}) = \Im \left[ \ln \left( \frac{u_j(\Omega_l, \mathbf{x}_k^{\text{src}})}{d_j(\Omega_l, \mathbf{x}_k^{\text{src}})} \right) \right], \quad (5.16)$$

for velocity-only inversions during the sequential inversion approach, which leads to the corresponding phase-only misfit functional

$$2E^{\text{P}}(\mathbf{m}; \mathbf{d}) = \sum_{l=1}^{N_\Omega} \sum_{k=1}^{N_s} \delta \mathbf{d}^{\text{P}}(\Omega_l, \mathbf{x}_k^{\text{src}})^T \delta \mathbf{d}^{\text{P}}(\Omega_l, \mathbf{x}_k^{\text{src}}), \quad (5.17)$$

Note that logarithmic phase-only residuals are independent of amplitudes, and thus do not require the compensation term as in Eq.(5.15).

The derivation below focuses on two-parameter velocity-attenuation inversions employing the conventional misfit function. (Readers are recommended to refer to Bednar et al. (2007) and Kamei et al. (2012b) for a detailed description of the phase-only objective function.) For the conjugate gradient method, the model vector is updated at each iteration,  $\delta\mathbf{m}$ , corresponding to

$$\delta\mathbf{m} = \alpha\boldsymbol{\gamma}, \quad (5.18)$$

where the steplength  $\alpha$  is computed by assuming linearity in the vicinity of the current model (Song et al., 1995), and the conjugate gradient direction  $\boldsymbol{\gamma}$  is obtained by a linear combination of preconditioned model gradients (Polak & Ribière, 1969). The model gradient  $\nabla_{\mathbf{m}}E$  is obtained by the adjoint method (Lailly, 1983; Tarantola, 1984; Pratt et al., 1998), so that the computationally expensive Fréchet kernel is not required in explicit form.

Following Kennett et al. (1988), and Williamson (1990), we partition the gradient into two vectors each representing a single parameter class to explicitly illustrate the characteristics of the two-parameter inversion problem yielding

$$\nabla_{\mathbf{m}}E = \begin{bmatrix} \nabla_{\mathbf{m}^{(1)}}E \\ \nabla_{\mathbf{m}^{(2)}}E \end{bmatrix}. \quad (5.19)$$

The magnitudes of each component of the gradient  $\nabla_{\mathbf{m}^{(j)}}E$  are not necessarily scaled in accordance with the variances of the model parameters  $\mathbf{m}^{(j)}$ . Instead the relative magnitudes of  $\nabla_{\mathbf{m}^{(1)}}E$  and  $\nabla_{\mathbf{m}^{(2)}}E$  are governed by the (arbitrary) choice of units, and by the corresponding singular values of the Fréchet derivative matrix. This lack of scaling leads to imbalances in the model updates between the two parameter classes. To avoid this, we precondition the model gradient by pre-multiplication by

$$\mathbf{P} = \begin{bmatrix} \mathbf{I} & \mathbf{0} \\ \mathbf{0} & \xi\mathbf{I} \end{bmatrix}, \quad (5.20)$$

where  $\mathbf{I}$  is the  $N_l \times N_l$  identity matrix, and  $\xi$  is a scalar that scales and balances the two gradient classes, and is referred to as an ‘attenuation penalty term’. The preconditioned gradient is thus

$$\tilde{\boldsymbol{\gamma}} = \mathbf{P}\nabla_{\mathbf{m}}E, \quad (5.21)$$

$$= \begin{bmatrix} \nabla_{\mathbf{m}^{(1)}}E \\ \xi\nabla_{\mathbf{m}^{(2)}}E \end{bmatrix}, \quad (5.22)$$

which illustrates that  $\xi \neq 1$  performs an implicit regularization: The condition  $\xi < 1$  penalizes the attenuation component of the model gradient, and  $\xi > 1$  penalizes the velocity component of the model gradient. (In Appendix Appendix 5.A, we discuss the relationship of the preconditioning matrix to the priori model covariance employed in the Bayesian inversion approaches developed by Tarantola & Valette (1982) and Tarantola (1988))

### 5.2.3.1 Computation of the gradient $\nabla_{\mathbf{m}}E$

The derivation below follows closely that of Pratt et al. (1998), but we expand the discussion to consider the behaviour of the multiparameter inverse problem. From Eq.(5.13), we write the gradient as

$$\nabla_{\mathbf{m}}E = \sum_{l=1}^{N_{\Omega}} \nabla_{\mathbf{m}}E(\Omega_l), \quad (5.23)$$

where  $\Omega_l = \omega_l - i/\tau_l$ . Following Pratt et al. (1998),

$$\nabla_{\mathbf{m}}E(\Omega_l) = \frac{\partial E(\Omega_l)}{\partial \mathbf{m}}, \quad (5.24)$$

$$= \sum_{N_s} \Re [\mathbf{K}(\Omega_l, \mathbf{x}_k^{\text{src}})^T \delta \mathbf{d}(\Omega_l, \mathbf{x}_k^{\text{src}})] \quad (5.25)$$

where  $\mathbf{K}(\Omega_l, \mathbf{x}_k^{\text{src}})$  is the Fréchet derivative matrix. Partitioning of this matrix into two matrices corresponding to the two parameter classes yields

$$\mathbf{K}(\Omega_l, \mathbf{x}_k^{\text{src}}) = \begin{bmatrix} \mathbf{K}^{(1)}(\Omega_l, \mathbf{x}_k^{\text{src}}) & \mathbf{K}^{(2)}(\Omega_l, \mathbf{x}_k^{\text{src}}) \end{bmatrix}, \quad (5.26)$$

where the  $p$ -th column of  $\mathbf{K}^{(j)}(\Omega_l, \mathbf{x}_k^{\text{src}})$  is given by  $\frac{\partial \mathbf{u}(\Omega_l, \mathbf{x}_k^{\text{src}})}{\partial m_p^{(j)}}$ . Then from Eq.(5.11)

$$\mathbf{K}^{(j)}(\Omega_l, \mathbf{x}_k^{\text{src}}) = \mathbf{S}^{-1}(\Omega_l) \mathbf{F}^{(j)}(\Omega_l, \mathbf{x}_k^{\text{src}}), \quad (5.27)$$

where  $\mathbf{F}^{(j)}(\Omega_l, \mathbf{x}_k^{\text{src}})$  is a matrix containing the virtual sources for each model parameter, and the  $p$ -th column of  $\mathbf{F}^{(i)}(\Omega, \mathbf{x}_k^{\text{src}})$  is given by

$$\mathbf{F}_p^{(j)}(\Omega_l, \mathbf{x}_k^{\text{src}}) = -\frac{\partial \mathbf{S}(\Omega_l)}{\partial m_p^{(j)}} \mathbf{u}(\Omega_l, \mathbf{x}_k^{\text{src}}). \quad (5.28)$$

The partial derivative  $\frac{\partial \mathbf{S}(\Omega)}{\partial m_k^{(j)}}$  may be interpreted as a ‘radiation pattern’ describing the scattering of the incident wavefield  $\mathbf{u}$  by the virtual sources (Beylkin & Burridge, 1990;

Malinowski et al., 2011). From Eqs (5.23) - (5.26),

$$\nabla_{\mathbf{m}^{(j)}} E = \sum_{l=1}^{N_\Omega} \sum_{k=1}^{N_s} \Re \left[ (\mathbf{F}^{(j)}(\Omega_l, \mathbf{x}_k^{\text{src}}))^t \mathbf{v}(\Omega_l, \mathbf{x}_k^{\text{src}}) \right], \quad (5.29)$$

where  $^t$  indicates the transpose of the matrix without a complex conjugation, and  $\mathbf{v}(\Omega, \mathbf{x}_k^{\text{src}})$  is the ‘backpropagated wavefield’

$$\mathbf{v}(\Omega_l, \mathbf{x}_k^{\text{src}}) = \mathbf{S}^{-1}(\Omega_l) [\delta \mathbf{d}(\Omega_l, \mathbf{x}_k^{\text{src}})]^*, \quad (5.30)$$

interpreted as the forward propagation of time-reversed (conjugated) residual wavefields (Pratt et al., 1998). We observe from Eq.(5.29) that the gradient is formed by a weighted convolution of the backpropagated residuals with the virtual source, and we interpret  $\frac{\partial \mathbf{S}(\Omega)}{\partial m_k^{(j)}}$  as a weighting term. (In Appendix Appendix 5.B, we describe an alternative form of the model gradient based on a correlation rather than convolution.)

### 5.2.3.2 Numerical implementation

In the development above, we have not specified the model parametrization for the velocity and attenuation classes. Interestingly, the only term dependent on the parametrization is  $\frac{\partial \mathbf{S}(\Omega)}{\partial m_k^{(j)}}$  in Eq.(5.28), i.e. the radiation pattern of the virtual sources, which acts as a weighting term on the convolution between the observed and backpropagated fields.

In acoustic waveform inversion, a slowness parametrization is typically used for its relatively linearity with respect to the phase of the waveforms (Sirgue & Pratt, 2004). For attenuation, a variety of parametrizations have been proposed: The imaginary part of complex-valued velocity (Song et al., 1995; Liao & McMechan, 1996), the imaginary part of the complex-valued slowness (Pratt et al., 2004),  $Q^{-1}$  (Kamei & Pratt, 2008),  $Q$  (Malinowski et al., 2011), and the imaginary parts of the squared complex-valued slowness (Hak & Mulder, 2010, 2011). By analogy to the slowness parametrization in the acoustic case, we choose

$$\mathbf{m}^{(1)} = \mathbf{s}_o^{(r)} = \Re [\mathbf{s}(\omega_o)], \quad (5.31)$$

$$\mathbf{m}^{(2)} = \mathbf{s}_o^{(i)} = \Im [\mathbf{s}(\omega_o)], \quad (5.32)$$

and we assume  $\mathbf{s}_o^{(i)}$  to be strictly non-negative (i.e. positive attenuation). Note that our parametrization is based on the complex slowness at a reference frequency  $\omega_o$ , and therefore is independent of the frequency set used for the forward modelling. (The frequency-dependent complex slowness,  $\mathbf{s}(\omega)$ , required for the forward modelling is recalculated

using Eqs(5.9) and (5.10) after updating  $\mathbf{s}_o$ .)

Instead of directly calculating the gradient with respect to  $\mathbf{s}_o^{(r)}$  and  $\mathbf{s}_o^{(i)}$ , we conduct two-step gradient calculation: First the model gradient is calculated at the current frequency  $\omega_l$  with respect to  $\mathbf{s}^{(r)}(\omega_l) = \Re[\mathbf{s}(\omega_l)]$ , and  $\mathbf{s}^{(i)}(\omega_l) = \Im[\mathbf{s}(\omega_l)]$ , where  $\omega_l = \Re(\Omega_l)$ , and then using the Jacobian of the coordinate change,  $\mathbf{J} = \frac{\partial(\mathbf{s}^{(r)}, \mathbf{s}^{(i)})}{\partial(\mathbf{s}_o^{(r)}, \mathbf{s}_o^{(i)})}$ , we obtain the model gradient at the reference frequency  $\omega_o$  with respect to  $\mathbf{s}_o^{(r)} = \Re[\mathbf{s}_o]$  and  $\mathbf{s}_o^{(i)} = \Im[\mathbf{s}_o]$  (see Section 5.2.3.3 below). This implementation is chosen i) because the gradient with respect to  $\mathbf{s}^{(r)}(\omega_l)$ , and  $\mathbf{s}^{(i)}(\omega_l)$  can be given in a simpler form than the gradient with respect to  $\mathbf{s}_o^{(r)}$  and  $\mathbf{s}_o^{(i)}$ , and also ii) because we can readily expand the formulation to any arbitrary parametrization (e.g.  $Q^{-1}$  instead of  $\mathbf{s}_o^{(i)}$ ) by defining the appropriate alternative Jacobian matrix. (A similar approach was also used by Hak & Mulder (2011) for the squared slowness parametrization.)

From Eq.(5.6), assuming a simple second-order finite difference scheme (Pratt & Worthington, 1990), we obtain

$$\frac{\partial S_{qr}(\Omega_l)}{\partial s_p^{(r)}(\omega_l)} = \delta_{pq} \delta_{qr} \Omega^2 \frac{\partial}{\partial s_p^{(r)}(\omega_l)} (c_q^{-2}(\omega_l)) = 2\delta_{pq} \delta_{qr} \Omega_l^2 s_p(\omega_l), \quad (5.33)$$

$$\frac{\partial S_{qr}(\Omega)}{\partial s_p^{(i)}(\omega_l)} = \delta_{pq} \delta_{qr} \Omega^2 \frac{\partial}{\partial s_p^{(i)}(\omega_l)} (c_q^{-2}(\omega_l)) = 2i\delta_{pq} \delta_{qr} \Omega_l^2 s_p(\omega_l), \quad (5.34)$$

(note we do not use an implied summation notation here). These equations imply that the partial derivative of the impedance matrix is zero everywhere except at  $\mathbf{x}_p$ . Thus from Eq.(5.28), the virtual source matrices for each parameter class are diagonal with a diagonal term equal to  $2\Omega_p^2 s_p(\omega_l)$  for the velocity parameter, and  $2i\Omega_p^2 s_p(\omega_l)$  for the attenuation parameter. Therefore the virtual sources for two parameter classes, have the same amplitude, but have a 90-degree phase-shift. From Eq.(5.27), these properties are also shared by the Fréchet derivatives of two parameter classes  $\frac{\partial \mathbf{u}(\Omega_l, \mathbf{x}_k^{\text{src}})}{\partial \mathbf{s}^{(r)}}$ , and  $\frac{\partial \mathbf{u}(\Omega_l, \mathbf{x}_k^{\text{src}})}{\partial \mathbf{s}^{(i)}}$ , (i.e. the forward wavefields generated from the virtual sources). The perturbation in the data

$$\delta \mathbf{u} = \left[ \frac{\partial \mathbf{u}(\Omega_l, \mathbf{x}_k^{\text{src}})}{\partial \mathbf{s}^{(r)}} \right]^T \delta \mathbf{s}^{(r)} + \left[ \frac{\partial \mathbf{u}(\Omega_l, \mathbf{x}_k^{\text{src}})}{\partial \mathbf{s}^{(i)}} \right]^T \delta \mathbf{s}^{(i)}. \quad (5.35)$$

Thus if we perturb  $\mathbf{s}^{(r)}$  and  $\mathbf{s}^{(i)}$  by the same amount, the perturbation in the data is governed by  $\delta \mathbf{s}^{(r)}$ , since  $\frac{s_p^{(i)}(\omega_l)}{2s_p^{(r)}(\omega_l)} = Q^{-1} \ll 1$ . In other words, the sensitivity of seismic waveforms to  $\mathbf{s}^{(i)}$  will be much smaller than  $\mathbf{s}^{(r)}$ . (A similar discussion was provided for velocity -  $Q$  parametrization by Malinowski et al. (2011).) Therefore, if the two model parameter classes are equally far from the true models, the largest singular values of the Fréchet derivative matrix for this choice of parametrization are likely to be associated

with a velocity perturbation rather than attenuation parameters. (Note that the re-scaling of the parameter classes by for example a model weighting matrix does not solve this issue, and still leads to an ill-conditioned Fréchet derivative matrix.)

From Eq.(5.29), the gradient becomes

$$\nabla_{\mathbf{s}^{(r)}(\omega_l)} E = \Re[\boldsymbol{\eta}(\omega_l)], \quad (5.36)$$

$$\nabla_{\mathbf{s}^{(i)}(\omega_l)} E = \Im[\boldsymbol{\eta}(\omega_l)], \quad (5.37)$$

where

$$\eta_p(\omega) = -2 \sum_{l=1}^{N_\Omega} \sum_{k=1}^{N_s} \Omega_l^2 [u_p(\Omega_l, \mathbf{x}_k^{\text{src}}) s_p(\omega_l) v_p(\Omega_l, \mathbf{x}_k^{\text{src}})]^*, \quad (5.38)$$

is the weighted convolution between the predicted and backpropagated wavefields at  $\mathbf{x}_p$  over all source-receiver pairs. The phase of  $\boldsymbol{\eta}(\omega_l)$ ,  $\arg(\boldsymbol{\eta}(\omega_l))$  distributes the weighted convolution between the observed and backpropagated wavefields into the velocity and attenuation components of the gradient.

Therefore ideally  $\arg(|\nabla_{\mathbf{s}^{(i)}(\omega_l)} E| / |\nabla_{\mathbf{s}^{(r)}(\omega_l)} E|) = \arg(\eta_p(\omega_l))$  approximates  $\arg(\delta s_p(\omega_l))$  where  $\delta s_p(\omega_l) = s_p(\omega_l) - s_{p,\text{true}}(\omega_l)$  in order to find the optimal steepest descent direction. However the convolution  $\eta_p(\omega_l)$  depends on errors in model parameters  $\mathbf{s}$  everywhere along the wavepaths (not only at  $\mathbf{x}_p$ ), caused by imperfect subsurface illumination due to the survey geometry, and by limited band-width of data. The convolution is further contaminated by data noise, and by modelization errors appearing in the residuals, including elastic effects not accounted for by the visco-acoustic assumption. Therefore the condition  $\arg(\eta_p(\omega_l)) \sim \arg(\delta s_p(\omega_l))$  is not guaranteed, and the gradient will contain cross-talk from the other parameter class. Some of the factors contributing to the cross-talk mentioned above can be mitigated by iterative inversion, or by data preprocessing, but most are native to the acquisition design and the inherent physical assumptions in the visco-acoustic model. Thus the cross-talk is inevitable and probably persistent throughout the inversion between the classes of parameters.

The inverse or approximate inverse of the Hessian matrix may be useful as a preconditioner to reduce the cross-talk, since the Hessian itself describes the defocusing of the gradient arising from incomplete illumination and limited bandwidth (Pratt et al., 1998). Particular off-diagonal elements of the Hessian  $\left(\frac{\partial^2 E}{\partial m_i^{(1)} \partial m_j^{(2)}}\right)$  describe the interaction between parameter classes (Kennett & Sambridge, 1998). The Hessian matrix is computationally expensive to invert, however the inverse Hessian can be approximated by computationally affordable L-BFGS (Brossier et al., 2009), truncated Gaussian (Métivier et al., 2012), or implicit Jacobian methods (Abubakar et al., 2012). What is more, the



Hessian is ill-conditioned due to the strong coupling between the velocity and attenuation components of the Fréchet derivative. Therefore we did not employ the Hessian matrix or its inverse in this study.

Alternatively, the cross-talk may be suppressed by a variety of regularization methods. For example, penalizing the attenuation component of the gradient may be helpful, as data show much weaker sensitivities to the attenuation parameter than to the velocity parameter. This motivates us to suggest the simple gradient preconditioning matrix proposed in Eq.(5.20), in which the key regularization parameter is the attenuation penalty term  $\xi$ . As described in Section 5.2.3, small values of  $\xi$  will eliminate artifacts in the attenuation model corresponding to small singular values. As some cross-talk may have larger singular values than the actual components of the model, additional regularization perhaps through smoothness constraints may need to be combined with the penalty (Scales et al., 1990).

As an alternative to regularization, we may invert the model parameters according to the hierarchical order of the sensitivity, an approach called sequential inversion (Watanabe et al., 2004; Pratt et al., 2004; Kamei & Pratt, 2008), in which we initially invert for the velocity model while fixing the attenuation model, and we update the attenuation parameters only after a highly accurate velocity model is obtained. This later approach assumes the velocity parameters are physically nearly-independent of the attenuation parameters, and allows us to restrict the search space in the second stage. We test both approaches in the sections to follow.

### 5.2.3.3 Coordinate change to reference frequency

We derived the gradient with respect to the current frequency  $\omega_l$  in Eqs (5.36) and (5.37). However as defined in Eqs (5.31) and (5.32), our parametrization classes are the slownesses  $\mathbf{s}_o^{(r)}$  and  $\mathbf{s}_o^{(i)}$  at the reference frequency  $\omega_o$ , which are independent of the modelling frequency. The coordinate change is

$$\begin{bmatrix} \frac{\partial E(\Omega_l)}{\partial s_{op}^{(r)}} \\ \frac{\partial E(\Omega_l)}{\partial s_{op}^{(i)}} \end{bmatrix} = \mathbf{J}(\omega_l) \begin{bmatrix} \frac{\partial E(\Omega_l)}{\partial s_p^{(r)}(\omega_l)} \\ \frac{\partial E(\Omega_l)}{\partial s_p^{(i)}(\omega_l)} \end{bmatrix}. \quad (5.39)$$

Table 5.2: Correlation lengths used to generate the model:  $a_x$  and  $a_z$  are the correlation lengths for x- and z-directions,  $a_x/\lambda_{800}$  and  $a_z/\lambda_{800}$  indicate the size of the heterogeneities relative to  $\lambda_{800}$ , where  $\lambda_{800}$  is the mean wavelength of each layer at 800 Hz, the highest frequency used for the inversion.

Layer	$a_x$ [m]	$a_z$ [m]	$a_x/\lambda_{800}$	$a_z/\lambda_{800}$
1	20.0	2.0	3.6	0.36
2	20.0	5.0	3.3	0.79
3	20.0	1.0	3.3	0.17

where  $\mathbf{J}^s(\omega_l)$  is the Jacobian of the coordinate change, and may be formed from the dispersion relationship defined in Eq.(5.10), so that

$$\begin{aligned} \mathbf{J}(\omega_l) &= \frac{\partial(s_p^{(r)}(\omega_l), s_p^{(i)}(\omega_l))}{\partial(s_{op}^{(r)}, s_{op}^{(i)})} \\ &= \begin{bmatrix} 1 & -2 \left( \frac{s_{op}^{(i)}}{s_{op}^{(r)}} \right)^2 \ln \left( \frac{\omega_l}{\omega_o} \right) \\ -\frac{2}{\pi} \ln \left( \frac{\omega_l}{\omega_o} \right) & 1 - \frac{2}{\pi} \frac{s_{op}^{(i)}}{s_{op}^{(r)}} \ln \left( \frac{\omega_l}{\omega_o} \right) \end{bmatrix} \end{aligned} \quad (5.40)$$

$$\sim \begin{bmatrix} 1 & 0 \\ -\frac{2}{\pi} \ln \left( \frac{\omega_l}{\omega_o} \right) & 1 \end{bmatrix}, \quad (Q^{-1} \ll 1). \quad (5.41)$$

The off-diagonal terms of this Jacobian map the effects of velocity dispersion relationship between two parameters; this correction increases as  $\omega_l$  diverges from  $\omega_o$ , and the most significant component of the Jacobian is the mapping from the velocity to the attenuation class. For  $Q_p^{-1} \ll 1$ , the Jacobian does not depend on the slowness model, as  $\frac{s_{op}^{(i)}}{s_{op}^{(r)}} \ll 1$  from Eq.(5.9). The velocity component becomes independent of the gradient of attenuation parameters. Note that this is a local coordinate change at  $\mathbf{x}_p$  to correct for the dispersion relationship, and does not influence the discussion regarding the cross-talk given above.

## 5.3 Synthetic tests

### 5.3.1 Model description and waveforms

We conduct visco-acoustic waveform inversion tests using the cross-well survey geometry following Song et al. (1995), Liao & McMechan (1996), and Pratt et al. (2004). The geometry provides a superior subsurface illumination than the surface survey geometry, and is amenable to mitigate the cross-talk between two parameter classes (Hak & Mulder (2010)). We created a three-layer model consisting of sedimentary rocks of generic sand-

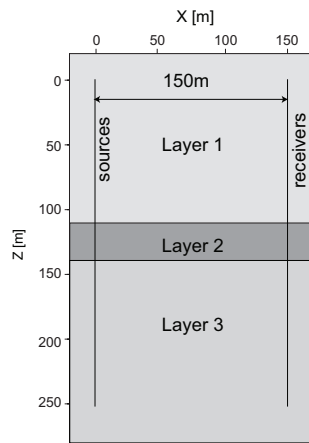


Figure 5.1: Schematic model of a synthetic cross-well survey test after Kamei & Pratt (2008). Source and receiver wells are located 150 m apart, and indicated by two vertical solid lines

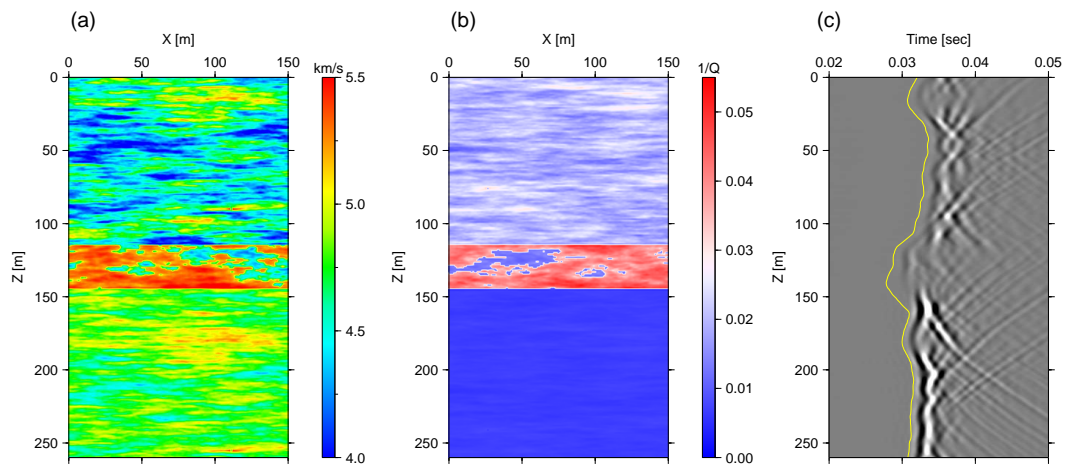


Figure 5.2: (a) True velocity model, (b) true attenuation model, (c) synthesized common-level gather. Yellow curve indicates the first arrivals.

Table 5.3: Probability distribution used to generate the model:  $r_{v_1}$  and  $r_{Q_1^{-1}}$  are the ratio of sandstone,  $\mu_{v_1}$  and  $\sigma_{v_1}$  are the mean and standard deviation of velocity distribution for sandstone, and  $\mu_{v_2}$  and  $\sigma_{v_2}$  are for shale.  $\mu_{Q_1^{-1}}$  and  $\sigma_{Q_1^{-1}}$  are the mean and standard deviation of  $Q^{-1}$  distribution for sandstone,  $\mu_{Q_1^{-1}}$  and  $\sigma_{Q_1^{-1}}$  for shale.

Layer	$r_{v_1}$ [%]	$\mu_{v_1}$ [km/s]	$\sigma_{v_1}$ [km/s]	$\mu_{v_2}$ [km/s]	$\sigma_{v_2}$ [km/s]	$r_{Q_1^{-1}}$ [%]	$\mu_{Q_1^{-1}}$	$\sigma_{Q_1^{-1}}$	$\mu_{Q_2^{-1}}$	$\sigma_{Q_2^{-1}}$
1 (sand)	100	4.5	0.25	N/A	N/A	100	0.020	0.0030	N/A	N/A
2 (sand&shale)	30	4.5	0.20	5.3	0.1	30	0.0133	0.0013	0.040	0.004
3 (sand)	100	4.8	0.15	N/A	N/A	100	0.0067	0.0033	N/A	N/A

stone and shale properties. The schematic model is shown in Fig. 5.1, and the actual velocity and attenuation model is shown in Fig. 5.2. The model is 190 m wide, and 300 m deep. Source (left) and receiver (right) wells are located with a 150 m horizontal separation, and 265 sources and receivers are deployed at 1 m vertical intervals.

We assume that sandstone is characterized by relatively strong velocity fluctuations, and by weak intrinsic attenuation, and that the shale is strongly attenuative but contains small heterogeneities. The three layers have the following characteristics: 1) The top layer (135 m thickness) comprises only sandstone, and strong scattering attenuation is expected. 2) The middle layer (30 m thickness) is shale-rich, and intrinsic attenuation is dominant. 3) The bottom layer (135 m thickness) is again a sandstone layer with only weak intrinsic attenuation, and with smaller velocity fluctuations than in layer 2. The synthetic velocity and attenuation models were deliberately left uncorrelated to allow the parameter resolution of the inversion approaches to be evaluated.

We followed the methodology described in Yamazaki & Shinozuka (1988) and Kamei, R., Hato, M. (2005), and employed a spectral-based approach to generate the randomly heterogeneous velocity and  $Q^{-1}$  models. The random heterogeneities were assigned into each layer by a two-dimensional ellipsoidal self-similar correlation function using parameters described in Table 5.2 (Frankel & Clayton, 1986; Ikelle et al., 1993; Yamazaki & Shinozuka, 1988). The correlation lengths for the vertical direction ( $a_z$ ) were selected to be less than a half wavelength (the approximate resolution of visco-acoustic waveform inversion estimated by Wu & Toksoz (1987)) for most of the frequency range used in the inversion, and we assumed a longer correlation length for the horizontal direction ( $a_x$ ) than  $a_z$ . The sub-resolution  $a_z$  insures the inclusion of scattering effects in our waveform inversion tests. While the same correlation lengths were assigned to the velocity and attenuation models, we generated the velocity and attenuation models independently, so that the two model parameters are uncorrelated. The probability distribution of the model parameters was assumed to be a Gaussian function for Layer 1 and 3 which consist of sandstone, and a bimodal superposition of two Gaussian functions for Layer 2 to represent sandstone and shale. We describe the parameters of the probability distribution in Table 5.3.

We modelled visco-acoustic Laplace-Fourier domain seismic wavefields between 100 - 850 Hz using the finite-difference modelling algorithm described in Section 5.2.2. We used a source wavelet with a central frequency at 500 Hz, and set the reference frequency,  $\omega_o$ , to be 100 Hz. We assigned a 1 m  $\times$  1 m grid elements to discretize the model, small enough to avoid the numerical dispersion (Jo et al., 1996). We employed two  $\tau$  values in this study;  $\tau = 0.051$ , and 0.0015 sec.

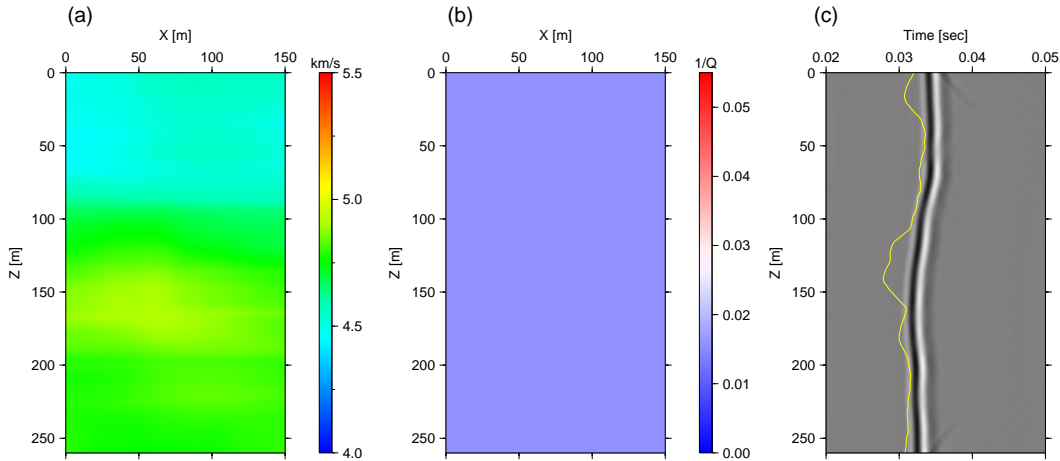


Figure 5.3: (a) Initial velocity model, (b) initial attenuation model, and (c) synthesized common level gather.

We display a time-domain common-level synthetic gather in Fig. 5.2c: The gather shows waveforms which are generated and received at the same depths. We obtained the gather by applying the inverse Laplace-Fourier transform to the Laplace-Fourier domain seismic wavefields generated by using  $\tau = 0.051$  sec. The  $\tau$  value was selected as 40 % of the record length (0.275 sec) to suppress the wrap-around effects as described by Brenders & Pratt (2007), and has a negligible effect on actual seismic waveforms. In Layer 1, the amplitudes of waveforms are relatively small when compared to Layer 3, and strong scattered arrivals are visible: These are due to the strong heterogeneities in the velocity structure of Layer 1. The synthetic waveforms in Layer 2 exhibit larger amplitude decays, but do not contain the scattered arrivals: The amplitude decay is largely due to the attenuative shale, rather than the heterogeneities in the velocity model. Layer 3 creates some scattering, but the amplitude decay is not evident as the perturbations in this layer are small, and as the intrinsic attenuation is very weak.

### 5.3.2 Inversion settings

We start inversion tests using the Laplace-Fourier wavefields generated with  $\tau = 0.051$  sec (sections 5.3.4 - 5.3.6): These inversion tests can be considered as an equivalent to pure frequency-domain waveform inversion because of the negligible damping effects. We first examine the effects of cross-talk between two parameter classes in Section 5.3.3. We then examine the simultaneous inversion approach in Section 5.3.4, and the sequential inversion approach Section 5.3.5. In these tests, we also evaluate the effects of the

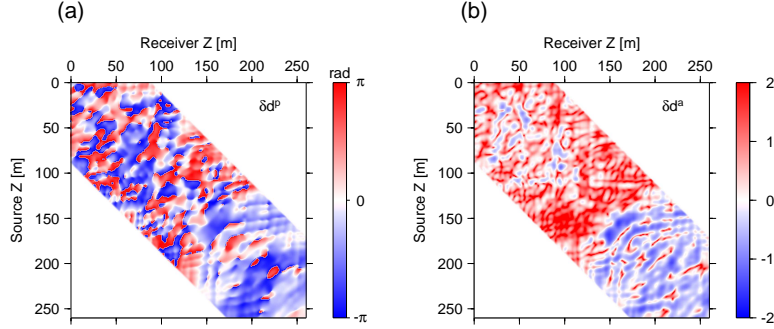


Figure 5.4: (Left) Phase residuals and (right) logarithmic amplitude residuals of the starting model at 500 Hz and  $\tau = 0.051$  sec.

attenuation penalty term  $\xi$  introduced in Section 5.2.3. In Section 5.3.6, we investigate the significance of smoothness constraints on stabilizing attenuation inversion. Then in Section 5.3.7, we explore the effects of stronger time-damping ( $\tau = 0.0015$  sec) on both the simultaneous and sequential inversion approaches. Finally we examine the sensitivity of visco-acoustic waveform inversion to data noise in Section 5.3.8.

As described in Section 5.2.3, we invert synthetic wavefields for real and imaginary parts of the complex-valued slowness at the reference frequency,  $\mathbf{s}_0^{(r)}$  and  $\mathbf{s}_0^{(i)}$ . After the inversion, we then extract  $Q^{-1}$  from the slowness parameters using Eq.(5.9), and we display the results as an attenuation model. Our observed data in sections 5.3.4 - 5.3.7 are Laplace-Fourier wavefields directly generated by the finite difference algorithm, instead of applying the Laplace-Fourier transform to the time-domain data in Fig. 5.2c. This is to avoid potential inversion errors arising from any data preprocessing and the forward and inverse transforms. In contrast, the observed data for the noise tests in Section 5.3.8 are generated by adding a Gaussian noise to the time-domain wavefields before converting to the Laplace-Fourier domain. We used 13 mono-frequency components in intervals of 50 Hz between 200 and 800 Hz. The frequency range is chosen to be valid for 1 m grids, and the frequency intervals are chosen by experiments to be as coarse as possible without significantly degrading the resultant images. We did not use multifrequencies as most of the inversions were conducted with noise-free synthetic data, and also as multifrequency tests (not shown) did not change our conclusions for cross-talk effects. We used a source wavelet estimated from a field cross-well data inverted by Pratt et al. (2008). Starting from the lowest frequency (200 Hz), model parameters are updated using 20 iterations at each frequency, before moving to the optimization of a higher frequency component. The source wavelet is updated after each iteration using the method described in Pratt (1999).

Our starting velocity model is a smoothed version of the true velocity model. We

generated this model by taking a  $150 \text{ m} \times 150 \text{ m}$  moving average of the original model shown in Fig. 5.3a. We generated a homogeneous model of  $Q^{-1}=0.0156$  (the average of the true model), and used this as a starting attenuation model. We computed synthetic waveforms from the starting model using the true source wavelet, and we display the common level gather in Fig. 5.3c with hand-picked arrivals in yellow. The predicted first arrivals from the starting model are mostly within a half cycle from the observed first arrivals in Layer 1 and 3, demonstrating the starting model will not cause a significant cycle-skipping problem in these layers (Song et al., 1995). We also display the frequency-domain residuals at 500 Hz for  $\tau = 0.051$  sec in Fig. 5.4: Instead of showing the conventional residual in Eq.(5.15), we show the phase residual,  $\delta d_j^p = \arg(u_j) - \arg(d_j)$  in Eq.(5.16), and the logarithmic amplitude residual,  $\delta d_j^a = \log(|u_j|/|d_j|)$  (Pyun et al., 2007). The phase residuals are large in Layer 1 and 2 due to the lack of heterogeneities in the model, and the lack of information from the shale (Layer 2) in the starting velocity model. Many ‘fringes’ in the phase residuals suggest potential cycle skipping at these traces at 500 Hz. Most of these fringes disappear at the lowest frequency used for the inversion. The amplitude residuals indicate that the starting model overestimates the amplitudes in Layer 1 and 2, and underestimate the amplitudes in Layer 3.

We precondition the model gradient using  $\mathbf{P}$  in Eq.(5.20), and by applying a smoothing operator at each step. We examine three values of  $\xi$ ; 1.0, 0.1 and 0.01. The condition  $\xi = 1.0$  indicates that no scaling nor implicit regularization is applied to the model gradient. As we decrease the value of  $\xi$ , the attenuation component of the gradient is penalized. When  $\xi < 0.001$ , the update on the attenuation model is almost entirely suppressed.

We apply smoothness constraints by preconditioning the model gradient using an elliptic low-pass wavenumber filter (Sirgue & Pratt, 2004). The filter is intended to suppress oscillations beyond the theoretical limit of waveform inversion,  $\kappa_o = 2\omega/c$ , where  $c$  is the phase-velocity (Wu & Toksoz, 1987). We select cut-off wavenumbers relative to  $\kappa_o$ , and set  $c = 4.5 \text{ km/s}$  (the average of the true velocity model) throughout this study. We start with applying a weak wavenumber filter to the both components of the model gradient in sections 5.3.3 - 5.3.5: The high-cut wavenumber is selected to be  $3\kappa_o/4$  and tapered off at  $\kappa_o$ , and the aspect ratio of the elliptic filter is set as  $1/2$  (we refer to this filter as Filter 1). In sections 5.3.6 - 5.3.8, we test a stronger wavenumber filter, which has cut-off wavenumbers of  $\kappa_o/2$  with a tapering area of  $\kappa_o/4$ , and aspect ratio of  $1/4$ . We refer to this filter as Filter 2.



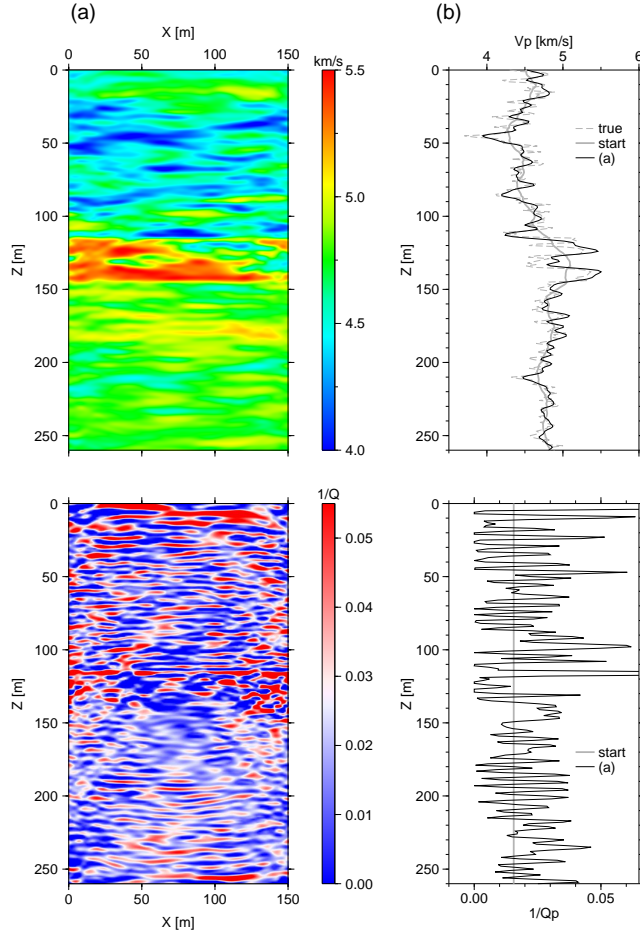


Figure 5.5: Impact of cross-talk on attenuation imaging: Simultaneous inversion results of Data-V. (Top) Velocity models and (bottom) the attenuation models obtained by simultaneous inversion with  $\xi = 1.0$ . (b) Vertical profiles of at  $X = 50$  m. Black lines indicate the inversion results, thick solid grey line the starting models, and grey dashed line the true models.

### 5.3.3 Effects of cross-talk

Before describing the inversion of the synthetic data set generated in Section 5.3.1, we first examine the effects of the cross-talk between velocity and attenuation parameters by creating and inverting two new visco-acoustic data sets. Each of the data set was generated from a subsurface model by perturbing only one of two model parameter classes from the starting models: The first data set was generated from the three-layered velocity model in Fig. 5.2a and the starting homogeneous attenuation model in Fig. 5.3b (we refer to this data set as Data-V), and the second data set from the three-layered attenuation model in Fig. 5.2b and the starting smooth velocity model in Fig. 5.3a (we refer to this data set as Data-Q). Any perturbation in the attenuation model inverted from Data-V

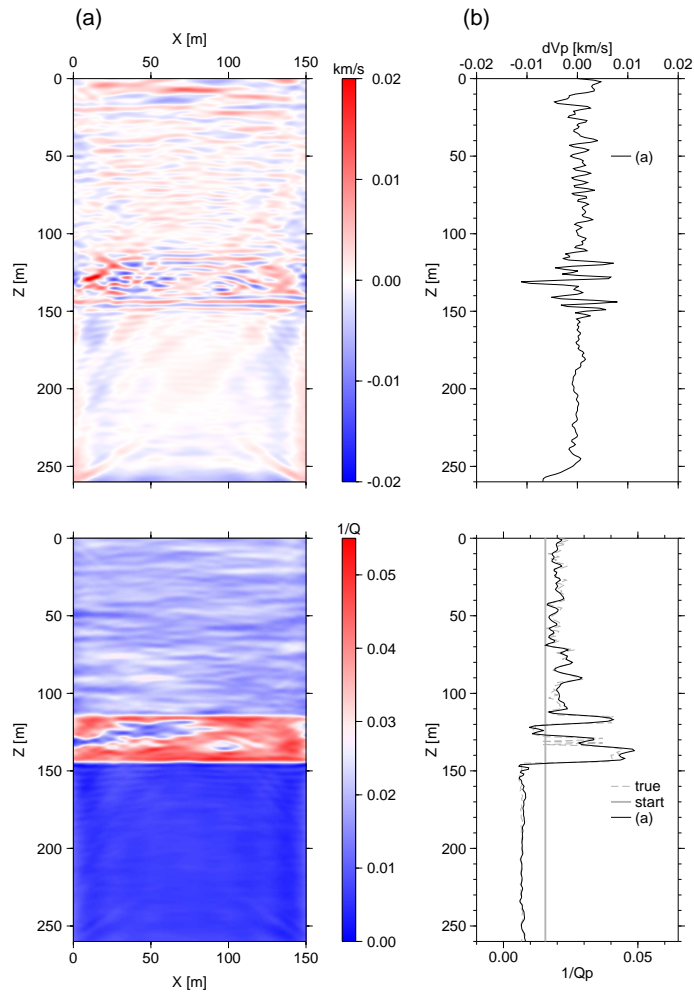


Figure 5.6: Impact of cross-talk on velocity imaging: Simultaneous inversion results of Data-Q. (Top) Errors in the inverted velocity model, and (bottom) the attenuation model obtained by simultaneous inversion with  $\xi = 1.0$ . (b) Vertical profiles of (a) at  $X = 50$  m. Black lines indicate the inversion results, thick solid grey line the starting models, and grey dashed line the true models.

will illustrate the undesired cross-talk associated with the ‘leakage’ of the velocity update due to the imperfect convolution to form  $\boldsymbol{\eta}$  in Eq.(5.38). The inversion from Data-Q set will in turn illustrate the effect of leakage of the attenuation model in the velocity model.

Using Data-V and Data-Q, we simultaneously inverted for the velocity and attenuation models following the strategy described in Section 5.3.2 using  $\tau = 0.051$  sec, and  $\xi = 1.0$ . For both data sets, the objective function steadily decreased between 70 - 99 % per frequency during the inversion. The total conventional misfit function,

$$E_{total} = \sum_{200Hz}^{800Hz} \delta \mathbf{d}^T \delta \mathbf{d}, \quad (5.42)$$

was reduced by the inversion to less than 0.1 % of  $E_{total}$  in the starting model after the inversion of both data sets, indicating the excellence of the data fit. We display the resulting velocity and attenuation models in Fig. 5.5 for Data-V, and in Fig. 5.6 for Data-Q. Note in Fig. 5.6a, we depict errors in the inverted velocity model instead of absolute velocity values to visualize small discrepancies.

In both inversion experiments, we successfully retrieved the desired perturbed model parameters, i.e. the three layered velocity model for Data-V, and the three layered attenuation model for Data-Q. The artifacts arising from the cross-talk are indeed present as unphysical oscillations for both parameters classes, although only dominant in the attenuation model obtained by Data-V. We observe small oscillations ( $< 5$  % of the true value) in the velocity image obtained from Data-Q shown in Fig. 5.6a. The total conventional misfit  $E_{total}$  barely changes if we re-compute these with the inverted velocity model, and the true attenuation model for Data-V, or with the inverted attenuation model and the true velocity model for Data-Q. This suggests that the objective function is insensitive to the unphysical oscillations observed in the final inversion models, and therefore that the oscillatory artifacts are associated with very small singular values of the system. The oscillations were difficult to eliminate, and were persistent in the attenuation model obtained from Data-V even after a large number of iterations (up to 900 iterations per frequency). The form of the unphysical oscillations changed as the velocity model was refined by increasing the iteration number, since the unphysical oscillations are a result of leakage from the velocity gradient to the attenuation gradient due to the imperfect convolution in Eq.(5.38). We also conducted the inversion using a wide bandwidth, and a wide source-receiver aperture. These reduced the amplitudes of oscillations, but could not completely remove the artifacts.

The effects of the cross-talk are attributed to the unequal scaling between two model parameters as described in Section 5.2.3, and the insensitivity of the seismic waveforms

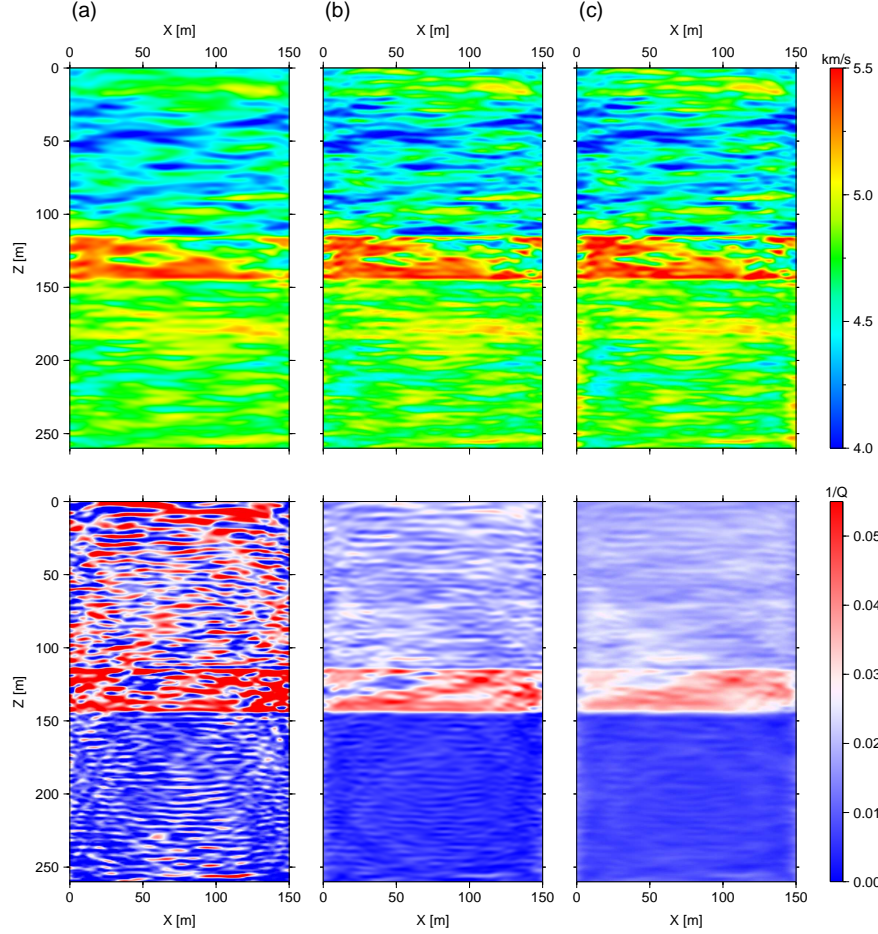


Figure 5.7: Simultaneous inversion results of noise-free data at  $\tau = 0.051$  sec generated from the model in Fig. 5.2: (Top) velocity models, and (bottom)  $Q^{-1}$  models obtained using (a)  $\xi = 1.0$  (b) 0.1, (c) 0.01.

to the unphysical oscillations. We found that the velocity and attenuation components of the model gradient were in fact similar in magnitudes for both experiments ( $0.5 < \left| \nabla_{\mathbf{s}_o^{(r)}} E \right| / \left| \nabla_{\mathbf{s}_o^{(i)}} E \right| < 2$ ), although  $|\delta s_o^{(i)}|$  is at least one-order smaller in magnitude than  $|\delta s_o^{(r)}|$ . Therefore when inverting Data-V, the unphysical attenuation update  $\alpha \gamma_{\mathbf{s}_o^{(i)}}$  induced by the cross-talk was large enough to deteriorate the attenuation image, since the steplength  $\alpha$  was chosen to update  $\mathbf{s}_o^{(r)}$ . In contrast, when Data-Q was inverted,  $\alpha$  was set optimal to update  $\mathbf{s}_o^{(i)}$  and therefore  $\alpha \gamma_{\mathbf{s}_o^{(r)}}$  is too small to influence the velocity image.

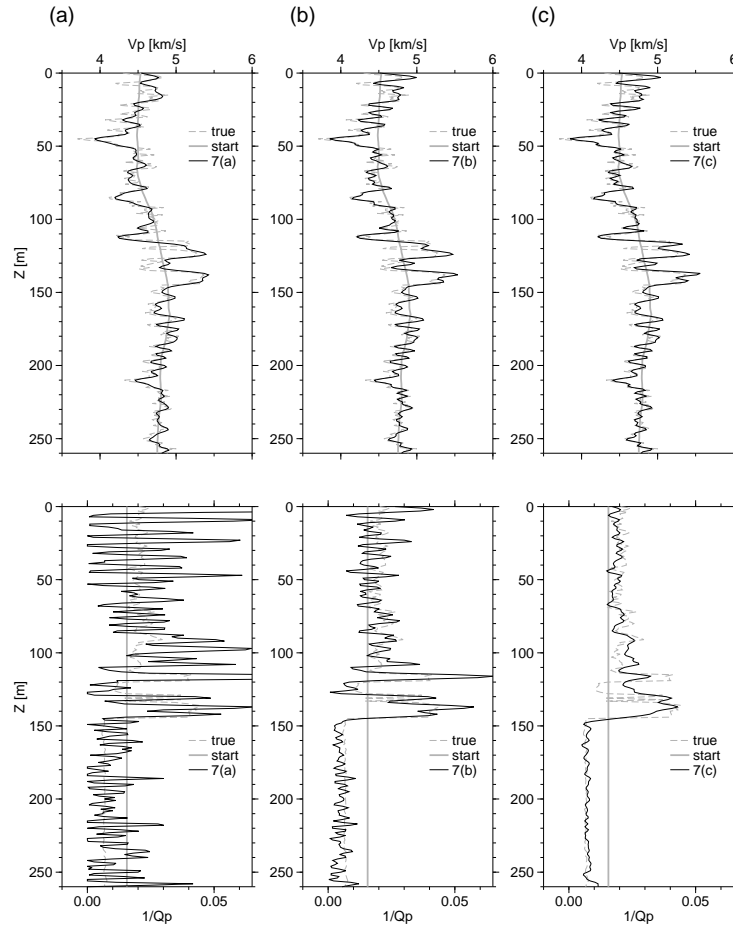


Figure 5.8: Vertical profiles of simultaneous inversion results shown in Fig. 5.7 at  $X = 50$  m: (Top) velocity models, and (bottom) attenuation models obtained using (a)  $\xi = 1.0$ , (b) 0.1, and (c) 0.01. Thick grey solid lines indicate the starting model, grey dashed lines the true model, black solid lines the inversion results.

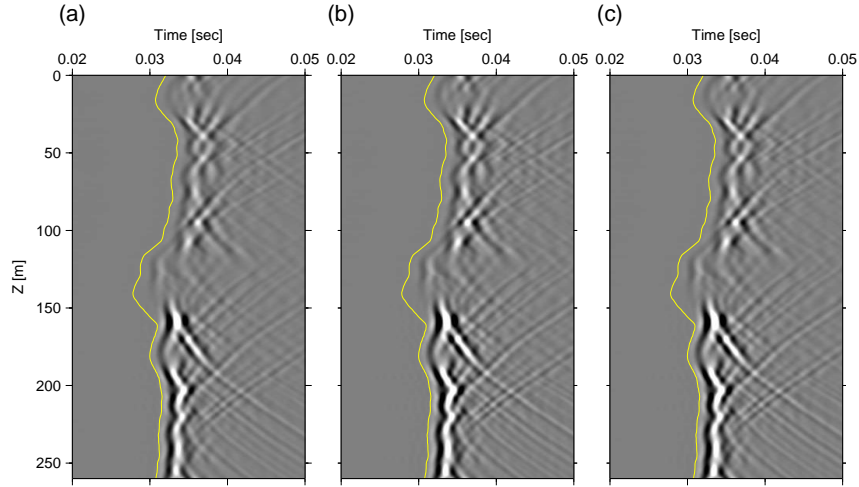


Figure 5.9: Synthetic common level gathers from the simultaneous waveform inversion results (Fig. 5.7) obtained using (a)  $\xi = 1.0$ , (b) 0.1, and (c) 0.01. These may be compared with the original data in Fig. 5.2c.

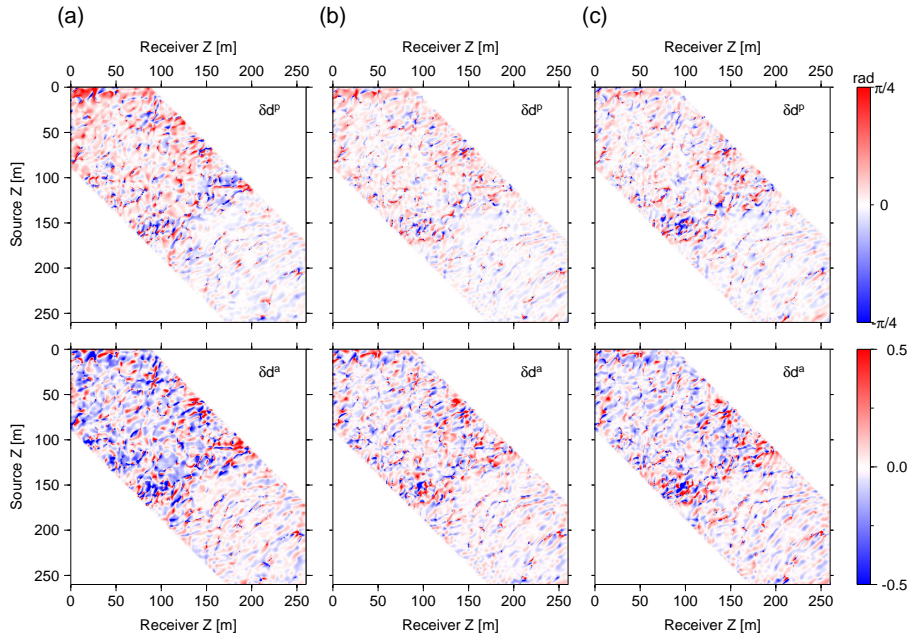


Figure 5.10: (Top) Phase residual ( $\delta d^P$ ) and (bottom) logarithmic amplitude residual ( $\delta d^A$ ) at 500 Hz and  $\tau = 0.051$  sec, computed from figures 5.7a-c. These may be compared with the residuals from the starting model in Fig. 5.4 (Note the range of colour bars differ from this figure).

### 5.3.4 Simultaneous inversion

We now describe the simultaneous inversion results of velocity and attenuation parameters using the Laplace-Fourier domain wavefields for  $\tau = 0.051$  sec generated from the original model as described in Section 5.3.1, and evaluate the effects of gradient preconditioning by varying the parameter  $\xi$  in Eq.(5.20). As described in Section 5.3.2 and applied in Section 5.3.3, both velocity and attenuation components of the model gradient were weakly smoothed by the wavenumber filter described in Section 5.3.2 as Filter 1.

We evaluated inversions for three values of  $\xi = 1.0, 0.1,$  and  $0.01$ . In all three inversion settings, the objective function decreased monotonically between 55 to 99 % per frequency. The reduction was largest at the lowest frequency (200 Hz), and smallest at the highest frequency (800 Hz). We display the resulting velocity and attenuation models in Fig. 5.7, and the vertical profiles at  $X = 50$  m in Fig. 5.8. To validate the waveform inversion results, we generated synthetic waveforms from the final models after re-estimating the source wavelet. The common-level gathers are displayed in Fig. 5.9. The Laplace-Fourier domain residuals from the final models are shown for  $\tau = 0.051$  sec in Fig. 5.10.

When the gradient was not scaled ( $\xi = 1.0$ ), the velocity model shows a good agreement with the true model, although slightly deficient in detailed features. The inverted attenuation model somewhat mimics the trend of attenuation values in three layers: Mild attenuation for Layer 1, strong attenuation for Layer 2, and weak attenuation for Layer 3. However the attenuation model contains strong unphysical oscillations, particularly in Layer 1 and 3. From the similarity of these oscillations to those in Fig. 5.5, we consider that the artifacts are caused by the cross-talk associated with the velocity updates.

By penalizing the attenuation parameters ( $\xi < 1.0$ ), we significantly suppressed the oscillations in the attenuation models, and also increased the resolution of the velocity model. At  $\xi = 0.1$ , waveform inversion delineated the two largest low attenuation anomalies in Layer 2. However the oscillations of attenuation parameters are still evident in Layer 1 and 3, and the  $Q^{-1}$  values in Layer 2 are overestimated. At  $\xi = 0.01$ , the attenuation model contains a very small level of oscillations, but as a trade-off, the low attenuation anomalies are overly smoothed in Layer 2. A larger number of iterations may have recovered these anomalies, but we stopped the inversion since the velocity model contains strong artifacts at the sides of the model, which became more significant as are increased the number of iterations. We consider that an optimal model may be obtained by choosing  $\xi$  between 0.01 and 0.1.

The discrepancies between the attenuation models are not quite obvious from the waveform fit (neither quantitatively nor qualitatively). The value of the total misfit

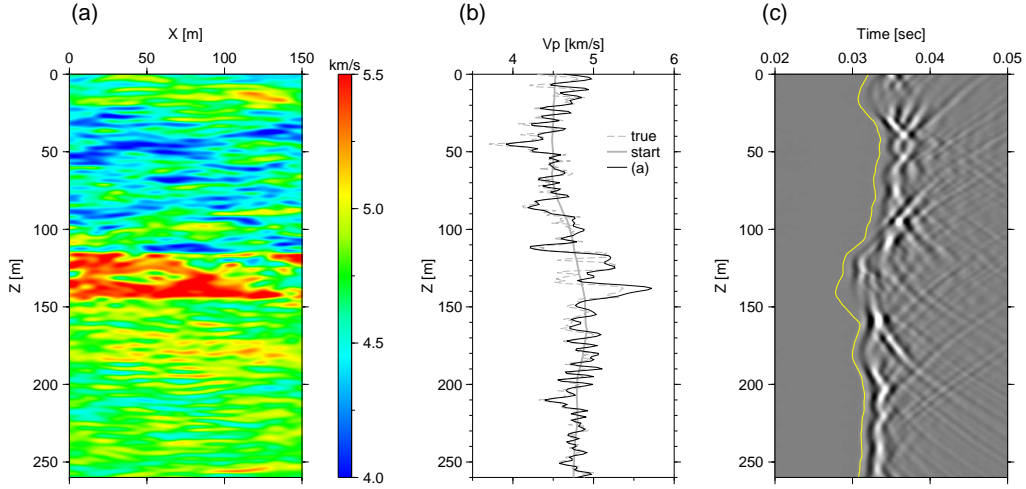


Figure 5.11: Stage 1 of sequential inversion tests of noise-free data at  $\tau = 0.051$  sec generated from Fig. 5.2: (a) Velocity model obtained by velocity inversion using the logarithmic phase-only objective function. (b) Vertical profile of (a) at  $X = 50$  m. Thick grey lines indicate the starting model, grey dashed lines the true model, black solid lines the inversion result. (c) Predicted common-level gather after velocity inversion.

function  $E_{total}$  computed from the final model is very small, and nearly identical for the three models: 0.85 % of the starting model for  $\xi = 1.0$ , 0.50 % for  $\xi = 0.1$ , and 0.65 % for  $\xi = 0.01$ . The predicted waveforms from all three inverted models reproduced well the features in the observed waveforms (Fig. 5.9), and significantly reduced the phase and amplitude residuals (Fig. 5.10). The discrepancies between the residuals are negligible between the inversion results from  $\xi = 0.1$  and 0.01. At  $\xi = 1.0$ , the phase residuals are slightly larger in Layer 1 than in the other models, due to the lack of small-scale heterogeneities in the final velocity model.

### 5.3.5 Sequential inversion

We used the same inversion settings as in Section 5.3.4, and evaluate the sequential inversion approach. We start the sequential inversion process by inverting for velocity parameters while fixing an attenuation model (stage 1). Then we invert for velocity and attenuation parameters starting from the stage 1 results (stage 2).

#### 5.3.5.1 Stage 1: Velocity inversion

We first inverted for the velocity model by minimizing the logarithmic phase-only objective function defined in Eq.(5.16) instead of the conventional objective function. The



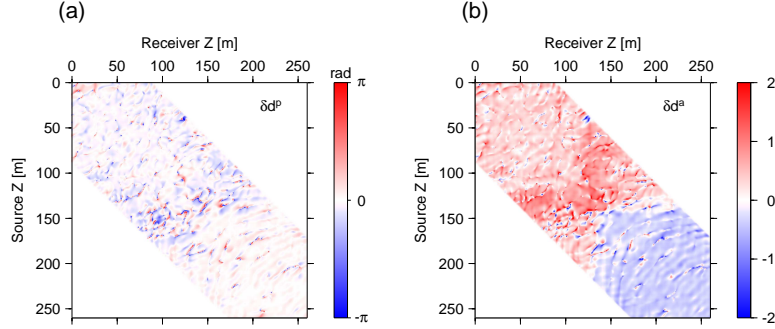


Figure 5.12: (Left) Phase residual ( $\delta\mathbf{d}^P$ ) and (right) logarithmic amplitude error ( $\delta\mathbf{d}^a$ ) after velocity inversion at 500 Hz and  $\tau = 0.051$  sec.

phase-only implementation allows us to focus on kinematic information, and to minimize artifacts arising from the incorrect attenuation model. In this inversion, we conducted 10 iterations per frequency instead of 20 iterations used in the previous sections: The obtained velocity model was sufficiently accurate after 10 iterations, and a larger number of iterations induced strong “X-shaped” artifacts probably due to a lack of an accurate attenuation model as observed for simultaneous inversion with  $\xi = 0.01$  in Section 5.3.4.

We display the inverted velocity model in Fig. 5.11 along with vertical profiles, and the predicted waveforms. The phase and amplitude residuals  $\delta\mathbf{d}^P$  and  $\delta\mathbf{d}^a$  after stage 1 are shown in Fig. 5.12. The obtained velocity model delineates detailed features in all three layers. When compared to the simultaneous inversion results, velocity-only inversion apparently retrieved slightly sharper structures in Layers 1 and 3. However in Layer 2, the resolution is slightly lower, and velocities are overestimated at some places, since errors in the attenuation model are most significant in this layer.

The predicted waveforms in Fig. 5.11a coincide very well with that of the observed waveforms displayed in Fig. 5.2c. The phase residuals  $\delta\mathbf{d}^P$  in Fig. 5.12a became almost negligible, which confirms that the kinematic component of the seismic waveforms were fit well by the velocity inversion. The amplitude residuals  $\delta\mathbf{d}^a$  shown in Fig. 5.12b are also much smaller than those of the starting model shown in Fig. 5.4b: This indicates that geometrical spreading effects were a substantial source of amplitude misfits at the starting model. The remaining amplitude residuals after the velocity inversion suggest that the predicted amplitudes are still larger in Layer 1 and 2, and smaller in Layer 3 than the observed values; this corresponds to the discrepancies between the starting and true attenuation model.

The observation can be further confirmed quantitatively by the decrease in misfit

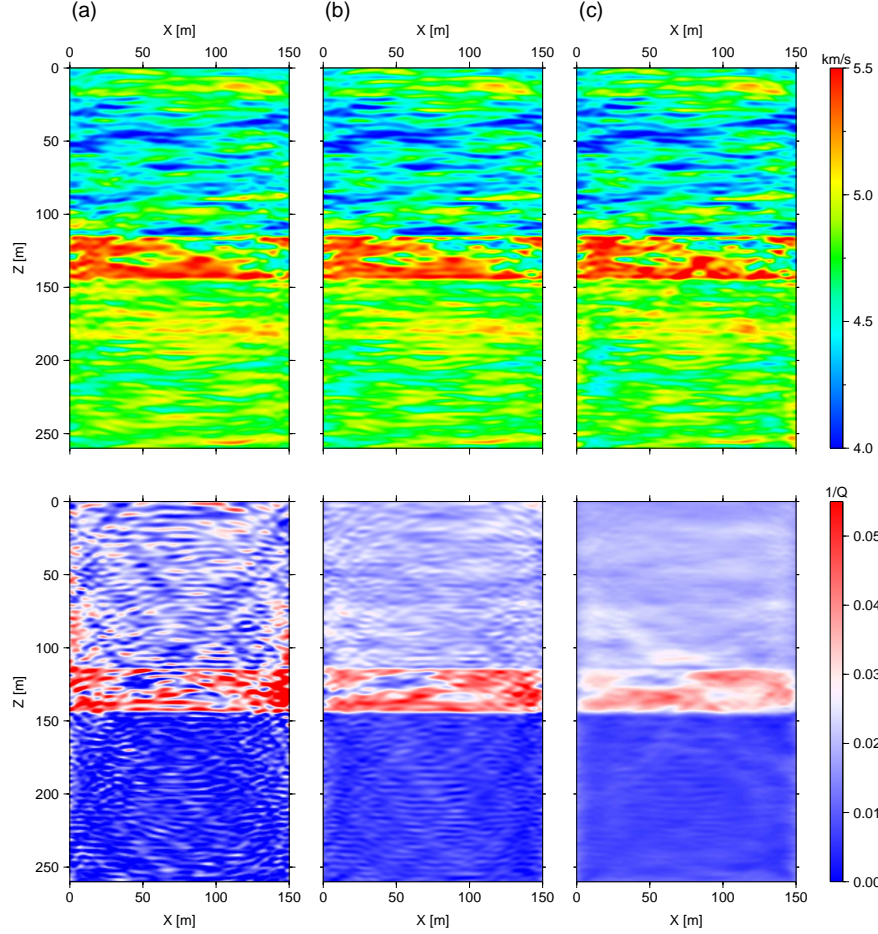


Figure 5.13: Sequential inversion results: (Top) velocity and (bottom) attenuation models obtained by using (a)  $\xi = 1.0$  , (b) 0.1, and (c) 0.01.

functions. The total logarithmic phase-only misfit function

$$E_{total}^P = \sum_{200Hz}^{800Hz} \delta \mathbf{d}^{PT} \delta \mathbf{d}^P, \quad (5.43)$$

was reduced to 5.7 % of that of the starting model, which confirms the good phase fit of the kinematic component of seismic waveforms. The total conventional misfit function  $E_{total}$  is 16.5 % of the starting model, and larger than the values obtained in the simultaneous inversion of Section 5.3.4 (which were less than 1.0 %). This again suggests the remaining misfit in the seismic amplitudes due to the lack of structures in the attenuation model as observed in  $\delta \mathbf{d}^a$ .

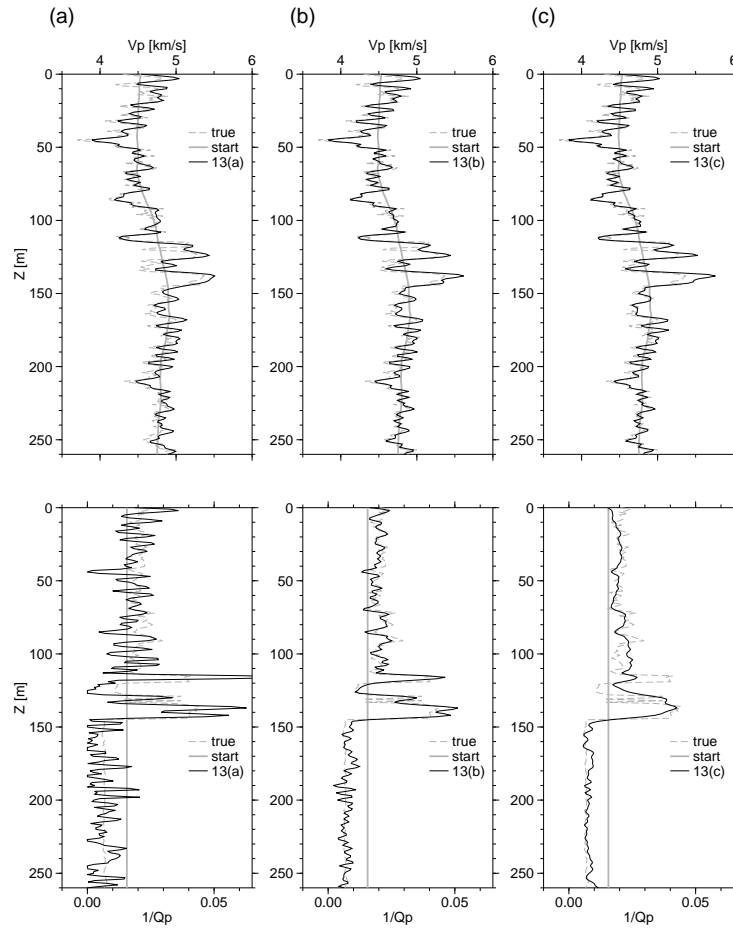


Figure 5.14: Vertical profiles of sequential inversion (top) velocity models and (bottom) attenuation models at  $X = 50$  m obtained by (a)  $\xi = 1.0$ , (b)  $0.1$ , and (c)  $0.01$ . Thick grey solid lines indicate the starting model, grey dashed lines the true model, black solid lines the inversion results.

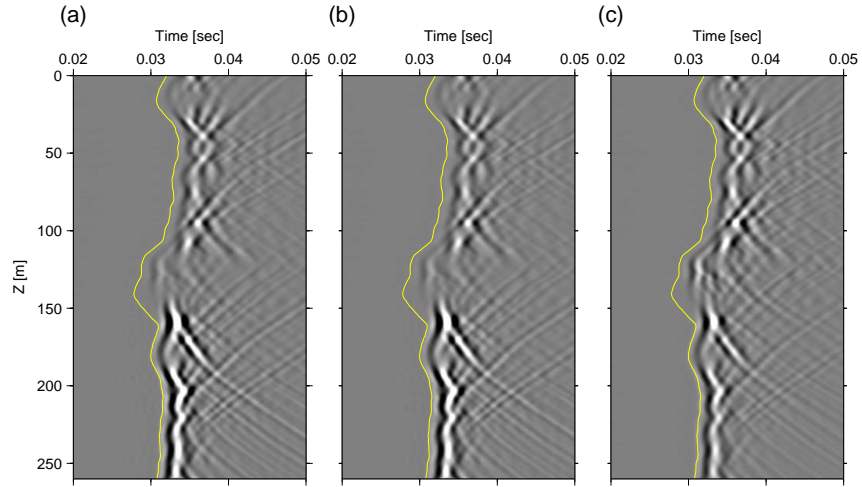


Figure 5.15: Synthetic common level gathers from the sequential inversion results shown in Fig. 5.13. The velocity and attenuation models were obtained with (a)  $\xi = 1.0$ , (b) 0.1, and (c) 0.01.

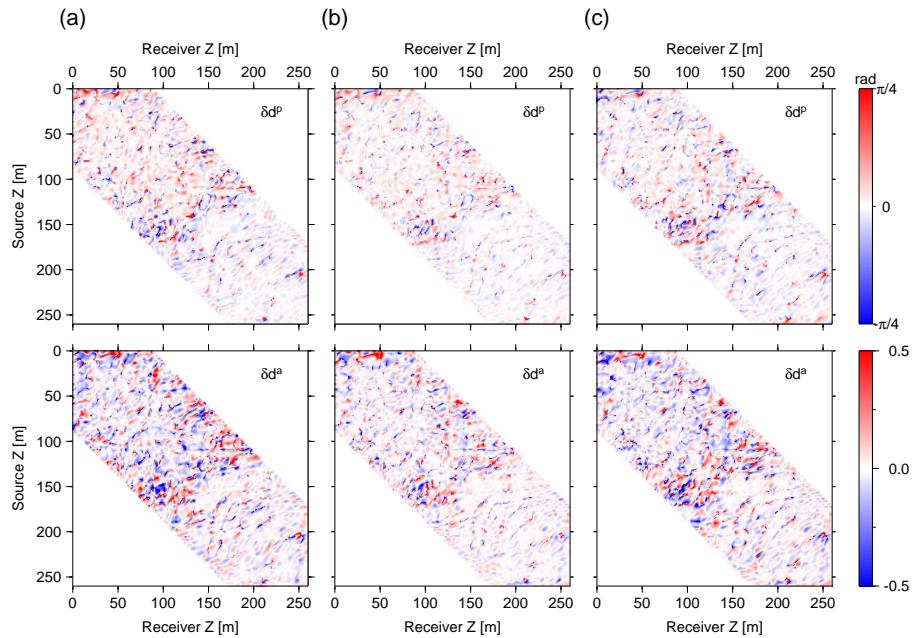


Figure 5.16: (Top) Phase error ( $\delta d^P$ ) and (bottom) logarithmic amplitude error ( $\delta d^A$ ) after sequential inversion at 500 Hz and  $\tau = 0.051$  sec, computed from 5.7a-c.

### 5.3.5.2 Stage 2: Velocity and attenuation inversion

As a second stage of the sequential inversion, we used the velocity model in Fig. 5.11 as a starting velocity model, and simultaneously inverted for velocity and attenuation parameters. We examined the same preconditioning matrix as in Section 5.3.4;  $\xi = 1, 0.1, 0.01$ . Again waveform inversion converged well: In all three inversion settings, the objective function monotonically decreased between 60 % (highest frequency) and 98 % (lowest frequency) per frequency.

After the second stage, the velocity models displayed in Fig. 5.13 do not show significant improvements from the Stage 1 result as expected from the excellent fit in the data kinematics after stage 1. The sequential inversion approach also reduced the unphysical oscillations seen with the simultaneous inversion approach. The final attenuation models from any choice of  $\xi$  delineate the characteristics in the true model: The long-wavelength attenuation structure are recovered well in all three layers, and the two largest low-attenuation anomalies in Layer 2 can be easily recognized.

As in the simultaneous inversion tests, an adjustment of the quantity  $\xi$ , is required to suppress the cross-talk, and to achieve high parameter and spatial resolution of both velocity and attenuation models. At  $\xi = 1.0$ , the attenuation structures in Layers 1 and 2 are closer to the true model than those obtained by the simultaneous inversion. However the inverted attenuation model still contains unphysical fluctuations, especially evident in Layer 3. The velocity values of the sandstone in Layer 2, which were over-estimated in the stage-1 velocity inversion, are now close to the true values, following the recovery of the background attenuation parameters. At  $\xi = 0.1$ , waveform inversion obtained the best velocity and attenuation models. Small oscillations are still present in Layer 3 in the attenuation model, as Layer 3 contains the smallest scale of velocity heterogeneities well beyond the resolution of waveform inversion. The smallest variance ratio  $\xi = 0.01$  almost entirely eliminated the oscillatory artifacts from the attenuation model, although the velocity model contains some artifacts at the sides of the model, and at depths between 145 and 200 m.

Synthetic waveforms from all three final velocity and attenuation models (figure 5.15) coincide very well with the observed waveforms (figure 5.11c). As observed with simultaneous inversion, the discrepancies in the final attenuation models are not apparent from the waveform fit and the total misfit function. Improvements from stage 1 can be mostly found in the amplitude fit, and are most evident in the strongly attenuative Layer 2. The total misfit function  $E_{total}$  decreased from 15 % of the starting model after the stage-1 velocity inversion to 0.7 % from the final model obtained with  $\xi = 1.0$ , 0.38 % with  $\xi = 0.1$ , and 0.61 % with  $\xi = 0.01$ , values comparable to those from the simultaneous

inversion results.

### 5.3.6 Smoothing of the model gradient

In sections 5.3.4 and 5.3.5, we showed that the preconditioning matrix, and the attenuation penalty term  $\xi$ , plays an important role in suppressing the unphysical oscillations arising due to the cross-talk, but we also observed that  $\xi$  itself may not sufficiently remove the oscillations without compromising the resolution, especially in Layer 3. Many authors have reported the importance of smoothing the attenuation component of the model gradient for visco-acoustic waveform inversion (e.g., Pratt et al., 2004; Malinowski et al., 2011). In this section we evaluate whether such smoothing constraints can optimize the spatial and parameter resolutions of the attenuation images

The previous inversion tests were conducted using a weak wavenumber Filter 1 described in Section 5.3.2, which was designed to eliminate high wavenumber oscillations beyond the theoretical resolution of waveform inversion  $\kappa_o$ . After testing several filters, we selected Filter 2 described in in Section 5.3.2 by reducing the largest wavenumber passed to a half of that in Filter 1,  $\kappa_o/2$ , with a tapering area of  $\kappa_o/4$ , by setting set the aspect ratio of the wavenumber filter as 1/4, also a half of that in Filter 1. We applied Filter 2 only to the attenuation component of the gradient. Note that we still apply Filter 1 to the velocity gradient as in sections 5.3.4 and 5.3.5. When we applied Filter 2 to the entire gradient, simultaneous inversion did not converge well with any value of  $\xi$ , and the retrieved velocity and attenuation structures were heavily contaminated by artifacts. This is because the excessive smoothness constraints created velocity models that could no longer span the observed data, and any amplitude decay caused by scattering due to the small-scale velocity features will be filtered out by Filter 2.

We repeated the simultaneous inversion, by applying Filter 1 to the velocity component, and Filter 2 to the attenuation component of the gradient. Again, we used  $\xi = 0.1$  for stage 2 of the sequential inversion. Both inversion approaches converged well, but the rate of reduction in the objective function per frequency was several percent lower than those in sections 5.3.4 and 5.3.5 as a result of the additional smoothing constraints.

We display the inverted velocity and attenuation models in Fig. 5.17. Filter 2 successfully eliminated most high wavenumber oscillations from the attenuation models obtained by both inversion approaches, and the retrieved attenuation models coincide well with the true model. The two low attenuation anomalies in Layer 2 are still clearly depicted, but the boundaries between Layer 1 and 2 are slightly rougher than the previous simultaneous and figures 5.7b and 5.13b. The sequential inversion approach yielded a smoother

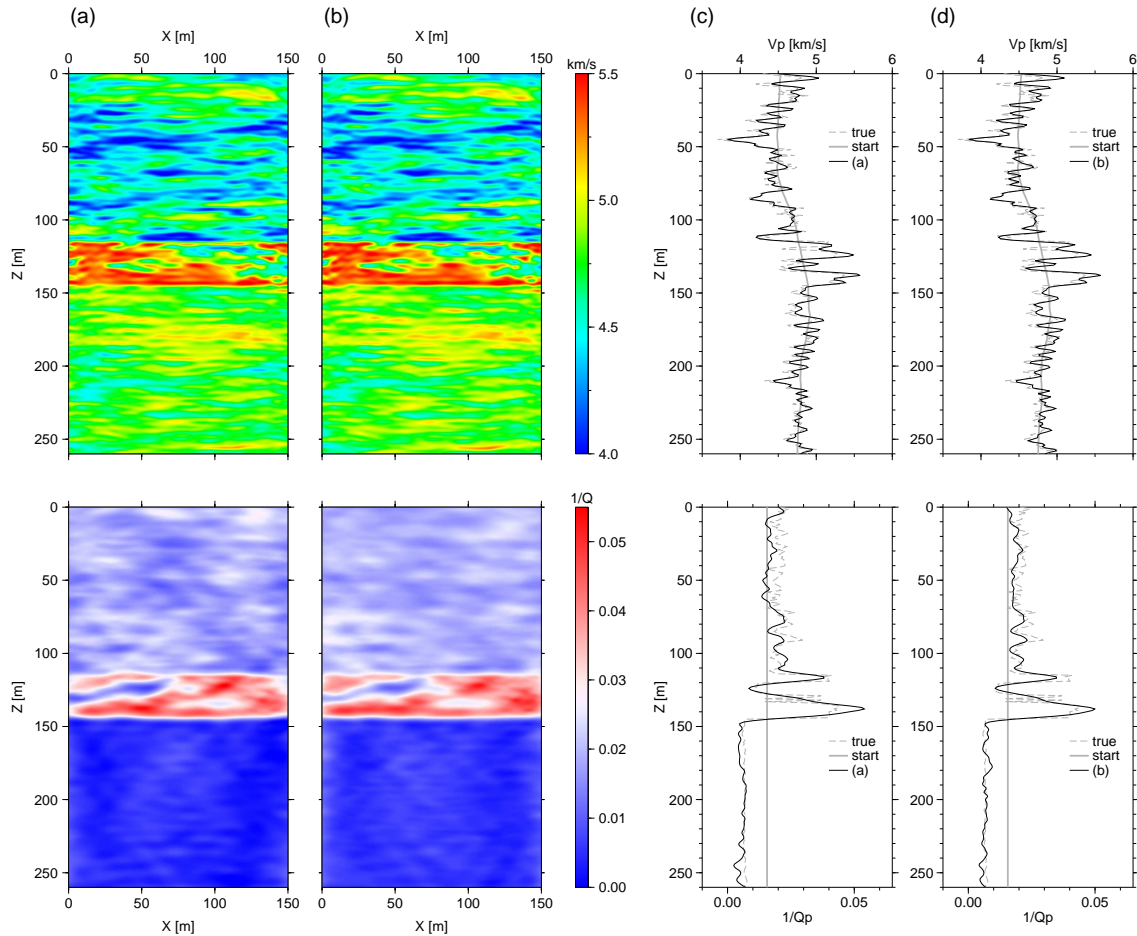


Figure 5.17: Impact of strong wavenumber filtering: (Top) Velocity and (bottom) attenuation models obtained by (a) simultaneous inversion and (b) sequential inversion.  $\xi = 0.1$ . The attenuation component of model gradient was filtered by Filter 2. (c) Vertical profiles at  $X = 50$  m of the models shown in (a), and (d) vertical profiles of (b). Thick grey solid lines indicate the starting model, grey dashed lines the true model, black solid lines the inversion results.

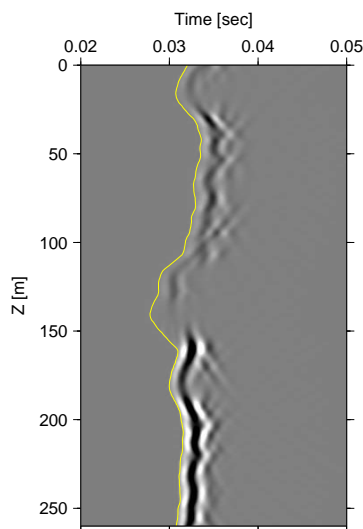


Figure 5.18: Effects of time-damping on waveforms at  $\tau = 0.0015$  sec after muting before the first arrival picks indicated by a yellow line.

result in Layer 1 than the simultaneous inversion approach. The inverted velocity models are as well resolved as in the previous inversion results shown in figures 5.7b and 5.13b, since Filter 1 was applied to the model velocity gradient in all these inversion tests.

Synthetic waveforms generated from the inversion results show a good agreement to the observed waveforms as the synthetic waveforms from the models obtained with Filter 2 in sections 5.3.4 and 5.3.5. The total misfit function  $E_{total}$  after the inversion was 0.52 % of the starting model after simultaneous inversion (0.50 % in Section 5.3.4), and 0.40 % after sequential inversion (0.36 % in Section 5.3.5). This suggests that the unphysical oscillations in the attenuation model eliminated by Filter 2 have little influence on the waveform fit, as also described in Section 5.3.3.

### 5.3.7 Effects of time-damping

The previous inversion tests in sections 5.3.4 - 5.3.6 were conducted using a single and large  $\tau$  value of 0.051 sec, which gives negligible damping effects on seismic waveforms. A cascading schedule for time damping was recommended as a form of the multi-scale method (e.g., Sirgue & Pratt, 2004; Shin & Cha, 2009; Shin et al., 2010; Brenders, 2011; Kamei et al., 2012c); By starting inversion at a smallest  $\tau$  and  $\omega$ , we focus on fitting low-frequency early arrivals, and retrieve smooth long-wavelength components of the model. This leads to less non-linear and more robust optimization process. Subsequently we



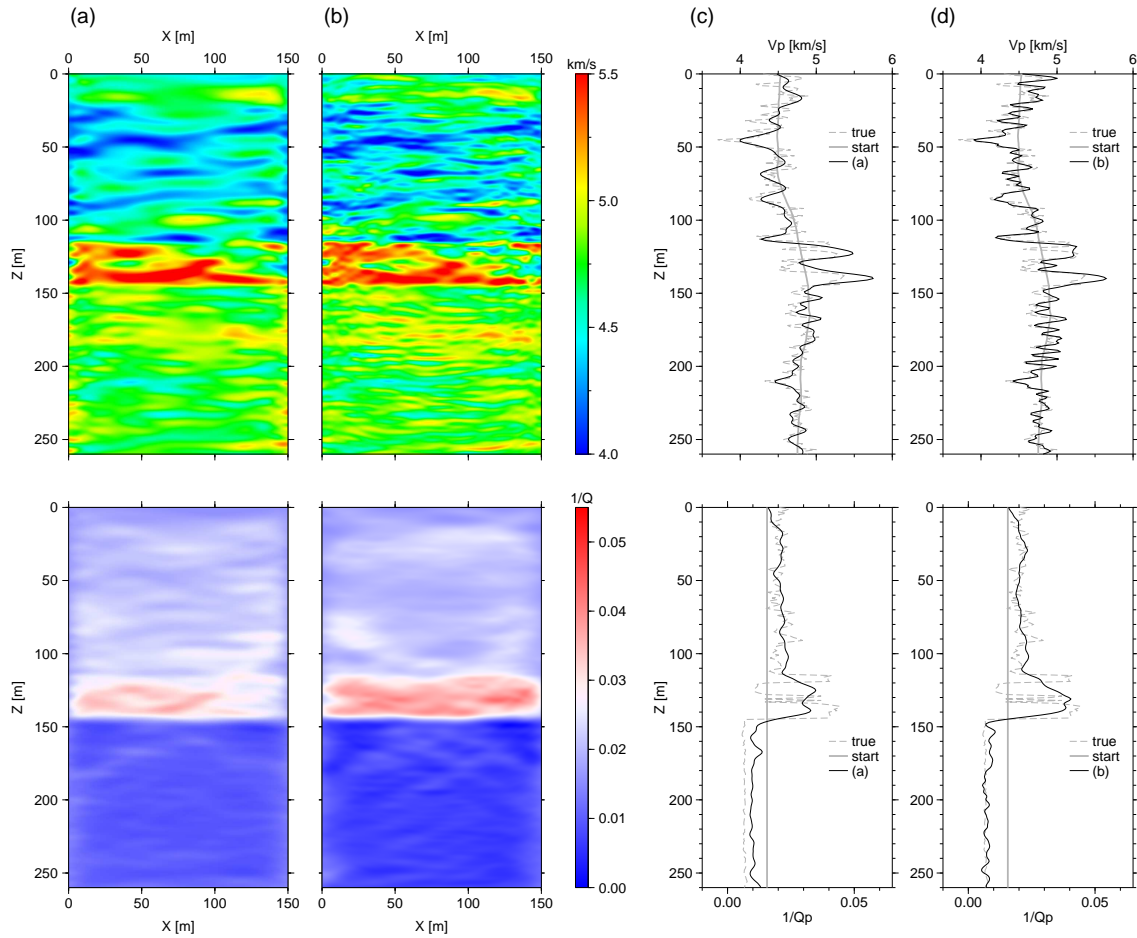


Figure 5.19: Impact of time damping: (Top) Velocity and (Bottom) attenuation models obtained by (a) simultaneous inversion with  $\xi = 0.01$ , and (b) sequential inversion with  $\xi = 0.1$ . (c) Vertical profiles at  $X = 50$  m of (a), and (d) vertical profiles of (b). Thick grey lines indicate the starting model, grey dashed lines the true model, black solid lines the models in (b), and the black dash lines the models in (c)

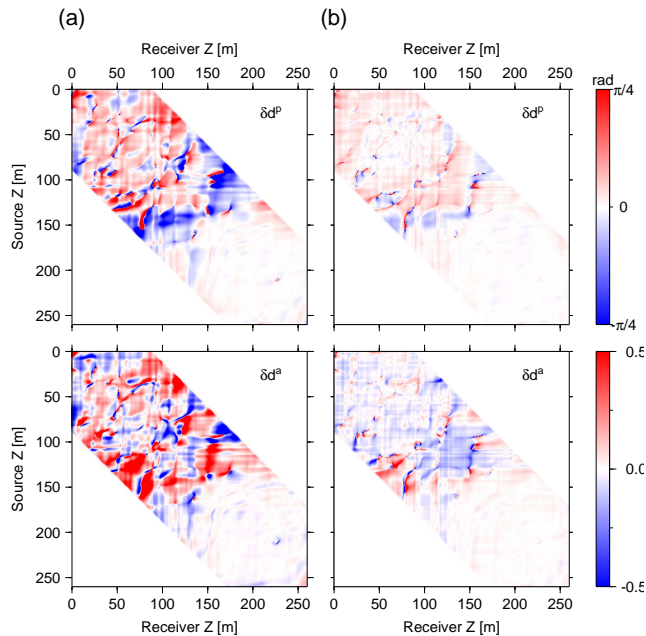


Figure 5.20: (Top) Phase residual ( $\delta\mathbf{d}^p$ ) and (bottom) logarithmic amplitude error ( $\delta\mathbf{d}^a$ ) at 500 Hz computed from the velocity models in Fig. 5.7. (a) Simultaneous inversion, and (b) sequential inversion.

sweep a range of  $\tau$  and  $\omega$  values to gradually incorporate small-wavelength components into the model. This full Laplace-Fourier inversion is one of the key components in successful waveform inversion of a surface data set, in particular, whose subsurface illumination is much reduced when compared to cross-well data sets (Sirgue & Pratt, 2004; Brenders & Pratt, 2007; Kamei et al., 2012a). The well-defined velocity and attenuation models from these inversion tests suggest that it may not be necessary to employ the multi-scale approach recommended by these authors. This is probably due to the high accuracy of the starting model, the lack of noise, and also the good spatial illumination provided by our cross-well acquisition geometry. However when applying visco-acoustic waveform inversion to a field data set, time damping may become necessary to accommodate a less accurate starting model, and to reduce the effects of data noise, modelization errors, etc. We consider that it is of value to evaluate the effects of time-damping on the attenuation imaging, even with the favourable nature of these synthetic data. Time-damping can be expected to smooth the attenuation images in the same manner as for the velocity inversion, but the effects on the cross-talk are not clear. We do not sweep a range of decay constants, and instead we focus on evaluating the effects of a single small decay constant of  $\tau = 0.0015$  sec: The time-damped wavefields displayed in Fig. 5.18 consist mostly of the first arrivals, and are suitable for examining such effects.

We evaluated both simultaneous and sequential inversion approaches for the time-damped data set. We define sequential inversion for the Laplace-Fourier domain as follows; i) we conduct velocity-only inversion for a series of decay constants, and then ii) we invert for both attenuation and velocity model. (Alternatively we may conduct the velocity-only inversion and the velocity-attenuation inversion at each  $\tau$  value, before proceeding to a larger  $\tau$  value.) As a quite accurate velocity model was obtained by stage 1 of the sequential inversion using  $\tau = 0.051$  sec, we assume this velocity model as the product of stage 1 of sequential Laplace-Fourier waveform inversion. We followed the preconditioning strategy employed in Section 5.3.6.

We tested three values of  $\xi$ , 1.0, 0.1, and 0.001, and obtained the best simultaneous inversion result with  $\xi = 0.01$ , and the best sequential inversion results with  $\xi = 0.1$ . The models were selected based on the convergence rate, the spatial resolution, and the parameter resolution. The objective function decreased 16 - 94 % for each frequency during simultaneous inversion and stage 2 of sequential inversion. We display the resulting models in Fig. 5.19, and the phase and amplitude residuals  $\delta\mathbf{d}^p$  and  $\delta\mathbf{d}^a$  from the models for  $\tau = 0.015$  sec in Fig. 5.20. Note that the displayed residuals are not to be quantitatively compared with those in figures 5.4 and 5.16 which were computed with  $\tau = 0.051$  sec.

As expected, the velocity and attenuation models generated by the simultaneous inversion approach shown in Fig. 5.19a are lower in resolution than the one obtained with  $\tau = 0.051$  sec displayed in Fig. 5.17a. We observe strong imprints of the velocity model in the attenuation model, which are particularly evident in Layer 2. The locations of the retrieved low attenuation anomalies coincide with those of the low velocity anomalies. We interpret the low attenuation anomalies as artifacts caused by the cross-talk, as our true velocity and attenuation models were not assumed to be correlated. The retrieved  $Q^{-1}$  values are higher than the true model in Layer 3; this might compensate for scattering loss caused by sub-resolution velocity heterogeneities.

The sequential approach retrieved the long wavelength components of the entire attenuation model including Layer 3. The attenuation model does not contain the imprints of the velocity model, but the low attenuation anomalies are also missing in Layer 2 due to the lack of later arrivals to constrain the structure. The velocity model is much higher in resolution than the simultaneous inversion results, since stage 1 of the sequential inversion was conducted by  $\tau = 0.051$  sec instead of by  $\tau = 0.0015$  sec.

The phase and amplitude residuals at  $\tau = 0.0015$  sec depicted in Fig. 5.20 describe drastic discrepancies between the sequential and simultaneous inversion results. Relatively large phase and amplitude residuals from the simultaneous inversion results indicate

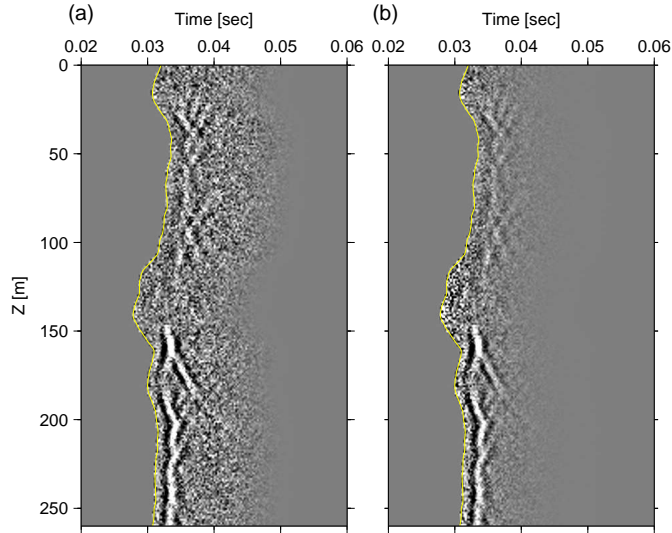


Figure 5.21: The common-level gather of the synthetic “observed” waveforms with Gaussian noise ( $S/N=5$ ) at (a)  $\tau = 0.051$  sec (b)  $0.0015$  sec.

the final velocity and attenuation models are poorly resolved. The sequential inversion reduced the residuals more significantly, confirming the superiority of the sequential inversion results to the simultaneous inversion results. This suggests that in order to fit waveforms even at  $\tau = 0.015$  sec and to suppress the cross-talk, we require more fine-scale velocity models than waveform inversion can retrieve at  $\tau = 0.015$  sec. The phase and amplitude misfit due to the small-scale features missing in the simultaneous inversion results is substantial enough to deteriorate the attenuation imaging.

### 5.3.8 Sensitivity to noise

In order to analyze the sensitivity to the noise, we added Gaussian noise with zero mean corresponding to a signal-to-noise ratio of 5 to the time-domain synthetic observed wavefields generated in Section 5.3.1. As conventionally conducted for preprocessing real-data, we picked first arrivals, and applied a time-window of 0.2 sec relative to the first breaks. We show the time-windowed data with Gaussian noise in Fig. 5.21a. We also explored the possibility of applying a small time-damping factor. The smallest  $\tau$  value available for the inversion was  $\tau = 0.005$  sec, since a smaller  $\tau$  value excessively amplified the noise between the beginning of the time-window and the first peaks, and unstabilized the inversion. We display the time-damped wavefields in Fig. 5.21b. Unfortunately waveform inversion with  $\tau = 0.005$  sec yielded the results similar to those with  $\tau = 0.051$

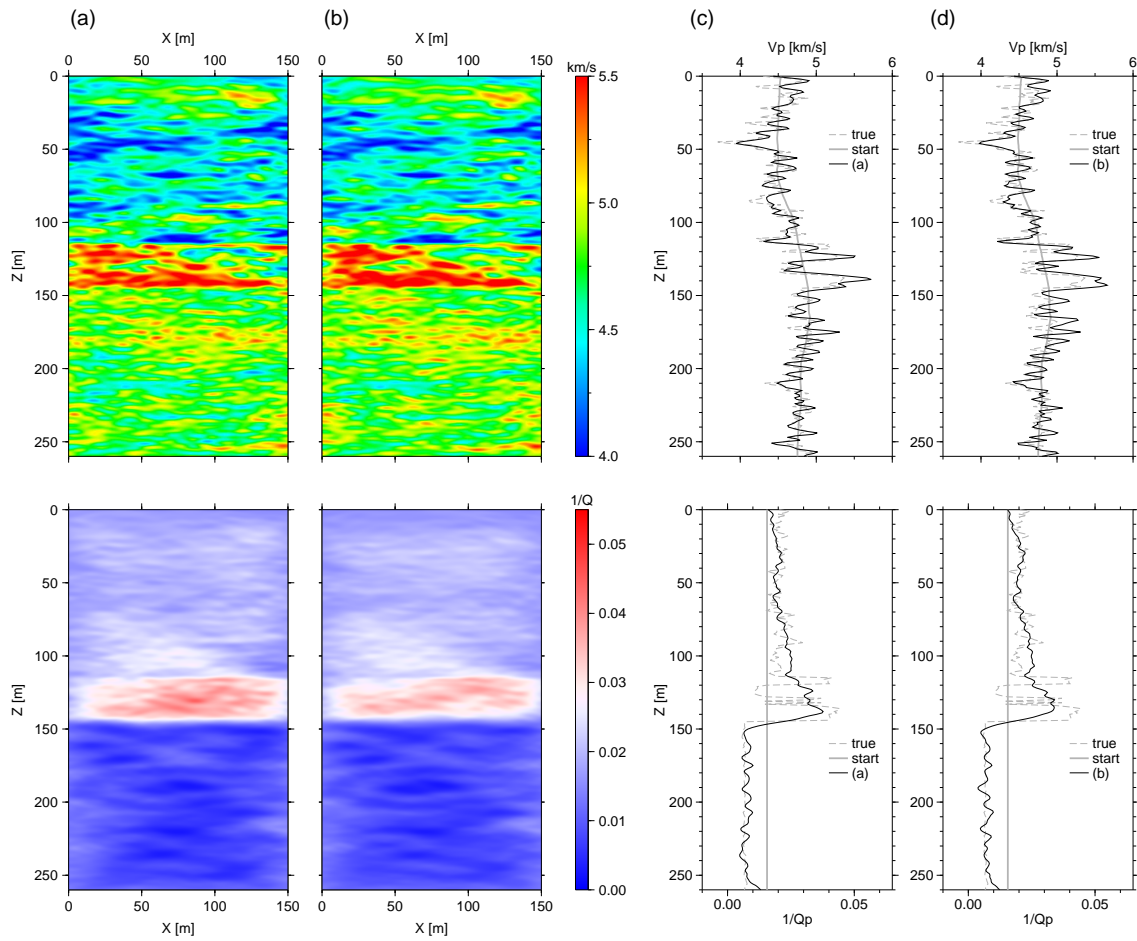


Figure 5.22: Impact of noise: (Top) Velocity and (Bottom) attenuation models obtained by (a) simultaneous inversion and (b) sequential inversion. (c) Vertical profiles of (b). Thick grey solid lines indicate the starting model, grey dashed lines the true model, black solid lines the inversion results.

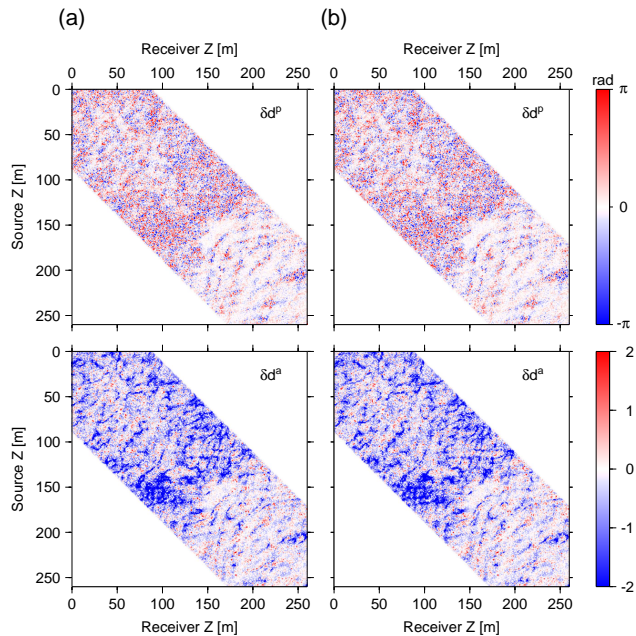


Figure 5.23: (Top) Phase error and (bottom) logarithmic amplitude error at 500 Hz and  $\tau = 0.051$  sec, computed from Fig. 5.22.

sec, and therefore we only discuss the effects of the noise using  $\tau = 0.051$  sec.

We conducted simultaneous and sequential inversion following the strategies in Section 5.3.6. We conducted 10 iterations per frequency instead of the 20 iterations used for the noise-free data. A larger number of iterations deteriorated velocity and attenuation images by adding too many artifacts. We selected the same cut-off vertical wavenumbers as in Section 5.3.6. We evaluated three values for  $\xi = 1.0, 0.1, 0.01$ , and obtained the best attenuation model with  $\xi = 0.01$  for both inversion approaches. We display the resulting velocity and attenuation models in Fig. 5.22 along with the vertical profiles, and the phase and amplitude residuals  $\delta\mathbf{d}^p$  and  $\delta\mathbf{d}^a$  from the final models in Fig. 5.23. Total misfit functional  $E_{total}$  remains relatively large; 60 % of the starting model for both simultaneous and sequential inversion strategies.

Gaussian noise degraded the quality of the velocity and attenuation models obtained for both inversion approaches by inducing oscillatory artifacts, when compared to the inversion results of the noise-free data shown in Fig. 5.17. Note that the discrepancies between the simultaneous and sequential inversion results are not significant. The final velocity models still delineate the true velocity features well, but horizontal features are contaminated by artifacts. The artifacts arise partially due to our mono-frequency strategy at each iteration, and these can be mitigated by inverting more than one frequency component at each iteration as suggested by Pratt & Shipp (1999), Plessix (2006),

Brossier et al. (2009) and others. The long wavelength components of the retrieved attenuation models agree well with the true attenuation model, but unphysical oscillations are evident especially in Layer 3. In Fig. 5.23, the phase and amplitude residuals are still large in Layer 1 and 2. However the phase residuals are incoherent and related to the noise, and therefore it may be difficult to improve waveform fits any further.

## 5.4 Discussion and conclusions

Visco-acoustic waveform inversion is ill-posed and often exhibits poor parameter resolution, or a cross-talk, between velocity and attenuation parameters (Song et al., 1995; Malinowski et al., 2011; Liao & McMechan, 1996; Kamei & Pratt, 2008; Hak & Mulder, 2011). We formulated visco-acoustic waveform inversion in the Laplace-Fourier domain, and conducted a series of inversion tests to explore robust inversion strategies to extract high-resolution independent velocity and attenuation models, and to mitigate the cross-talk issue. Seismic waveforms show different sensitivities to the two parameter classes of velocity and attenuation, and the largest singular values of the Fréchet derivatives are associated with velocity perturbations. The severe cross-talk between the parameter classes is a result of the phase-only differences in the convolutional terms between forward and backpropagated wavefields, and is persistent throughout the inversion, since errors remain in the model parameters beyond the resolution limit of the data, and since there are factors associated with acquisition parameters (e.g. incomplete surface illumination, data bandwidth, data noise), and with the physical assumptions we implement (e.g. modelling errors including elastic effects).

In Section 5.3.3, we examined the significance of cross-talk on the velocity and attenuation images by perturbing only one of the model parameter classes. The leakage of the velocity update induced strong oscillatory artifacts onto the attenuation model, while errors in the attenuation model had little influence on the velocity model. We suggested that the oscillations correspond to the very small singular values of the system (i.e. belonging to an approximate null-space), as they hardly affected the data fitness, and we also suggested that the cross-talk is dominant only on the attenuation image due to poor scaling of the parameter classes in the gradient.

In subsequent inversion tests (sections 5.3.4 - 5.3.8), we demonstrated the importance of the regularization scheme, and the effectiveness of the sequential inversion approach for visco-acoustic waveform inversion. Without a careful design of inversion strategies, the attenuation image is heavily contaminated by unphysical oscillations arising from the cross-talk as described in the previous paragraph. Conversely, visco-acoustic waveform

inversion reconstructed detailed features present in the true velocity model regardless of the quality of the accompanying attenuation model. The resolution of the velocity model was slightly reduced in the presence of excessive unphysical oscillations in the model, and negatively affected if the attenuation model was very far from the model.

We attribute the superior robustness of the velocity model to the different sensitivities of the seismic waveforms to the velocity and attenuation parameter classes: As demonstrated in Section 5.3.5, a large portion of amplitude errors can be significantly reduced by obtaining an accurate velocity model and by properly accounting for geometrical spreading effects. Therefore waveform inversion preferentially updates velocity parameters (probably corresponding to the large singular values), and contaminates the attenuation update by the cross-talk, particularly during the early stage of the inversion as described by Liao & McMechan (1996) and Hak & Mulder (2011).

We regularized the attenuation parameters by the combination of a simple preconditioning matrix and smoothness constraints, the approach being similar to the one employed for the real data set by Malinowski et al. (2011). The preconditioning matrix is assumed to be diagonal, and the attenuation penalty term  $\xi$  played a primary role in suppressing the cross-talk by penalizing the attenuation update with  $\xi < 1.0$  for both simultaneous and sequential inversion. As too small a value of  $\xi$  prevents the update of attenuation parameters and degrades the velocity image, some of artifacts can be removed by applying additional strong smoothing constraints to the attenuation component of the gradient with a moderate value of  $\xi$ . Thus an adequate value for  $\xi$  needs to be searched for: The value depends on the condition of waveform inversion (starting model, frequency bandwidth, survey geometry, noise-level), and thus is specific to each inversion problem. We illustrate in Appendix Appendix 5.C, that  $\xi$  may be determined from the examination of the trade-off curve between the data fitness and the resolution of the model, instead of choosing it in an ad-hoc manner. The successful application of this simple regularization scheme invokes interest in a more elaborate and formal regularization method such as Tikhonov methods (Pratt & Chapman, 1992; Aster et al., 2005).

Sequential inversion is another effective strategy to reduce the cross-talk as pointed out by Watanabe et al. (2004), Rao & Wang (2008) and Kamei & Pratt (2008). The initial velocity inversion restricts the size of the search space during the subsequent two-parameter inversion, and significantly reduces the amount of the cross-talk appearing in the attenuation model. However we also found that the sequential inversion approach itself is not sufficient to eliminate the cross-talk, and that a non-trivial portion of the cross-talk arises from the limited resolution in the velocity model, limited bandwidth, and



incomplete subsurface illumination. The gradient preconditioning by  $\xi$  was still required, but the optimal value of  $\xi$  was apparently larger than that of simultaneous inversion (see also Appendix Appendix 5.C). This indicates that the regularization strategy depends on the quality of an initial model when inverting for both parameter classes.

Visco-Acoustic waveform inversion with strong time-damping in Section 5.3.7 suggested that full Laplace-Fourier waveform inversion may require the adoption of the sequential inversion approach. The limited resolution in the velocity model obtained from the time-damped wavefields apparently failed to sufficiently reproduce the amplitude decay caused by the geometrical spreading and scattering. Such amplitude errors may become the null-space in the data domain.

Our tests above were conducted using a synthetic data set generated by the same visco-acoustic forward modelling code as used for the inversion, and can be categorized as an “inverse crime”. The Gaussian data noise tests in Section 5.3.8 showed that regularized waveform inversion successfully delineate major elements of the velocity and attenuation models, although lower in spatial-resolution when compared to noise-free data results.

In this chapter, we addressed the cross-talk and the sensitivity problem of visco-acoustic waveform inversion, but we did not apply singular value decomposition (SVD) analysis, a powerful tool to analyze model space, because of the computational cost. The SVD analysis may be conducted with a smaller model, and this will reveal more detailed behaviour of the ill-posed visco-acoustic waveform inversion. We also did not investigate several important factors contributing to the cross-talk such as frequency bandwidth, survey geometry, and modellization errors. In particular, we did not assess the limitation of the acoustic assumption: Elastic effects affect amplitudes of even P-wave components by P-SV conversion, and may contaminate the attenuation imaging. In future study, we will further validate regularized visco-acoustic inversion for these aspects, and apply the method to field data sets.

## Appendix 5.A Relationships between preconditioning matrix and model covariance

In Section 5.2.3, we developed waveform inversion from the point of view of optimization. Alternatively we may develop the inversion from the Bayesian point of view as described in Tarantola (1988), in which case the objective function is

$$E'' = \delta \mathbf{d}^T \mathbf{C}_d^{-1} \delta \mathbf{d} + \delta \mathbf{m} \mathbf{C}_m^{-1} \delta \mathbf{m}, \quad (\text{Appendix 5.A.1})$$

where  $\delta\mathbf{m} = \mathbf{m} - \mathbf{m}_o$ ,  $\mathbf{m}$  is the priori model,  $\mathbf{C}_d$  is the priori data covariance describing measurement errors, and  $\mathbf{C}_m^{-1}$  is the priori model covariances describing our knowledge about the model independent from the data measurement. This leads to

$$\nabla_{\mathbf{m}} E'' = \Re [\mathbf{K}^T \mathbf{C}_d^{-1} \delta\mathbf{d} + \mathbf{C}_m^{-1} \delta\mathbf{m}]. \quad (\text{Appendix 5.A.2})$$

To obtain the steepest descent direction,  $\boldsymbol{\gamma}''$ , the gradient needs to be multiplied by  $\mathbf{C}_m$  (Tarantola, 1988),

$$\boldsymbol{\gamma}'' = \mathbf{C}_m \Re [\mathbf{K}^T \mathbf{C}_d^{-1} \delta\mathbf{d} + \delta\mathbf{m}]. \quad (\text{Appendix 5.A.3})$$

We set  $\mathbf{C}_d^{-1} = \mathbf{I}$  for simplicity, and ignore the second term of Eq.(Appendix 5.A.3) in which case

$$\boldsymbol{\gamma}'' = \mathbf{C}_m \Re [\mathbf{K}^T \delta\mathbf{d}]. \quad (\text{Appendix 5.A.4})$$

We further assume the velocity and attenuation parameters are independent, and describe

$$\mathbf{C}_m = \begin{bmatrix} \sigma_{m^{(1)}}^2 \mathbf{I} & \mathbf{0} \\ \mathbf{0} & \sigma_{m^{(2)}}^2 \mathbf{I} \end{bmatrix}, \quad (\text{Appendix 5.A.5})$$

where  $\sigma_{m^{(j)}}^2$  is the priori estimate of the variance of  $\mathbf{m}^{(j)}$ . Eq.(Appendix 5.A.4) is equivalent to Eq.(5.21), by setting

$$\mathbf{P} = \mathbf{C}_m, \quad (\text{Appendix 5.A.6})$$

and further the attenuation penalty term in Eq.(5.38) is

$$\xi = \frac{\sigma_{m^{(1)}}^2}{\sigma_{m^{(2)}}^2}. \quad (\text{Appendix 5.A.7})$$

This indicates that the model preconditioning matrix and the model covariance are mathematically equivalent, and the condition  $\xi < 1$  indicates that the variance of the attenuation parameter is smaller than that of the velocity parameter. The value of  $\xi$  would be 0.0002, if we were to select  $\xi$  simply as the square of the ratio between the average values of  $\mathbf{s}_o^{(r)}$  and  $\mathbf{s}_o^{(i)}$  from the starting model. However our inversion tests in sections 5.3.4 and 5.3.5, and Appendix Appendix 5.C suggest that such a small choice of  $\xi$  leads to a non-optimal velocity and attenuation model. Furthermore  $\xi$  primarily performs as a regularization parameter, and the optimal  $\xi$  value depends on the fitness of the data in the initial velocity model, contradicting the original definition given by Tarantola (1988). Hence we avoid the use of the ‘model covariance’ terminology in our chapter.

## Appendix 5.B Alternative expression for gradient and anti-causal propagation

In Section 5.2.3, we derived the gradient as

$$\nabla_{\mathbf{m}^{(j)}} E = \sum_{l=1}^{\Omega_l} \sum_{k=1}^{N_s} \Re [\mathbf{F}^{(j)t}(\Omega_l, \mathbf{x}_k^{\text{src}}) \mathbf{v}(\Omega_l, \mathbf{x}_k^{\text{src}})^*], \quad (5.29 \text{ again})$$

and interpreted the gradient as a convolution of a virtual source term  $\mathbf{F}^{(j)}$  with the back-propagated complex-conjugate of the residuals  $\mathbf{v}(\Omega_l, \mathbf{x}_k^{\text{src}}) = \mathbf{S}^{-1}(\Omega_l) \delta \mathbf{d}(\Omega_l, \mathbf{x}_k^{\text{src}})^*$ . As the gradient is real, Eq.(5.29) can be rewritten by

$$\begin{aligned} \nabla_{\mathbf{m}^{(j)}} E &= (\nabla_{\mathbf{m}^{(j)}} E(\omega))^*, & (\text{Appendix 5.B.1}) \\ &= \sum_{l=1}^{\Omega_l} \sum_{k=1}^{N_s} \Re [\mathbf{F}^{(j)T}(\Omega_l, \mathbf{x}_k^{\text{src}}) [\mathbf{S}^{-1}(\Omega_l)]^* \delta \mathbf{d}(\Omega_l, \mathbf{x}_k^{\text{src}})] & (\text{Appendix 5.B.2}) \end{aligned}$$

(Pratt et al., 1998), which leads to the alternative interpretation that the gradient is formed by a zero-lag cross-correlation between the virtual source and the backpropagated wavefield, which are now defined as

$$\mathbf{w}(\Omega_l, \mathbf{x}_k^{\text{src}}) = [\mathbf{S}^{-1}(\Omega_l)]^* \delta \mathbf{d}(\Omega_l, \mathbf{x}_s), \quad (\text{Appendix 5.B.3})$$

$$= \mathbf{v}^*(\Omega_l, \mathbf{x}_k^{\text{src}}), \quad (\text{Appendix 5.B.4})$$

the form adopted by Liao & McMechan (1996) in the frequency domain, and by Tarantola (1988) in the time domain. While  $\mathbf{v}$  can be interpreted in time domain as the propagation of the time-reversed residuals, the wavefield  $\mathbf{w}$  is the propagation of residuals backwards in time with negative (anti-causal) attenuation. The negative attenuation arises from the fact that the conjugate of the impedance matrix in Eq.(Appendix 5.B.4) means the conjugate of the slowness field from the wave equation in Eq.(5.6). Note that the anti-causal attenuation does not indicate the amplification of the wavefields at a location far from a receiver location which acts as a source for the back-propagation, but rather ensures that seismic wavefields diminish in the distance as propagating backwards in time (i.e. they amplify as it travels to a receiver location forwards in time). Therefore this ensures the stability of wave propagation as described by Tarantola (1988).

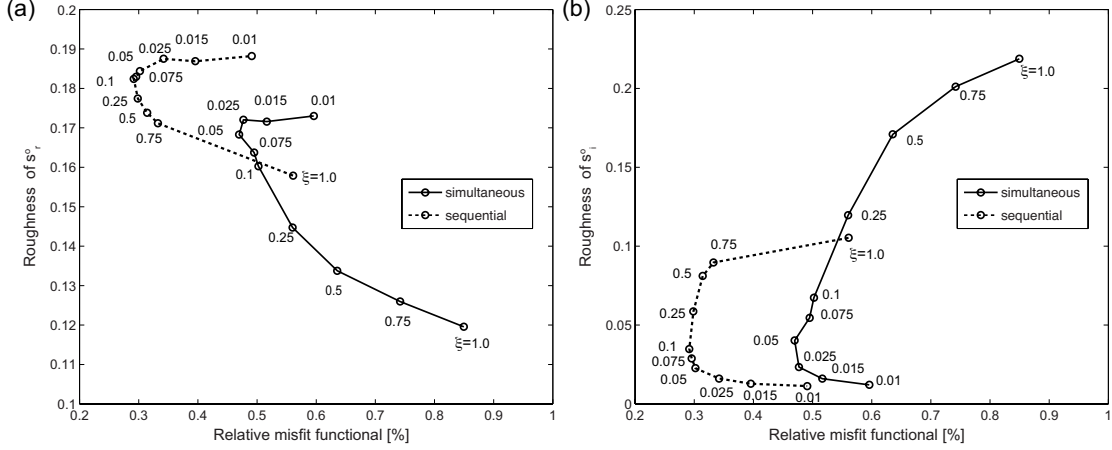


Figure 5.24: Trade-off curves between the total-conventional misfit  $E_{total}$  and the roughness of (a)  $s_o^{(r)}$  and (b)  $s_o^{(i)}$  for simultaneous (solid) and sequential inversion (dashed) at  $\tau = 0.051$ . Both velocity and attenuation components of the model gradient were weakly smoothed by Filter 1 with a suite of inversion results by varying  $\xi$ .  $E_{total}$  was plotted relative to the value from the starting models.

## Appendix 5.C Choice of $\xi$ based on trade-off curves

The parameters for the regularization scheme may determined based on knee-points of trade-off curves between data misfits and model resolution, and between data misfits and model norms (Aster et al., 2005; Pratt & Chapman, 1992). In visco-acoustic waveform inversion, we aim to reduce the unphysical oscillations in the attenuation model, and thus it may be beneficial to investigate the trade-off between the data misfit, and the roughness (the inverse of smoothness) of the model. Following Pratt & Chapman (1992), we define the roughness for each parameter class by

$$\sqrt{(\mathbf{R}_x \mathbf{m}^{(j)})^T (\mathbf{R}_x \mathbf{m}^{(j)}) + (\mathbf{R}_z \mathbf{m}^{(j)})^T (\mathbf{R}_z \mathbf{m}^{(j)}) + (\mathbf{R}_{\nabla^2} \mathbf{m}^{(j)})^T (\mathbf{R}_{\nabla^2} \mathbf{m}^{(j)})}, \quad (\text{Appendix 5.C.1})$$

where  $\mathbf{R}_x$  and  $\mathbf{R}_z$  are the first differential operators in  $x$ - and  $z$ - directions, and  $\mathbf{R}_{\nabla^2}$  is the Laplacian operator. In a typical regularized inversion problem, for example anisotropic traveltime tomography described in Pratt & Chapman (1992), the roughness decreases, and the data misfit increases, as increasing the penalty to model parameters. The knee-point of the trade-off curve divides the region between where the penalty dominantly affects the roughness of the model, and where it affects the data misfit.

We plotted trade-off curves for simultaneous and sequential visco-acoustic waveform inversion in Fig. 5.24: the roughness of  $s_o^{(r)}$  and  $s_o^{(i)}$  are plotted against the total conventional data misfits  $E_{total}$  for various values of  $\xi$  between 0.001 and 1.0: We employ

the same strategies as in sections 5.3.4 and 5.3.5), and used  $\tau = 0.051$  sec. Note that  $\xi$  penalizes the attenuation parameter, but not the velocity parameters. Variations in the data misfit relative to the starting model are very small (less than 1 % of the value for the starting model), but we consider the discussion is meaningful as these inversion tests are performed for the noise-free and synthetic data.

We observe the trade-off curves from visco-acoustic waveform inversion show unique behaviours when compared to those from the usual regularized inversion. As  $\xi$  becomes smaller, the penalty on attenuation parameters increases, and both the data misfits and the roughness of the attenuation model ( $\mathbf{s}_o^{(i)}$ ) monotonically decrease, until reaching a knee point, for both inversion approaches. In contrast the roughness of the un-penalized velocity parameter ( $\mathbf{s}_o^{(r)}$ ) increases as  $\xi$  decreases. The unusual reduction in the data misfits is particularly evident in simultaneous inversion approach, and can be associated with the increase in the resolution in the velocity model which the objective function is more sensitive to (compare Fig. 5.7a and b, for example). This suggests that the appropriate value of  $\xi$  changes the inversion paths, and accelerates the convergence of the inversion, by balancing two components of the model gradient.

The velocity and attenuation models are optimally reconstructed at the vicinity of the knee points. The knee point coincides between two classes of model parameter, but differs between inversion strategies ( $\xi = 0.025$  for simultaneous inversion, and  $\xi = 0.075$  for sequential inversion). As  $\xi$  further decreases, the data residuals begin to increase, while the inverted attenuation model starts to lose the internal structures, and the velocity model to contain “X-shaped” artifacts. The optimal range for  $\xi$  is apparently wider for the sequential inversion approach than for the simultaneous inversion approach, which further supports the proposal that Stage 1 velocity inversion of the sequential inversion approach stabilizes the velocity-attenuation inversion.

The experiments demonstrate that  $\xi$  can be determined based on the examination of the trade-off curves for both parameter classes. The discrepancies in the data misfits are small, and may not be apparent if we apply the method to a field data set. This suggests that an alternative definition of data residuals (e.g. the logarithmic amplitude residuals  $\delta\mathbf{d}^a$ ) to measure the fitness of the data should be explored.

## References

- Abubakar, A., Li, M., Lin, Y., & Habashy, T. M., 2012. Compressed implicit Jacobian scheme for elastic full-waveform inversion, *Geophysical Journal International*, **189**(3), 1626–1634.

- Aki, K. & Richards, P. C., 1980. *Quantitative seismology*, W. H. Freeman & Co.
- Aster, R. C., Borchers, B., & Clifford, T. H., 2005. *Parameter estimation and inverse theory*, Elsevier Academic Press.
- Bednar, J. B., Shin, C., & Pyun, S., 2007. Comparison of waveform inversion, part 2: phase approach, *Geophysical Prospecting*, **55**(4), 465–475.
- Beylkin, G. & Burridge, R., 1990. Linearized inverse scattering in acoustics and elasticity, *Wave motion*, **12**, 15–52.
- Brenders, A. J., 2011. *Strategies For Waveform Tomography of Long-offset, 2-D Exploration Seismic Data*, Ph.D. thesis, University of Western Ontario.
- Brenders, A. J. & Pratt, R. G., 2007. Full waveform tomography for lithospheric imaging: results from a blind test in a realistic crustal model, *Geophysical Journal International*, **168**(1), 133–151.
- Brossier, R., Operto, S., & Virieux, J., 2009. Seismic imaging of complex onshore structures by 2D elastic frequency-domain full-waveform inversion, *Geophysics*, **74**(6), WCC105–WCC118.
- Bunks, C., Saleck, F. M., Zaleski, S., & Chavent, G., 1995. Multiscale seismic waveform inversion, *Geophysics*, **60**(5), 1457–1473.
- Carcione, J. M., 2000. A model for seismic velocity and attenuation in petroleum source rocks, *Geophysics*, **65**(4), 1080–1092.
- Chapman, M., Liu, E., & Li, X.-Y., 2006. The influence of fluid-sensitive dispersion and attenuation on AVO analysis, *Geophysical Journal International*, **167**(1), 89–105.
- Frankel, A. & Clayton, R. W., 1986. Finite Difference Simulations of Seismic Scattering: Implications for the Propagation of Short-Period Seismic Waves in the Crust and Models of Crustal Heterogeneity, *Journal of Geophysical Research*, **51**(B6), 6465–6469.
- Gao, F., Levander, A., & Zelt, C., 2006. An iterative approach for geophysical diffraction tomography: Implication for true amplitude migration, *SEG Technical Program Expanded Abstracts*, **25**(1), 3325–3329.
- Gardner, G. H. F., Gardner, L. W., & Gregory, A. R., 1974. Formation velocity and density —The diagnostic basics for stratigraphic traps, *Geophysics*, **39**(6), 770–780.
- Hak, B. & Mulder, W. A., 2010. Migration for velocity and attenuation perturbations, *Geophysical Prospecting*, **58**(6), 939–951.
- Hak, B. & Mulder, W. A., 2011. Seismic attenuation imaging with causality, *Geophysical Journal International*, **184**(1), 439–451.
- Hustedt, B., Operto, S., & Virieux, J., 2004. Mixed-grid and staggered-grid finite-difference methods for frequency-domain acoustic wave modelling, *Geophysical Journal International*, **157**(3), 1269–1296.

- Ikelle, L. T., Yung, S. K., & Daube, F., 1993. 2-D random media with ellipsoidal auto-correlation functions, *Geophysics*, **58**(9), 1359–1372.
- Jo, C.-H., Shin, C., & Suh, J. H., 1996. An optimal 9-point, finite-difference, frequency-space, 2-D scalar wave extrapolator, *Geophysics*, **61**(2), 529–537.
- Kamei, R. & Pratt, G., 2008. Waveform Tomography strategies for imaging attenuation structure with cross-hole data, *the 69th Conference and Exhibition of the EAGE, Rome, Italy..*
- Kamei, R., Pratt, R., & Tsuji, T., 2012a. On Acoustic Waveform Tomography of wide-angle OBS data — Strategies for preconditioning and inversion, *Geophysical Journal International (under review)*.
- Kamei, R., Pratt, R., & Tsuji, T., 2012b. Discussion on advantages in phase-only inversions in the Laplace-Fourier domain waveform inversion - Application from the Nankai subduction zone, *Geophysical Prospecting (under review)*.
- Kamei, R., Pratt, R. G., & Tsuji, T., 2012c. Waveform tomography imaging of a megasplay fault system in the seismogenic Nankai subduction zone, *Earth and Planetary Science Letters*, **317-318**, 343–353.
- Kamei, R., Hato, M., M., 2005. Random heterogeneous model with bimodal velocity distribution for Methane Hydrate exploration, *Exploration Geophysics*, **36**, 41–49.
- Kennett, B. L. N. & Sambridge, M., 1998. Inversion for multiple parameter classes, *Geophysical Journal International*, **135**(1), 304–306.
- Kennett, B. L. N., Sambridge, M. S., & Williamson, P. R., 1988. Subspace methods for large inverse problems with multiple parameter classes, *Geophysical Journal*, **94**(2), 237–247.
- Lailly, P., 1983. The seismic inverse problem as a sequence of before stack migrations, in *Conference on inverse scattering: theory and application*, pp. 206–220, SIAM, Soc. Industr. appl. Math., Philadelphia, PA.
- Liao, Q. & McMechan, G. A., 1996. Multifrequency viscoacoustic modeling and inversion, *Geophysics*, **61**(5), 1371–1378.
- Malinowski, M., Operto, S., & Ribodetti, A., 2011. High-resolution seismic attenuation imaging from wide-aperture onshore data by visco-acoustic frequency-domain full-waveform inversion, *Geophysical Journal International*, **186**(3), 1179–1204.
- Mallick, S. & Frazer, L. N., 1987. Practical aspects of reflectivity modeling, *Geophysics*, **52**(10), 1355–1364.
- Mavko, G., Mukerji, T., & Dvorkin, J., 1998. *The rock physics handbook: Tools for seismic analysis of porous media*, Cambridge University Press.
- Métivier, L., Brossier, R. J., & Operto, S., 2012. Towards gauss-newton and exact newton

- optimization for full waveform inversion., *EAGE Conference & Exhibition incorporating SPE EUROPEC 2012 Copenhagen, Denmark, 4 - 7 June 2012*, p. P016.
- Mora, P., 1987. Nonlinear two-dimensional elastic inversion of multioffset seismic data, *Geophysics*, **52**(9), 1211–1228.
- Mosegaard, K. & Tarantola, A., 1995. Monte Carlo sampling of solutions to inverse problems, *Journal Of Geophysical Research*, **100**(B7), 12431–12447.
- Mulder, W. a. & Hak, B., 2009. An ambiguity in attenuation scattering imaging, *Geophysical Journal International*, **178**(3), 1614–1624.
- Phinney, R. A., 1965. Theoretical Calculation of the Spectrum of First Arrivals in Layered Elastic Mediums, *Journal of Geophysical Research*, **70**(20), 5107–5123.
- Plessix, R.-E., 2006. A review of the adjoint-state method for computing the gradient of a functional with geophysical applications, *Geophysical Journal International*, **167**(2), 495–503.
- Polak, E. & Ribière, G., 1969. Note sur la convergence de méthodes de directions conjuguées., *Revue Fr. Inf. Rech. Oper.*, **16-R1**, 35–43.
- Pratt, R. G., 1999. Seismic waveform inversion in the frequency domain, Part 1: Theory and verification in a physical scale models, *Geophysics*, **64**(3), 888–901.
- Pratt, R. G. & Chapman, C. H., 1992. Traveltime tomography in anisotropic media-II. Application, *Geophysical Journal International*, **109**(1), 20–37.
- Pratt, R. G. & Shipp, R. M., 1999. Seismic waveform inversion in the frequency domain, Part 2: Fault delineation in sediments using crosshole data, *Geophysics*, **64**(3), 902–914.
- Pratt, R. G. & Worthington, M. H., 1988. The application of diffraction tomography to cross-hole seismic data, *Geophysics*, **53**(10), 1284–1294.
- Pratt, R. G. & Worthington, M. H., 1990. Inverse theory applied to multi-source cross-hole tomography. Part 1: Acoustic wave-equation method, *Geophysical Prospecting*, **38**(3), 287–310.
- Pratt, R. G., Shin, C., & Hicks, G., 1998. Gauss-Newton and full Newton methods in frequency-space seismic waveform inversions, *Geophysical Journal International*, **133**(2), 341–362.
- Pratt, R. G., Hou, F., Bauer, K., & Weber, M. H., 2004. Waveform tomography images of velocity and inelastic attenuation from the Mallik 2002 Crosshole Seismic Surveys, in *Scientific results from the Mallik 2002 Gas Hydrate Production Research Well Program, Mackenzie Delta, North Territories, Canada*, vol. 585 of **Bulletin**, pp. 1–14, eds Dallimore, S. R. & Collet, T. S., Geological Survey of Canada.
- Pratt, R. G., Sirgue, L., Hornby, B., & Wolfe, J., 2008. Crosswell Waveform Tomography



- in fine-layered sediments: Meeting the challenges of anisotropy, *the 69th Conference and Exhibition of the EAGE, Rome, Italy*.
- Pyun, S., Shin, C., & Bednar, J. B., 2007. Comparison of waveform inversion, part 3: amplitude approach, *Geophysical Prospecting*, **55**(4), 477–485.
- Rao, Y. & Wang, Y., 2008. The Strategies for Attenuation Inversion with Waveform Tomography, *70th EAGE Conference & Exhibition*.
- Ravaut, C., Operto, S., Improta, L., Virieux, J., Herrero, A., & Dell’Aversana, P., 2004. Multiscale imaging of complex structures from multifold wide-aperture seismic data by frequency-domain full-waveform tomography: application to a thrust belt, *Geophysical Journal International*, **159**(3), 1032–1056.
- Scales, J., Docherty, P., & Gersztenkorn, A., 1990. Regularisation of nonlinear inverse problems: imaging the near-surface weathering layer, *Inverse Problems*, **6**, 115–131.
- Sears, T. J., Barton, P. J., & Singh, S. C., 2010. Elastic full waveform inversion of multicomponent ocean-bottom cable seismic data: Application to Alba Field, U. K. North Sea, *Geophysics*, **75**(6), R109–R119.
- Sen, M. K. & Stoffa, P. L., 1991. Nonlinear one-dimensional seismic waveform inversion using simulated annealing, *Geophysics*, **56**(10), 1624–1638.
- Shin, C. & Cha, Y. H., 2009. Waveform inversion in the Laplace-Fourier domains, *Geophysical Journal International*, **177**(3), 1067–1079.
- Shin, C., Koo, N.-H., Cha, Y. H., & Park, K.-P., 2010. Sequentially ordered single-frequency 2-D acoustic waveform inversion in the Laplace-Fourier domains, *Geophysical Journal International*, **181**(2), 933–950.
- Shipp, R. M. & Singh, S. C., 2002. Two-dimensional full wavefield inversion of wide-aperture marine seismic streamer data, *Geophysical Journal International*, **151**(2), 325–344.
- Sirgue, L., 2003. *Inversion de la forme d’onde dans le domaine fréquentiel de données sismiques grands offsets.*, Ph.D. thesis, l’Ecole Normale Supérieure de Paris.
- Sirgue, L. & Pratt, R. G., 2004. Efficient waveform inversion and imaging: A strategy for selecting temporal frequencies, *Geophysics*, **69**(1), 231–248.
- Sirgue, L., Barkved, O. I., Dellinger, J., Etgen, J., Albertin, U., & Kommedal, J. H., 2010. Full waveform inversion : the next leap forward in imaging at Valhall, *First Break*, **28**, 65–70.
- Smithyman, B., Pratt, R. G., Hayles, J., & Wittebolle, R., 2009. Detecting near-surface objects with seismic waveform tomography, *Geophysics*, **74**(6), WCC119–WCC127.
- Song, Z.-M. & Williamson, P. R., 1995. Frequency-domain acoustic-wave modeling and inversion of crosshole data: Part I—2.5-D modeling method, *Geophysics*, **60**(3), 784–

795.

- Song, Z.-M., Williamson, P. R., & Pratt, R. G., 1995. Frequency-domain acoustic-wave modeling and inversion of crosshole data: Part II—Inversion method, synthetic experiments and real-data results, *Geophysics*, **60**(3), 796–809.
- Takam Takougang, E. M. & Calvert, A. J., 2012. Case History Seismic velocity and attenuation structures of the Queen Charlotte Basin from full-waveform tomography of seismic reflection data, *Geophysics*, **77**(3), B107–B124.
- Tarantola, A., 1984. Inversion of seismic reflection data in the acoustic approximation, *Geophysics*, **49**(8), 1259–1266.
- Tarantola, A., 1988. Theoretical background for the inversion of seismic waveforms including elasticity and attenuation, *Pure and Applied Geophysics*, **128**(1-2), 365–399.
- Tarantola, A. & Valette, B., 1982. Inverse Problems = Quest for Information, *Geophysics*, **50**, 159–170.
- Watanabe, T., Nihei, K. T., Nakagawa, S., & Myer, L. R., 2004. Viscoacoustic wave form inversion of transmission data for velocity and attenuation, *The Journal of the Acoustical Society of America*, **115**(6), 3059–3067.
- Williamson, P., 1990. Tomographic inversion in reflection seismology, *Geophysical Journal International*, **100**, 255–274.
- Wu, R.-S. & Toksoz, M. N., 1987. Diffraction tomography and multisource holography applied to seismic imaging, *Geophysics*, **52**(1), 11–25.
- Yamazaki, F. & Shinozuka, M., 1988. Digital Generation of Non-Gaussian Stochastic Fields, *Journal of Engineering Mechanics*, **114**(7), 1183–1197.
- Zeng, Y. Q., He, J. Q., & Liu, Q. H., 2001. The application of the perfectly matched layer in numerical modeling of wave propagation in poroelastic media, *Geophysics*, **66**(4), 1258–1266.

# Chapter 6

## General Conclusions and Discussions

### 6.1 Conclusions

In this thesis, I presented several examples demonstrating that visco-acoustic Laplace-Fourier domain waveform inversion provides quantitative fine-scale velocity and attenuation imaging for crustal exploration data, and cross-well survey data. I used Ocean Bottom Seismograph (OBS) data from the Nankai subduction zone in Chapters 2-4: I formed the reliable and detailed velocity image in detail, and I explored the inversion strategies for the crustal imaging. In Chapter 5, I developed robust inversion strategies for visco-acoustic inversion, and illustrated these with a synthetic study generated using a cross-well geometry. In all inversion experiments, I used local conjugate gradient methods.

In Chapter 2, I presented a high-resolution velocity image obtained by Waveform Tomography for the Nankai subduction zone with an emphasis on geological interpretation. I described the significant geological insights provided by Waveform Tomography: The obtained velocity image successfully delineated features not previously identified in the migration images, as well as imaging the previously identified features. Substantial improvements were recognized in the extensive distribution of low velocity zones extending from the inner to outer wedge, along the mega-splay fault. This suggests the remarkably large area of high pore-pressure regions at the vicinity of the mega-splay fault.

In Chapter 3, I described detailed inversion procedures for the OBS data, and discussed key strategies in the crustal imaging. I also validated the final velocity image by scrutinizing time-domain synthetics, pre-stack depth migration images from the independent studies, source estimates, and resolution tests. Unfortunately a lack of deep boreholes precluded the comparison of estimated velocity values with direct measurements. Future drilling and associated logging data scheduled in 2012 and 2013 by Integrated

Ocean Drilling Project can be used to further verify the Waveform Tomography velocity model.

The key inversion strategies I identified are i) availability of low frequency components and large offset data that reduces non-linearity and increases the depth illumination. ii) A highly accurate traveltime tomography result that further mitigates the non-linearity. iii) Hierarchical inversion approach in which phase spectra are inverted first to reduce artifacts from the acoustic assumption, and amplitude information is only introduced in the final stages. iv) A Laplace-Fourier domain approach that facilitates a multiscale approach to mitigate non-linearity by restricting the inversion to the low frequency components and early arrivals first, and sequentially including higher frequencies and later arrivals. v) Careful preconditioning of the gradient is properly preconditioned to eliminate undesirable high-wavenumber components. vi) A strategy for source estimation that reduce the influence of the instrumental design. Nevertheless, the elastic checkerboard tests revealed that elastic effects were not completely eliminated, and degraded the velocity image below the mega-splay fault which exhibits a large velocity contrast.

In Chapter 4, I evaluated the performance of four classes of  $L_2$  misfit functionals such as i) conventional phase-amplitude, ii) conventional phase-only, iii) logarithmic phase-amplitude, and iv) logarithmic phase-only misfit function. The inversion experiments demonstrated the well-known dependence of the gradient-based optimization methods on the data scalability. The conventional phase-amplitude misfit functional is most severely affected by the scaling issue, and results in a poor subsurface illumination. The useful part of the image was limited to a shallow subsurface and strong velocity discontinuities which corresponds to large-amplitude near-offset traces and strong reflections. The other misfit functionals illuminated much deeper parts of the model than the conventional phase-amplitude misfit functional. These misfit functionals are constructed solely from phase information (conventional and logarithmic phase misfits), or by amplitude scaling (through the use of logarithmic phase-amplitude misfits). The discrepancies in the final inversion results are small for these amplitude-scaled misfit functionals.

From the investigation of the hierarchical two-stage inversion, I confirmed that kinematics is a primary source of velocity information, and that the dynamic information is less informant. I suggested that phase-only inversion is sufficient for the velocity imaging, and the addition of amplitude information has only limited influences on velocity images and also on the data misfit. The amplitude information needs to be incorporated by utilizing the logarithmic phase-amplitude misfit functionals, as the conventional phase-amplitude misfit functional cannot retain the phase fitness obtained by the phase-only misfit functional. This two-stage inversion approach is suitable for suppressing the po-

tential artifacts arising from amplitude errors due to source/receiver coupling effects and elastic effects.

In Chapter 5, I presented inversion strategies for visco-acoustic waveform inversion using a synthetic velocity and attenuation model for a cross-well survey. This multi-parameter problem is ill-posed as a result of different sensitivities and severe cross-talk arises between velocity and attenuation parameters. I demonstrated that the cross-talk is inherent and persistent throughout the inversion. Cross-talk arises from the imperfect convolution (correlation) between back-propagated wavefields, and forward wavefields due to errors in model parameters beyond the resolution, incomplete surface illumination, data band-width, and modelling errors. These imperfections map preferentially into the cross-talk in the attenuation model as a form of unphysical oscillations. In contrast the velocity model is little affected by the cross-talk, because of the scaling between parameter classes. The conventional misfit functional shows little sensitivity to the presence of these artifacts, indicating that the induced oscillations correspond to the model space with the small eigenvalues in the system. Moreover the strong sensitivity of the misfit functional to the velocity structure leads to dominant updates on velocity parameters, and the corruption of the attenuation model, particularly in the early stage of visco-acoustic waveform inversion.

To solve these issues, I proposed an attenuation penalty term that is used to precondition the gradient by controlling the magnitudes of the updates to the attenuation parameters. This strategy is effective for simultaneous inversion of velocity and attenuation, and for sequential inversion (a two-stage approach in which only the velocity models are recovered in the first stage). Further regularization using a smoothing term applied to the attenuation parameters is also effective in reducing the cross-talk, which is often highly oscillatory. The sequential inversion approach restricts the search space for attenuation parameters, and appears to be important in retrieving a reliable attenuation model when strong time-damping is applied. In a final test, I successfully carry out visco-acoustic inversions of noise-contaminated data.

## **6.2 Future study**

### **6.2.1 Perspective on the Nankai subduction data**

The demonstrated reliability and resolution of the velocity image obtained by waveform tomography suggests many possible future research areas in the central part of the Nankai subduction zone. Additional parameter types may be inverted to further constrain rock

properties most particularly associated with pore-fluid distributions. The P-wave attenuation parameter will be the next parameter that should be inverted for, by employing the inversion strategies presented in Chapter 5. The limitation of the acoustic assumption addressed in Chapter 3 needs to be carefully analyzed and in case of excessive disturbances, visco-elastic forward modelling may need to be incorporated even when generating P-wave attenuation images. Full elastic waveform inversion may be investigated as well, as the Poisson's ratio is another class of elastic parameter directly associated with the pore-pressure distribution. The full OBS data set comprises in three components particle-velocity components, and the distinct P-to-S converted wave arrivals studied by Tsuji et al. (2011a) further encourage the application of elastic waveform inversion.

Our P-wave velocity model may be converted to pore-pressure estimates by combining with available well-log information and rock physics (Tsuji et al., 2011b; Saffer & Tobin, 2011). Such study will further contribute to the understanding of the behaviour of the mega-splay fault during and between large earthquakes. Although we provided a qualitative and realistic resolution analysis in Chapter 3, quantitative uncertainty analysis will be useful in estimating the errors in any physical quantities derived from our velocity model.

We did not re-migrate the reflection data due to the lack of the access to the pre-stack reflection data acquired in 2007 (Moore et al., 2007). Re-migration with the new waveform tomography model will surely improve the quality of migration image particularly underneath the outer ridge. Nevertheless, the reflection data set was acquired with a 3D geometry, and the application of 3D acoustic waveform inversion is highly desired. The denser source and receiver distributions will likely enable us to retrieve finer scale structures, and to constrain the structures above the mega-splay fault in the inner wedge where waveform inversion did not provide a clear image. The main concerns regarding the 3D imaging are the computational costs of forward modelling, and the short length of the streamer cables (6 km) from the 3D data. The relatively short cable length will limit the depth of penetration, but will not preclude the application of waveform inversion (Takam Takougang & Calvert, 2011).

## **6.2.2 Perspective on waveform inversion**

### **6.2.2.1 Visco-acoustic waveform inversion**

We demonstrated that a hierarchical regularized inversion approach is important for visco-acoustic waveform inversion. We implemented the approach by employing the Laplace-Fourier domain inversion, by fitting data progressively from the most robust

data component (phase) to least robust component (amplitude), and by sequentially weighting the most robust model component (velocity) to less robust model component (attenuation) as shown in Chapter 5.

The two implementations can be readily combined: First velocity structure is retrieved by employing the phase-only objective function. Then, while still restricting the inversion to velocity parameters, we attempt to fit the remaining amplitude errors arising from geometrical spreading and scattering. This stage needs to be performed by optimizing the logarithmic phase-amplitude misfit functional. Finally velocity and attenuation inversion can be conducted with the conventional phase-amplitude misfit functional. As suggested in Chapter 2, the logarithmic misfit functional may be more suitable to keep the level of fitness in the phase, and this needs to be explored. The second stage may be skipped since the contribution of this amplitude information to the velocity structure is trivial as discussed in Chapter 4, and since the lack of attenuation structures may lead to incorrect velocity model, as suggested in Chapter 5.

### 6.2.2.2 Laplace-domain waveform inversion

While Laplace-Fourier domain waveform inversion is an efficient tool in the implementation of the multiscale method, several issues need further investigation. First accurate first arrival picks are required to suppress excessive amplification of waveforms before the actual first arrivals, as pointed out in Chapter 3. This raises a concern over the application of the method to a data set with a low signal-to-noise ratio, or to a large volume data set like from the 3D surface acquisition. Secondly, an optimal scheduling scheme for temporal frequencies and decay constants has not yet been developed. We implemented the method by inverting for a range of frequency while fixing a decay constant. Shin et al. (2010) suggested a variety of alternative scheduling strategies. Brenders & Pratt (2007) and Kamei et al. (2011) suggested that different scheduling schemes lead to distinct velocity models. However it remains difficult to select the optimal model by means of conventionally employed quality control tools, such as the validity of the predicted waveforms, the comparison with migration images, and the coherency in the source estimates. Thirdly, the relationship between a complex frequency (or complex Laplace constant) and the subsurface illumination have not yet been derived analytically. Laplace-Fourier waveform inversion is equivalent to the frequency-domain waveform inversion with infinite decay constants, and equivalent to Laplace-domain waveform inversion at zero frequencies. Virieux et al. (2012) suggested the Bücklund transform, in which case the equation become equivalent to the diffusive case. We may choose the inverse of the decay constant proportional to a temporal frequency. These observations may lead to deeper under-

standing of the Laplace-Fourier domain inversion, and may aid in the development of an optimal scheduling scheme.

### 6.2.2.3 Optimization methods

Throughout this thesis, model parameters have been estimated using the conjugate gradient method to minimize  $L_2$  objective functions with a relatively simple regularization method. More elaborate optimization methods and regularization methods need to be explored. First, Hessian-based optimization methods may accelerate the convergence, and may serve to handle the data scalability issue described in Chapter 4 for the conventional objective function. Full Newton methods and Gauss-Newton methods may not yet be feasible, due to the computational costs of the Fréchet derivative matrix and the inverse Hessian, and also due to the ill-conditionedness of the Hessian matrix. However Brossier et al. (2009a) demonstrated that the L-BFGS method, a quasi-Newton method, is an effective alternative to the Hessian method; the L-BFGS method replaces the Hessian with the iteratively formed approximate Hessian. It would be interesting to compare the quality of velocity imaging between the combination of the conjugate-gradient method and the phase-only inversion, and that of the L-BFGS method, and the conventional phase-amplitude inversion.

We confirmed in Chapter 4 the importance of selecting an appropriate objective function in yielding the best depth illumination, and in making the inversion well-posed. Our investigation was limited to the velocity model building, and to the objective functions constructed from  $L_2$  data norms. Attenuation inversion may be better posed if we focus on the amplitude information. As demonstrated by Crase et al. (1990) and Brossier et al. (2009b), an  $L_1$  or Huber norm may perform better if the observed data contain outliers. Alternatively the objective function may be formed based on the coherency in the source estimates (Pratt & Symes, 2002) or the coherency of the image-domain gathers (Symes, 2008). The idea of examining source coherencies may be particularly attractive as the function was suggested to be less non-linear than the conventional  $L_2$  norms (Pratt & Symes, 2002).

The ill-posedness of waveform inversion may be further mitigated by implementing additional preconditioning and regularization schemes. For example, a priori knowledge about the subsurface structure may be incorporated by adopting a Laplacian dip filter constructed from migration images (Guitton et al., 2012). For the multiparameter inversion problem, more sophisticated regularization methods (especially Tikhonov methods) may be employed.

The highly non-linear nature of waveform inversion demands a very accurate starting



velocity model. Initial model building based on traveltime tomography methods is usually elaborate, and often requires extensive manual editing of first arrival (or reflection arrival) for successful waveform inversion. The condition may be relaxed by utilizing well-behaved alternative objective function such as the one based on the coherency of source estimates (Pratt & Symes, 2002). Alternatively we may use other velocity building methods to yield the starting model such as the Laplace-domain waveform inversion method proposed by Shin & Cha (2008). Waveform inversion based on global optimization algorithms may one day be used to develop a smooth model within a global minimum (Singh & Minshull, 1994). The computational costs may be overwhelming, but may be manageable by restricting the inversion to the lowest frequency components.

#### **6.2.2.4 Towards 3D full elastic waveform inversion**

The ultimate goal of waveform inversion may be the extraction of full elastic tensors spatially distributed in 3D from entire seismic records. While the recovery of all 21 parameters is not yet practical, the maturity of 2D acoustic inversion suggests the development of waveform inversion can be more focused on 2D elastic and 3D acoustic waveform inversion.

Various 3D implementation has already been employed extensively in hydrocarbon exploration by using both time-domain methods and frequency-domain methods (Ben-Hadj-Ali et al., 2008; Vigh & Starr, 2008; Sirgue et al., 2010). To date these have been implemented with acoustic assumption, without the application of time-damping. The application of Laplace-Fourier waveform inversion may be costly, but worth investigation. Moreover as suggested for the Nankai subduction data set, 3D waveform inversion may be applicable to academic data sets. Perhaps the more important development for the crustal-scale imaging may be a 2.5 D implementation (Song & Williamson, 1995; Zhou et al., 2012), which enables the proper handling of point-sources, and also to incorporate exact geometries of out-of-plane sources and receivers geometries (Smithyman & Clowes, 2013).

The hierarchical approach will be an critical element in elastic, and possibly anisotropic waveform inversion, as suggested by Tarantola (1986), Brossier et al. (2009a), Sears et al. (2010). Careful handling of variable model parameter sensitivities and cross-talk is critical in developing optimum regularization schemes, and multiparameter inversion strategies: Singular value decomposition, while expensive, will provide critical insights into the problem. The objective function may also need to be scrutinized, as each model parameter class naturally influences waveforms in a distinct manner.

The time has come for waveform inversion to depart from a simple 2D acoustic world,

to more realistic but more complicated 3D anisotropic visco-elastic world. Of course the development of waveform inversion for such a system is a medium to long term research program. It is important to identify and prioritize those physical parameters which is resolvable and significant in the data. In this fashion, deeper insights into the subsurface geological processes and systems can emerge.

## References

- Ben-Hadj-Ali, H., Operto, S., & Virieux, J., 2008. Velocity model building by 3D frequency-domain, full-waveform inversion of wide-aperture seismic data, *Geophysics*, **73**(5), VE101–VE117.
- Brenders, A. J. & Pratt, R. G., 2007. Full waveform tomography for lithospheric imaging: results from a blind test in a realistic crustal model, *Geophysical Journal International*, **168**(1), 133–151.
- Brossier, R., Operto, S., & Virieux, J., 2009a. Seismic imaging of complex onshore structures by 2D elastic frequency-domain full-waveform inversion, *Geophysics*, **74**(6), WCC105–WCC118.
- Brossier, R., Operto, S., & Virieux, J., 2009b. Robust elastic frequency-domain full-waveform inversion using the L1 norm, *Geophysical Research Letters*, **36**(20), L20310.
- Cruse, E., Pica, A., Noble, M., McDonald, J., & Tarantola, A., 1990. Robust elastic nonlinear waveform inversion: Application to real data, *Geophysics*, **55**(5), 527–538.
- Guittou, A., Ayeni, G., & Díaz, E., 2012. Constrained full-waveform inversion by model reparameterization, *Geophysics*, **77**(2), R117–R127.
- Kamei, R., Brenders, A. J., & Pratt, R., 2011. A discussion on the advantages of phase-only waveform inversion in the Laplace-Fourier domain: Validation with marine and land seismic data, *SEG Technical Program Expanded Abstracts*, pp. 2476–2481.
- Moore, G. F., Bangs, N. L., Taira, A., Kuramoto, S., Pangborn, E., & Tobin, H. J., 2007. Three-Dimensional Splay Fault Geometry and Implications for Tsunami Generation, *Science*, **318**(5853), 1128–1131.
- Pratt, R. & Symes, W., 2002. Semblance and differential semblance optimisation for waveform tomography: a frequency domain implementation, in *Sub-basalt imaging, Journal of Conference Abstracts*, vol. 7, pp. 183–184.
- Saffer, D. M. & Tobin, H. J., 2011. Hydrogeology and Mechanics of Subduction Zone Forearcs: Fluid Flow and Pore Pressure, *Annual Review of Earth and Planetary Sciences*, **39**(1), 157–186.
- Sears, T. J., Barton, P. J., & Singh, S. C., 2010. Elastic full waveform inversion of

- multicomponent ocean-bottom cable seismic data: Application to Alba Field, U. K. North Sea, *Geophysics*, **75**(6), R109–R119.
- Shin, C. & Cha, Y. H., 2008. Waveform inversion in the Laplace domain, *Geophysical Journal International*, **173**(3), 922–931.
- Shin, C., Koo, N.-H., Cha, Y. H., & Park, K.-P., 2010. Sequentially ordered single-frequency 2-D acoustic waveform inversion in the Laplace-Fourier domains, *Geophysical Journal International*, **181**(2), 933–950.
- Singh, S. C. & Minshull, T. a., 1994. Velocity structure of a gas hydrate reflector at Ocean Drilling Program site 889 from a global seismic waveform inversion, *Journal of Geophysical Research*, **99**(B12), 24221–24233.
- Sirgue, L., Barkved, O. I., Dellinger, J., Etgen, J., Albertin, U., & Kommedal, J. H., 2010. Full waveform inversion : the next leap forward in imaging at Valhall, *First Break*, **28**, 65–70.
- Smithyman, B. R. & Clowes, R. M., 2013. Waveform tomography in 2.5D: Parameterization for crooked-line acquisition geometry, *Journal of Geophysical Research (under review)*.
- Song, Z.-M. & Williamson, P. R., 1995. Frequency-domain acoustic-wave modeling and inversion of crosshole data: Part I—2.5-D modeling method, *Geophysics*, **60**(3), 784–795.
- Symes, W. W., 2008. Migration velocity analysis and waveform inversion, *Geophysical Prospecting*, **56**(6), 765–790.
- Takam Takougang, E. M. & Calvert, A. J., 2011. Application of waveform tomography to marine seismic reflection data from the Queen Charlotte Basin of western Canada, *Geophysics*, **76**(2), B55–B70.
- Tarantola, A., 1986. A strategy for nonlinear elastic inversion of seismic reflection data, *Geophysics*, **51**(10), 1893–1903.
- Tsuji, T., Dvorkin, J., Mavko, G., Nakata, N., Matsuoka, T., Nakanishi, A., Kodaira, S., & Nishizawa, O., 2011a.  $V_p/V_s$  ratio and shear-wave splitting in the Nankai Trough seismogenic zone : Insights into effective stress , pore pressure , and sediment consolidation, *Geophysics*, **76**(3), WA71–WA82.
- Tsuji, T., Hino, R., Sanada, Y., Yamamoto, K., Park, J.-O., No, T., Araki, E., Bangs, N., von Huene, R., Moore, G., & Kinoshita, M., 2011b. In situ stress state from walk-around VSP anisotropy in the Kumano basin southeast of the Kii Peninsula, Japan, *Geochemistry Geophysics Geosystems*, **12**(9), 1–18.
- Vigh, D. & Starr, E. W., 2008. 3D prestack plane-wave, full-waveform inversion, *Geophysics*, **73**(5), VE135–VE144.

- Virieux, J., Brossier, R., Garambois, S., Operto, S., & Ribodetti, A., 2012. Making Seismic Data as CSEM Data through the Backlund Transform, *EAGE Expanded Abstracts, EAGE Saint Petersburg International Conference & Exhibition (Ru)*, p. B002.
- Zhou, B., Greenhalgh, S., & Greenhalgh, M., 2012. Wavenumber sampling strategies for 2.5-D frequency-domain seismic wave modelling in general anisotropic media, *Geophysical Journal International*, **188**(1), 223–238.

# Curriculum Vitae

**Name:** Rie Miyoshi (Kamei)

**Post-Secondary Education and Degrees:** Kyoto University  
Kyoto, Japan  
2003 B.Eng.

Kyoto University  
Kyoto, Japan  
2005 MEng.

The University of Western Ontario  
London, ON, Canada  
2012 Ph.D.

**Honours and Awards:** Best presentation in 112th Meeting, Society of Exploration Geophysicists In Japan  
2010

**Related Work Experience:** Teaching Assistant  
Kyoto University, Queen's University, The University of Western Ontario  
2003 - 2011

Research Internship  
Internship at TOTAL USA in Houston, United States  
2010

## **Publications:**

Kamei, R., Hato, M., Matsuoka, T. 2005 Random heterogeneous model with bimodal velocity distribution for Methane Hydrate exploration, *Exploration Geophysics*, **36**, 41-49.

Kamei, R., Pratt, R. G., Tsuji, T., 2012. Waveform Tomography Imaging of a Megasplay Fault System in the Seismogenic Nankai Subduction Zone, *Earth and Planetary Science Letters*, **317-318**, 343-353.

Kamei, R., Pratt, R. G., Tsuji, T., 2012. On Acoustic Waveform Tomography of wide-angle OBS data - Strategies for preconditioning and inversion. *Submitted to Geophysical Journal International*.

Kamei, R., Pratt, R. G., 2012, Inversion strategies for visco-acoustic waveform inversion. *Submitted to Geophysical Journal International*

Kamei, R., Pratt, R. G., Tsuji, T., 2012. On misfit functions for Laplace-Fourier waveform inversion, with applications to wide-angle OBS data. *Submitted to Geophysical Prospecting*

Tsuji, T., Kamei, R., Pratt, R. G., 2012. Evolution of sequential mega-splay faults and the forearc basin in the Nankai Trough. *Submitted to Geophysical Research Letters*

## **Referred conference paper:**

Kamei, R., Matsuoka, T., 2005. Random Heterogeneous Velocity Model Application to Methane Hydrate Exploration, , *the 66th Conference and Exhibition of the EAGE*, Madrid, Spain.

Kamei, R., Pratt, R.G., 2008. Waveform Tomography strategies for imaging attenuation structure with cross-hole data, *the 69th Conference and Exhibition of the EAGE*, Rome, Italy.

Kamei, R., Pratt, R. G., 2010. Acoustic Waveform Tomography of OBS data in the Nankai subduction zone, *the 81st SEG Annual Meeting*, Denver.

Kamei, R., Pratt, R. G., Tsuji, T., 2011. Waveform Tomography imaging of deep crustal faults — Application to Nankai Subduction Zone, *the 72nd EAGE Conference & Exhibition*, Vienna, Austria.

Kamei, R., A. Brenders, Pratt, R. G., 2011. A discussion on the advantages of phase-only waveform inversion in the Laplace-Fourier domain: Validation with marine and land seismic data, *the 82nd SEG Annual Meeting*, San Antonio.

Kamei, R., Pratt, R. G., T., Tsuji, 2011. Waveform Tomography Imaging of a Megasplay Fault System in the Seismogenic Nankai Subduction Zone, *the 10th SEGJ International*

*meeting*, Kyoto, Japan.

Pratt, R. G., Kamei, R., Brenders, A., 2011. Full Waveform Inversion: A hierarchical approach from Traveltime Tomography through Acoustic Waveform Tomography, *the 10th SEGJ International meeting*, Kyoto, Japan.

Afanasiev, M., Pratt, R. G., Kamei, R., 2012. Crosshole waveform inversion: Quantifying anisotropy through simulated annealing, *the 73rd SEG Annual Meeting*, Las Vegas.

Kamei, R., Pratt, R. G., 2012. Wide-band multifrequency waveform inversion in the Laplace-Fourier domain, *the 73rd SEG Annual Meeting*, Las Vegas.